UNIVERSITÀ
DEGLI STUDI
DI PADOVA

Sede Amministrativa: Università degli Studi di Padova

Dipartimento di Ingegneria Industriale

CORSO DI DOTTORATO DI RICERCA IN INGEGNERIA INDUSTRIALE
CURRICULUM: Ingegneria Energetica
CICLO XXXIII

STUDY OF BODY FORCE MODELLING FOR COUPLED FAN/AIRFRAME SIMULATIONS

Coordinatore: Ch.ma Prof.ssa Luisa Rossetto
Supervisore: Ch.mo Prof. Ernesto Benini

Dottorando: Andrea Magrini

Abstract

Future aircraft concepts proposed to alleviate the environmental impact of the ever-growing aviation sector feature airframe-embedded engines or ultra-high bypass ratio turbofans installed on the wings. In either cases, a tight propulsive system integration will expose the engine fan to distorted inflow conditions, generated by S-shaped intake ducts, short nacelle cowls or boundary layer ingestion. This thesis presents a study of a body force model as a coupled simulation approach for fan/intake interaction. Without properly replicating the fan effect, in fact, the simulations of these novel aircraft configurations not always provide physically consistent results, and neither the required fan design can be properly studied. In the thesis, the trend towards ultra-high bypass engines as mid-term evolution is first analysed, showing the importance of an integrated approach for their design and performance evaluation at system level. After that, the development of a compressible Reynolds-Averaged flow solver as a stand-alone tool where a selected body force model has been implemented is reported. Indications on model calibration, data extraction from higher-fidelity simulations, validity, accuracy and limitations are provided, using a high-bypass transonic fan as reference model, validated against experimental data. Finally, the set of developed numerical tools is employed to carry out a sensitivity study on the aerodynamics of nacelle intakes at high incidence, comparing the standard decoupled approach with the body force model.

Sommario

Le architetture aeronautiche proposte per alleviare il crescente impatto ambientale del settore dell'aviazione si caratterizzano per la presenza di motori integrati nella fusoliera ovvero installati sulle ali, ma ad elevatissimo rapporto di diluizione. In entrambi i casi, lo stretto accoppiamento tra telaio e sistema propulsivo incrementa l'esposizione della soffiante del motore a condizioni di ingresso distorte, generate da prese dinamiche ad S, gondole con prese d'aria corte, o ingerimento dello strato limite. Questa tesi presenta lo studio di modelli a forze di volume come approccio accoppiato per la simulazione dell'interazione soffiante/presa dinamica. L'assenza di una corretta replicazione dell'effetto della soffiante, infatti, porta a risultati non sempre fisicamente coerenti ed impedisce l'adeguata progettazione delle pale. La tesi affronta dapprima l'evoluzione verso l'impiego di motori ad altissimo rapporto di diluizione, come rimedio a medio termine, mostrando l'importanza di un approccio integrato per la progettazione e la valutazione delle prestazioni propulsive a livello di sistema. In seguito, è descritto lo sviluppo di un codice comprimibile per equazioni di Navier-Stokes mediate alla Reynolds, quale strumento a sé stante in cui è stato implementato un modello a forze volumetriche derivato dalla letteratura. Il documento riporta indicazioni relativamente alla calibrazione del modello, l'estrazione di dati da simulazioni a maggiore livello di affidabilità, la validità, l'accuratezza e le limitazioni dell'approccio. Il caso di riferimento adottato consiste in una moderna soffiante transonica ad elevato rapporto di diluizione, per cui è stato validato un modello computazionale a partire da dati sperimentali. Infine, l'insieme degli strumenti di analisi sviluppati è stato impiegato per uno studio di sensibilità dell'aerodinamica di prese d'aria di motori a turboventola operanti ad alta incidenza, confrontando l'approccio standard disaccoppiato con il modello a forze volumetriche.

Contents

List of Figures

List of Tables

Abbreviations

ACR Area Capture Ratio.

AD Actuator Disk.

BFM Body Force Model.

BLI Boundary Layer Ingestion.

BPR By-Pass Ratio.

CFD Computational Fluid Dynamics.

CFL Courant-Friedrichs-Lewy number.

CRM Common Research Model.

CST Class/Shape Transformation.

FDM Finite Difference Method.

FEM Finite Element Method.

FPR Fan Pressure Ratio.

FVM Finite Volume Method.

GTF Geared Turbo Fan.

LPT Low Pressure Turbine.

MFCR Mass Flow Capture Ratio.

OPR Overall Pressure Ratio.

PSI Propulsion System Integration.

RANS Reynolds-Averaged Navier-Stokes.

SA Spalart-Allmaras.

SFC Specific Fuel Consumption.

SLC Streamline Curvature.

TDB Thrust/Drag Bookkeeping.

TET Turbine Entry Temperature.

TPR Total Pressure Ratio.

TPS Turbo-Powered Simulator.

TSFC Thrust Specific Fuel Consumption.

TTR Total Temperature Ratio.

UHBPR Ultra-High By-Pass Ratio.

VAN Variable Area Nozzle.

VHBPR Very-High By-Pass Ratio.

VPF Variable Pitch Fan.

Nomenclature

C_d Drag coefficient.

C_l Lift coefficient.

C_m Moment coefficient.

C_p Pressure coefficient.

M Mach number.

Re Reynolds number.

α angle of attack.

γ Specific heat ratio.

μ Dynamic viscosity.

b blockage factor.

f_n Normal force.

f_p Parallel force.

Chapter 1

Introduction

1.1 Introduction

On 2 May 1952, the first passenger flight on a jet propelled aircraft, the De Havilland DH106 Comet, took off from London, towards Johannesburg. Despite nowadays the date and the event are not that much remembered, they marked an historical turn towards a new era of human mobility. The civil aviation market has seen an impressive growth ever since, with an outlook of further increasing the number of transported passengers by a factor of 7 by 2050 [122]. The scientific evolution of the relatively young flight science and the huge technological progress in many other fields have led, in about 50 years, to a substantial improvement of noise, pollutant emissions, and fuel consumption. For instance, the fuel burnt per seat of a Boeing 777-200, a 2000s aircraft, was only 30% of that of the Comet [17]. The individual aircraft evolution, however, have been offset by the huge growth of the volume of flights. In response to this overall negative trend, international institutions have set ambitious targets to mitigate the environmental impact of the aviation sector. In 2001, European Commission ACARE 2020 vision [44] foresaw a 50% reduction in fuel-burn and noise, and 80% in take-off/landing NOx emissions, relative to year-2000 aircraft. Whilst these targets will not be achieved, a new FlightPath 2050 vision [72] has been released in 2011, requiring new limits of 75%, 65% and 90% on the same basis, respectively. This needs, therefore, the seek of either new technological stepchanges or novel aircraft paradigms.

In parallel to futuristic designs [92], a smoother change of current technology is also pursued, on a shorter-term basis. On the engine side, the propulsive efficiency can be theoretically improved by lowering the specific thrust [19], while increased Overall Pressure Ratio (OPR) and Turbine Entry Temperature (TET) improve the thermal efficiency[119]. Low specific thrust engines feature reduced Fan Pressure Ratio (FPR) and higher By-Pass Ratio (BPR), directly improving the specific fuel consumption and the noise figures [109, 197, 305]. The benefits brought about by high BPR are, nonetheless, counterbalanced by increased fan diameter, nacelle drag, engine weight, and enhanced installation effect of the propulsive unit. Overall, there is a risk that the gains in uninstalled engine performance are totally or partially lost upon system integration[158].

The installation effect is traditionally quantified by the difference between the individual component performance in isolated condition and the performance after assembly into the wing body [298]. Its phenomenology is due to alteration of pressure and velocity fields due to the presence of nacelle, pylon and jet efflux from nozzles [217]. Hence, a number of problems are to be tackled to allow for full exploitation of Ultra-High By-Pass Ratio (UHBPR) engines. Without a careful evaluation of system aspects, more traditional procedures based on sequential and decoupled design are likely to fail in finding a real working optimum. This encourages a tighter cooperation between the engineers working on different aspects of the air vehicles, as the sensitivity of engine operating conditions to the external flow field, and vice versa, is becoming more relevant.

In that respect, developing more coupled procedures for the design and the analysis of turbofan engines featuring a closely coupled airframe integration or operating with an inherent sensitivity to the airframe presence has become mandatory for their deployment. This thesis is focused on the evaluation of the suitability of a reduced order model to better represent the effect of the fan on the flow field, especially at specific flight conditions where this is strongly affected by the fan/intake interaction. The numerical method, which is referred to as body force in the literature, finds a large applicability in all those situations where it is important, if not indispensable, to model the fan as a responsive system that exerts a compression work on an incoming fluid and reacts to the boundary conditions in accordance with the conservation principles. Body force models have been found to greatly improve the simulation of intake flows at incidence and crosswind, providing sound solutions for boundary layer ingesting configurations and allowing to have a first-order prediction also of the fan characteristics in distorted conditions. Before entering into the details of the model, the currently available methods that are applied to design the nacelle components and to study the interactions with the airplane structure are presented.

The following sections give an overview of UHBPR engines design studies in terms of thermodynamic cycle, nacelle, and exhaust, to show how these are affected by the increased bypass ratio and how it impacts the sizing of the main aircraft components. The challenges related to UHBPR turbofans implementation are thus highlighted, also from the point of view of experimental testing, delineating the framework in which the scope of this study lies. In the following chapter, a more detailed analysis of numerical methods for installed engines and the limitations of a decoupled approach in fan/intake modelling for some cases are provided, to motivate the purpose of the present research.

1.2 Installation effects on UHBPR engine design

The adoption of high BPR engines to increase propulsive efficiency, specific fuel consumption and noise signatures brings about a series of issues and challenges that were already clear when their adoption was first considered. Borradaile [19] effectively described the difficulties associated to high BPR, low specific thrust units: conflicting requirements for nacelle design, reduced stability margin and inlet distortion for low FPR fan, fan - Low Pressure Turbine (LPT) coupling, reduced noise frequency and problem-

atic integration of the powerplant. All these topics characterise the UHBPR turbofans and, as it will be shown throughout the review, this has pushed the scientific and industrial community towards elaborating advanced design and analysis tools to propose remedies in each area.

Zimbrick [305], comparing low BPR turbofans of early '90s with the advantages in Thrust Specific Fuel Consumption (TSFC) achievable by using UHBPR engines, described the chain of effects caused by low Specific Fuel Consumption (SFC) units. A number of conflicting requirements associated to an UHBPR are immediately evident, for which an optimal choice of the relevant parameters must consider several aspects at the same time, making the design more complex and interdependent. The relationship between BPR, FPR, OPR and TSFC is provided in [169]. Considering integration effects, the optimal bypass ratio minimising the TSFC is expected to fall between 14 and 16 for a small class airplane, with a corresponding FPR as low as 1.3 [224]. Guha [93] derived an explicit analytical equation linking the optimum fan pressure ratio to BPR, ambient conditions, specific thrust and efficiency of energy transfer between the core and bypass flow.

A number of studies in open literature was devoted to analysing possible engine configurations for UHBPR, aimed at estimating the best compromise solutions and technologies, needed to conciliate some of the requirements. In the following section the engine concepts cycle design proposed for UHBPR are reviewed.

1.2.1 Engine concepts and cycle design

The design of different UHBPR engine concepts and thermodynamic cycles reported in the literature are based on predictive assessments of operational costs and propulsive efficiency, considering how they are impacted by installation effects. Christie [39] proposed a Propulsion System Integration Model (PSIMOD) for the engine cycle design. Its model assessed the propulsion system integration and, furthermore, the overall flight characteristics and mission fuel burn.

UHBPR fan installation on hybrid and all-lifting aircraft concepts is described in Felder [75] and Hall [99] for two different wing bodies, where distributed electric propulsion is employed to decouple power generation and usage and realize an effective higher bypass ratio with large low FPR embedded Boundary Layer Ingestion (BLI) fans.

Larsson [146] conceptually designed a Geared Turbo Fan (GTF) and a geared open rotor engines with Entry Into Service (EIS) in year 2020. A number of constraints regarding engine components and operability for a short haul application were considered. Kestner [132], Krishnan [140], Aloyo [5] and Yang [294] conducted trade-off studies for GTF, Variable Area Nozzle (VAN) and Variable Pitch Fan (VPF) for UHBPR engines. Daggett [49] presented a 2003 NASA research on Ultra Efficient Engine Technology (UEET), addressed to assess the performance of three advanced General Electric (GE) and Pratt & Withney (P&W) powerplants on a technology study airplane. The study is unique in defining optimum fan diameters for high bypass ratio turbofan, targeting 2015-year UEET. A parent aircraft, Boeing 777-200ER, was re-adapted with new optimised composite wing and three sizes of baseline GE90-94B and P&W PW4090

engines were considered. The GE family featured an advanced direct drive counter-rotating fan, while the P&W had a geared fan on medium and big engine. Among the three engine sizes, the medium one appeared to be the best suited, featuring a BPR 14.3 with an approximate fan diameter of 3.604 m.

Bijewitz [16] presented a similar study of two evolutionary improved UHBPR turbofan engines for an entry-into-service of year 2035+, for a medium to long range advanced aircraft of 340PAX. It was found that the optimum BPR and the relative improvement potential are dependent on the assumptions of the technology level, the associated component efficiencies, the block fuel exchange rates for SFC, and the drag and weight. Berton [15] carried out an optimisation of engine independent design parameters for an aircraft of Boeing 737 class. The outcome of the study suggested that low ramp weight, used as a cost indicator, could be minimised by high-FPR (1.70), high-OPR , direct-drive turbofan. In a follow-up analysis [96], the authors partially revised some of the assumptions of the first research, but in terms of aircraft system, the trend of the first study was confirmed.

Giesecke [81] carried out a thermodynamic and mechanical investigation of an over-wing UHBPR for a regional aircraft. The engine technology level was extrapolated for year 2025. Compared to the fixed nozzle UHBPR engine with standard under the wing installation, the over-the-wing mounted VAN turbofan was claimed to bring an additional 1.7% reduction in fuel mass per mission and a 0.8% lower DOC. The five-year EU FP7 project ENOVAL, ended in June 2018, addressed low pressure system of UHBPR (12-20), ultra-high OPR (50-70) engines [45]. The project analysed numerous components and aspects of modern turbofan, from low pressure ratio, low noise fan modules, including low pressure spool and power gear-box (PGB), to aeroacoustic technologies and components design, manufacturing and integration. The wide number of methods and topics examined, and the results achieved in terms of extension of technology readiness level (TRL), are expected to have an important outcome in future engine systems.

Given the complexity of the problem affecting a full exploitation of larger BPR, it has been shown by various authors that simultaneous attainment of cost and emission indicators is likely to be possible only in a Pareto optimal sense, in a way that the best configuration depends on which aspect is considered predominant. The segment most involved in UHBPR is the 300PAX class, like Boeing 777-200 and Airbus A330 aircraft, where gains in SFC have a big leverage. Moreover, higher BPR can be more easily accommodated. Summary of reviewed research suggested engine diameter now exceeding 3 m, with optimal BPR between 14 and 16. According to Dagget [49], lowering FPR below 1.4 would result in further enlargement of fan size, and the increased nacelle weight and drag were found to offset the efficiency gain once the engine is installed.

1.2.2 Nacelle design

Despite the complexity of all the phenomena related to installation, the single components are typically first optimised for individual performance, allowing to applied established procedures in the decoupled design, where constraints other than aerodynamic can be more easily included. In particular, the design of the nacelle external cowl

appears as a constrained problem where multiple operating conditions and geometric bounds must be considered [305]. Dagget [49] describes the main parameters defining the nacelle size. Among them, the overall length L_{nac} and maximum diameter D_{max} are the most important. An optimal trade-off exists, for which the total drag is minimised. The multiple operating conditions and metrics naturally specify a multi-point and multi-objective problem that can be best addressed using CFD and optimisation algorithms.

Albert [3] presented a fully automatic procedure for nacelle and intake multi-point optimisation at cruise and static run for minimum peak Mach number, using Class/Shape Transformation (CST) [141, 142], B-Spline and Super-ellipse polynomial model (SP) parameterisation. The CST led to best results, with peak Mach numbers at cruise reduced up to 14% in the external cowl. Christie [40] employed a generalisation of this method (iCST) for nacelle geometry definition. Robinson [215] used the tool to carry out multi-objective optimisation for a fixed length nacelle, designed for two UHBPR engine architectures. Tejero [249, 250] used the same framework to derive the relative importance of the design variables and general guidelines for shape factors of short and slim nacelles. Fang [74] previously used the combination of CST+Kriging for axisymmetric and 3D nacelle optimisation. The adoption of elaborated tools based on automatic shape optimisation, statistical analysis and meta-modelling appears to have become a standard in the multi-objective constrained design of nacelle.

1.2.3 Exhaust design

Similarly to the nacelle cowl, the exhaust system where the mass flow elaborated by the engine is ejected into the free stream is subject to pressure forces acting on its surfaces that are also affected by integration and determine a thrust variation [173]. The nozzle internal drag is about 1.5-2% of engine thrust, amounting to 15-20 drag counts. The scrubbing drag introduces an additional 0.3-0.9% thrust loss [67]. Moreover, as the BPR is increased the engine sensitivity to variations of gross thrust in enhanced, requiring high-fidelity CFD models and advanced tools for geometry parameterisation, design space exploration and data post-processing of exhaust system.

Zhang [303] pointed out the accuracy requirements for thrust estimation from nozzle simulation. The accuracy of CFD solutions of nozzle flows was tested and improved throughout a series of AIAA Propulsion Aerodynamic Workshops [38, 256, 257]. Goulos [90] presented an integrated framework for separate-jet nozzle design. The sensitivity of performance metrics with respect to the physical dimensions were studied in a DSE and design guidelines were provided. In a following study [91], a response surface model based was employed for optimisation of overall velocity coefficient (core + bypass), reaching a 1.4% increase in net thrust.

Wang [283] performed LES on an UHBPR jet exiting from an isolated serrated nozzle, to predict near-field turbulence and far-field acoustics. Tyacke [269] continued the study in the installed case using LES-RANS, to produce a large high-fidelity validated aeroacoustic database of installed engines. Among other problems, indeed, noise gen-

eration is becoming quite important with the constant enlargement of civil aviation volume, and it is another aspect influenced by mutual interaction of aircraft components.

The European research (FP6) project VITAL [51, 63, 116, 280] characterised the installation effects for a high BPR engine using advanced numerical and measurement techniques. Dezitter [63] examined the accuracy of CFD solvers for predicting the aerodynamic flows of different nozzles installed under the wing. The CFD solvers were found appropriate for capturing the installation effects and a serrated nozzle produced a low-frequency reduction and a high-frequency increase in the acoustic signature.

1.3 Experimental approaches for powered engine simulators

In the past, due to the inadequacy of numerical tools, the quantification of engine installation penalties was assessed primarily in wind tunnels [23, 33, 298]. Even with the availability of more powerful resources and turbulent flow solvers enabling to do this analysis via CFD, experimental tests still represent an indispensable stage. Engine simulation is a key component in wind tunnel testing of engine-airframe integration. A powered engine simulator (PES), i.e. a fan stage inside a nacelle, is a complete approach to simulating engine inlet and exhaust. Traditionally, they have been predominantly powered by air turbines Turbo-Powered Simulator (TPS), fed with externally supplied compressed air. In wind tunnel testing the replication of only certain flow similarity parameters is strived for, given the impossibility of fully satisfying all the dynamic similarities. De Wolf [288] discussed TPS technology and similarity with increasing bypass ratio. In the case of externally supplied airflow, the total mass flow rate at inlet is deficient, and intake shape must be modified to replicate pressure distribution [144].

One of the key issues in wind tunnel testing with installed engines is the correct determination of the net thrust delivered by the engine simulator. In general the wind tunnel balance measures the overall forces and moments occurring on the model. The installed drag is computed by subtracting to the net balance force the thrust produced. The latter is obtained from TPS calibration, where static thrust is measured at controlled discharge conditions. Typical accuracies on gross thrust values are 0.2 - 0.3 percent of the full thrust value [103, 288]. Procedure descriptions can be found in [52, 69, 137, 138]. Von Geyr [79] elaborated precise definitions of engine simulator calibration coefficients in wind tunnel experiments and numerical computations. The external flow Mach number was identified as being important in the thrust bookkeeping. Burgsmuller [26] presented a general and qualitative overview of TPS testing. AGARD [173] and Covert [47] provided guidelines for thrust measurement mainly for in-flight situations, but some work can also be transferred to wind tunnel testing. In an early paper, Hall [102] and later on Mikkelsen [174] discussed functional dependencies for discharge and thrust coefficients for (long radius ASME) nozzles and venturi ducts. Mikkelsen [175] concluded that CFD and experimental results are complementary and that both are required for effective performance determinations. Wright [290] demonstrated statistical error analysis of the velocity coefficient of a flow-through nacelle. Yoder [296] and Dippold [297] compared experiments and CFD results for discharge and thrust co-

efficients of different types of (mostly conical) convergent nozzles. A similar study was performed earlier by Thornock [255] comparing experiment and analytical expressions. Harris [103] described wind tunnel testing with TPS technology over the course of time.

Burgsmuller [27] presented an overview of the work carried out in past European framework programmes, for three engine types, namely a conventional turbofan, a VHBR and an UHBR. Wind tunnel testing and CFD simulations showed lift loss and drag increase upon engine installation increasing with bypass ratio. McCall [168] highlighted some key results of wind tunnel tests with high bypass ratio engine nacelles in various configurations and sizes. Doornbos [66] gave an overview of TPS testing procedures in the wind tunnel to obtain interference drag values for half-models. Tompkins [261] described relatively modest modification of exhaust nozzles of an existing TPS unit to move from low bypass, high fan pressure ratio to high bypass, low fan pressure ratio simulation. Hoheisel [110] discussed essential engine simulation parameters and focuses on the thrust ratio between TPS and full scale engine, examining its influence on drag behaviour using theory, CFD and wind tunnel experiments conducted in various European programs. Welge [286] described in quite some detail a TPS testing procedure for installed testing of the DC-10 aircraft with an intermediate wind-on assessment of the isolated engine simulator. Shea [228] used TPS on a blended-wing-body aircraft in NASA's NFAC, reporting calibration strategies and propulsion-airframe integration results.

In summary, powered engine simulators represent a key technology for the empirical verification of the aircraft system performance and the huge amount of work in the past has led to established procedures for model scaling and accurate data quantification. However, in the framework of the tighter coupling between engine and airframe for UHBPR turbofan, a series of issues emerges, related to duplication parameters, calibration procedures, TPS operation, thrust/drag bookkeeping. The effect of the external flow field on thrust calculation, the possibility of nozzle suppression, the core and bypass jet interference, the absence of core flow, are all topics that wind tunnel specialists will have to cover, eventually adapting the existing procedures to account for the specificity of UHBPR engines.

1.4 Scope of the work

The challenges related to UHBPR implementation have been briefly described, first presenting how the key design parameters of the engine cycle are modified when considering the chain of effects related to high-BPR, low-SFC units, and what the reviewed literature suggests as optimal ranges. The advances in modelling and optimisation of nacelle components have also been presented, highlighting the importance acquired by statistical and optimisation methods to derive figures of merits between the geometric design variables. Finally, the engine simulators for wind tunnel tests have been shortly reviewed.

The complexity of the interactions characterising the novel UHBPR turbofans requires the employment of advanced numerical tools and empirical verification through

experimental campaigns, in order to measure the global system performance and ensure that the improvement in individual components is not lost after their assembly. However, in view of the enlarged intersection between the domain of dependence of each subsystem, a revision of common approaches for computational and experimental simulations should be pursued. The enhanced sensitivity of the engine working point to ambient conditions invites the adoption of closely coupled models for estimating its response in the numerical environment and the assessment of duplication parameters, thrust calculation and TPS operation during wind tunnel tests.

This PhD programme is focused on the study of an engine blade model based on a body force distribution. By approximately representing the effect of the compressor rows on the flow, body force models allow to capture the main physical features of fan/intake coupling and reproduce complex flow patterns arising in specific flight conditions, like take-off, crosswind operation, boundary layer ingestion, and inlet distortion, without a direct simulation of the entire compression rig, thus greatly reducing the computational effort. Whilst the motivation to employ such a tool has been preliminarily given through the review of the installation effects on UHBPR engines and the outlook of future airplane concepts, its adoption is still limited and the literature is deficient in thoroughly reporting its true nature in terms of fidelity, reliability, accuracy and validity. The work was articulated in three main stages, with the purpose of developing a platform where to implement, test and validate the body force model, in order to acquire a more complete understanding of the method before employing it in suitable applications.

Chapter 2 reviews the computational approaches for the simulation of installed engines and the available models for the simplified representation of compressor blade rows. Chapter 3 describes the stand-alone fluid dynamic solver developed to implement the selected model, serving as a computational platform allowing to test different formulations and approaches to validate the implementation versus higher-fidelity tools and experimental data. Chapter 4 thoroughly presents this validation activity, assessing the calibration procedure, the duplicated parameters, the domain of validity, the limitations and the issues of the body force model. Having examined in detail its behaviour, chapter 5 reports its application to intake flows, evaluating the influence of geometric parameters on the intake performance metrics and comparing the closely coupled approach with traditional power settings based on pressure boundary conditions on the fan face plane. A summary of the study and final considerations are provided in the concluding chapter 6.

Chapter 2

Computational methods for installed aero-engines

The installation effect in aeronautics is usually defined as the difference between the individual component performance in isolated condition and the performance after integration into aircraft system [298]. Considering a standard underwing-mounted engine, this integration has a mutual effect on the flow field around the wing and the engine nacelle, which cannot be reconstructed by superimposing that of the two parts taken separately. The measurement of this nonlinear term in terms of change of drag and thrust quantifies the installation effect, which can be established after a consistent Thrust/Drag Bookkeeping (TDB) has been derived. In the case of UHBPR turbofans, the increased nacelle size and the lower fan pressure ratio enhance the sensitivity of drag and thrust to the installation position, as either the nacelle and wing pressure fields are more closely related due to the tighter integration, and the engine operates with close to critical Fan Nozzle Pressure Ratio (FNPR) and possibly unchoked core. The force equivalence at steady cruise operation requires, therefore, a change of the engine thrust setting to compensate for the installation effect, that can offset the benefits brought about by the theoretically better propulsive efficiency of low specific thrust turbofans. The phenomenology of installation has been described as an alteration of pressure and velocity fields due to the presence of nacelle, pylon and jet efflux from nozzles [217]. The gulley between nacelle and wing, for instance, creates a velocity jet causing suction peaks, vortex drag penalty and in some cases even shock induced separation. Downstream of engine nozzle, the jet/free-flow interaction interferes as well with wing pressure side, inducing viscous and profile drag. The installation drag for the NASA Common Research Model twin-engine aircraft is 23 drag count (1 dc = 0.0001), amounting to 16.6% of the total cruise drag. The situation is even more complicated at high-lift and low-speed conditions, where deployed high-lift devices interact with the high-speed jets and can influence the engine operating conditions at low-thrust settings due to backpressure alteration.

Whilst for standard aircraft configurations the installation can be conveniently computed in Computational Fluid Dynamics (CFD) simulations where the components are

first simulated individually (Wing Body and Isolated Nacelle) and then together to find the differences (Wing Body Nacelle Pylon), in BLI aircraft this decomposition is artificial and does not lead to very useful information. Notwithstanding the high level of accuracy reached by the computational models and the guidelines that can be derived using data reduction methods from statistical analysis, in the framework of future concepts with tightly integrated or completely embedded propulsive units, it is emerging the need to devise more coupled approaches to design the interacting components and study their performance at a system level.

In the past, due to the inadequacy of numerical tools, wind tunnel tests represented a primary source of information [23, 33, 298]. With the availability of more powerful resources and turbulent flow solvers, such kind of analyses can be done naturally with CFD, although wind tunnel tests still represent an indispensable stage. The following section reviews approaches for measuring the impact of engine installation effects on aircraft aerodynamic performance, highlighting the published studies, the numerical methodology and the main findings.

2.1 Computational approaches for engine installation effect

The traditional workflow for engine integration relies on the design of aircraft components based on isolated analysis and successive assembling to evaluate interference effects [185]. In that phase, changes to the orientation and positioning of nacelle with respect to wing, as well as partial redesigning the joints are used to mitigate the interference and comply with other constraints, defining an interference boundary where the nacelle should fit. This is set by safety and maintenance criteria, such as ground clearance, nose-gear collapse, engine failure. The continuous expansion of the capabilities of numerical tools and computational power has made possible to carry out detailed studies of the integrated powerplant flow field, making the airframe and engine manufacturers more aware of the installation effects and guiding the final choice of the engine positioning onto the aircraft structure.

2.1.1 Computational modelling of integrated engines

A key element in the development of future civil aircraft is robust assessment of the mutual interactions and, furthermore, the thrust and drag characteristics of the combined engine and aircraft configuration. The experiences from a series of Drag Prediction Workshops [178] were useful to improve numerical modelling [258], validated against a large number of experimental tests [23, 213] for a reference wing body, the NASA Common Research Model (CRM) [277]. The measure of aircraft performance metrics requires the definition of a consistent TDB method, where forces acting on the airplane are separated in thrust and drag contributions. AGARD [173] and SAE [219] described in-flight thrust determination, reporting general principles for force decomposition. Zhang [303] presented a TDB method for separated dual-flow nozzles of a turbofan, with focus on nozzle metrics. Christie [39] proposed a modified near-field TDB

procedure to avoid interpolating forces on highlight plane and captured streamtube. Robinson [214] compared the approach with wake momentum loss from wind tunnel tests. In addition to near-field methods, based on direct integration of surface forces, far-field methods for drag extraction are also possible, where the whole computational volume is considered and scanned for different drag contributions (e.g wave, viscous, spurious, induced). Fan [73] presented a review of these methods. Tognaccini [260] revised entropy drag extraction for powered conditions. Destarac [61] defined several physical drag components for far-field method, employing it for pre-entry thrust [162], internal nacelle drag [164] and installation effects quantification [163]. Trapp applied farfield method to nacelle drag. Vos [279] showed reduced grid sensitivity and 20 dc differences for NASA CRM of DPW-IV for far-field method, compared to near-field. The same case was studied in [232, 271] with similar conclusions. Deng [58] confirmed the better drag result for CRM using far/middle-field. In that respect, numerical results obtained at ONERA using the proprietary finite volume code elsA and far-field method for the sixth DPW are presented by Hue [117]. For the powered-off nacelle the major effect related to drag increase was a higher friction on the larger wetted surface and modification of the flow path resulting in shock wave displacement and consequent variation of the pressure field on the wing. In the powered-on condition, instead, there are two main effects to be considered: the change in drag caused by modification of the flow field around wing and nacelle and the change of thrust caused by variation in velocity and discharge coefficient of the nozzles.

Oliveira [185] presented results of integration study for Embraer 170 aircraft using 3D Euler solutions, deemed to be conservative in terms of pressure coefficient alteration caused by engine assembly. The nacelle was moved vertically and horizontally, with chord normalized displacements from -0.16 to -0.08, and from -0.28 to -0.05, respectively. He concluded that the horizontal displacement is more sensitive to generation of suction peaks on wing lower side, compared to vertical displacement, and that an optimum trade-off between them exists. A small toe angle is also necessary to align the relative flow to the highlight plane at cruise.

Devine [62] performed turbulent Reynolds-Averaged Navier-Stokes (RANS) CFD simulations using Spalart-Allmaras and a commercial solver on DLR-F6 aircraft with wing mounted nacelle, comparing standard and compression pylon shape. He found that the new thinner shape could lead to 6 dc saving at cruise lift coefficient.

Sibilli [233] reported the implementation of a Propulsion System Integration (PSI) module, applied to two new concepts engines from NEWAC EU project, a three-shaft direct-drive high bypass ratio turbofan with an intercooled core, and a two-shaft geared high bypass turbofan with actively controlled core. The numerical tool was devoted to quantification of net propulsive force influence of engine positioning. Nacelle and exhaust were designed according to engine specifications for size, BPR, mass flow rate, thrust and total status at nozzles. Nacelle was designed according to NACA and standard procedures, while exhaust system considered geometric constraints and was manually refined through successive RANS CFD simulations. The nacelle generated were finally installed on NASA CRM, after a manual improvement of pylon design to elim-

inate shocks on its inboard side. The half aircraft model was simulated using steady RANS, with $\kappa - \omega$ turbulence model and 14M nodes grids. The installation effect was then evaluated at different vertical and horizontal displacement of the nacelle. The range of horizontal positions, computed from root wing trailing edge, was 0.85-1.25 x/c, while the range of vertical position, calculated from wing leading edge, was 0.5925-0.633 y/c. Confirming the indications from previous studies, the horizontal position had the largest effect on interference drag. By using a engine performance modeller, the impact of engine distance from wing LE on cruise fuel consumption was 3.67% between the extrema for the intercooled engine, and 6.4% for the actively controlled core engine.

Christie [39] studied the interference effect of nacelle position with respect to wing using CFD and proposed a modified near-field method to compute nacelle drag. He reported the vertical and horizontal displacement of several nacelles mounted on existing aircraft, which is graphically depicted in Figure 2.1. The region above the dashed line was found to give unacceptable interference drag in wind tunnel tests [33]. A test matrix was derived to assess the installation effect. To this purpose, NASA CRM was used and two nacelles, one with diameter 3.133 m and the other with diameter 4.018 m, were tested for three flight conditions and three positions, for a total of 18 cases. Vertical position was [-0.116 -0.116 -0.050] y/c, while associated horizontal position was [-0.074 -0.200 -0.200] x/c. Simulations were carried out using a commercial solver with steady RANS and a 30M node grid. A large variation in nacelle drag a different trend was found for the two configurations at different flight conditions. The installation drag resulted to be negative in most of the cases, with only two positions were a large increase of airframe drag was caused by wing shock pattern alteration. This also led to change of pressure distribution and loss of lift. The author remarks that, for this reason, comparison should be done at equal lift coefficient, rather than equal angle of attack, as in practice the lift should be recovered by increasing the incidence and, in turns, the drag.

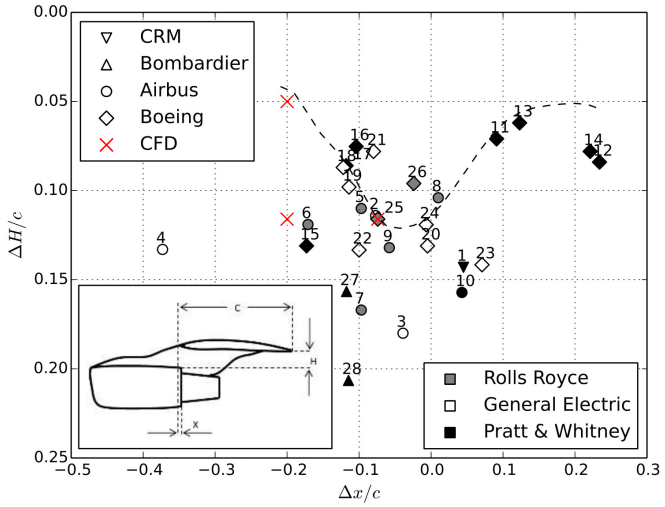

Figure 2.1: Mounting position for several existing engines. Taken from [39].

Stankowski [243] presented a computational framework for the assessment of engine installation effects, by analysing nacelle position and size and phase of flight. The reference aircraft was NASA CRM, on which two engines with different BPR were installed. The first engine, denoted E1, was representative of a typical modern turbofan, with BPR = 10.4 and overall pressure ratio (OPR) of 50. The second, denoted as E2, had a BPR = 17.8 and OPR = 58 and featured a diameter 1.23 times larger than E1. According to engine performance and thrust requirement of 55686 N at M = 0.82 and 35000 ft of altitude for CRM, four flight phases were defined, in terms of engine operating conditions. A CFD tool was first validated for axisymmetric throughflow nacelle and then applied to NASA CRM. The simulations employed a commercial density-based solver, with $\kappa - \omega$ SST turbulence model and 30M nodes grid for wing+nacelle configuration. An example of Mach number contours for two engines is shown in Figure 2.2. The experimental observation of an installation drag due to nacelle/pylon of about 25dc at M = 0.85, up to a C_l of 0.5 was not very accurately replicated, although the trend was captured. By means of drag breakdown, the relative merit of airframe components in terms of pressure and viscous contributions to the total drag was also reported, showing a progressive increase of wing and fuselage pressure drag from 0° to 4° of angle of attack, and in parallel a reduction of viscous components. The impact of engine position was assessed on nine points, given by [-0.067, -0.267, -0.45]x[-0.065, -0.13, -0.195] $[x/L_{nac}]$x$[y/L_{nac}]$ (positions taken from wing LE to nacelle TE). The interference on net thrust was mainly affected by horizontal position. For airframe drag, closer nacelles gave less interference; the nacelle drag, instead, was always reduced by wing mounting. The largest engine E2 exhibited lower sensitivity to installation position. The overall effect at constant vertical force coefficient was +27dc for E1 and +36dc for E2, the difference approximately scaling with increased nacelle size. The computational results appeared to be consistent with previous wind tunnel tests of TPS for engines of analogous size. In terms of fuel consumption over a nominal cycle, the larger engine benefited from a -4.8%, compared to E1, when the effects of engine weight, installation, and throttle dependent interference were included.

Following the previous study, Otter [189] continued the analysis on exhaust installation effect, using the same engines. The main metrics for nozzle operation are its velocity coefficient C_V, defined as the ratio of the actual nozzle gross propulsive force, the force acting on nozzle exit plane, to the thrust obtained through an isentropic expansion to atmospheric pressure, and the discharge coefficient C_{disch}, defined as the ratio between the actual mass flow rate and the ideal isentropic mass flow rate. Otter analysed the sensitivity of these coefficients to engine installation position, again on a nine point matrix [0.35, 0.20, 0.05]x[0.07, 0.12, 0.17] $[x/c]$x$[y/c]$, and aircraft angle of attack. Example of pressure coefficient distribution at different incidence is shown in Figure 2.3. The largest engine exhibited a greater sensitivity of C_V to axial position, up to three times bigger than E1. It was explained by a modification of the core cowl and core plug afterbody forces. The change in ambient pressure where the nozzle discharges caused, instead, a variation of C_{disch}, from -2% to -10% for E1 and from 0.75% to -1% for E2. This has an importance in engine operating conditions, as either it will not be able to operate at the

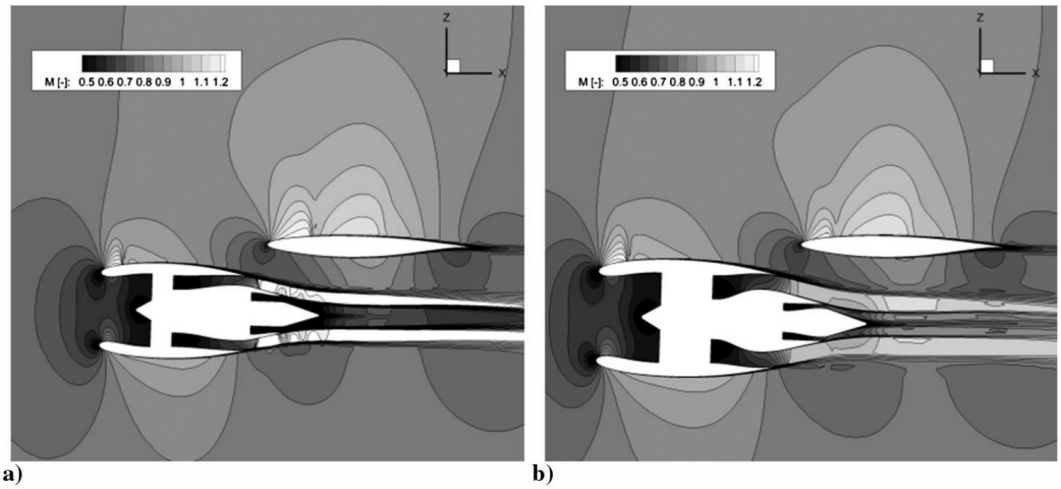

Figure 2.2: Mach number contours for E1 (a) and E2 (b) engines at cruise. From [243].

prescribed uninstalled point, or a modification of nozzle area will be necessary to reset the operative point. C_{disch} also varied from 3.7% to -13% over a range of incidence from 0° to 4°, highlighting the necessity of considering installation and flight conditions in engine calibration.

Recently, Tyacke [269] published a LES-RANS analysis of installed UHBPR coaxial jets, aimed at producing a large high-fidelity validated aeroacoustic database of installed engines. Among other problems, indeed, noise generation is becoming quite important with the constant enlargement of civil aviation volume, and it is another aspect influenced by mutual interaction of aircraft components.

Ritter [212] reported an engine positioning study for a high-lift wing. A UHBPR turbofan representative, with maximum diameter 2.9 m and take-off thrust rating BPR of 19, was placed below an infinite DLR-F15 wing with slat and flaps, without pylon. The sensitivity analysis involved ten positions, with 50 mm steps in vertical and horizontal displacement, with $\alpha = 0°, 5°, 10°$. An in-house CFD solver with Spalart-Allmaras turbulence model was used. The drag and lift resulted more sensitive to vertical position, with an increase of both when engine was put vertically closer to the wing, starting from the reference horizontal position. Globally, no predominant direction could be found for a favourable lift and drag development. Slat cut-out was also examined for engine in top left position (-100 mm along x and +100 mm along y), giving different polar characteristics and flow pattern, as illustrated in Figure 2.4 for skin friction distribution at $\alpha = 5°$.

2.1.2 Engine positioning studies

The first attempts of automatic optimisation of nacelle position were made by the use of Euler solver. Koc [136] used it for DLR-F6 wing-pylon-nacelle assembly. As the

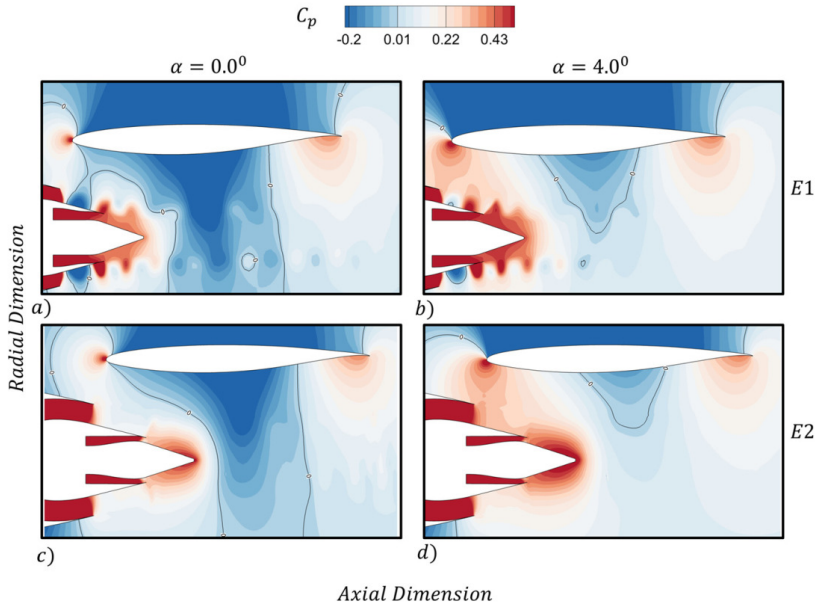

Figure 2.3: Pressure coefficient at discharge zone for E1 (upper) and E2 (lower) engine at different incidence. From [189].

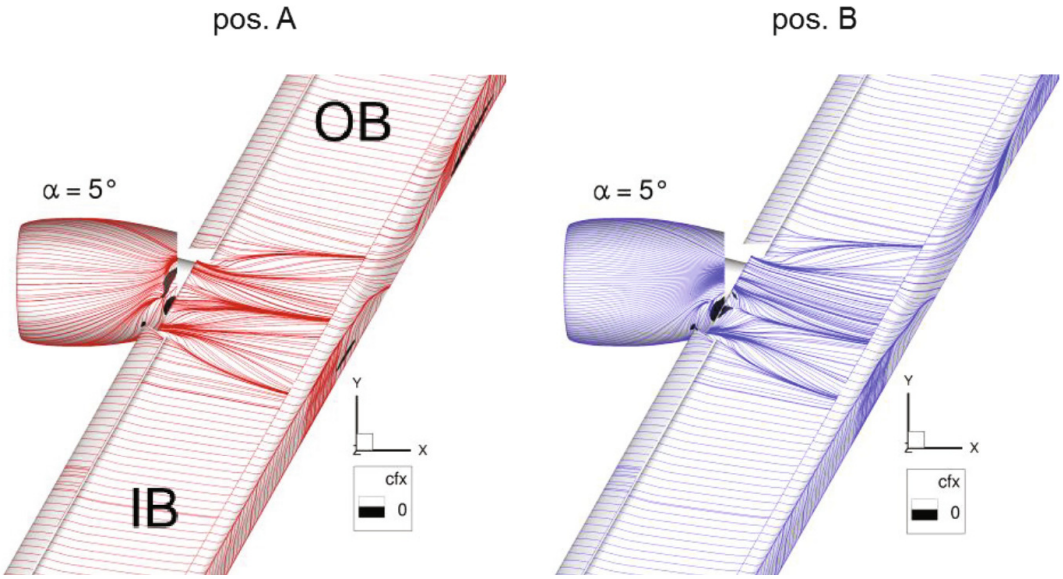

Figure 2.4: Skin friction coefficient for two different slat cut-out at low incidence. From [212].

baseline was characterised by a shock wave at the pylon at climb, where $\alpha = -2.9°$, the inviscid optimisation allowed to suppress the loss and gain 19.7% of drag, at fixed C_L. Smith [238] reported a similar result, that is the elimination of shock wave in nacelle lower lip and trench region after inviscid optimisation of a throughflow nacelle and wing shape. The baseline geometry represented a single-aisle transport with a 34.38m of span, an aspect ratio of 10.0 and cruise Mach number of 0.785. The engine featured a fan diameter of 2.1844 m, a BPR of 15 and a capture area ratio of 0.73 at cruise. The nacelle was placed with a vertical offset of 13.4% of local wing chord at nozzle lip from wing leading edge.

Jing [153] used free-form deformation (FFD) and particle swarm (PSO) for aerodynamic optimisation of wing mounted nacelle, minimising cruise drag coefficient at constant lift, for DLR-F6 with through-flow nacelle. The nacelle position was varied, keeping the baseline geometry. Despite the advanced optimisation framework, the drag coefficient improved of 3.6 drag counts only. Lei [150] successively extended the optimisation to a full aircraft, simulated using Spalart-Allmaras turbulence model with a steady open source RANS solver and a 16.8M grid. Wing and tail shape were modified and nacelle installation parameters (vertical and horizontal coordinates, and toe angle) were slightly varied. This led to a 2.7% reduction in total drag, mainly due to suppression of shock waves and lower wing side suction peaks. This time, a BPR = 8 single core engine was present into the nacelle, powered by suitable boundary conditions.

Epstein [70] carried out a viscous optimisation of wing camber to minimise drag coefficient at three design points, two at cruise, with $C_L = 0.575$, Re = 40e06, M = 0.845 and 0.86, and one at take-off. The wing-mounted nacelle was kept unchanged, positioned close to the wing leading edge, at around 7% of local chord, and not overlapped to the wing. The optimised wing lead to improvement of lift/drag polars and reduction of drag divergence Mach, with a mechanism similar to previously described works.

Hooker [111] presented a thorough revision of an alternative over the wing nacelle (OWN) installation, as compared to traditional under-the-wing (UWN), for four engines with BPR 5.5, 9.0 and 38.0. CFD simulations were carried out using a 12M mesh and a NASA flow solver. He came to the usual conclusion for UWN, that an upward movement of nacelle can produce a negative, i.e. favourable, interference effect. For OWN, trailing edge mounting appeared to mitigate the otherwise strong interference, and such a configuration was selected, among other 5, to redesign the wing through optimisation. The final conclusions of its study were that an OWN TE ultra fan engine could reach up to 5% improvement in aerodynamic performance compared to standard UNW LE, and a better aeroacoustic trace, at the cost of additional wing weight. In this configuration, due to the close interaction between engine and wing, combined optimisation of wing and pylon shape was required to achieve satisfactory level of performance.

2.2 Summary of numerical studies outcomes

From this brief overview, it appears that while the issues coming from large engines are known and the necessity for carefully examining the best trade-off at system level is evident, the dearth of studies quantifying the sensitivity of engine installation does not provide a unique picture. The vertical positioning of the nacelle can be regarded more uniformly as less impacting the installation drag, and it is constrained by other practical considerations, in particular ground clearance. The horizontal position, instead, gives more variability but the net effect seems to be problem dependent. Furthermore, the wing penetration was either positive or negative in the examined literature. What appears to emerge is that an optimal placement should act on both the direction, as it is their combined modification that leads to best installation drag. Pitch and toe angle also require tweaking to compensate for wing upwash. On the engine operation side, the importance of installed nozzle appears relevant as well. A change in discharge conditions can alter the operative point on the speedline, causing reduced stall margin or decreased efficiency. In a standard approach, nozzle resizing is necessary to restore uninstalled operating conditions.

From the numerical standpoint, the resources needed to perform CFD simulations of full aircraft body with wing mounted nacelle are very high. The current methodology is based on steady RANS simulations solely, in practice. Typical grid sizes are above 20M cells for coarse mesh, whilst grid refinement easily leads to exceed 100M [259]. Despite such large count, matching experimental data for pressure coefficient distribution in zones affected by installation effect is still difficult [258].

In order to properly quantifying the very small variation in drag counts related to different engine placement or pylon shapes, not only is the validity of computational RANS model to be assessed, but also the accuracy of thrust/drag book-keeping method employed. In addition, the engine effect has to be somehow introduced to simulate powered conditions. Direct modelling is not feasible, as it would require other tens of millions of cell, but it is usually implemented via boundary conditions specifying ingested mass flow rate and total status at nozzle exit. The suitability of these simplification is examined in the next section for fan-intake interaction cases.

2.3 Review of fan-intake interaction

The mass flow passing through the highlight plane of a nacelle is determined by the engine suction and the external velocity. The engine can be viewed as a turbomachinery operating within a duct and its working point is determined by the crossing of the power and resistance curves. Being part of the duct, the intake, which refers to the inner part of the nacelle cowl, contributes, together with the nozzle condition and the throttle setting, to fixing the engine working point on its speedline. It is, therefore, the mutual interference between the engine and intake/nozzle that sets the mass flow rate ingested and the total status at nozzle exit plane. A correct determination of fan-intake interaction is essential to predict the effective working condition of a flying propulsive

unit. Several computational and experimental studies have been devoted to analysing this problem, either focused on the external aerodynamic side, or on the fan operating point. From an aerodynamic side, in fact, the intake must supply the engine with a clean flow throughout the entire envelope, while minimising the external nacelle drag. The lip is the most critical location, as its design is a compromise between a slim shape with sharp leading edge, favouring the cruise, and a rounder shape with a thicker nose necessary at take-off to avoid separation and reduce the distortion level. A fan operating in a distorted flow, in fact, can move towards the stall point and incur a stability and efficiency drop. Therefore, it is important to account for both aspects, the external nacelle characteristic and the fan working condition, when designing the intake.

The flow field over an intake operating at incidence is quite complex. The stagnation point moves well outside the highlight, causing a suction peak and a region of high Mach number, possibly resulting in a shock-wave inducing a separation. Two vortices are formed in the lower lip, that are ingested by the fan. However, the rotor is able to keep its operating characteristics even in non-uniform conditions, inducing a flow redistribution to maintain a constant discharge condition, as long as the distortion is not too high to cause the blade stall. Schulze [224] reported an extensive experimental investigation of scales dynamics of a stalled nacelle. A laminar separation bubble can form near the cowl leading edge, followed by a turbulent bubble just inside. The turbulent separation bubble is a highly unsteady phenomenon and gives rise to two counter-rotating vortices that are swallowed downstream by the rotor. The blade, therefore, sees a local change of incidence which can bring to stall or aeroelastic failure. Erbslöh [71] presented wind tunnel tests of nacelle at incidence, to study the potentials of energising boundary layer with air jets, to control separation. Oil flow visualisation, depicted in Figure 2.5, shows the complex flow pattern previously described, with a primary separation line marked S1, two focal points F, a secondary separation line S2, and a saddle point S.

The presence of the fan was found to cause an extension of separation-free operation and attenuation of distortion in the experimental campaign of Hodder [108]. Motycka [176] reported that the separation angle is Reynolds and configuration dependent. Larkin [145] indicated that the extent of separation delay was 3° to 4° relative to flow-through case, based again on wind tunnel tests. Experimental assessment of nacelle sensitivity to ground atmospheric gust, characteristic of take-off/landing conditions, was carried out by Übelacker [270], who showed that distortions have a critical effect on both attached and separated flow regime, changing the mean phase-locked flow and fluctuation velocities in the nacelle, potentially affecting fan stability.

Kennedy [130] studied the influence of fan modelling for CF34-3A turbofan engine, by comparing simulation with and without fan interaction with experimental data. The presence of the fan was confirmed to delay separation and reduce distortion level, causing a significant change in the path of ingested flow. Cao [30] carried out a systematic analysis of fan-intake interaction at different intake length over nacelle diameter L/D ratios using a body force method, previously validated against uRANS. Confirming previous findings, at decreasing L/D the fan had the effect of either increasing the separation angle of attack or reducing the distortion level. At fan face, low sensitivity of

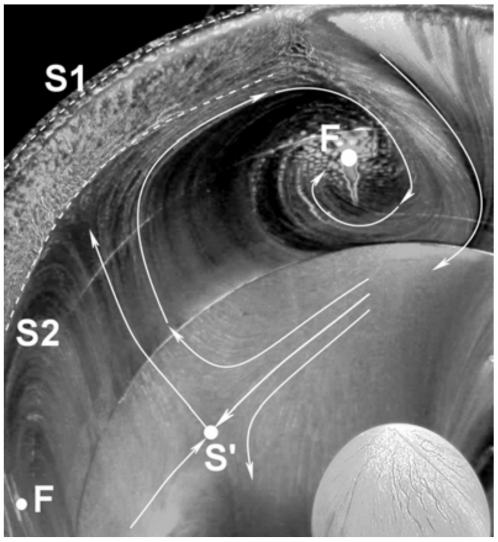

Figure 2.5: Oil flow visualization of intake at incidence, showing separation lines and vortices. From [71].

separation level to L/D was reported. The suppression mechanism was attributed to the flow acceleration close to the casing caused by redistribution of the mass flow induced by the fan. This effect rapidly decades upstream of fan face, but is independent of L/D, explaining the constancy of reduction level and the lower sensitivity of fan presence for higher L/D. The separation delay was found to be 5 deg at L/D = 0.17, and zero for L/D = 0.44.

The European project ASPIRE, involving several research centres and Airbus, investigated design methods for advanced nacelles of future UHBRP engines. A low pressure ratio fan installed on an short cowl (L/D $\sim$ 0.30) isolated nacelle was studied by Burlot [28] using different modelling techniques, including low-order methods like Actuator Disk (AD) and Body Force Model (BFM). The authors concluded that AD model was inadequate to reproduce distorted conditions, whilst BFM provided realistic distortion transfer. Even if steady RANS led to results closer to uRANS, in terms of fan characteristics, their mixing plane boundary between fan and OGV did not allow to simulate distortion transfer and they recommend uRANS for accurate fan efficiency estimation. Stuerner [244] performed uRANS computation, assessing the influence of time step size on the resolution and comparing results obtained with engine specified through standard boundary conditions. The simplest approach provided axysimmetric solutions, with larger homogeneity, compared to the full fan simulations, as expected. This difference could be important for cases like exhaust jet interaction with airframe or high-lift devices. Furthermore, the drag on external nacelle was also found to be lower of about 4% for the full modelled case, mostly due to pressure distribution change, indicating that for thrust/drag book-keeping flow non-uniformities might become relevant. A code-to-code comparison between DLR, NLR, ONERA and Airbus for the same case was also

presented in [170].

Schnell [224] summarized a series of activities carried out at DLR related to short intake and low pressure ratio fan . V2500 two spool, FPR ∼1.7, BPR = 4.8 turbofan, powering A320, was simulated with 60° total pressure inlet distortion and compared with an FPR = 1.35, BPR ∼ 14 fan, designed at DLR and designated Fan135. As shown in other studies, the rotor blades crossing the distortion see an induced incidence that brings them operating closer to spill point, as shown in Figure 2.6 left. A similar effect is viewed for low FPR fan, although the distorted characteristics are influenced in different ways. Sectors closer to the distortion boundary operate well beyond the steady-state stability margin, whilst for V2500 the local sector characteristics are less spread. More details of the comparison are provided in [225], where it is remarked that low FPR fan is subject to large variations of blade forces, which are challenging boundary conditions for the aeromechanic design. Furthermore, stronger incidence effects from the streamline curvature are observed and the distortion is propagated downstream with reduced attenuation, compared to high FPR fan.

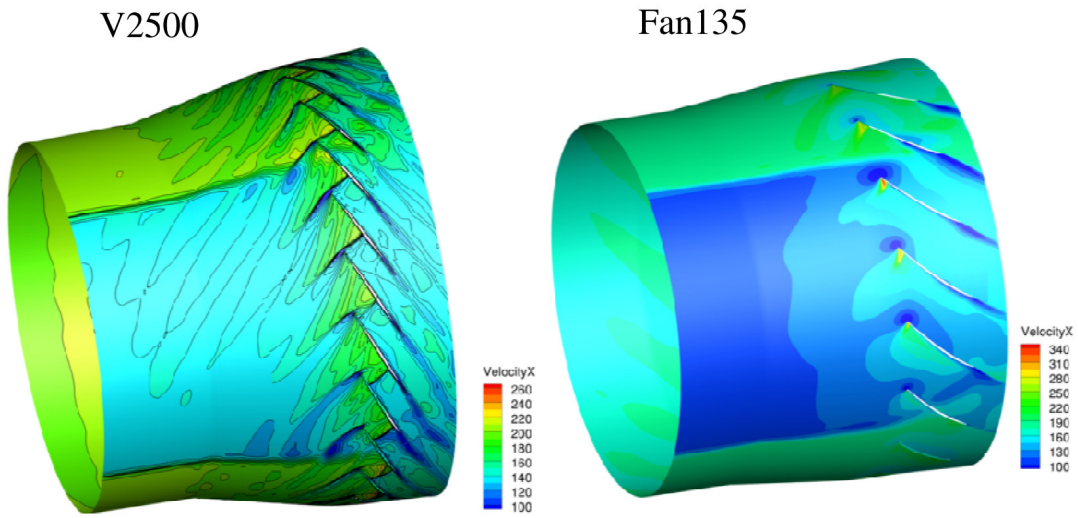

Figure 2.6: Instantaneous Mach contour of full annulus uRANS for high FPR V2500 and low FPR Fan135 turbofan. From [224].

Wartzek [284] carried out an experimental investigation of the Darmstadt transonic compressor with two realistic distortion patterns, one generated with a beam, representing inlet separation, and one generated via a delta wing, representing a ground vortex. The latter distortion did not lead to significant variation in compressor characteristic, whilst for the beam case, the separation was ingested into the rotor and led to a substantial change on the inflow, with one passage overloaded near to machine stall.

Barthmes [10] provided an insight in distortion transfer mechanism for the same compressor using uRANS, identifying three main mechanisms: upstream flow field redistribution, associated to a combined state of distorted static pressure, axial velocity,

and inflow angle; transport trough the rotor, related to static pressure variation between clean and distorted region; information exchange between distorted and undistorted region, due to altered pressure difference on blades crossing the region boundary. For the examined case, although the blades at the exit of the affected zone operated temporarily well beyond the stability margin, no compressor stall occurred. In terms of pressure, a drop in blade loading and a significant increase was found, at entering and leaving the distorted sector, respectively. Also, a large modification of shock wave system resulted at 100% speed, bringing a breakdown of the tip clearance vortex. Haug [105] presented the previous computational study more in depth, by analysing rotational speeds of 65% and 100% at near stall and peak efficiency. The author found that the interaction of the rotor with the distorted flow depends on rotational speed and operating point, and the blade tip vortex was subject to different breakdown and recovery. The amplitude of blade loading variation appeared larger at 100% of the speed, despite the general trend of variation was similar for the same operating point at different speeds.

Peters [201] described a computational framework for the evaluation of short intake nacelles for low pressure ratio fans, using BFM and uRANS. The author discussed the design practice driven by competing requirements at cruise and off-design, which are also different from the top to the bottom sections. Assessment of nacelle drag and fan performance on three configurations, with L/D of 0.50, 0.25 and 0.19, showed that the combined effect of external drag and fan efficiency decrease, at lowering L/D, determine a non-monotonic trend of propulsive efficiency for L/D between 0.25 and 0.50, suggesting the existence of an optimum inside this range. For L/D = 0.25, the external drag was reduced by 16%, with an almost zero change in propulsive efficiency, relative to the standard cowl.

2.4 Limitations of the decoupled approach

The literature review has unequivocally shown how the presence of the fan has a large impact on the flow development and on the pressure and velocity fields just upstream and downstream of the engine volume, particularly at off-design conditions and in the case of short and slim intakes. As highlighted before, the engine/airframe interaction problem is two-side: on the one hand, the aerodynamic engineer takes care of the external nacelle shape and the impact of exhaust jets on the wing and on the pylon, assuming a given fixed-state engine working point, provided as a boundary condition; on the other hand, the engine engineer assumes that the necessary mass flow rate can be provided by the intake and exhausted by the nozzle into a certain atmospheric pressure, at given flight boundary conditions. However, these two aspects are certainly correlated. Whilst a decoupled design can be effective for certain configurations, and close to the reference condition, it would be preferable to allow for a physical exchange of information between those two conceptually separated areas, especially when, as it is the case of short inlets, strong mutual interaction occurs. With a crude modelling of respective boundaries, predictions can be inaccurate or even unphysical.

For the case of UHBPR installed engines, it has been pointed out that the aerody-

namic interaction between the propulsive unit and the airframe is enhanced by the large size, the tight physical integration and the specific thermodynamic state at which the engine is designed to operate, with low specific thrust, low fan presssure ratio and unchoked nozzle during some flight phases. The net propulsive force results from the balance between thrust and drag forces. Not only from a physical point of view the true influence of the engine on the flow field becomes indispensable at off-cruise, but also from a propulsive point of view, as the sensitivity of the working condition on the external flow field affects both the thrust and the drag. Moreover, UHBPR turbofans have an impact on the overall aircraft sizing, concerning the geometric arrangement to respect all the necessary clearances, but also the aerodynamic surfaces. For instance, the engine failure event must be controlled by sufficient vertical rudder area and the windmilling drag of the failed engine is very difficult to be computed.

Most of the phenomena in exam have been shown to be highly three-dimensional and unsteady. Despite the powerful resources available nowadays, the computational cost of full-annulus uRANS simulations, even of an isolated nacelle, is still unaffordable in normal practice. It is here believed that leaner, though inevitably less accurate, models would be useful in allowing for a more physics-based coupling of the internal and external aerodynamics, improving the relative boundary conditions and naturally accounting for the interference effect. This work will be devoted, therefore, to the study and implementation of simplified models that have been shown to have the potentials of highly reducing the computational cost of a more integrated approach in the simulation of installed jet-engines, but still capturing the main features of the phenomenon.

2.5 Simplified models for engine representation

The most limiting hypothesis of standard powered nacelle boundary conditions used is the constancy of mass flow rate with inlet state and the spatial evenness of total pressure and temperature at nozzle exit plane. The engine response to different inlet and outlet conditions, in fact, is not modelled and the converged simulation can give misleading, although sometimes conservative, results. In order to overcome this inherent limitation, several approaches have been used, aimed at recreating a transfer function of a turbomachinery cascade. Here we are in particular interested in axial fan models, as it is the most prominent turbo component in high BPR engines.

A variety of methods has been devised in the literature to reproduce the cascade effect on the flow, without a detailed geometric modelling. They will be briefly reviewed and classified into three main classes, in agreement with [251]: 1D methods, 2D throughflow methods, 3D throughflow methods. Regardless of their accuracy and complexity, all the approaches are based on removing the cascade, made up of several metal blades, and adding to the mean axisymmetric flow a force corresponding to the average overall reaction exchanged by the flow and the blades. In this way, the circumferential-averaged flow field leaves the blade region with a distribution that should be close to the one obtained by performing a circumferential average of the real three-dimensional flow exiting a solid cascade. The effect that the blades have on the flow is represented

by the forces exchanged, that are then added to the solved equations as source terms. They can be shown to originate due to the axisymmetric representation, but this concept can be extended also to generic three-dimensional flows, as it will be shown in the case of 3D throughflow methods. In the following, the three aforementioned classes will be reviewed.

2.5.1 2D Throughflow methods

Streamline Curvature Throughflow

Marble [165] first derived thermodynamics relations for an axisymmetric blade row, highlighting the influence of body forces on flow turning and losses. The force normal to relative velocity is responsible for the former effect, whilst the component parallel to relative velocity for the latter. The first implementation of Marble's ideas was the so-called Streamline Curvature (SLC) [287], solving the circumferential averaged inviscid equations of motion. The term streamline curvature derives from the radial equilibrium assumption (REA),

$$\frac{\partial p}{\partial r} = \rho \frac{v_\theta^2}{r}$$

allowing to capture the curvature of streamlines in the meridional plane. The models were then extended by adding entropy generation [112, 125], incidence, deviation and lean effects [59, 123], endwall boundary layer and turbulent mixing losses [76, 77, 152, 184, 223], shock losses [21, 222]. The possibility of including custom correlations to model a variety of phenomena and its low computational requirements made SLC the backbone of preliminary blade design from 1960, and it is still a valid tool [60]. However, this method is not compatible with transonic flows, as the mass flow rate must be specified, no shock wave can be reproduced, choking is not naturally captured and neither stall can be accurately determined, since reverse flow is not admitted.

CFD-based Throughflow

In order to overcome these limitations, the so called CFD-based throughflow tools were developed. They rely on solving the steady passage-averaged Euler equations in a time marching fashion, by adding forces similarly to SLC, to induce the flow to follow the blade mean camberline and to add viscous losses. The force component responsible for the flow turning and isentropic work is generally obtained with an implicit equation, enforcing adjacency of the relative velocity vector to the blade mean camberline [199]. These methods can be regarded as semi-implicit. Again, the solution is axisymmetric and is found in the meridional plane of the blade row, allowing also multi-stage calculations. However, the transonic regime is naturally accounted for and shock waves can be reproduced, although with some limitations. Spurr [242] first presented a time marching throughflow of this kind, followed by Damle [50]. Baralon [8] included a normal blockage factor in the model, improving the choking mass flow rate

prediction, and highlighted the impossibility of a circumferential-averaged representation to capture shock waves that are not normal to the meridional plane, which occurs for supersonic axial Mach number. A CFD-based throughflow was shown to be able to deal with transonic compressors [8, 126, 245] and give good results, provided that it still relies on many external inputs for losses, deviation and incidence [235]. Again, this level of empiricism makes it possible to obtain high accuracy for calibrated cases, including also complex phenomena, like cooling and three dimensional losses [190, 191, 202, 211]. In order to overcome the need for external inputs, Simon [234] first proposed a Navier-Stokes throughflow, which inherently captures endwall losses. He also studied the so-called high-order throughflow, where a series of rigorous and mathematically consistent averages are performed, according to Adamczyck [1] approach. In fact, circumferential averaging neglects higher order terms, which are the fluctuations of real three-dimensional solutions with respect to the axisymmetric one. Baralon [7] found that some of these terms are important in determining flow angle and mixing losses, especially near the tip. Simon remarked that among all, the stress terms coming from the average operation that are most important are the viscous and blade forces and the circumferential stresses, representing the momentum and energy transfer between the 3D and axisymmetric flow field, and they are analogous to Reynolds stress for RANS averaging [236, 254].

2.5.2 3D Throughflow

2D throughflow methods represent an evolution of SLC, but they are similar in essence, as they provide an axisymmetric representation that can be useful for analysis and design purposes, allowing a very rapid estimation of compressor map and, with CFD-based methods, also of complex flows with transonic and reversed regions, leakage, 3D losses and across multi-stage machines. However, due to their inherent two-dimensionality, their are not suitable to be used in engine/airframe interaction problems that are three-dimensional by nature. A generalisation of 2D throughflow is based on having again a distribution of source terms, inducing in the flow the effect of real blades in terms of work and losses, but this time the body force field is space-varying and function of local flow variables. In this way, although mathematically derived from a circumferential-averaged flow field, it can be used to study three dimensional phenomena, which are then obtained by superimposing point-by-point an axisymmetric solution. The expression for local forces can be either derived from a lookup table database, be an explicit function of local flow variables or be obtained implicitly by solving a differential equation. We can, therefore, distinguish four sub-categories within this class.

Interpolation-based methods

Interpolation-based methods use a previously formed database, obtained by three-dimensional CFD or experimental tests, to include body forces within the volume swept by the blade. Many works employing this approach were done at the MIT group led by Prof. E. Greitzer, to study compressor stall. Choi [37] obtained body force field from

RANS computations and included into an Euler solver. By use of dimensional analysis, he showed that for supersonic high-Reynolds flows, the force magnitude is proportional to Mach number only. Kiwada [135] proposed a method called "Blade Force Average" (BFA), that will be discussed later, to extract body force from steady 3D RANS simulations and incorporate these forces into a CFD solver, to study stall inception. He also extended the extrapolated the extracted forces beyond the stability limits of the compressor using SLC. Patel [195] linked the forces to the local flow coefficient times the overall flow coefficient and found that the force slope is important in determining the stall point and inception type. Walker [281] used forces derived from SLC, again to study compressor stall, highlighting the importance of capturing the axial component for stall onset and type determination. Kerner [131] introduced the concept of "Force-Flow Reconciliation", in order to associate a unique flow to a given force field applied to the fluid, and examined the relation between stall inception and endwall forces.

Explicit methods

Methods belonging to this sub-category make use of an explicit analytic formula to determine the magnitude of body forces. Compared to the interpolation-based approach, they can capture more accurately the response to local flow changes and be used more naturally to study three-dimensional cases. However, external inputs are still required and the effort is put on the calibration, for which some force fields extracted from 3D solutions might be necessary as well. They can be viewed, in a way, as a local interpolation of a force database, which should be more physics-based than a simple look-up table approach. One of the first developed method of this kind is due to Gong [87], who derived an explicit relation for the force responsible for flow turning, based on a pressure balance for a two-dimensional staggered flat plate cascade and a cross-passage momentum balance. Calibration coefficients based on experimental data were used for proper scaling. Hsiao [113] used the model to study NASA stage 35 compressor and compared it with experimental observations for a powered nacelle, showing the fan effect on separation angle of attack. Plas [207] employed the model to study a BLI engine configuration. More recently, Kim [133] used a partially revised version it to optimise the S-duct inlet of NASA N3-X hybrid wing body. Similar modifications are reported by Li [154] for the study of supersonic inlet/fan coupling.

Peters [200] improved Gong's model by using full blade forces, extracted from 3D steady RANS, to express the calibration coefficients locally, included 3D blade effects and radial forces and reformulated the parallel force component, responsible for losses and entropy generation. The model was devoted to the study of short intakes for a low pressure ratio fan and was extensively compared to uRANS, showing a good agreement with the higher fidelity approach. Thollet [253] compared the original Peters model, that did not have blockage terms, with the model including blockage terms, showing that blade blockage is determinant in matching choking mass flow rate and improves simulation convergence. The same author assessed the influence of the pressure based term in Gong's model, finding that its inclusion is debatable and removing it usually improves map prediction.

Hall [101] proposed a modified model, where the normal force component is expressed as a function of blade geometry and flow quantities only, without the need for calibration based on external inputs. The model was devoted to the analysis of BLI configurations. The author showed that the dominant source of flow redistribution for non-uniform fields occurring in BLI engines is the inviscid one, and it can be captured without the necessity of modelling the viscous force component [100]. The model could be conveniently used for blade design, given its simplicity, but it was mostly thought for low-speed flows. Hill [106] introduced modifications to the baseline Hall's model, by adding a compressibility correction factor. The procedure, however, was iterative and cumbersome, requiring a large number of iterations and causing loss of the original simplicity. Indeed, Aykadin [2] employed the baseline version for studying NASA R4 SDT fan and TF8000 propulsor installed on D8 BLI aircraft, finding qualitative agreement with experimental data. Thollet [251] proposed to integrate Hall's model with blockage terms, a compressibility correction factor with Mach number scaling and entropy fix and losses modelled with a simple skin friction coefficient, obtaining good improvements compared to the baseline version for NASA SDT fan stage.

Thollet also devised one of the last available body force models, based on a lift/drag analogy. In respect of MIT formulations (Gong, Peters, Hall), it keeps a simple single-point calibration procedure and a straightforward implementation on existing solvers [251]. The model was compared in [252] with Gong's and an interpolated BF approach, showing superiority to simpler formulations. Godard [84] employed the L/D model to study MASCOT2 Safran/GE engine in nacelle crosswind case with encouraging results [85].

Semi-explicit models

In semi-explicit models, an explicit formulation is used in conjunction with some interpolation-based parameters. An example of this approach is the work of Kottapalli [139] for centrifugal compressor, who reported convergence issues for three-dimensional transonic cases. Chima [35] developed a tool that could be run in 2D throughflow mode to rapidly determine the compressor characteristics, 3D steady-state to study response to radial distortion and 3D unsteady to study rotating stall. Body forces were input at a single operating point from RANS calculations and were scaled to other points using normalized characteristic maps. The code was also used to model a serpentine inlet, fan, and nozzle assembly [36]. Guo [95] combined a 2D throughflow like approach, were normal force is determined from relative velocity adherence to blade camberline, with a parallel force model distributing a bulk entropy increase on the blade surface, to study a multi-stage compressor operating with inlet distortion. Brand [22] proposed a modified version of Peters model, where normal force is derived from momentum equation, accounting for compressibility, and parallel force used streamwise entropy gradient, fitted from RANS extracted data. The model, however, exhibited a large sensitivity to external calibration inputs. Defoe [54, 55] combined the steady body force model of Gong with other two components to study noise generation: a rotor-locked disturbance field periodic over a blade passage and a rotating disturbance field with

once-per-revolution periodicity to alter shock system and generate multiple pure tone (MPT) noise. Patel [196] integrated the model with Peters modifications and included some other improvements.

Implicit models

Implicit models are more similar to 2D throughflow, as a time-evolved differential equation is used to compute the magnitude of the force. Within non-axisymmetric tools of this kind, the work done at University of Cambridge is the most significant. Cao [29] proposed a so-called Immersed Boundary with Smeared Geoemtry (IBMSG) method, conceptually similar to immersed boundary methods (IBM), mainly used for finite-difference (FD) codes to deal with generic shape bodies. In the IBMSG, the relative velocity is constrained to be parallel to local wall surface, which is virtually represented by the blade mean camberline. As it happens for 2D throughflow, all the problems of including incidence, deviation and of leading edge discontinuity appear. In contrast, the method lends to be employed in conjunction with different levels of resolutions, from steady Euler equations to LES. Cao first applied it to the NASA Rotor 67 in clean and distorted inlet configuration. Watson [285] applied it to a modern high aspect ratio fan and to the Darmstadt rotor, obtaining a good agreement with RANS. Moreover, it was employed in a multi-fidelity approach for fan-to-flap assessment of engine integration using LES as flow solver. Inlet-fan interaction for a high BPR modern fan was studied by Cui [48] for a short inlet ($L/D \sim 0.45$). Ma employed LES with IBMSG to model the Darmstadt Rotor, achieving good match of total pressure distributions. He also investigate a subsonic rotor with an annular beam generating inlet distortion, confirming the influence of fan location on the perturbed flow. Recently, the same author published a comparison between RANS and LES using IBMSG for a parametric analysis of a fan subject to inlet distortion, caused by a circular beam of varying height and placed at different axial distance from fan face [160]. The important outcome of their study was that whilst in the absence of the fan the difference between RANS and LES are large, due to the limiting capability of RANS models, in the installed-fan case the discrepancies are substantially mitigated, as the main effect is due to mass flow redistribution caused by fan suction. This result confirms Hall's findings [100], that even an inviscid solution can capture the main distortion pattern. The difference between RANS and LES was reduced as a distortion generator was placed closer to the fan, indicating that for a short inlet design a mixed-fidelity modelisation based on RANS is only marginally penalised with respect to high-fidelity LES.

2.5.3 1D methods

One-dimensional methods model the blade effect on the fluid as a sudden change of some flow quantities across a plane. The AD concept comprises all this class of methods and was originally conceived by Glauert [82] to represent propellers. It consists in imposing pressure and enthalpy jumps and flow deviation across a thin plane, placed within the blade region. Downstream conditions depend on upstream flow and are eval-

uated using pre-formatted tables, containing angles, pressure and temperature variations on the span, for several values of incidence and Mach numbers. Despite it was born for propellers and also used in rotorcraft dynamics, the AD model could be exploited also for a lumped fan description. Joo used it to study the asymmetric performance of a turbofan operating behind a non-axisymmetric intake and due to the presence of the engine pylon [127]. Marquéz [166] described a complex AD model for assessment of contra-rotating open rotor, validating against uRANS with good agreement. Wiart [143] employed AD for the ONERA NOVA aircraft, featuring various engine configurations, also BLI. Godard [85] described the use of a RANS-based database to be used for the AD model, where upstream and downstream conditions taken from 3D RANS are circumferentially averaged and expressed in the AD axial location by means of conservation equations. A series of interpolations, based on bilinear polynomials or Radial-Basis Functions (RBF) then allowed to obtain the exit state in the simulation, given the entry condition. Compared to more advanced formulations, the AD was found unable to correctly reproduce the correct fan/intake interaction. The inherent limitations, that do not allow to capture flow redistribution, choking or shock waves, do not make the must suitable candidate to represent the highly complex phenomena occurring in transonic fans operating at distorted conditions.

2.5.4 Summary of methods

The variety of methods available has been classified according to the dimensionality, presenting the main logic and related limitations. Figure 2.7 summarises the categories according to their qualitative accuracy. On the rightmost column, 1D methods have been shown to be overly simplified to be employed with sufficient reliability in fan-intake interaction problems, as they provide results very similar to 0D models, where total or static quantities are specified at boundaries. In the central column, 2D methods give obvious advantages over the previous class, and they appear to be mostly used for design purposes. In fact, the body force terms are implicitly derived from the supplied geometry. However, they still require a substantial external input as regards losses, mixing and deviation models, which can make the calibration accurate but not generalisable and probably less capable of handling the multiple distortion figures characterising airframe-interacting engines. In the leftmost column are the 3D-based methods, which in principle can provide the greatest flexibility and accuracy. Provided that blind interpolation-based approaches have robustness and extrapolation issues, explicit and implicit methods have a wider potentials in dealing with generic flow fields, as they are more physics-based. Notwithstanding the attractiveness of implicit methods, which require less external inputs and have been successfully applied in conjunction with eddy-resolving schemes, explicit ones offer higher simplicity, easier implementation, possibility of dedicated calibration and low computational overhead. In this work, therefore, explicit methods only will be considered, studying their implementation, behaviour, applicability and validity.

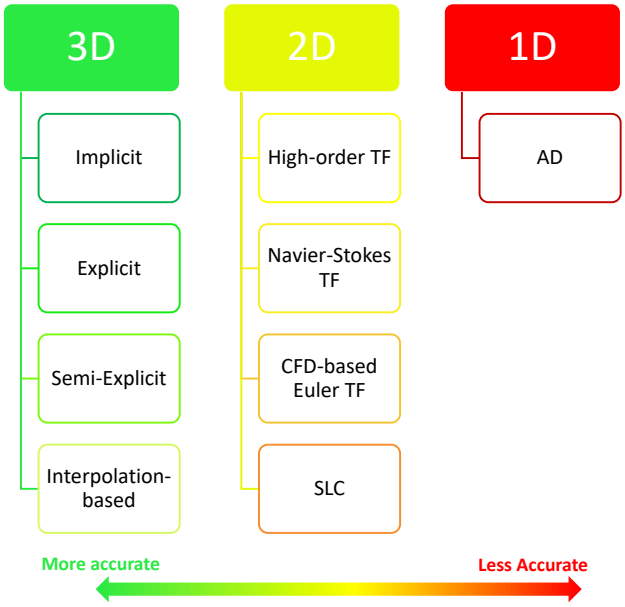

Figure 2.7: Summary of simplified models for engine representation.

Chapter 3

Development of a compressible CFD solver

The simplified methods for engine representation described in section 2.5 are all based, except for SLC and some AD, on the solution of Euler or RANS equations for compressible flows, to whom proper source terms are added to reflect the blade effect on the flow. The implementation of a BFM model, belonging to the class of explicit methods, requires, therefore, the availability of a compressible Navier-Stokes solver, where the model is to be inserted. In the literature, BFM was added to in-house codes [253] and to commercial solvers [200] that allow to include some user-defined functions. Although the use of an existing commercial software could provide sufficient flexibility to produce a custom implementation of a BFM, exploiting the underlying solution algorithms, within this PhD programme it was chosen to develop an in-house flow solver from scratch. The creation of a compressible flow solver is a troublesome and complex activity, requiring a knowledge on several fields and a large amount of time to master the computational techniques and the flow physics involved. The motivation to start the development of a new CFD program arose from the will to provide the research group with a series of in-house software tackling the advanced design and analysis of turbomachinery using a multi-fidelity approach, ranging from one-dimensional models to Direct Numerical Simulations (DNS). The availability of a staple CFD program, in fact, guarantees the largest freedom in implementing several simplified methods with an easy and complete access to the core flow solver and the possibility of testing different approaches, not only restricted to explicit 3D BFMs, but also to CFD-based throughflow or implicit methods, for instance, in a stand-alone application. The reach of a validated, fast, efficient and general purpose code was well-beyond the PhD scope and horizon and takes several years and many people working on it. The ambition of the project was, in contrast, to create a simple and easy-to-use platform for testing, benchmarking and developing CFD-based engine models. Given the limited amount of time and resources available within the doctoral programme, it was decided to target the validation of a RANS 2D axisymmetric swirl code implementing an explicit BFM model. Future re-use and extension of the core flow-solver might lead to deal with 3D flows

in generic domains. From a numerical standpoint, it is a cell-centred Finite Volume, density-based, second-order accurate with high-resolution discretisation of convective fluxes, time-explicit for steady or unsteady simulation. In the remainder of this chapter, the basis of computational methods employed are briefly reported, together with some validation test-case. A more detailed discussion of the numerical methods is given in Appendix A, whilst additional test cases are shown in Appendix B.

3.1 Numerical methods

The solution of the discretised RANS equations in the developed solver was based on the Finite Volume Method Finite Volume Method (FVM). It is a widespread discretisation technique, that has become popular for fluid dynamics equations starting from the 70s, thanks to the foundation work made at the Imperial College of London [88, 147, 194]. The method is naturally applied to conservation laws, which are treated in their integral form, allowing to inherently capture discontinuous phenomena, deal with generic domains, and avoid complicated mappings from the physical to the computational space. Compared to other discretisation methods like Finite Difference Method (FDM) and Finite Element Method (FEM), the former based on discrete approximation of derivatives, the latter on variational principles, FVM offers larger flexibility in handling distorted and complex domains arising in industrial problems, maintaining the physics of the equations solved and their conservation nature. In contrast, other methods are preferred to tackle fluid dynamics problems from a more scientific point of view, like in the case of turbulent, reacting or multi-phase flows, employing high-order discretisation of LES, DNS or Euler equations.

The application of the FVM to the Navier-Stokes equations gives the so-called semi-discretised form:

$$\frac{\partial}{\partial t}\vec{\overline{\mathbf{U}}}\,\Omega + \sum_{f\in\Omega}\left[\overline{\overline{\mathbf{F}}}_c \cdot \hat{n}A\right]_f = \sum_{f\in\Omega}\left[\overline{\overline{\mathbf{F}}}_d \cdot \hat{n}A\right]_f \tag{3.1}$$

The equation contains three terms, one related to the time-derivative, and the other two being the convective and diffusive fluxes at the control volume boundaries. The solver developed was based on cell-centre representation, meaning that the cell-average conservative variable $\vec{\overline{\mathbf{U}}}$ is attributed to the centre of the control volume. In the following, the basis for the calculation of each term will be presented.

3.1.1 Flux discretisation

The flux tensors of equation 3.1 are summed over the faces of the finite volume and their net balance determines the rate of variation of the cell-averaged variable inside the control volume. On each face, the flux must be integrated according to a quadrature formula, like the Gauss-Lobatto rule for instance. The use of a single integration point at the centre of the face with a unit weight gives a second order accurate integration,

which was employed in the present solver. The very different nature of the convective and diffusive flux terms require a different numerical treatment for their calculation. The functional used in the numerical solver can be called numerical flux function. It is often a suitable approximation of the physical flux, that is more conveniently calculated but preserves the mathematical and physical characteristics of the exact flux.

Convective flux

The convective flux $\mathbf{F}_c = \overline{\overline{\mathbf{F}}}_c \cdot \hat{n}$ is expressed in the one-dimensional case as:

$$\mathbf{F}_c = \left\{ \begin{array}{c} \rho u \\ \rho u u + p \\ (E+p)u \end{array} \right\} \tag{3.2}$$

It was computed using the Flux-Difference Splitting (FDS) approach, where a local Riemann problem is solved at each cell interface $i + 1/2$:

$$\mathbf{F}_{i+1/2} = \tilde{\mathbf{F}}(\mathbf{U_i}, \mathbf{U_{i+1}}) \tag{3.3}$$

In the present solver, the first-order Godunov scheme [262], Roe's solver [216] and Toro's HLLC [262] are available. The approximate solvers employ linear reconstruction, which makes them second order accurate on smooth solutions.

Diffusive flux

The viscous flux of the Navier-Stokes equations has an elliptic diffusive nature and central schemes are suitable to approximate the state at cell-to-cell interfaces. In the current implementation, the following formula is used for gradient approximation from cells to the right and to the left of the interface:

$$\nabla\phi_{ij} = \frac{1}{2}\left(\nabla\phi_i + \nabla\phi_j\right) + \alpha_{ij}\left(\phi_L - \phi_R\right), \qquad \alpha_{ij} = \frac{2}{3}\frac{\hat{n}_{ij}}{|\hat{n}_{ij} \cdot (\vec{\mathbf{r}}_i - \vec{\mathbf{r}}_j)|} \tag{3.4}$$

where ϕ_L and ϕ_R denotes the boundary extrapolated values, coming from solution reconstruction, $\vec{\mathbf{r}}_i$ and $\vec{\mathbf{r}}_j$ are the cell centres positions and $\hat{n}_{ij}$ the face unit normal vector. This formulation was chosen according to the findings of Jalali [124] for anisotropic meshes.

3.1.2 Gradient reconstruction

The linear reconstruction requires an estimation of the cell gradients to extrapolate the cell centre variable to the faces. The boundary extrapolated values in the current code are obtained using either the Green-Gauss (GG) and Least-Squared (LSG) method. Many variants of these methods are available in literature, see for instance [239] for a review. Without entering too much into details, they are conservative schemes

naturally arising in finite volume, that are applicable to generic elements and unstructured grids. Differently from finite differences, which are best exploited in structured grids with three orthogonal directions (eventually in the generalised coordinates space) that allow for a straightforward approximation of derivatives, for instance with centred or skewed schemes involving an increasing number of points in the stencil for high order, in general unstructured domains there is no preferential direction that allows for a simple incremental ratio calculation using cell centre values. Instead, keeping the integral form of finite volume, one can build schemes that make use of conservation principles and divergence theorem.

The Green-Gauss gradient reconstruction makes direct use of the Divergence Theorem (DT):

$$\nabla\overline{\phi} = \frac{1}{V}\int_{\Omega} \nabla\phi \, dV = \frac{1}{V}\int_{\Omega} \nabla\cdot\phi\mathbf{I} \, dV = \frac{1}{V}\oint_{\partial\Omega} \phi \, \hat{n} \, dA \tag{3.5}$$

The formula uses the same calculation method of the other fluxes and can reuse most the structure of the core solver. The function value at the face centre can be obtained by linear interpolation of cell values:

$$\phi_{ij} = g_c \, \phi_i + (\, 1 - g_c) \, \phi_j, \qquad g_c = \frac{|r_{iF}|}{|r_{iF} + r_{jF}|} \tag{3.6}$$

making the method second-order accurate with $\mathcal{O}(h^2)$ for regular cartesian grids with equal spacing h. In presence of non-uniform spacing however, leading truncation error does not cancel out and the method becomes $\mathcal{O}(h)$. For skewed meshes or unstructured grids with non-vanishing skewness, moreover, the truncation error is $\mathcal{O}(1)$, which makes it not convergent [247]. This is due to the fact that the line joining the cell centres sharing the face does not pass through the face integration point. Remedies to this situation have been proposed, based on application of iterative corrections [57, 183, 248, 263], which are also treated in a deferred correction approach for pressure-based codes, using implicit pressure-velocity coupling [56, 177]. However, these corrections are computationally heavy, not robust and can at most mitigate the error in gradient reconstruction, without fully restoring second order accuracy. Therefore, the GG method appears suitable only in regular grids with low skewness and structured arrangement. For more general cases of meshes with mixed elements or unstructured tetrahedral, other specific algorithms have been developed.

The least square gradient reconstruction, in the form proposed in [186], is a conservative reconstruction technique applicable to generic grids. The method is derived in section A.4. It is based on a Taylor expansion of the mean cell gradient and requires the solution of a constrained overdetermined system of equations. For second order accuracy, the system matrix can be reduced to be 2×2 in two dimensions and easily solved. The use of weights in the expression of the least-square problem allows to maintain second-order accuracy even with skewed and high-aspect ratio grids.

3.1.3 Stencil selection and limitations of standard methods

The Green-Gauss method employs all the face neighbours of the cell whose gradient is to be computed, and can be regarded as a central scheme. For quadrilateral cells, or hexahedral in three dimensions, the computational molecule involves four extra cells, centred around the element under consideration. The Least Squared Gradient was developed with unstructured grids in mind, and can naturally include an arbitrary number of cells in the stencil. A variety of stencil selection techniques are therefore available to improve the accuracy of the method for unstructured, mixed-elements or distorted grids. The *face-neighbour* stencil is stable for regular grids, both quadrilateral and triangular, but becomes unstable for deformed meshes [98]. In cases having larger distortion, high aspect-ratio or curved faces, modifications to computational molecule for LSG have been proposed, in order to reduce discretisation errors. Nishikawa [182] compares *face-* and *vertex-neighbour* stencil with *face2*, in which face neighbours of face neighbours elements are added, a symmetric stencil based on geometric parameters, and *F-decreasing augmentation*, in which extra cells are added to the symmetric stencil to reduce the Frobenius norm of the pseudo-inverse matrix. They are depicted in Figure 3.1 for a skewed triangular mesh.

The inclusion of more elements to the stencil has been shown to increase robustness, accuracy and stability, but comes at a high computational expense for large molecules and an unavoidable overhead for adaptive selection. Mixed formulations and node weighting have also been proposed [65, 129, 300], together with data dependent weights for LSG [203]. One of the most challenging case for second order methods is high aspect ratio cells on curved faces. Katz [129] showed that both standard GG and LSG fail with that type of grid, which is normally employed in high Reynolds flows. For LSG, an approximate mapping onto curved faces was shown to provide accurate gradients by Diskin [64] and Jalali [124].

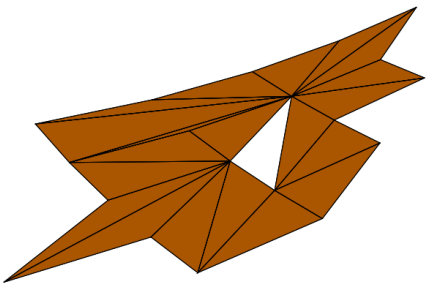

(a) Vertex stencil (20 cells).

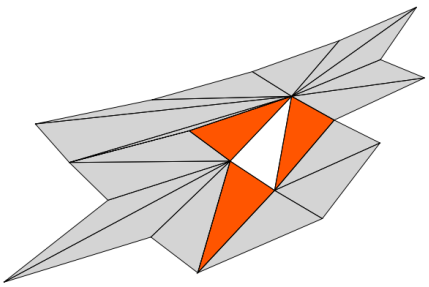

(b) Face neighbor stencil (3 cells).

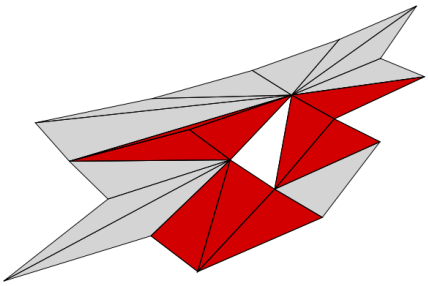

(c) Face2 stencil (9 cells).

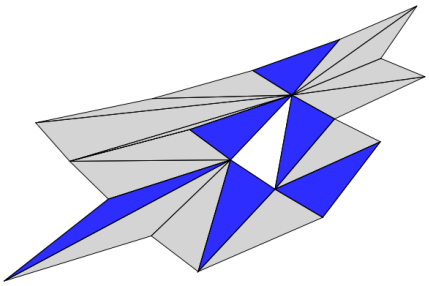

(d) Symmetric stencil (6 cells).

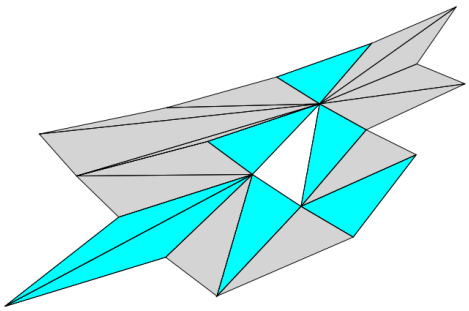

(e) Symmetric/F-decreasing stencil $\{symF_j\}$ (7 cells).

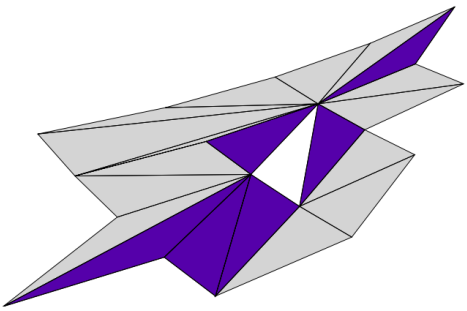

(f) Face/F-decreasing stencil $\{\text{faceF}_j\}$ (6 cells).

Figure 3.1: Stencil selection techniques for LSG. Adapted from [182].

3.1.4 Gradient Limiter

In order to avoid unphysical oscillation in the vicinity of a discontinuity, special treatments to the advection schemes are required. A suitable gasdynamic scheme should be such that it provides high numerical accuracy in regions of smooth flow, to capture the solution with a low truncation error using a reduced number of grid points, and is able to sharply reproduce the discontinuities that may arise. It is well known that first order schemes introduce numerical diffusivity to the equation, leading to a spreading of the shock thickness over time, whilst second order schemes are dispersive and produce over- and undershoots, which may lead to negative values of density or pressure, causing failure of the solution process. In order to switch between these two desired characteristics, so-called high-resolution schemes have been developed, blending first to second-order accuracy, depending on the local solution. This property, that is adaptiveness, is a form of nonlinearity, where the scheme coefficients are functions of the solution field itself. This has allowed to overcome a famous theorem by Godunov, for which *there are no monotone linear schemes for the advection equation of second or higher order of accuracy*. The previously called special treatment, therefore, consists in applying a nonlinear limiter to the reconstructed cell slope or face flux. The choice of the limiter comes from the attainment of desired qualities, like monotonicity-preserving or Total Variation Diminishing (TVD) schemes. For the 1D case, the following definitions hold [231]:

Definition 3.1 (Monotone scheme)**.** A scheme:

$$u_j^{n+1} = u_j^n - \lambda \left(\tilde{f}\left(u_{j-p}, \ldots, u_{j+q}\right) - \tilde{f}\left(u_{j-p-1}, \ldots, u_{j+q-1}\right) \right) \equiv G\left(u_{j-p-1}, \ldots, u_{j+q}\right)$$

with $\lambda = \frac{\Delta t}{\Delta x}$, is said to be monotone if G is a monotonically nondecreasing function of each argument.

Definition 3.2 (TVD)**.** A scheme is said to be Total Variation Diminishing (TVD) if

$$TV(u_j^{n+1}) \leq TV(u_j^n)$$

with $TV = \sum_j |u_{j+1} - u_j|$

A monotone scheme is TVD, and a TVD scheme is monotonicity-preserving, that is it does not introduce new extrema in the solution [104]. A regularisation of the framework for choosing a limiter was due to Sweby [246], who also derived some properties of the function in order to fulfil the TVD property [13]. Van Leer had introduced, before, the idea of MUSCL (Monotone Upstream–centred Scheme for Conservation Laws) type schemes [149, 272, 273], where the piecewise-constant reconstruction of Godunov first-order method was replaced by a piecewise-linear reconstruction, to whom apply limiters and avoid oscillations. The MUSCL framework has become standard practice in second-order FVM in the RANS context. Zhang [304] provided a review of TVD schemes. Whilst most classical limiters were developed for one-dimensional case and can be straightforwardly applied in structured grids, where a predominant direction

can be always uniquely identified, for unstructured grids so-called multi-dimensional limiters have been derived [24, 114, 192, 301]. In that approach, the stencil involves a number of spatially distributed neighbour cells, to account for the multi-dimensionality of the problem. Famous multi-dimensional limiters for unstructured grids are due to Barth [9] and Venkatakrishnan [278], who proposed a differentiable version of the former, in order to improve convergence. In the current implementation, the high-order differentiable limiter of Michalak-Ollivier Gooch has been employed [171], where a modification to Venkatakrishnan's was introduced, including a successive extension of the computing stencil [265] proposed by Tsoutsanis. The limiter was derived with time-accurate resolution using k-exact reconstruction in mind, and thus exhibits superior performance in terms of accuracy and mesh sensitivity. It is computed separately for each conservative variable and applied to the gradient of boundary extrapolated values used to compute the convective flux using the approximate Riemann solver:

$$U_{i+1/2} = U_i + \psi\left(U_j, U_{j+1}, \ldots, U_{j+m}\right) \nabla\left(U\right) \cdot \left(\mathbf{x}_{i+1/2} - \mathbf{x}_i\right) \tag{3.7}$$

The limiter function ψ reduces the reconstruction to first-order, by assuming a zero value, in cells where this is required by the rapid variation of the solution. Ideally, it should activate, i.e. be less than one, only in those regions, in order to avoid introducing numerical viscosity. The sensing mechanism itself and the stencil determine the effectiveness in the trigger. For second-order reconstruction in two dimensions, the current solver uses vertex neighbouring for determination of solution extrema, which is required by the limiter algorithm. Note that this task, i.e. comparing the computing cell value with those of many other nearby elements is computationally expensive and the use of asymmetric and adaptive stencils, especially in high-order k-exact reconstruction, is troublesome for parallel implementation.

3.1.5 Time discretisation

Equation 3.1 represents the so-called semi-discretised formula of a FV scheme. In fact, the temporal derivative is still retained undiscretised, while the fluxes integral have been approximated by means of quadrature rules. This approach is consistent with the Godunov method, where the numerical flux function is the advective flux evaluated with the status taken at $t = t_0$, on the $t = 0$ axis of the local Riemann problem:

$$\tilde{\mathbf{F}}_{i+1/2} = \tilde{\mathbf{F}}\left(\mathbf{U}_{\mathbf{i+1/2}}\right) = \int_{\partial\Omega} \mathbf{F}\left(\mathbf{U}(x_{i+1/2}, t\right) = \mathbf{F}\left(\mathbf{U}_{i+1/2}, 0\right) \tag{3.8}$$

By keeping the time derivative, it appears that after a proper flux discretisation one gets an ordinary differential equation (ODE) in time:

$$\Omega \frac{\partial}{\partial t}\mathbf{U} = -\sum_{f\in\Omega} \left[\mathbf{F}_c \cdot \hat{n}A\right]_f + \sum_{f\in\Omega} \left[\mathbf{F}_d \cdot \hat{n}A\right]_f = \mathbf{R}\left(\mathbf{U}\right) \tag{3.9}$$

where the fluxes can be summarised by the right hand side of the equation, $\mathbf{R}\left(\mathbf{U}\right)$ which is called the residual. The nonlinear ODE can then be solved using any of the standard methods, provided that they possess the required numerical stability.

The time marching methods can be divided into two big families: explicit and implicit. In the former, the solution at time $n+1$ depends entirely on the known solution value at time n, and can be directly computed once the residual is known. In the latter, it depends also on the unknown at next time level, making the relationship implicit. This requires solving an equation (actually a system of equations) at each time step, making the time advancement more costly and difficult. In comparison, implicit schemes can be unconditionally stable, allowing the selection of large time steps. In fact, explicit schemes suffer from the stringent CFL stability condition, requiring $\Delta t < CFL_{max} \times \Delta x/a$. For Euler equations, a can be taken as the largest eigenvalue of the Jacobian matrix, which is the maximum wave speed $u + c$, with c the speed of sound. Therefore, a can be large and considering that for high-Reynolds wall-bounded flows the boundary layer must be discretised with very thin cells, the deriving time step requirement for a $CFL_{max} = 1$ is very small, taking a huge number of iterations to advance the solution. Among explicit methods, the Runge-Kutta class has become popular for its suitability with the mixed hyperbolic-parabolic nature of centrally-discretised compressible Navier-Stokes equations. A popular method is the three-stage, third order TVD scheme of Shu and Osher [89], written as:

$$U^{(1)} = U^n \tag{3.10}$$

$$U^{(2)} = U^{(1)} + \Delta t R^{(1)} \tag{3.11}$$

$$U^{(3)} = \frac{3}{4}U^{(1)} + \frac{1}{4}U^{(2)} + \frac{1}{4}\Delta t R^{(2)} \tag{3.12}$$

$$U^{(n+1)} = \frac{3}{4}U^{(n)} + \frac{2}{3}U^{(3)} + \frac{2}{3}\Delta R^{(3)} \tag{3.13}$$

with a maximum CFL of $1/n_d$, where n_d is the dimension of the problem.

Countless optimised versions with larger allowable CFL, e.g. the strong stability preserving RK(4,5) of Spiteri [241], or low dissipation and dispersion error for computational aero acoustics [14] can be also found in the literature.

3.2 Code development roadmap

After presenting the basis of the computational methods employed, the adopted work plan for the development, validation and verification of the flow solver is here reported. As the project started from scratch, a certain amount of time was devoted to acquiring the theory of numerical methods, the physics of compressible flows and the programming skills needed. The workflow in Figure 3.2 shows the path followed. After gathering the necessary information, a systematic approach was followed, tackling problems of increasing complexity and interposing milestone validations or verification between each successive step. The first problem approached was 1D diffusion and linear advection equation. Despite being simple, these model equations possess most of the fundamental properties that are also part of the full Navier-Stokes system, and they

allowed to familiarise with the numerical techniques and the programming logic. In particular for the advection equation, most of the tools needed for the two- and three-dimensional discretisation were already required at 1D level. The solution of transport of a scalar into a uniform imposed velocity field allows to study the differences between the spatial and temporal discretisation schemes, posing also the basis of high-resolution limited schemes for discontinuous solutions. In addition to standard benchmarks for 1D linear convection and diffusion, the theory of TVD schemes and space-time coupling was assessed for 1D Euler equations, representing the second major step. Solving for the non-linear hyperbolic system of conservation laws in one dimension introduced most of the physics and programming kernels that have been used in 2D problems since, as stated in previous section, convective flux calculation is done essentially in a one-dimensional formulation. Analytical solutions of 1D Euler equations are available for the model case, which is the Riemann initial boundary value problem. Comparison between exact and approximate Riemann solvers and time-marching algorithms constituted an essential basis of validation of convective flux discretisation. Extension to two dimensions was, therefore, relatively straightforward, except for the gradient reconstruction. In fact, as the code was thought to be applicable in general domains, its internal data structures and also the numerics are unstructured and the gradient reconstruction techniques presented in section A.4 were employed.

Despite not strictly necessary for the kind of problems targeted, dealing with through-flow solutions, it was chosen to keep the code generic for possible further extension. An important part of the development, indeed, not lumped in a specific period, dealt with the geometry discretisation and the mesh quantities calculation and storage. Differently from structured Cartesian meshes and typical Finite Differences domains, a lot of geometrical quantities are needed by FVM, such as cell, node and face centres, areas, volumes, normals, Gauss integration points, connectivity and data hierarchy. All this information must be stored in memory, as it is frequently accessed during runtime and on-line calculation becomes inefficient. Continuous improvement of data structures and mesh topology information was attempted during the development. When the baseline structure of the code was available, the implementation and validation of gradient reconstruction techniques in generic domains was possible, representing the third building block of the code. At that point, a 2D inviscid solver was available and after a proper verification it was extended from first order Godunov to high-resolution, adding the gradient limitation technique of Section 3.1.4.

The validation of the 2D Euler code was concluded by the first year of the doctoral programme. Inclusion of diffusive terms made the solver viscous and allowed subsequently to validate the 2D Navier-Stokes equations against analytical solutions or verify them against available benchmarks in the literature. Among them, Stokes first and second problem, Couette and Poiseuille flow, 2D Green vortex, lid-driven cavity, double shear layer, flow past a laminar cylinder were used as reference solutions. A very important part in flow modelling is represented by boundary conditions. If during the early development periodic boundaries can be used, that do not introduce any approximation, simulating different flows require consistent, accurate and well-posed bound-

ary values. Throughout the development, different types of boundary conditions have been implemented and tested, ranging from simple extrapolation to attempts to incorporate finer formulations based on non-reflective boundary conditions. The approach commonly employed in RANS FVM codes, however, do not require and neither allow that level of accuracy, which is instead essential to solvers tackling DNS or LES. Having verified the correctness and robustness of the 2D Navier-Stokes solver, the following step was the conversion to a Reynolds-Averaged formulation. The turbulence model used was Spalart-Allmaras one equation model, for which NASA Turbulence Modelling Resource web page [179] provided valuable information for implementation and verification. RANS solution with time-explicit techniques is always problematic, as the magnitude of the non-linear source terms can cause divergence, requiring special treatments to be observed. Nonetheless, verification of the implementation was finally successful and the last move was rewriting the solver in cylindrical coordinates for axisymmetric swirl flows. This adds another out-of-plane equation to be solved, but the axisymmetric hypothesis removes some terms from the equations so that the additional computational cost is limited and most of the routines can be reused with minor modifications. The development of the core flow solver, in what is needed for the body force model, was concluded after eighteen months from the beginning of the doctoral programme. In the remainder of this chapter, the main steps of the development and validation are reported. Further test cases are presented in Appendix B.

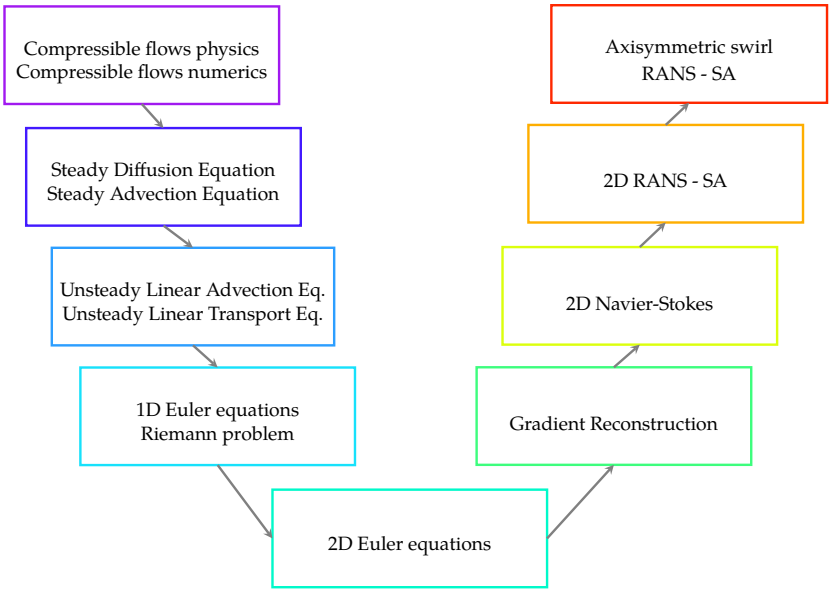

Figure 3.2: Workflow for code development

3.3 Linear advection equation

The model equation for convection is the one-dimensional linear advection:

$$\begin{cases} \dfrac{\partial \phi}{\partial t} + a\dfrac{\partial \phi}{\partial x} = 0 \phi(x, t0) = \phi_0(x) \end{cases} \tag{3.14}$$

It is an hyperbolic equation with constant wave speed a and the solution uniform on characteristic lines $x - at = constant$, such that the scalar ϕ is simply convected with speed a:

$$\phi(x, t) = \phi_0(x - at) \tag{3.15}$$

With this simple model it is possible to implement various space and time schemes to evolve the solution, enabling to highlight several features of numerical schemes, such as accuracy, stability, diffusion and dispersion errors. For instance, Figure 3.3 shows the result for the advection of a square wave for two seconds with unit velocity using different spatial schemes and Second Order Upwind Euler (SOUE) in time. The discretisation grid had one hundred equally spaced elements. The CFL number was kept equal to 0.5 in all the schemes. The square wave advection is a challenging test case for all the methods as the solution is discontinuous and contains a lot of harmonics that are subject to dispersion error by even order methods, causing the appearance of over- and under-shoots and wiggles in the solution. Indeed, central difference in space completely destroys the scalar distribution after a few characteristic times. The first order upwind method (FOU), instead is monotonicity preserving but has a lot of numerical dissipation and the initial profile is rapidly smeared and lost as well. The second order upwind scheme (SOU) has second order accuracy in space but is not bounded and the solution also has over- and under-shoots due to the discontinuity. The introduction of slope limiters helps improving the reconstruction near the steep gradients and tries to avoid the formation of new extrema. It can be noticed that the MINMOD limiter is more "generous" and more dissipative that the SUPERBEE, which instead is more compressive. The QUICK scheme, using quadratic reconstruction, is not limited but again gives rise to oscillations.

These kind of cases represented the first implementation of numerical schemes and were used to gain a better understanding of the numerics and error behaviour. It is evident how the choice of the spatial and time scheme is interdependent for time accurate simulations and must adapt to the mathematical model. Having set up the basic integration algorithms, some two-dimensional cases where also diffusion was added to the linear advection were studied, but are omitted here.

3.4 1D Euler equations. Riemann problem

The previously studied model equations, despite very useful, are not fully representative of the non-linear nature of the hyperbolic system of conservation laws formed by Euler equations, which were tackled starting from the one-dimensional case. The

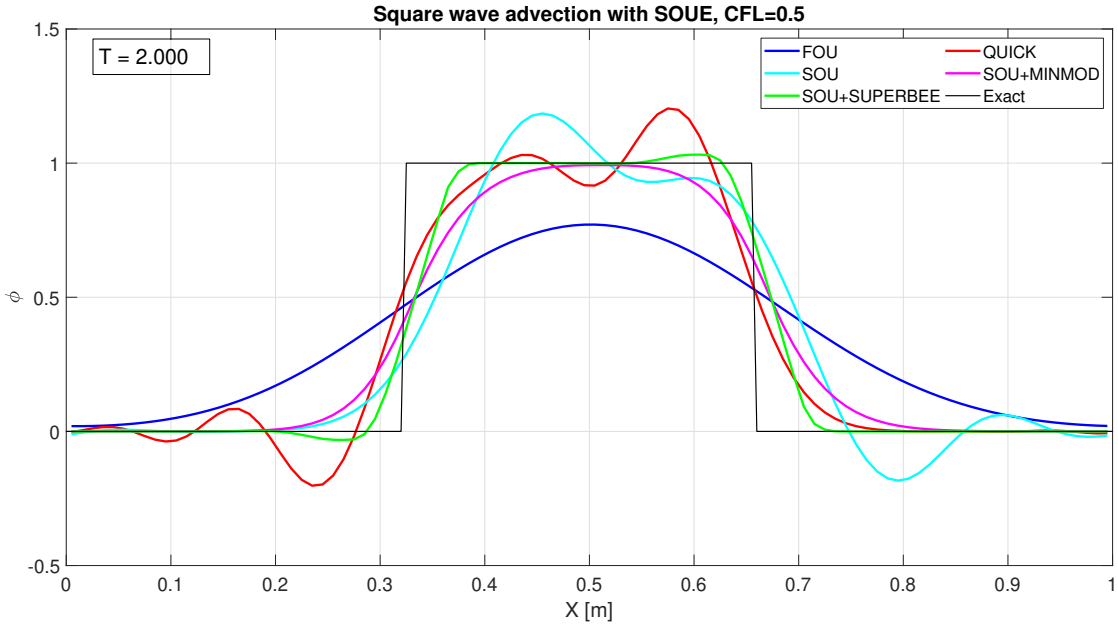

Figure 3.3: Comparison of spatial scheme for linear advection of a square wave. Grid size is 100 cells. CFL = 0.5

initial boundary value problem of reference, known as Riemann problem, requires the evolution in time and space of an initial uniform field separated in two discontinuous regions:

$$\mathbf{U}(x,0) = \begin{cases} \mathbf{U_L} \text{ if } x < 0 \\ \mathbf{U_R} \text{ if } x > 0 \end{cases} \tag{3.16}$$

The solution in the space-time axis is so separated by four regions by the three fundamentals waves arising, compressive, expansive or contact. A complete discussion is given in [262]. The Riemann problem can thus be solved exactly by a conditional check on which wave is present on each point, once estimates for the wave speeds have been obtained. This reference solution can be used to validate the flux integration schemes adopted. Here the Godunov first-order upwind and high-resolution schemes were considered. For instance, Figure 3.4 shows the Riemann problem Test 1 of Toro solved with MUSCL scheme with characteristic waves limiting and HLLC approximate Riemann solver, comparing the numerical and exact solution after 0.302 time units. The computational grid had one hundred equispaced points. The problem has one expansion fan in the left region and a shock wave in the right one, separated by a contact line, visible in the density change. The shock wave for the velocity is almost entirely captured in three cells and the solution is in agreement with its exact counterpart.

A series of problems like this were solved with different schemes, adopting first order, TVD schemes with slope or waves limiters, and WENO, and Forward Euler (FE)

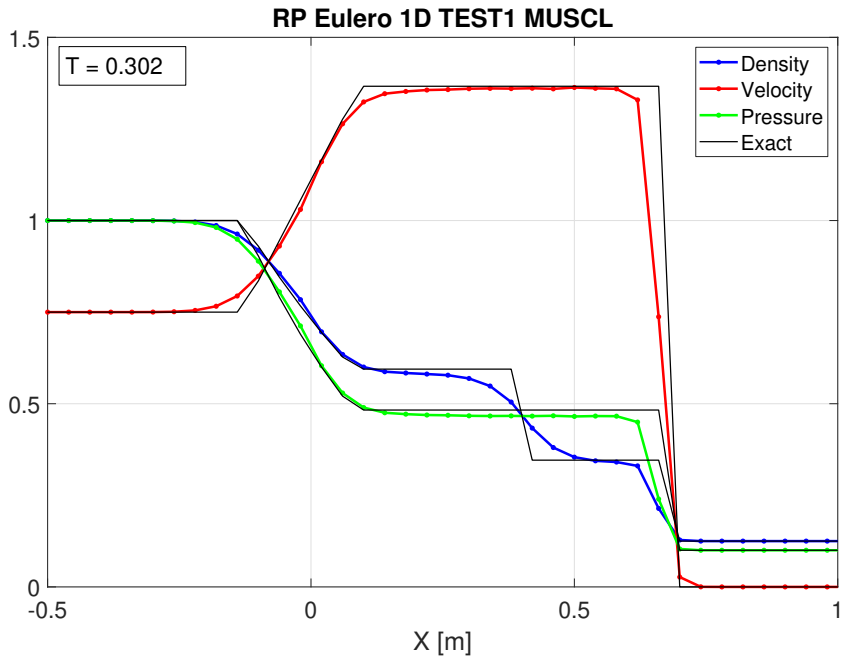

Figure 3.4: Riemann problem Test 1 of Toro [262] solved with MUSCL-Hancock, HLLC Riemann solver and Forward Euler in time, CFL = 0.5

or Runge-Kutta algorithms in time. These benchmarks allowed to familiarise with the different techniques and the non-linearity of advective flux, establishing the procedures for the set-up of approximate Riemann solvers and their employment in flux reconstruction. After consolidating the understanding of the 1D Euler equations, the following step described in the next section was extension to two dimensions.

3.5 2D Euler equations

The solution process of the Euler equations in two dimension was essentially analogous to the one-dimensional case, in that an unsplit Godunov solver was adopted, where flux is computed on each face of the domain elements solving the local projected 1D Riemann problem, using rotational invariance of Euler equations. A number of verification and validation cases are available to assess the correctness of the implementation.

3.5.1 Isentropic vortex convection

A common test case with an analytical solution is the convection of an isentropic vortex over a periodic domain. The solution is initialised with

$$\begin{cases} \rho = [1 - \dfrac{(\gamma-1)b^2}{8\gamma\pi^2} e^{1-r^2}]^{\frac{1}{\gamma-1}}, \; p = \rho^\gamma \\ u = u_\infty - \dfrac{b}{2\pi} e^{\frac{1}{2}(1-r^2)}(y - y_c), \; v = v_\infty + \dfrac{b}{2\pi} e^{\frac{1}{2}(1-r^2)}(x - x_c) \end{cases}$$

where $b = 0.5$ is the vortex strength, $r = \sqrt{((x-x_c)^2 + (y-y_c)^2)}$ is the distance from the vortex centre. The domain was squared with bounds $[0; 10] \times [0; 10]$. This will result in a simple convection of the structure, which makes possible to determine the discretisation error after propagation in time. Figure 3.5 shows snapshots of the vortex being convected with the oblique velocity at different instants of time. Figure 3.6 depicts the L_∞ and L_1 norm of the error after an integration time of $10s$, corresponding to a full period for the domain with side length of 10 units, as a function of the grid size h. The time integrator was Runge-Kutta RK3-TVD, whilst second order limited reconstruction was used for advection terms. The slope of both norms is -2, confirming second order accuracy of the convective solver and the good behaviour of the limiter, that did not activate given the smoothness of the solution.

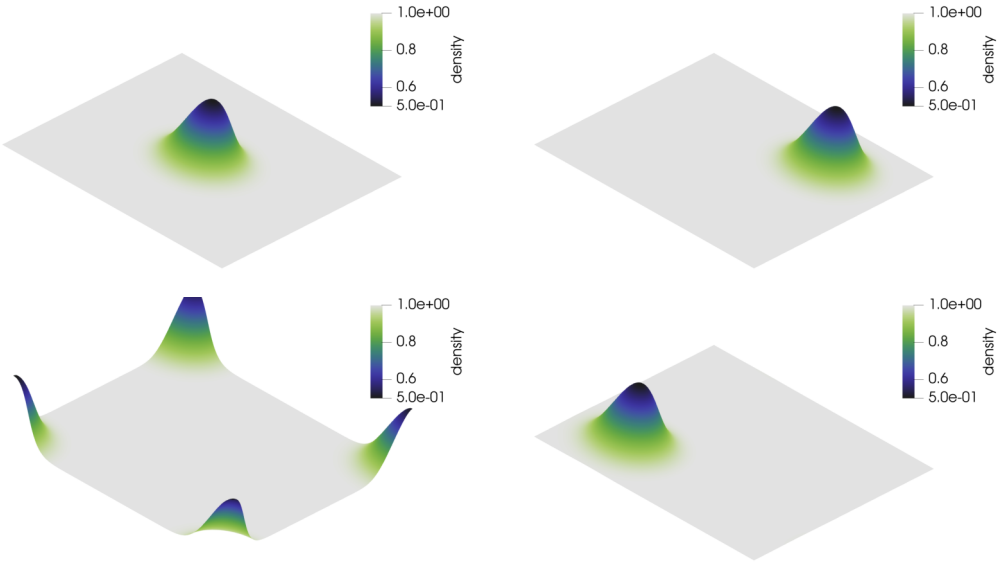

Figure 3.5: 2D isentropic vortex convection. Snapshots at different times.

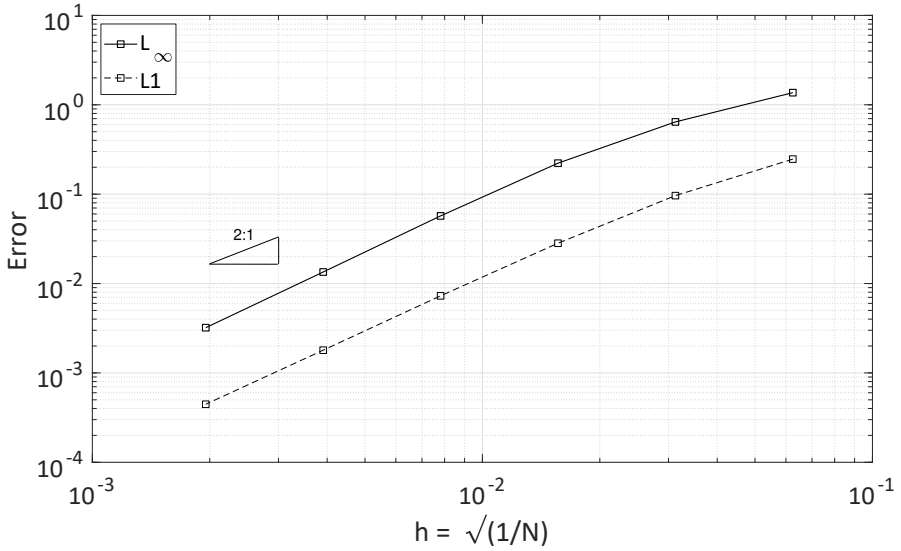

Figure 3.6: 2D isentropic vortex convection error after t = 10 s

3.6 2D Navier-Stokes equations

After the validation and verification of the high-resolution convective solver, the code was extended to include the viscous fluxes of Navier-Stokes equations. Before looking at the available analytical solutions, the gradient reconstruction method, which is the basis of diffusive fluxes calculation, was validated on the model equation $\nabla^2\phi = 0$, the steady Poisson equation. Figure 3.7 illustrates the L_∞ and L_1 norm of the reconstruction using the LSG method on a square domain. The test function was in the form of $sin(k_x x - \alpha)sin(k_y y - \beta)$ and periodic or exact Dirichlet boundary conditions were imposed. The method converged to 2nd order accuracy on both norms and even in the case of a high aspect ratio of 10000, which is often found in wall-clustered grids for high-Reynolds flows.

To examine the influence of skewness, which was shown to have a detrimental effect on truncation error convergence for some methods, a butterfly domain with curved wall was examined, using as test function $tanh(10(x - 0.5))tanh(20y)$. The domain with the solution is depicted in Figure 3.8b. The L_∞ the L_1 norm of the mean absolute error in Figure 3.8b again converge with -2 slope in the logscale both for a unit aspect ratio and for an AR=10000, proving that the LSG gradient reconstruction method implemented keeps second order accuracy for stretched cells on curved domains with smooth functions.

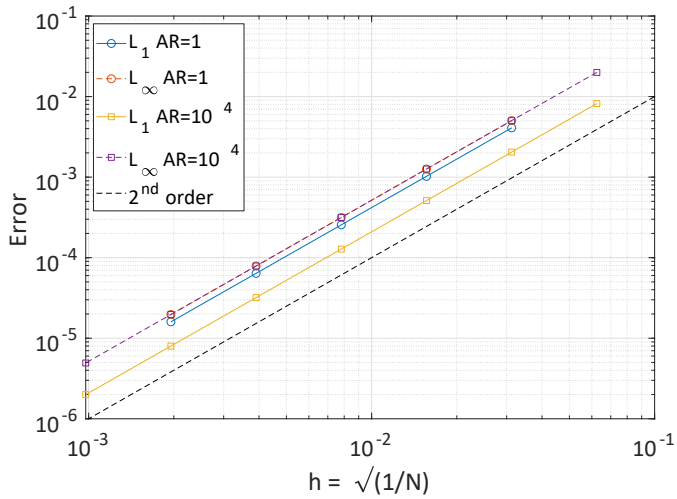

Figure 3.7: Error scaling for gradient reconstruction

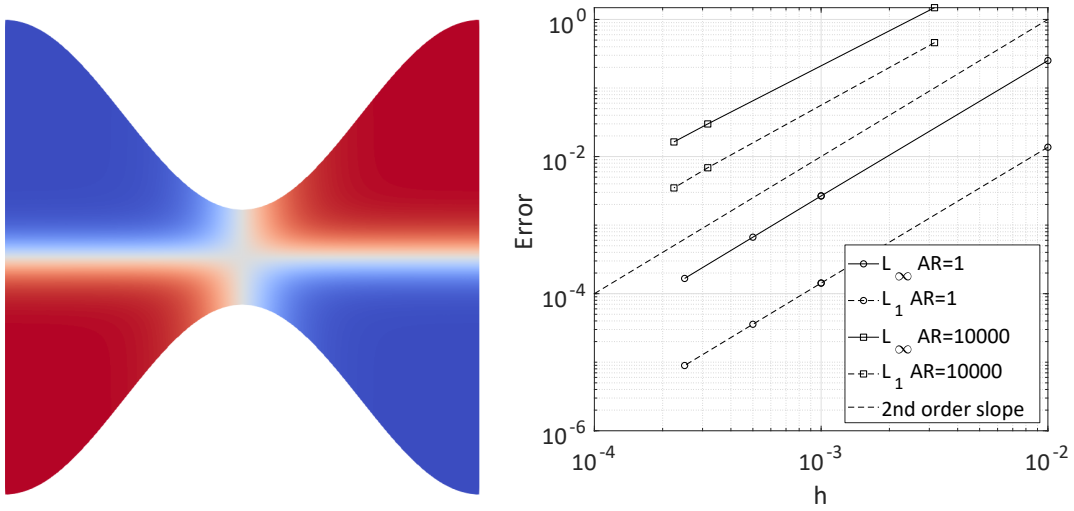

(a) Domain and test function

(b) Error scaling

Figure 3.8: Error scaling for LSG gradient reconstruction on curved domain.

3.6.1 Couette Flow

A few laminar flow cases of Navier-Stokes equations possess an analytical solution, making them suitable for direct validation. Among them, the simplest one is the planar Couette flow over a channel with parallel walls and infinite out-of-plane length, where wall velocity is imposed. The well-known solution is a linear velocity profile for the incompressible case, with a parabolic temperature profile for isothermal walls:

$$\tilde{U}(Y) = Y \tag{3.17}$$

$$\tilde{T}(Y) = \frac{T(y) - T_0}{T_1 - T_0} = [1 + \frac{1}{2} Pr\, Ec(1 - Y)]Y \tag{3.18}$$

$$Y = y/L,\ U = u/U,\ Pr = \frac{c_P\, \mu}{k},\ Ec = \frac{U^2}{c_P \Delta T} \tag{3.19}$$

where L is the channel height, U is the imposed upper wall velocity and $T_1,\ T_0$ the imposed upper and lower wall temperature. Figure 3.9a displays the velocity and temperature profile for progressively refined grids, proving that the linear function is always exactly matched, whilst the parabolic shape is closer and closer to the reference solution. Figure 3.9b proves the second order convergence for the L_∞ and L_1 norm of the absolute error on the reconstructed quadratic temperature profile.

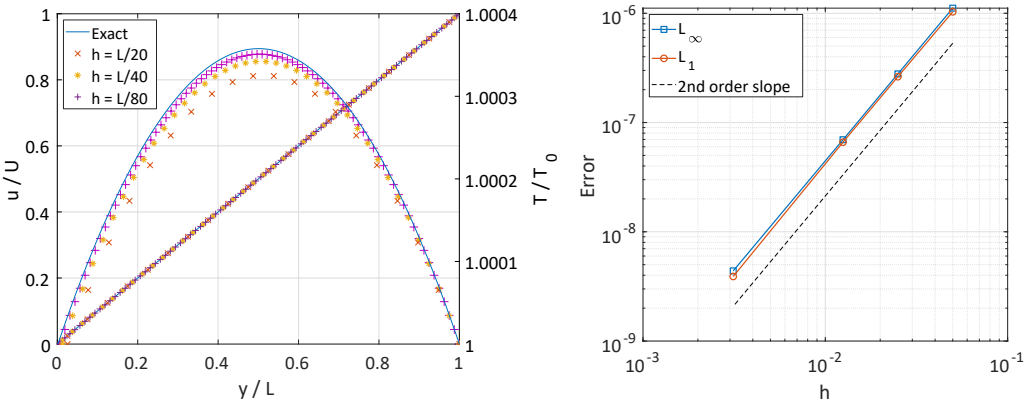

(a) Velocity and temperature profile (b) Temperature error scaling

Figure 3.9: Planar Couette flow.

3.7 2D RANS

The successful validation and verification of the solution of 2D Navier-Stokes equations cleared the way to the transformation into a RANS solver. The RANS equations are conceptually obtained through the ensemble-averaging of the Navier-Stokes equations, after each derived variable has been expressed as the sum of a mean and a perturbed

value, $\phi = \bar{\phi} + \phi'$. This is known to give rise to a set of equations which are formally identical to the original ones, but with the addition of stress terms which are responsible for the momentum and energy transfer from the unsteady to the averaged solution, called Reynolds stresses. When they are modelled with the Boussinesq approximation, they are given an analogous expression to the unsteady viscous stresses but using a different viscosity, called eddy viscosity:

$$-\rho\overline{u_i' u_j'} = \tau_{ij}' = 2\mu_t \bar{S}_{ij} - \frac{2}{3}\rho\kappa\delta_{ij} \tag{3.20}$$

With this approximation, where $\bar{S}_{ij}$ is the symmetric part of the averaged velocity gradient and κ is the turbulent kinetic energy, which is often neglected in the expression in RANS modelling, it is sufficient to add to the laminar viscosity μ its turbulent counterpart μ_t in the viscous fluxes. Despite this is a little modification for the flow solver, the eddy viscosity is unknown and it must be provided by additional equations, forming the turbulence model. In addition, a variety of issues regarding the need of additional quantities and numerical stability makes the development of a RANS solver quite difficult. In the current implementation, the one equation Spalart-Allmaras turbulence equation model was employed [240]. It provides a transport equation for a modified viscosity $\tilde{\mu}$, that is related to μ_t vi a nonlinear relation, and it is widely used in external aerodynamics and industrial problems.

3.7.1 Spalart-Allmaras turbulence model

The Spalart-Allmaras (SA) model has been corrected and extended throughout the years, from its first appearance in 1994, to overcome a series of instabilities of the original version [4]. The one used in this code is called *SAneg-noft2* in the reference NASA Turbulence Modelling Resource TMR [179]:

$$\frac{\partial \rho\tilde{\nu}}{\partial t} + \vec{\nabla}\cdot\left(\rho\vec{U}\tilde{\nu}\right) = \tag{3.21}$$

$$= \rho\left(P - D + T\right) + \frac{1}{\sigma}\vec{\nabla}\cdot\left[\rho\left(\nu + \tilde{\nu} f_n\right)\vec{\nabla}\tilde{\nu}\right] +$$

$$+ \frac{c_{b2}}{\sigma}\left(\vec{\nabla}\tilde{\nu}\right)^2 + \frac{1}{\sigma}\left(\nu + \tilde{\nu}\right)\vec{\nabla}\rho\cdot\vec{\nabla}\tilde{\nu} \tag{3.22}$$

where:

$$\nu_t = \tilde{\nu} f_{v1}, \qquad f_{v1} = \frac{\chi^3}{\chi^3 + c_{v1}^3}, \qquad \chi = \frac{\tilde{\nu}}{\nu} \tag{3.23}$$

The source terms of production P, destruction D, and trip term T are given by:

$$P = \begin{cases} c_{b1}\left(1 - f_{t2}\right)\tilde{S}\tilde{\nu},\ if\ \tilde{\nu} \geq 0 \\ c_{b1}\left(1 - c_{t3}\right)\tilde{S}\tilde{\nu},\ if\ \tilde{\nu} < 0 \end{cases} \tag{3.24}$$

$$D = \begin{cases} \left(c_{w1} f_w - \dfrac{c_{b1}}{\kappa^2 f_{t2}}\right)\left[\dfrac{\tilde{\nu}}{d}\right]^2,\ if\ \tilde{\nu} \geq 0 \\ -c_{w1}\left[\dfrac{\tilde{\nu}}{d}\right]^2,\ if\ \tilde{\nu} < 0 \end{cases} \tag{3.25}$$

$$T = f_{t1}\left(\Delta u\right)^2 \tag{3.26}$$

S is the vorticity magnitude, d is the distance to the closest wall. The other variables and functions are:

$$\tilde{S} = \begin{cases} S + \bar{S}, & if\ \bar{S} \geq -c_{v2}S \\ S + \dfrac{S\left(c_{v2}^2 S + c_{v3}\bar{S}\right)}{\left(c_{v3} - 2c_{v2}S\right)S - \bar{S}}, & if\ \bar{S} < -c_{v2}S \end{cases} \tag{3.27}$$

$$\bar{S} = \frac{\tilde{\nu}}{\kappa^2 d^2 f_{v2}} \tag{3.28}$$

$$f_{v2} = 1 - \frac{\chi}{1 + \chi f_{v1}}, \qquad f_n = \begin{cases} 1,\ if\ \tilde{\nu} \geq 0 \\ \dfrac{c_{n1} - \chi^2}{c_{n1} + \chi^3},\ if\ \tilde{\nu} < 0 \end{cases} \tag{3.29}$$

$$f_w = g\left[\frac{1 + c_{w3}^6}{g^6 + c_{w3}^6}\right]^{1/6}, \qquad g = r + c_{w2}\left(r^6 - r\right), \qquad r = min\left(\frac{\tilde{\nu}}{\tilde{S}\kappa^2 d^2},\ r_{lim}\right) \tag{3.30}$$

The model default constants are:

$$\begin{aligned} &c_{b1} = 0.1355,\ \sigma = 2/3,\ c_{b2} = 0.622,\ \kappa = 0.41 \\ &c_{w1} = c_{b1}/k^2 + (1 + c_{b2})/\sigma\ c_{w2} = 0.3,\ c_{v1} = 7.1,\ r_{lim} = 10 \end{aligned} \tag{3.31}$$

This variant of the model allows the transported modified turbulent viscosity $\tilde{\nu}$, which is the evolved quantity, to become locally negative. This might happen for under-resolved grids near the boundary layer, and without a specific treatment it would cause an instantaneous crash of the computation due to negative density. The SA-neg variant changes the destruction and production terms when this happens, such that the negative $\tilde{\nu}$ becomes a passive scalar and the system automatically tries to restore to a positive state. The trip term T was not used, assuming fully turbulent conditions, which must be enforced by choosing at freestream a turbulent viscosity ratio greater than 10 or $\chi > 3$.

3.7.2 Computation of wall distance via partial differential equations

As it can be noticed from the above equations, the production and destruction terms require the knowledge of the distance d from the closest wall. This adds noticeable complexity to the code, as the problem of finding the minimum distance between elements in a set is complex and laborious. A variety of techniques are available, based on Nearest Neighbour (NN) search with calculation of Euclidean distance, of course not directly, as this would require $O(n^2)$ operations, but using graph theory and smart sorting, or on model equations. This second way allows to obtain accurate results even for complex geometric interfaces and curved walls, where the distance must be evaluated precisely between the cell centre an the reconstructed boundary wall geometry, considering curvature. Far from the wall, the inverse quadratic dependence of the distance in the model variables allows a much rougher estimation, as outside the boundary layer the source terms are very close to zero.

The approach followed in the current implementation is based on solution of a differential equation. There are three reference models in this framework [266, 267]: Poisson, Hamilton-Jacobi and Eikonal equation. The Poisson equation

$$\nabla^2\phi = -1 \tag{3.32}$$

was proposed by Spalding and can be used to retrieve a near-wall only accurate distance by using the gradient of ϕ.

The Hamilton-Jacobi equation

$$\begin{cases} H(\vec{\nabla}\phi, x) = \epsilon\nabla^2\phi \\ H(\vec{\nabla}\phi, x) = F(x)|\vec{\nabla}\phi| - 1 \\ d = F(x)\phi \end{cases}$$

gives the distance from the front propagation velocity $F(x)$, but is not very practical to be solved.

Finally, the Eikonal equation is a simplification of the Hamilton-Jacobi

$$|\vec{\nabla}\phi| = 1 \tag{3.33}$$

that allows to directly solve for $d = \phi$ exactly in all the domain, and it is the one chosen in the current implementation. All the equations can be solved in $O(NlogN)$ operations [267]. Dedicated methods have been proposed for their solution, see [267] for a review. For the specific case of the Eikonal equation, it can be turned into a transport-like form by setting $U = \vec{\nabla}\phi$ and adding a pseudo-time term:

$$\frac{\partial\phi}{\partial t} + U \cdot \vec{\nabla}\phi = 1 \tag{3.34}$$

In that form, it is possible to reuse part of the flow solver algorithms employed for the convective fluxes. Details of the solution procedure are here omitted and can be found

in [20, 292, 293]. The time-marching algorithm is best advanced to steady state using implicit time stepping, or explicit time stepping with multigrid. As developing these techniques specifically for this subtask was reckoned too expensive, a first order upwind flux calculation with RK51 explicit time stepping with implicit residual smoothing was finally employed. The finite volume solution of the Eikonal equation was found to require particular care at the boundaries, to obtain sufficient accuracy. As the target flow solver will have to operate mostly in logically rectangular structured domains, it was decided to employ the more benign finite difference approximation in curvilinear coordinates. This limits the current applicability of the method to structured domains, but it is sufficient for the scope of this PhD programme, and given that the wall distance calculation is a separated module in the program, a future extension to general unstructured domains using FVM will be always possible.

Figure 3.10 shows examples of wall distance calculation. For the planar wall case, the solution is exactly linear. For curved walls, the boundary face centroid does not fall in the actual curved line for a planar face. Higher order FVM suffer from this condition and high-order meshing can be used. Despite its tolerability in a second order accurate code, to enhance the local accuracy a cubic interpolation of face vertices was used to find a better boundary node where to impose the zero-distance condition. This was easily allowed by the FD discretisation, whilst it would have been more difficult for cell-centred FVM.

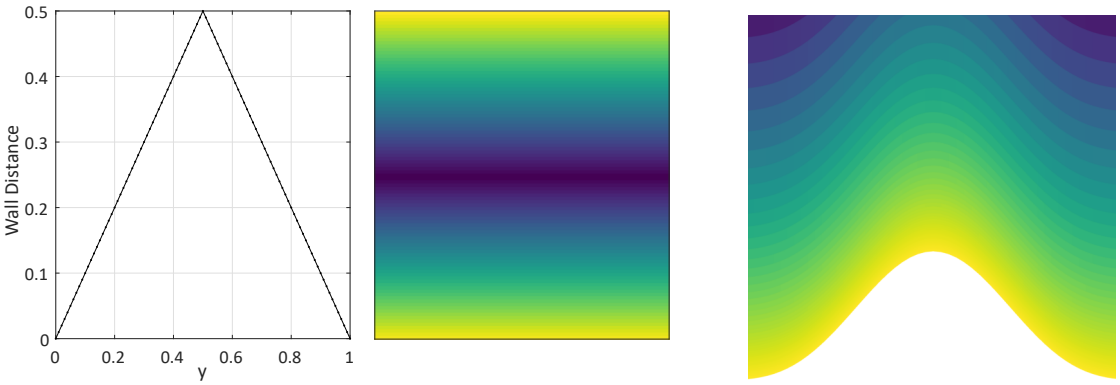

(a) Wall distance profile for rectangular domain

(b) Wall distance contour for bumped wall

Figure 3.10: Wall distance calculation using Eikonal equation.

3.7.3 Numerical methods

The equation for modified turbulent viscosity has the form of a transport equation with source terms. For the convective and diffusive fluxes, the same discretisation employed for the inviscid and laminar terms can be reused and the two sets of equations can be solved in a decoupled manner. For the convective part, a first order upwind discretisation can be used, providing sufficient accuracy with more stability to a second order inviscid solver [32]. If the turbulent variable is convected with second order accuracy, instead, a coupling of the convective fluxes using a modified HLLC-SA solver is preferable [6]. The presence of source terms in RANS models pose, however, a common stability issue, as they have a large varying magnitude that can induce divergence and negative density or pressure. Spalart [240] already highlighted this in the original paper, proposing a matrix splitting for implicit time stepping to ensure the positivity condition. However, this badly affects the convergence rate [302], and other remedies have been proposed [157, 230]. Given the fact that convergence to steady state is sought, the use of an implicit flow solver would be preferable. Specific treatments of the turbulent terms have been developed for this approach, to reduce numerical stiffness and improve convergence ratio of wall-clustered grids [25].

The implementation of an implicit time stepping (ITS) was explored during the development of the code. LU-SGS and BLU-SGS techniques (see Appendix A) were successfully tested for Euler equations for a variety of boundary conditions. The methods were then extended to Navier-Stokes and RANS equations, but without a fully operability. Within the limited timescale of this PhD programme, the whole task of ITS coding appeared infeasible, given that the flow solver was not the ultimate aim of the research, but only a necessary mean to study simplified methods for turbomachinery. It was chosen, therefore, to keep an explicit time stepping approach, enhancing the stability of the algorithm with a point-implicit source terms treatment. In this procedure, only the Jacobian of the source terms with respect to the turbulent variable are computed and acts as a restriction of the explicit time step [18]:

$$\frac{1}{\Delta t_{eq}} = \left[\frac{1}{\Delta t_{exp}} - \frac{\partial Q}{\partial \tilde{\nu}}\right] \tag{3.35}$$

Positive Jacobian contributions reduce the time step trying to increase the stability. The Jacobians of the source terms are very complicated due to the highly nonlinear formulations of the model, and are approximately computed.

In the framework of explicit time stepping, in addition to remedies to instability, there exist other ways to improve the algorithm efficiency. For steady-state calculations, acceleration techniques can be used to speed up the convergence. Among them, the simplest one is the adoption of local time stepping, where each cell is evolved to its maximum allowable time step. Other methods are the implicit residual smoothing (IRS) and multigrid [18, 68, 198]. The latter is based on multiple grid levels that exchange residuals among them to cut off high-frequency errors that are responsible for long evolution to reach convergence. The former is a way to extend the stability region of the explicit time algorithm by locally smoothing the residual in an implicit way.

IRS can be performed on different ways and according to the grid arrangement. For structured grids, a tridiagonal linear system can be formed in each cell to compute the smoothed residual [78], whilst for unstructured grids an iterative smoothing can be applied, for instance based on Laplacian operator [167]. A discussion of the smoothing effect on the stability of the methods and the acceleration mechanism is given in [97]. The method can be applied on a central or an upwind stencil, with different effectiveness according to the kind of problem [41]. In the current implementation, a central Laplacian implicit residual smoothing for unstructured grids is used:

$$\vec{R}_i^* + \sum_{j=1}^{N} \epsilon \left(\vec{R}_i^* - \vec{R}_j^* \right) = \vec{R}_i \tag{3.36}$$

where $\vec{R}_i^*$ denotes the smoothed residual, ϵ is a smoothing parameter and the sum involves the central stencil around the cell i. The implicit equation is solved with Jacobi iterations, that converge in just a couple of steps due to diagonal dominance. With $\epsilon = 0.5$ it is usually possible to double the CFL of the explicit RK.

3.8 2D Axisymmetric swirl solver

The final step required by the baseline flow solver was the conversion into cylindrical coordinates for axisymmetric flows with swirl. This step required a modification of the divergence operators and the inclusion of proper source terms to the equations, coming from the application of the same operators in cylindrical coordinates. The compressible Navier-Stokes equations in cylindrical coordinates read:

$$\frac{\partial \mathbf{U}}{\partial t} + \frac{\partial \mathbf{F_c}}{\partial z} + \frac{\partial \mathbf{G_c}}{\partial r} + \frac{\partial \mathbf{H_c}}{r \partial \theta} = \frac{\partial \mathbf{F_v}}{\partial z} + \frac{\partial \mathbf{G_v}}{\partial r} + \frac{\partial \mathbf{H_v}}{r \partial \theta} + \frac{1}{r}\mathbf{S_c} + \frac{1}{r}\mathbf{S_v} \tag{3.37}$$

where the fluxes and the source term coming from the divergence theorem are:

$$\mathbf{U} = \left\{ \begin{array}{c} \rho \\ \rho u_z \\ \rho u_r \\ \rho u_\theta \\ E \end{array} \right\} \tag{3.38}$$

$$\mathbf{F_c} = \left\{ \begin{array}{c} \rho u_z \\ \rho u_z u_z + p \\ \rho u_z u_r \\ \rho u_z u_\theta \\ (E+p)\, u_z \end{array} \right\} \quad \mathbf{G_c} = \left\{ \begin{array}{c} \rho u_r \\ \rho u_r u_z \\ \rho u_r u_r + p \\ \rho u_r u_\theta \\ (E+p)\, u_r \end{array} \right\} \quad \mathbf{H_c} = \left\{ \begin{array}{c} \rho u_\theta \\ \rho u_\theta u_z \\ \rho u_\theta u_r \\ \rho u_\theta u_\theta + p \\ (E+p)\, u_\theta \end{array} \right\} \tag{3.39}$$

$$\mathbf{F_v} = \begin{Bmatrix} 0 \\ \tau_{zz} \\ \tau_{zr} \\ \tau_{z\theta} \\ \theta_{zz} \end{Bmatrix} \quad \mathbf{G_v} = \begin{Bmatrix} 0 \\ \tau_{rz} \\ \tau_{rr} \\ \tau_{r\theta} \\ \theta_{rr} \end{Bmatrix} \quad \mathbf{H_v} = \begin{Bmatrix} 0 \\ \tau_{\theta z} \\ \tau_{\theta r} \\ \tau_{\theta\theta} \\ \theta_{\theta\theta} \end{Bmatrix} \tag{3.40}$$

$$\mathbf{S_c} = \begin{Bmatrix} -\rho u_r \\ \rho u_r u_z \\ \rho \left(u_\theta u_\theta - u_r u_r \right) \\ -2\rho u_r u_\theta \\ -\dfrac{u_r}{r} \left(E + p \right) \end{Bmatrix} \quad \mathbf{S_v} = \begin{Bmatrix} 0 \\ \tau_{zr} \\ \tau_{rr} - \tau_{\theta\theta} \\ 2\tau_{r\theta} \\ \theta_{rr} \end{Bmatrix} \tag{3.41}$$

$$\begin{aligned}
\tau_{zz} &= \mu \frac{\partial u_z}{\partial z} - \frac{2}{3}\mu \left(\frac{\partial u_z}{\partial z} + \frac{\partial u_r}{\partial r} + \frac{u_r}{r} + \frac{\partial u_\theta}{r \partial \theta} \right) \\
\tau_{rr} &= \mu \frac{\partial u_r}{\partial r} - \frac{2}{3}\mu \left(\frac{\partial u_z}{\partial z} + \frac{\partial u_r}{\partial r} + \frac{u_r}{r} + \frac{\partial u_\theta}{r \partial \theta} \right) \\
\tau_{\theta\theta} &= \mu \left(\frac{\partial u_\theta}{r \partial \theta} + \frac{u_r}{r} \right) - \frac{2}{3}\mu \left(\frac{\partial u_z}{\partial z} + \frac{\partial u_r}{\partial r} + \frac{u_r}{r} + \frac{\partial u_\theta}{r \partial \theta} \right) \\
\tau_{zr} &= \mu \left(\frac{\partial u_z}{\partial r} + \frac{\partial u_r}{\partial z} \right) \quad \tau_{z\theta} = \mu \left(\frac{\partial u_z}{r \partial \theta} + \frac{\partial u_\theta}{\partial z} \right) \quad \tau_{r\theta} = \mu \left(\frac{\partial u_r}{r \partial \theta} - \frac{u_\theta}{r} + \frac{\partial u_\theta}{\partial r} \right) \\
\theta_{ii} &= u_j \tau_{ij} + k \frac{\partial T}{\partial x_i}
\end{aligned} \tag{3.42}$$

If the equations are multiplied by the radius r, they can be simplified by grouping the divergence theorem terms [42], and by use of the Pappo-Guldino theorem it is possible to update the volume and area integrals operator only by multiplication of $2\pi r$, allowing for a little intrusive modification of the Cartesian solver [299].

In order to verify the correct implementation in the new reference frame, the Taylor-Couette problem was solved. In the cylindrical case, it deals with the axisymmetric flow between two circular pipes rotating at different speeds. The solution is nonlinear in the form $Ar + B/r$ and cannot be exactly computed for a second order solver, differently from the planar case. Moreover, it exhibits an instability when the Taylor number $Ta = \dfrac{\Omega^2 R_1 \left(R_2 - R_1 \right)^3}{\nu^2}$ exceeds 1700, with the formation of complex vortical structures with varying topology. Figure 3.11 reports the u_θ profile for a laminar stable case at $M = 0.1$, proving a close match with the analytical solution, that confirmed the correct conversion of the Cartesian solver into an axisymmetric one.

Axisymmetric Transonic Bump

The NASA TMR axisymmetric transonic bump case was used for the verification of the RANS-SA code. It is the analogous of the 2D bump channel problem, but for a

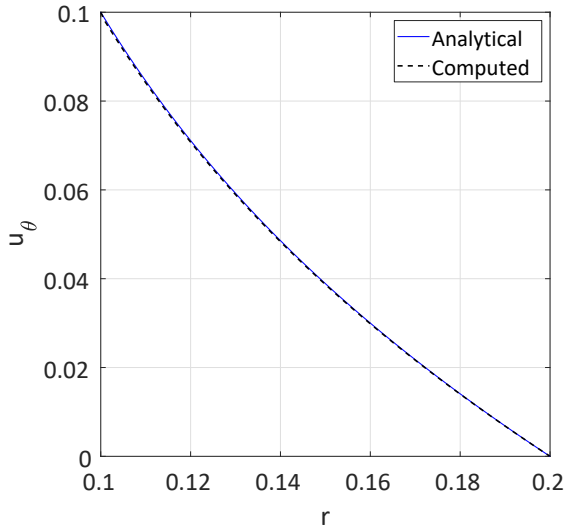

Figure 3.11: Laminar Taylor-Couette flow solution

circular pipe and at transonic regime. Freestream conditions were $M = 0.875$, $Re/L = 2.763 \times 10^6$ $[1/m]$ and were imposed in all boundaries other than the no slip bumped wall. The hump produces a shock wave impinging on the boundary layer in a lambda structure, which is followed downstream by a separation bubble. Figure 3.12 depicts the Mach number contours for the 361x161 grid, illustrating the situation.

Pressure coefficient distribution along the wall is reported in Figure 3.13a, where close agreement with the reference solution can be noticed. The boundary layer velocity profiles at different streamwise locations are shown in Figure 3.13b. Again, apart from small variations that can be attributed to the different grid levels under comparison, the match is very good.

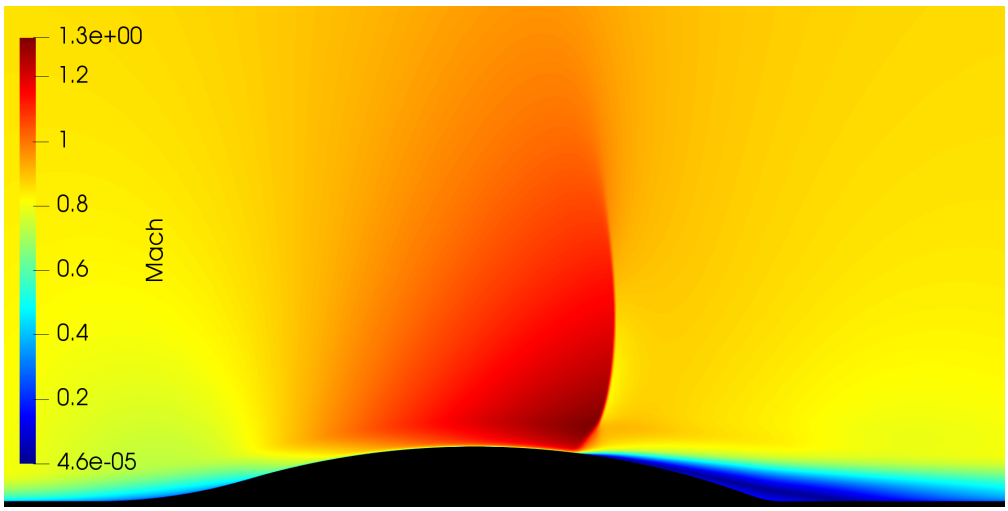

Figure 3.12: NASA TMR Axisymmetric transonic bump case at $M = 0.875$, $Re/L = 2.763 \times 10^6$. Mach number contours.

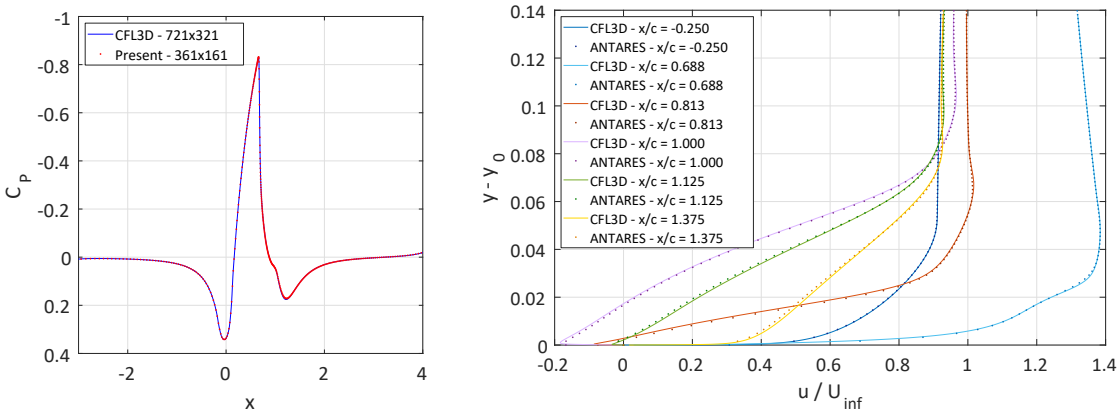

(a) Wall pressure coefficient

(b) Velocity profiles at different streamwise locations

Figure 3.13: NASA TMR Axisymmetric transonic bump case at $M = 0.875$, $Re/L = 2.763 \times 10^6$.

3.9 Parallelisation

In the context of computational fluid dynamics, the huge cost of the numerical methods makes the use of high-performance computing (HPC) techniques unavoidable. The topic of code parallelisation is vast and complicated. In CFD problems, domain decomposition is the standard approach in the Single Program Multiple Data (SPMD) paradigm. For unstructured finite volume solvers, the mesh graph must be distributed to the computing nodes using a suitable algorithm. A variety of them is available on open-source libraries, the most used of which is METIS [128], based on k-way multilevel partitioning. In a distributed memory environment, the Message-Passing Interface (MPI) library is used to establish communication between the computing units, that exist independently on each other and have a closed access to a reserved portion of the memory. This allows to employ computational nodes physically residing on different machines. The achievement of sufficient levels of parallel scalability is complicated by the large number of information that must be stored by a FVM and shared between neighbour processes. In implicit solvers, moreover, the full domain matrices must be split and solved in parallel, which is far from straightforward.

In the present project, tackling the implementation and assessment of body force models, most of the cases can be solved in a logically rectangular domain with a limited number of cells (in the order of 10^5). The parallelisation of a serial code requires several months of full work to reach an acceptable level, and an advanced knowledge to be acquired during the trial-and-error procedure that is inevitable in HPC software engineering. Again, this was thought to fall outside the scope of the PhD programme, and a full parallelisation was avoided. Instead, in a shared-memory environment, the OpenMP standard was employed for suitable computational kernels in the code. As the main task in FVM is flux calculation, the method does not land itself to loop parallelisation, since the cell residual must be accessed and updated by many faces at the same time, with the likely occurrence of the race condition. Unless using some custom colouring technique to coordinate the loops, only cell sweeps can be easily parallelised among tasks. Task parallelism, which is a Multiple Program-Multiple Data (MPMD) paradigm, has been proposed as a remedy, but it is an advanced cutting-edge approach. The adoption of OpenMP parallelisation has granted a reduction of computational time of roughly 25% for a typical run of the current code. Despite the limited advantage, no other easy modification would be possible to speed-up the iterations, apart from facing the full MPI parallelisation.

3.10 Conclusion

The workflow for the development of a RANS axisymmetric swirl flow solver has been unfolded, presenting the logical steps that led to implement and validate the computational tool from scratch. A systematic approach was followed to establish the correctness and robustness of the implementation. The second order accuracy has been proved by examining the error scaling for analytical solutions on all the numerical al-

gorithms that build up the FVM code. The RANS-SA model has been compared to reference solutions, showing a consistent and accurate behaviour. At the end of the process, the baseline flow solver was, therefore, available to allow the implementation of simplified methods for axial turbomachinery representation. This subject is discussed in the next chapter.

Chapter 4

Body force model validation

The axisymmetric swirl compressible RANS solver, whose development and validation was described in the previous Chapter 3, served as a stand-alone baseline tool where to implement and validate a body force model for axial fan. The code was called ANTARES (A Navier-Stokes Tool for Axisymmetric Rapid Engine Simulation) and it was used for the simulations presented in the remainder of the chapter, proving to be effective in granting the largest freedom and exploration during the test of different approaches and calibration strategies for the chosen BFM. As explained before, in the BFM context the flow equations are supplied with external forces that represent the force and energy transfer between the fully three-dimensional flow solution to the circumferential-averaged field and amount to the average momentum and work that the metal blades exert on the fluid. They appear, therefore, as source terms in the flow equations. The circumferential-averaged flow equations solved by the BFM program are:

$$\frac{\partial r\mathbf{U}}{\partial t} + \frac{\partial r\mathbf{F_c}}{\partial z} + \frac{\partial r\mathbf{G_c}}{\partial r} = \frac{r\partial\mathbf{F_v}}{\partial z} + \frac{r\partial\mathbf{G_v}}{\partial r} \tag{4.1}$$

$$-\frac{r}{b}\left(\mathbf{F_c}-\mathbf{F_v}\right)\frac{\partial b}{\partial z} - \frac{r}{b}\left(\mathbf{G_c}-\mathbf{G_v}\right)\frac{\partial b}{\partial r} + r\mathbf{S_c} + r\mathbf{S_v} + r\mathbf{S_b} + r\mathbf{S_n} + r\mathbf{S_p} \tag{4.2}$$

The source terms are:

$$\mathbf{S_c} = \left\{ \begin{array}{c} 0 \\ 0 \\ \rho u_\theta u_\theta + p \\ -\rho u_r u_\theta \\ 0 \end{array} \right\} \quad \mathbf{S_v} = \left\{ \begin{array}{c} 0 \\ 0 \\ -\mu\left[\frac{4}{3}\frac{u_r}{r} - \frac{2}{3}\left(\frac{\partial u_z}{\partial z} + \frac{\partial u_r}{\partial r}\right)\right] \\ \mu\left[-\frac{u_\theta}{r} + \frac{\partial u_\theta}{\partial r}\right] \end{array} \right\} \tag{4.3}$$

$$\mathbf{S_b} = \begin{Bmatrix} 0 \\ \frac{1}{b} p \frac{\partial b}{\partial z} \\ \frac{1}{b} p \frac{\partial b}{\partial r} \\ 0 \\ 0 \end{Bmatrix} \tag{4.4}$$

$$\mathbf{S_n} = \begin{Bmatrix} 0 \\ f_{nz} \\ f_{nr} \\ f_{n\theta} \\ f_{n\theta}\Omega r \end{Bmatrix} \quad \mathbf{S_p} = \begin{Bmatrix} 0 \\ f_{pz} \\ f_{pr} \\ f_{p\theta} \\ f_{p\theta}\Omega r \end{Bmatrix} \tag{4.5}$$

$\mathbf{S_c}$ and $\mathbf{S_v}$ come from the application of the divergence theorem in cylindrical coordinates. $\mathbf{S_n}$ and $\mathbf{S_p}$ come from the force applied to the fluid, decomposed in a normal and parallel component, according to a frame of reference locally aligned with the relative velocity vector. Ω is the rotational speed of the machine, to whom the force is synchronous and exerts a work $(f_{n\theta} + f_{p\theta})\ \Omega r$. b is the metal blockage parameter. $\mathbf{S_b}$ and the other terms involving b are due to the thickness of the blade and appear in the circumferential-averaging procedure. The expression of the force source terms depends on the body force model employed and it will be disclosed farther in this chapter.

The metal blockage b is defined as:

$$b = \frac{\theta_s - \theta_p}{2\pi Z} \tag{4.6}$$

where θ_s and θ_p represent the suction and pressure side circumferential angle of the blade, respectively, and Z is the number of blades in the row. It can be shown to be equivalently acting as a multiplier to the conservative variables and fluxes, $\tilde{\mathbf{U}} = b\mathbf{U}$ and it ranges from 0, meaning solid material and no fluid, to 1, where there is no solid. It has the effect of reducing the flow area felt by the fluid and it is important in the transonic regime to correctly reproduce the choking mass flow rate [8, 234, 253]. By treating the blockage-related terms as source terms, after application of divergence theorem, right-hand-side contributions appear also in the density equation, making the scheme non-conservative. However, if the blockage gradients are computed with the same method used for the flow variables, a very little effect is found, and with this treatment the ANTARES solutions had a typical inlet-outlet mass imbalance less than 0.05%, although for some cases near stall or choke it could grow up to 0.1%.

4.1 Body Force Model

In chapter 2 an overview of the throughflow methods for turbomachinery has been given, citing the main explicit body force models available in the literature. The largest class of methods have been devised at MIT starting from the '90s, and the major upgrade was given by Peters [200], who included the blockage, improved the parallel force model

and systematised the calibration procedure. An attempt to further improve this version was made by [22], but with partial success and no other published development, to this author's knowledge. More recently, Thollet proposed a new model inspired to Peters' and based on a lift/drag analogy [251]. Its L/D model was used to tackle inlet distortion and BLI configurations [84, 252]. The author also proposed a modification of Hall's inviscid model [101], that has been used for the same purpose [12] and also with design in mind [83]. Compared to Peters, its calibration is easier and based on a lower number of inputs. Given this feature and its recent application to a variety of problems with apparent promising results, it was decided to employ it inside ANTARES. Prior to any proposal for a possible improvement in this field, indeed, it is important to assess the implementation procedure, the behaviour and the reliability of the model, which cannot be simply understood by a literature review.

The Thollet L/D model is given by:

$$f_n = \frac{2\pi\sigma}{h}\left(\beta - \beta_n^0\right) \tag{4.7}$$

$$f_p = \frac{K_p}{h}W^2 \tag{4.8}$$

$$K_p = K_p^0 + 2\pi\sigma\left(\beta - \beta_p^0\right)^2 \tag{4.9}$$

$$h = \frac{2\pi\sigma r cos(\kappa)}{Z} \tag{4.10}$$

$$\kappa = r\frac{\partial\theta_m\left(z,r\right)}{\partial z} \tag{4.11}$$

f_n is the normal force component, responsible for the flow turning, and f_p is the parallel force causing entropy rise across the streamlines. The normal force is proportional to the deviation of the relative flow with respect to a reference angle β_n^0, which includes a correction to the metal camber surface angle κ. Similarly, the parallel force features a bucket profile with a quadratic dependency on a deviation term, with the minimum losses set by K_p^0. The model calibration parameters are β_n^0, β_p^0, and K_p^0. The first one is computed by inverting the normal force equation 4.7. Both the normal force modulus and the relative flow angle $\beta = atan\left(\frac{w_\theta}{w_z}\right)$ must be supplied from a circumferential-averaged fully 3D peak efficiency calculation using a standard approach with solid blade modelling. The same β equates to β_p^0, such that the losses through K_p are minimum at peak efficiency. K_p^0 is computed by inverting the parallel force equation, where the last input is the f_p modulus. Both f_n and f_p are extracted from the 3D simulation using one of the available methods, which will be discussed in the next section. The geometric inputs are the number of blades Z, the mean camber surface $\theta_m(z,r)$ and its angle κ, the solidity $\sigma(z,r)$ and the modified pitch h.

4.2 Force extraction

As most of the explicit body force models require, the force field must be extracted from a standard 3D simulation. Figure 4.1 summarizes the workflow to obtain the force distribution on the blade and consequently the model input parameters. The case is first simulated using a standard 3D approach. The solution is then circumferentially-averaged and reduced to a bidimensional field on the meridional plane, whose support is a background mesh. The averaged field is interpolated from this background mesh to the body force mesh, and finally the blade forces are computed. With this input, on each cell on the body force region it is possible to calculate the specific model coefficients, which are a spatial distribution of axial and radial coordinate $f(z, r)$. The existing methods to reconstruct the forces from the averaged 3D solution are discussed in the following.

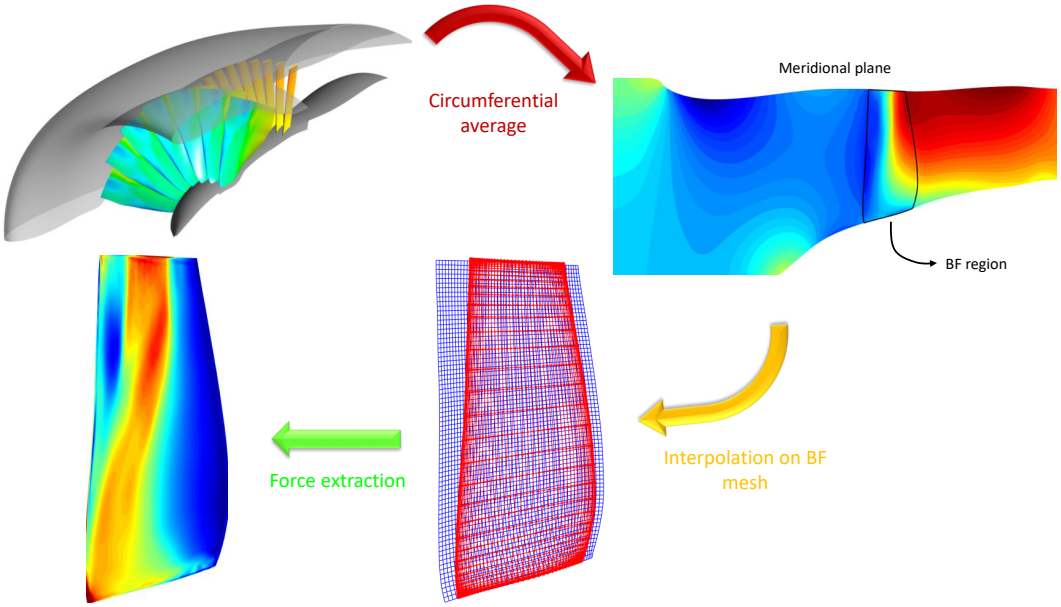

Figure 4.1: Force extraction work flow

As some geometric features are required by most BF models, a geometry analysis tool was built in Matlab, to allow extraction and manipulation of the blades. In particular, the blade surface, its mean camber with the angle on the $z - r\theta$ plane and the normals, the spacing and the solidity are needed. If the blade geometry is given by a points on a series of layers, on each section the pressure and suction side are first interpolated. Then, the mean camber line is iteratively computed and the full pressure, suction and mean surfaces are fitted through a suitable functional $\psi(z, r)$ (cubic spline, thin plate spline, biharmonic interpolation). With that available, it is possible to extract the $\theta(z, r)$ surfaces, the $\beta(z, r)$ and $\kappa(z, r)$ angles distribution, the thickness, the pitch, the solidity and the blockage factor. All these data must be interpolated on the

cell centre of the body force mesh to calibrate the model. Figure 4.2 shows a snapshot of the visual output of the developed geometric tool, reporting for each layer the main computed parameters.

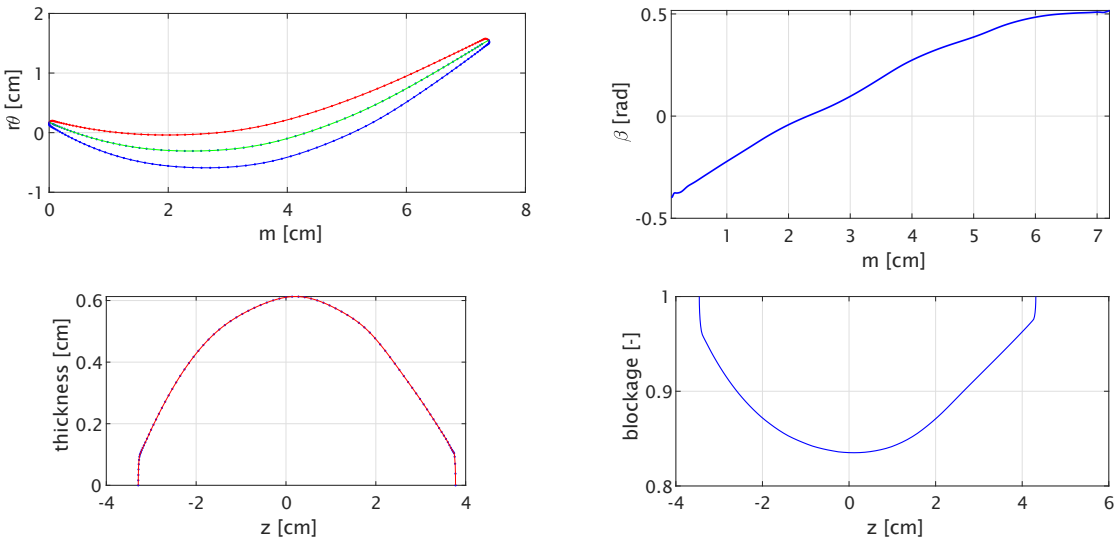

Figure 4.2: Snapshot of geometry manipulation tool output.

4.2.1 Peters

Peters detailed his force extraction procedure in the Appendix B of his thesis [200], to which the reader is referred if interested. The normal force is computed by first extracting the pressure at two points, one in the suction and one in the pressure side, where the normal to the local averaged relative velocity vectors intercepts the blade surfaces, as shown in Figure 4.3. The resulting normal force is

$$\vec{f}^{bl}_{n,A}(z,r) = \hat{n}_{ps} p_{ps} + \hat{n}_{ss} p_{ss} \tag{4.12}$$

$$\overline{f}^{bl}_{n,A}(z,r) = \frac{f^{bl}_{n,A}(z,r)}{\overline{\rho}\dfrac{2\pi r}{Z} K cos(\overline{\beta})} \tag{4.13}$$

where bar variables denotes circumferential average, K a free area factor similar to blockage, and β is the local relative flow angle. The method is difficult to implement, because involves computing intersection with the geometry, which can be difficult for large deviations.

4.2.2 Thollet

Thollet [251] highlighted another possibility, directly descending from the passage-averaged equations, in which the resulting source terms are isolated and the force cylin-

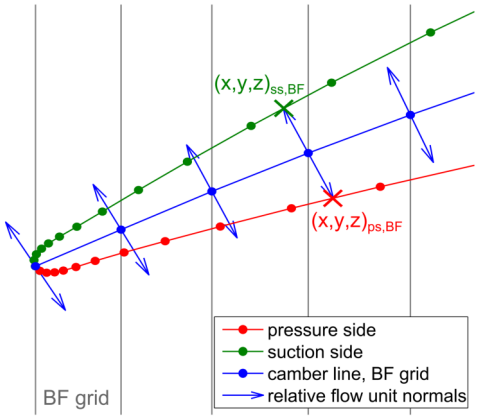

Figure 4.3: Peters blade pressure force extraction

drical components derived:

$$F_z = \frac{P_{ss} - P_{ps}}{\Delta\theta}\frac{\partial\theta_m}{\partial z} + \frac{\tau^{ps}_{p,z} + \tau^{ss}_{p,z}}{r\Delta\theta} + \frac{P_{ss} + P_{ps}}{2b}\frac{\partial b}{\partial z} \tag{4.14}$$

$$F_r = \frac{P_{ss} - P_{ps}}{\Delta\theta}\frac{\partial\theta_m}{\partial r} + \frac{\tau^{ps}_{p,z} + \tau^{ss}_{p,r}}{r\Delta\theta} + \frac{P_{ss} + P_{ps}}{2b}\frac{\partial b}{\partial r} \tag{4.15}$$

$$F_\theta = \frac{P_{ss} - P_{ps}}{r\Delta\theta} + \frac{\tau^{ps}_{p,\theta} + \tau^{ss}_{p,\theta}}{r\Delta\theta} \tag{4.16}$$

$\theta_m = \dfrac{\theta_{ps} + \theta ss}{2}$ is the blade mean camber surface, $\Delta\theta = \theta_{ps} + \theta ss$ is the angular extent of the blade thickness and p in the stress subscript denotes the parallel direction. The force now is expressed in its components and can be easily projected into the relative flow frame to get its normal and parallel component. However, as the author pointed out, the need to interpolate forces on the geometry persists and any error on blade mean camber surface reflects on the right direction of the force.

4.2.3 Blade Force Average

Kiwada [135] faced the force extraction problem when studying stall inception, pointing out how the averaging operation applied to the 3D Navier-Stokes equation must be carried out consistently. Since averaging does not commute for nonlinear terms, $\overline{\mathfrak{L}(\phi)} \neq \mathfrak{L}(\overline{\phi})$, $\mathfrak{L}$ a nonlinear operator, averaging must be applied to the whole sides of Navier-Stokes equations, whilst using averaged primitive variables to find the residual would introduce additional higher order terms. As in the Thollet method, the forces are

found as the averaged flux residual:

$$\overline{F_z} = \frac{1}{b}\frac{\partial}{\partial z}\left[b\left(\overline{\rho u_z u_z + p - \tau_{zz}}\right)\right] + \frac{1}{b}\frac{1}{r}\frac{\partial}{\partial r}\left[br\left(\overline{\rho u_z u_r - \tau_{zr}}\right)\right] - \frac{\overline{p}}{b}\frac{\partial b}{\partial z} \tag{4.17}$$

$$\overline{F_r} = \frac{1}{b}\frac{\partial}{\partial z}\left[b\left(\overline{\rho u_r u_z - \tau_{rz}}\right)\right] + \frac{1}{b}\frac{1}{r}\frac{\partial}{\partial r}\left[br\left(\overline{\rho u_r u_r + p - \tau_{rr}}\right)\right] - \frac{\overline{p}}{b}\frac{\partial b}{\partial r} - \frac{\left(\overline{\rho u_\theta u_\theta - \tau_{\theta\theta} + p}\right)}{r} \tag{4.18}$$

$$\overline{F_\theta} = \frac{1}{b}\frac{\partial}{\partial z}\left[b\left(\overline{\rho u_z u_\theta - \tau_{\theta z}}\right)\right] + \frac{1}{b}\frac{1}{r}\frac{\partial}{\partial r}\left[br\left(\overline{\rho u_\theta u_r - \tau_{\theta r}}\right)\right] + \frac{\left(\overline{\rho u_\theta u_r - \tau_{\theta r} + p}\right)}{r} \tag{4.19}$$

In this way the forces are conserved from the averaged 3D solution and the body force calculation. The cell force is again already decoupled and it can be obtained by the same flux balance computation used in the core flow solver, if the divergence theorem is used to convert the derivatives into surface fluxes.

4.2.4 Marble thermodynamic approach

The above methods deal directly with the force values and if consistently applied they should ideally guarantee a direct correspondence between the reference circumferentially averaged flow field and the one obtained once these forces are reinserted into an axisymmetric flow solver. However, the different procedures for their application introduce a number of error sources and difficulties that limit the accuracy and the resolution of the reconstructed field. Marble long before derived explicit equations from the energy and entropy balances along the meridional streamlines of an axisymmetric flow field, that are at the base of the SLC throughflow method [165]:

$$v_m \frac{\partial\left(r u_\theta\right)}{\partial m} = r f_\theta \tag{4.20}$$

$$v_m \frac{\partial h^0}{\partial m} = \Omega r\, f_\theta \tag{4.21}$$

$$v_m \frac{\partial s}{\partial m} = -\frac{W}{T} f_p \tag{4.22}$$

where $v_m = \sqrt{u_z^2 + u_r^2}$ is the meridional velocity, $\partial/\partial m = \partial/\partial z + \partial/\partial r$, W is the relative velocity. The second equation, descending from the first by application of Euler equation for turbomachinery, points out that the circumferential force component performs work onto the flow increasing its total enthalpy along the meridional streamlines. In the relative velocity frame, both the normal and parallel θ-components exert work on the fluid. The parallel component itself causes the entropy rise, as from the Crocco's theorem. From these equations it is also possible to isolate the force components, as first exploited by Thollet in the BFM context, who used the circumferentially mass-averaged entropy, tangential velocity and relative flow angle to compute their values. The distribution will conserve the energy and entropy rise, rather than the force value.

f_p can be obtained directly once the entropy gradient has been computed. As common in correlations for turbomachinery, the entropy rise can be assumed linear from

leading edge to trailing edge, which also smooths the parallel force value. f_θ is found with the first equation and

$$f_x = f_{p,x} - (f_\theta - f_{p,\theta}) \frac{W_\theta}{W} \tag{4.23}$$

$$f_{n,\theta} = f_\theta - f_{p,\theta} \tag{4.24}$$

$$f_{n,r} = -tan(\lambda) f_{n,\theta} \tag{4.25}$$

Despite this approach is much more easily implemented, it has the disadvantage that the boundary layer or shock losses are already naturally included in the viscous flow solver, and they will be applied a second time by the body force field.

4.2.5 Comparison of force extraction methods

The first three methods are theoretically equivalent but their implementation is different and can be quite complicated, as in the Peters'. The choice of the best suited method should be based on the quantitative comparison between the BF simulation and the reference averaged 3D solution. However, in practice the specific procedure might limit the resolution and prevent a good agreement. To assess this important aspect, the force methods (Peters, Thollet and BFA) were applied to a transonic fan, derived from the NASA Rotor 67 to whom a lean and sweep distribution were added. The presence of these three-dimensional features allowed to highlight the capability of the force extraction method to deal with radial components, which, as it will be treated later, are sometimes crudely modelled in BFM. The reference 3D solution was a single-passage steady-state simulation performed with ANSYS CFX commercial solver. The raw data necessary for each method were computed using a custom script in the software post-processing module CFD Post and processed in a MatLab code. The derivatives of the flux variables were computed using second order central difference and the forces interpolated on the body force meridional grid using bicubic interpolation.

Figure 4.4 shows the normal force extracted using the three methods. The similarity in the distributions implicitly validates the implementation, as quite different algorithms must be used for each approach. This also explains the differences in terms of absolute values and smoothness. The magnitude is comparable inside the blade. The averaged three-dimensional shock structure is highlighted by the oblique band descending from the blade tip to the hub leading edge. This pattern is present in all the methods. The force exhibits two peaks and degrades towards the trailing edge, outside the shock area, again consistently among the methods. However, near the leading edge and the endwalls there is more variation. Peters and Thollet, requiring the wall pressure and stress, are closer. In particular, at the hub no effect is visible, whilst at the blade tip they both produced a local high increase, greater for Peters, centred around mid chord. The BFA, conversely, has a more refined pattern not present elsewhere. At the hub, a boundary layer effect is visible, with a gently force degradation. At the blade tip, where a gap was present, secondary flows traces appear, detaching from the shock onset and running

towards lower span. The increased resolution comes at the cost of lower smoothness, as highlighted by the fragmented contour lines. It must be considered that despite a consistency in the interpolation algorithms across the methods was sought, the necessity of a different number of interpolation steps has an effect on the recomputed force field, its smoothness and resolution. Whilst the latter was evidently better for the BFA, in principle it could be possible to obtain a different smoothness using other interpolation schemes.

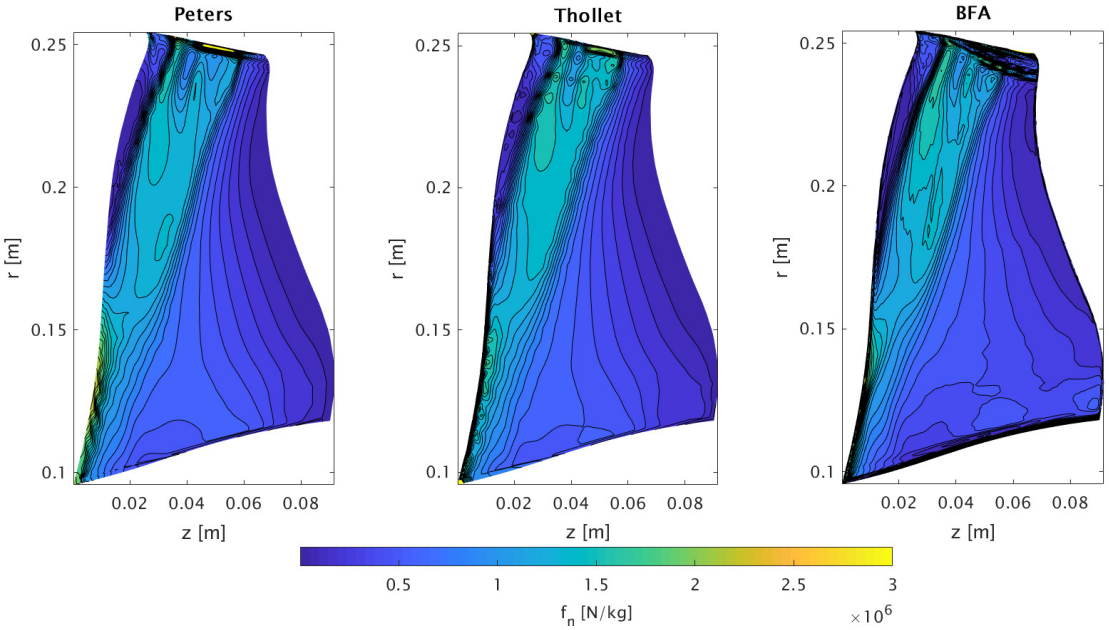

Figure 4.4: Comparison of extracted normal force field using different methods for a transonic compressor derived from NASA R67.

The advantage of the BFA over the other two models is that these interpolations do not involve blade wall quantities, removing the need to reconstruct the solid blade geometry and the data field on top of that. Figure 4.5 compares this method with the thermodynamic one based on Marble's equations for another transonic fan. The result is quite similar, both in distribution and in magnitude. The wrinkle of the contours near the leading and trailing edge and at the endwalls are equally captured, with just a finer trace for Marble near the blade tip.

As regards the parallel force, its extraction is more difficult since it is more sensitive to small errors on the direction that can give rise to negative values. Figure 4.6 compares the loss coefficient K_p^0 computed with the first three methods, for the same transonic blade of Figure 4.4, derived from R67. In this case, Peters and BFA have similar traces, with a loss increment in the boundary layer and near the smeared shocks. The Thollet implementation resulted in a smoother distribution. On average, the outcome was comparable in the absolute value. Areas of negative losses can be recognised for all the figures, in particular towards the trailing edge at mid span and locally near blade tip.

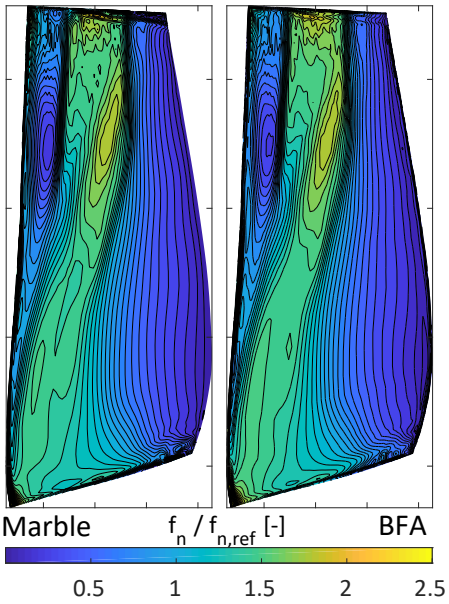

Figure 4.5: Comparison of extracted normal force field using BFA and Marble method for a transonic fan blade.

Although not standard, the addition of negative losses, i.e. a parallel force in the direction of the velocity, is tolerated by the BFM and poses no numerical difficulty. Negative values also arose when the thermodynamic relations were used, as the linear entropy variation assumed only used the leading and trailing edge values, neglecting the real history across the streamline. At the hub, the boundary layer entropy is convected radially along three-dimensional streamlies, causing a net decrease from leading to trailing edge. This assumption greatly affects the loss distribution, which was much smoother than the one derived with a force-based approach. As a matter of fact, however, either it is the combined effect of parallel and normal force that determines the local and bulk flow parameters, and there remain a certain level of arbitrariness in the absolute value and distribution of the losses.

As a final comment on the force extraction methodology, the use of inputs from the different methods to set the model calibration parameters resulted, in fact, in a little variation of the integral performance indexes. For this reason, the Blade Force Average procedure was retained for the normal force extraction, requiring less interpolation, which makes it less prone to error and biases, and giving the three-dimensional force vectors. This is important when 3D effects are accounted for, as the simple knowledge of the normal force magnitude is insufficient. This normal force should be known as the component in the local relative velocity frame of reference, and not just as an absolute value. Depending on the flow turning direction, a wrong sign in f_n can cause its spring-like equation in the model to have a negative elastic constant that causes divergence. With Marble's equation this information is not available, but it is better suited to provide a parallel force value, although accounting for viscous and shock losses. In conclusion,

the BFA was preferred for the normal force extraction, which was in very good agreement with Marble's as shown in Figure 4.5, while the thermodynamic approach for the parallel force calculation, providing a smoother distribution.

Finally, the set of passages leading from the 3D CFD simulation to the force field, made up of the circumferential averaging procedure on the background mesh, the extraction of blade geometric data and their interpolation, the calculation of the equation residuals through each averaged flux term, the interpolation from the background onto the body force mesh and the ultimate force decomposition, should be all regarded as part of the body force model, which is not built solely by the force equations, but from the whole instruction and calibration procedure, which is, however, often omitted when presenting a BFM result.

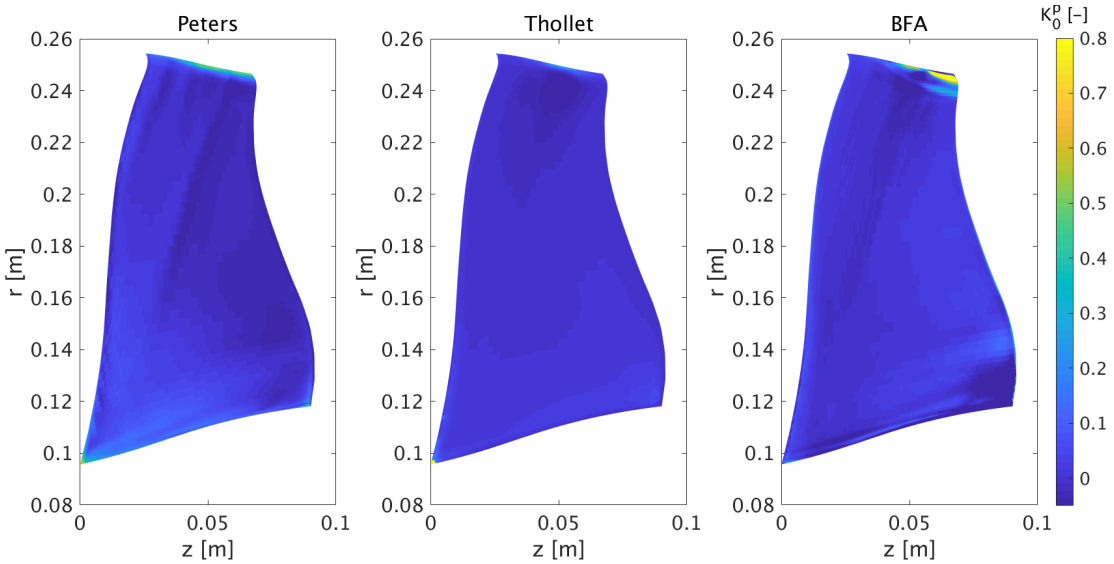

Figure 4.6: Comparison of loss coefficient computed using difference models.

4.3 Force decomposition

The reconstructed force field from the passage-averaged Navier-Stokes equations is made up of the three cylindrical force components. In the current implementation, the reference three-dimensional solution was computed using ANSYS CFX, which solves the RANS equations in cartesian coordinates. The fluxes are first constructed in cylindrical coordinates by applying the proper transformation and then circumferentially-averaged. The residuals of the averaged fluxes form the cylindrical force components. As the L/D model requires the normal and parallel part, the force vector on each cell must be locally projected into the frame of reference given by the relative velocity. With f_n and f_p, the model input coefficients can be retrieved. During a BF simulation, conversely, the normal and parallel force must be projected into the local axis of the solver,

either cylindrical or Cartesian. ANTARES was written in cylindrical coordinates, but in case of implementation on a Cartesian solver the force must be rotated from cylindrical to Cartesian coordinates and split into the momentum and energy equations. For both these tasks, the normal and parallel direction must be uniquely defined. This is always true for a two-dimensional flow, but there is no single normal vector for a three-dimensional domain.

In the throughflow context, the flow is usually first regarded as two-dimensional, to avoid any ambiguity in the normal and parallel direction definition, and then the radial out-of-plane force component is set as in equation 4.23, using the lean angle [234, 251]. However, this decomposition does not conserve the force magnitude. A better approach is to lay down the normal force on a plane containing the normal to the blade mean camber surface and the relative velocity vector [101]. The normal side should point towards the blade concavity, as the centrifugal force turning the flow is inward. This defines a unique frame of reference and assumes that the radial component is a pressure force normal to the blade mean camber surface.

Referring to Figure 4.7, it can be noted that the normal force can be expressed into a rotated frame of reference $< z_3, \theta_3, r_3 >$, obtained from the initial $< z, \theta, r >$ by application of the following rotations:

1. rotation of β around r
2. rotation of $-\lambda$ around θ_1
3. rotation of $-\delta$ around z_2

In the $< z_3, \theta_3, r_3 >$ reference, the normal force is written

$$\vec{F_n}^{\,3} = \{0, -f_n, 0\}^T$$

By applying the above rotations in the opposite verse and order, it is possible to express the force in the standard frame:

$$\vec{F}_n = \begin{bmatrix} -f_n\, sin(\delta) sin(\lambda) cos(\beta) + f_n\, cos(\delta) sin(\beta) \\ -f_n\, sin(\delta) sin(\lambda) sin(\beta) - f_n\, cos(\delta) cos(\beta) \\ -f_n\, sin(\delta) cos(\beta) \end{bmatrix} \tag{4.26}$$

The angles involved in the calculation are so expressed:

$$\beta = atan\left(w_\theta / w_z\right); \quad \lambda = atan\left(w_r / \sqrt{w_\theta^2 + w_z^2}\right); \tag{4.27}$$

The angle δ is not known a priori. If the plane where the normal force lies is chosen to contain also the normal to the blade mean camber surface, then $\delta = -lean$, $tan(lean) = \dfrac{1}{r}\dfrac{\partial \theta_m(z,r)}{\partial r}$. By computing δ from the extracted force field at peak efficiency, this assumption appeared valid, as outside the boundary layer the equality was closely satisfied. Close to stall, the force direction is more varying and it has a greater importance in the stall phenomena. In principle, δ could be modelled as well with and additional relation accounting for its variation along the speedline.

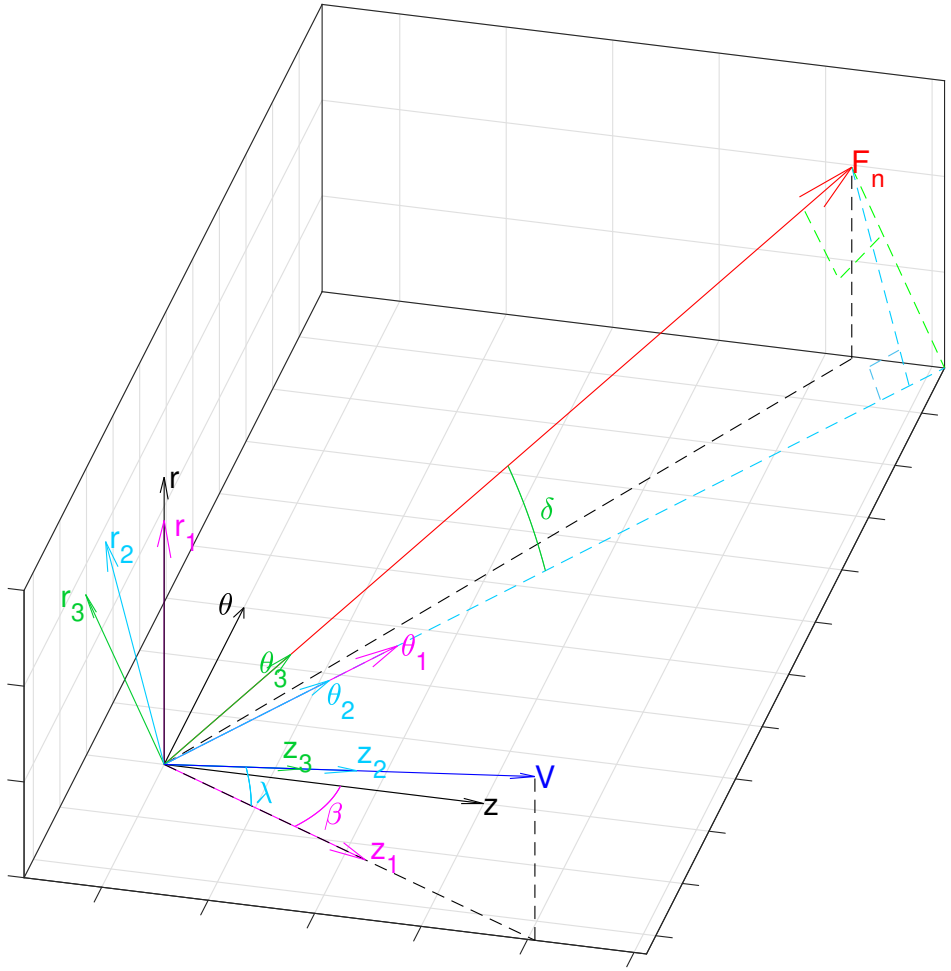

Figure 4.7: Three-dimensional normal force decomposition.

4.4 Test case

The validation of the body force model implemented in ANTARES was done using a test case representative of a high by-pass turbofan with design BPR=8.89, the NASA/GEAE R4 [1]. The engine, made up of a transonic fan with Outlet Guide Vanes (OGV) and an axisymmetric nacelle, has been used by some authors in the BFM context [2, 148, 196], and in particular by Thollet [251], allowing for a direct comparison. It is shown in Figure 4.8 and its characteristics are summarised in Table 4.1. It has been employed in a large series of experiments for the Source Diagnostic Test (STD) aeroacoustic programme and valuable experimental data are available in the NASA repository [118, 120, 208, 209, 268, 274].

Table 4.1: NASA/GEAE R4 characteristics.

	Fan	OGV baseline
No Blades	22	54
Aspect Ratio	2.0	3.51
Hub/Tip ratio	0.30	0.50
Chord [mm]	91.694	39.878
Solidity	1.73	1.52
Stagger [deg]	37.10	10.29
t_{max}/c tip	0.028	0.0698

4.4.1 CFD model validation

In order to obtain the reference 3D solutions to be post-processed to extract the circumferential-averaged flow field and the force distribution, a CFD model for the NASA R4 turbofan was first validated. The experimental database covered the rotor-only Rotor Alone Nacelle (RAN), and the full stage cases. The engine was experimentally tested either with a fixed and variable-area nozzle and a bellmouth inlet, to record the speedline at take-off (Nc=100%), cutback (Nc=87.5%) and approach (Nc=61.7%) and also at single point with the nozzle representative of a flight specimen. Table 4.2 reports the design point and the take-off fixed nozzle single-point.

Table 4.2: NASA/GEAE R4 fan performance

Op. Point	Nc [rpm]	$\dot{m}$ [kg/s]	TPR	η_{iso}
Design	12657	45.586	1.488	92.4 %
Take-Off	12657	44.08	1.508	91.2 %

[1] The author wish to thank Dr. Edmane Envia from NASA Glenn for sharing the blade geometry

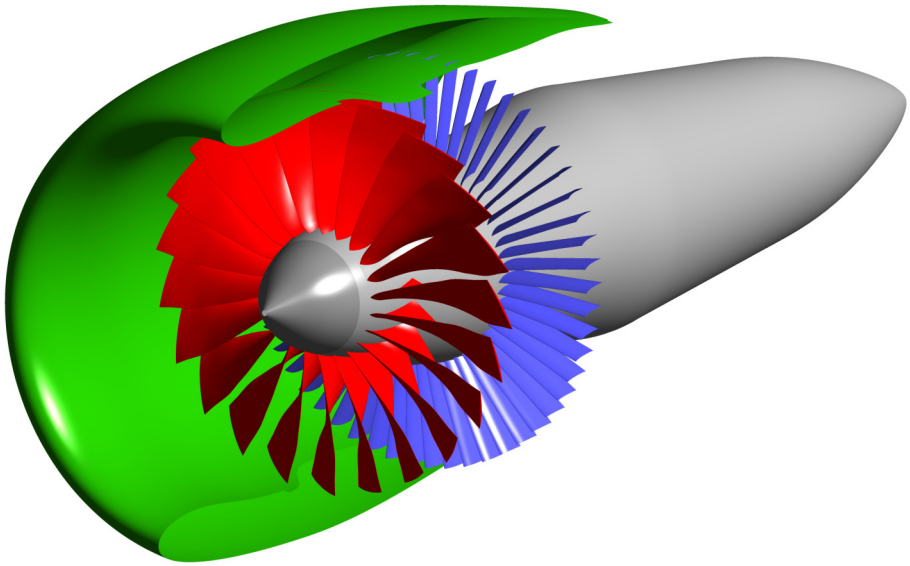

Figure 4.8: Three-dimensional view of NASA/GEAE R4 stage.

The engine was simulated in different configurations, summarised in Table 4.3, to replicate the experimental set-up. The rotor was first tested alone in a contoured ducted intake and with a variable pressure outlet, to draw its characteristic map. The case was then run again but with the OGV downstream of the rotor. The second step was the simulation of the engine installed within its nacelle, exposed to the undisturbed external flow. The full stage was simulated either with a variable pressure outlet, again to record the whole speedline performance indexes, and also at fixed point, with the nozzle discharging in the freestream flow.

Table 4.3: NASA/GEAE R4 3D CFD matrix of tested configurations.

Configuration	Blade row	Intake	Outlet	External flow
Ducted rotor	Fan	Duct	Variable Pressure	No
Ducted stage	Fan+OGV	Duct	Variable Pressure	No
Nacelle+stage	Fan+OGV	Nacelle	Variable Pressure	Yes
Single-point stage	Fan+OGV	Nacelle	Nozzle exhaust	Yes

Computational Model

The CFD analysis was carried out using the ANSYS CFX suite. A series of multi-block structured computational grids were created using ANSYS TurboGrid Advanced Topology Management (ATM) utility. Different grid levels were employed to study the mesh sensitivity. For the rotor the mesh size were coarse (1.5M nodes), medium (2.1M nodes) and fine (3.8M). A sample of the medium mesh for the ducted rotor case is shown in Figure 4.9. The influence of turbulence model was first assessed for $\kappa-\omega\ SST$, $\kappa-\epsilon\ RNG$ and Spalart-Allmaras. The first resulted in a closer match with reference values and was retained in all the simulations. The meshes employed had a refined boundary layer with $y^+ < 1$. Grid convergence was measured using the standard procedure described in [31] by means of the Grid Convergence Index (GCI). For the registration of the characteristic maps, the average pressure at the outlet was varied, whilst total temperature and pressure were imposed at the inlet. For simulations involving also the external flow, the nacelle containing the engine was placed within a cylindrical wedge domain with the inlet, outlet and upper ceiling located 10 diameters far from the nacelle for speedline tracing, and 80 diameters fan for take-off single-point operation, where the full jet exhaust was present. The static pressure at the domain outlet was fixed to give a freestream Mach number of 0.10 to simulate the wind tunnel quasi-static conditions. For fan+OGV simulations, a mixing plane was placed as interface between the rotating and stationary domain.

The mesh convergence study revealed a global little mesh influence on the selected levels. The total pressure exhibited a slightly higher variation, compared to the other indexes, with a limited improvement on the experimental prediction. The GCI^{21}_{fine} parameter for the adiabatic efficiency was at worst 0.73% near stall, with values one order of magnitude lower elsewhere, indicating limited sensitivity to grid size. The fine mesh was chosen anyway, to have the highest accuracy, and the results presented hereafter are referred to this grid level. For full-annulus calculations, finer meshes could be employed.

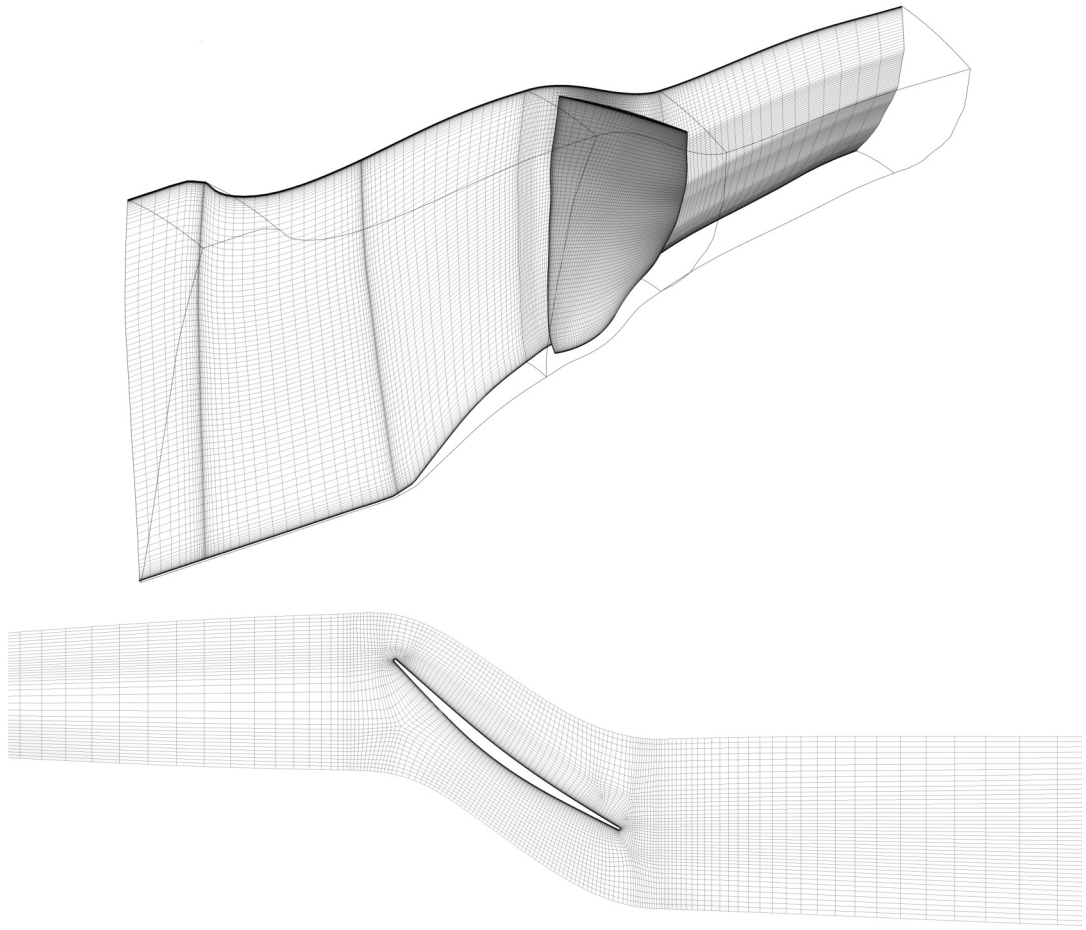

Figure 4.9: Ducted rotor medium mesh sample.

Rotor Alone Characteristic Maps

The first case studied was the ducted rotor alone. The performance maps at $N_c = 100\%$ were obtained by varying the outlet pressure and are reported in Figure 4.10. The total pressure and total temperature ratio experimental curve trends are matched, although an offset in absolute terms is present. At the design point, the predicted TPR is 1.485, versus an experimental value of 1.492, with a -0.47% relative difference. The total temperature rise in the same point is 1.129 for the CFD versus 1.130 for the experiment. The isentropic efficiency curve on the right hand figure shows good agreement. The trend is well matched and the peak efficiency is correctly reproduced at a mass flow rate of 46 kg/s, with a CFD value of 93.08%, compared to the 93.2% wind tunnel datum. Far from the design point, the choking mass flow rate is accurately captured, and the efficiency slope at lower flow rates is also in agreement, despite a faster drop for the TPR and TTR. Overall, the accuracy of the simulation was judged positively, given that the difference between wind tunnel and numerical data was always within 1% and likely to fall in the experimental uncertainty band. In addition, the use of a bellmouth inlet in wind tunnel test seemed to have an influence on the curve slopes towards the stall, as spanwise profiles were better matched at single-point take-off operation when the nacelle and the external flow were simulated, and this operation point was at a lower than design mass flow rate.

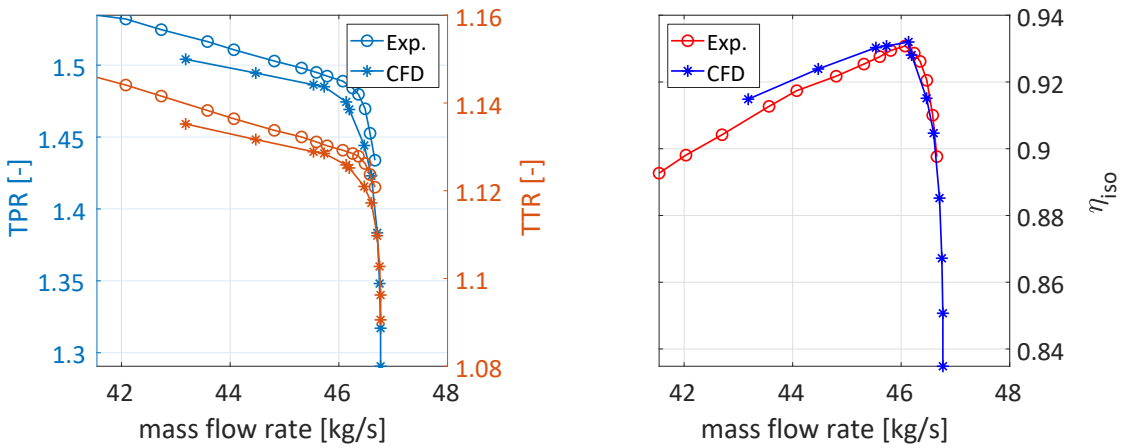

Figure 4.10: Ducted rotor alone performance maps at $N_c = 100\%$.

Stage Characteristic Maps

Figure 4.11 reports the characteristic maps for the Fan+OGV ducted case with the fine grid for $N_c = 100\%$. Downstream of the fan, Figure 4.11a, the total pressure ratio curve shape is matched, with an almost constant underprediction of 1% relative to the experimental data. The fan isentropic efficiency is similarly captured, with a 0.5% positive offset in the CFD, but again a very close distribution. The peak efficiency occurred at a slightly lower mass flow rate than experimental, but the difference was small (93.26%

CFD vs 93.07% experiment). The characteristic curves downstream of the OGVs in 4.11b reveal a behaviour consistent with the one described for the rotor. The total pressure rise is even closer (less than 1% difference at peak efficiency), and as seen in the rotor alone case, the slope tends to reduce faster towards the stall, as a consequence of the slightly different inflow conditions during wind tunnel tests. The efficiency has an overprediction of 1.38 points at peak efficiency and around one point elsewhere, but the trend is again quite similar. The absence of precise indications on the axial location of measuring planes during experimental tests could explain the presence of an offset in the CFD data, but a good replication of the curve shapes. Even for the complete stage, in summary, the CFD model appeared to consistently predict the integral machine performance, with good accuracy.

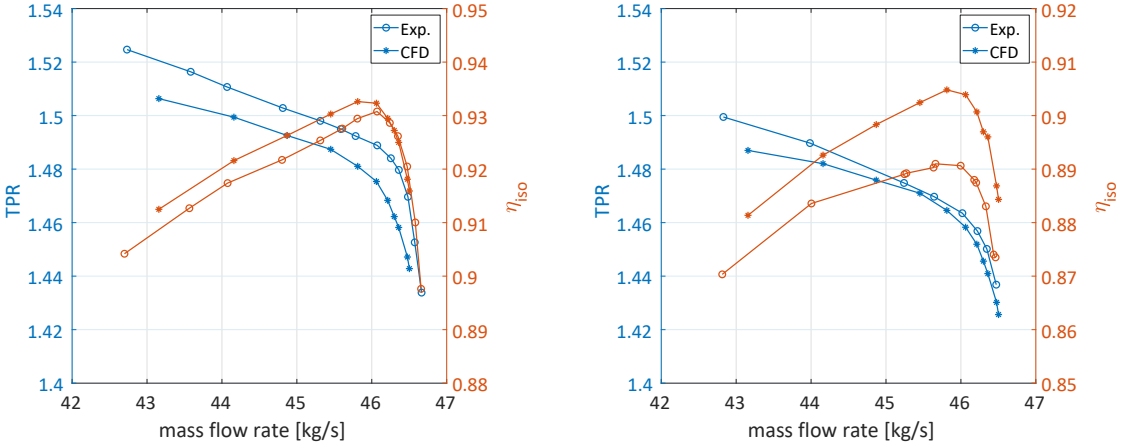

(a) Fan

(b) Fan+OGV full stage

Figure 4.11: Fan+OGV ducted stage performance maps at $N_c = 100\%$.

Take-Off Single-Point Operation

At take-off single-point operation the full engine was placed into an undisturbed flow and the intake stream tube and the full jet expansion were simulated. Table 4.4 summarizes the simulation and wind tunnel data. The agreement is very good for all the reported parameters.

Table 4.4: NASA/GEAE R4 fixed nozzle take-off operation. Comparison of fine-mesh CFD result and wind tunnel data.

	$\dot{m}$ [kg/s]	TPR	TTR	η_{iso}
Exp.	44.09	1.511	1.136	91.7 %
CFD	44.07	1.510	1.1357	92.1 %

The circumferential-averaged spanwise profiles of total pressure, total temperature

and isentropic efficiency downstream of rotor blade for the fine mesh calculation at single-point take-off operation fan+OGV case are depicted in Figure 4.12. The total pressure ratio curve obtained in the 9x15 wind tunnel of Figure 4.12a is replicated by the CFD analysis, although there is a positive offset of about 1% below 30% of span, that becomes negative at higher span due to a kink in the experimental rake profile. The agreement is better for the W8 wind tunnel test data. The total temperature rise in the same figure, available only for the 10x15 wind tunnel, is very well matched, instead. The offset in TPR reflects in a slight overestimation of the 10x15 isentropic efficiency distribution in Figure 4.12b, but the drop above 75% of the span is well reproduced. The W8 data have a higher efficiency below that span. The reported experimental uncertainty for the W8 tunnel are $\pm 0.7\%$ on pressure rise and $\pm 3.5\%$ on adiabatic efficiency. The numerical curve falls between the two experimental datasets and the uncertainty band, proving a sufficiently accurate estimation.

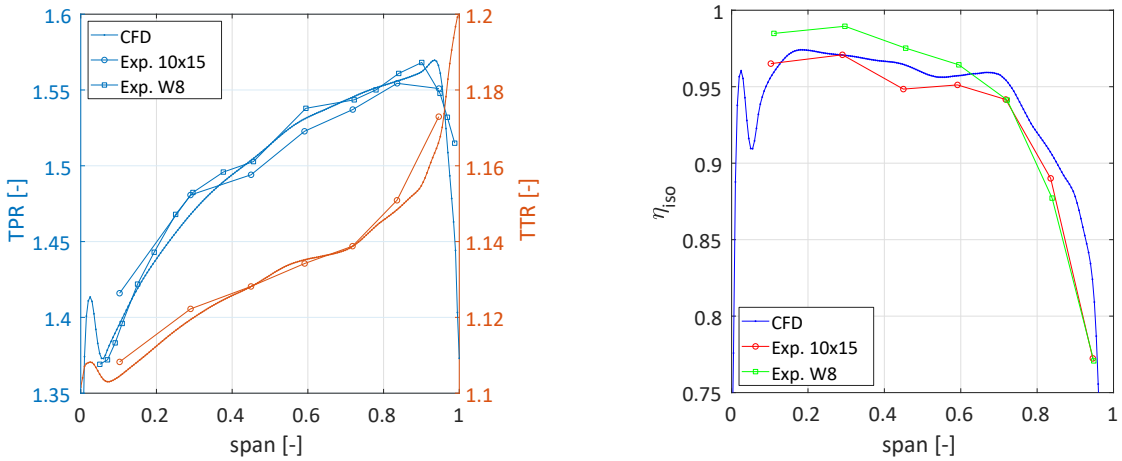

(a) Total Pressure and Total Temperature ratio

(b) Isentropic efficiency

Figure 4.12: Comparison of experimental and calculated circumferential-averaged spanwise profiles downstream of rotor blade for fan+OGV single-point take-off operation

Figure 4.13 compares the mean axial velocity downstream of the rotor blade Laser Doppler Velocimetry (LDV) measurement with the CFD result. The experimental distribution presents a clear wake trace over the span, connected to a lower speed region at the blade tip, where secondary tip vortex and flow reverse occur. A high speed area, from 50% to 80% of span is also visible. The numerical contours show a similar wake trace connecting the hub boundary layer (not captured in the experiment) to the tip flow. The radial straightening of the wake towards the shroud is also captured. However, a larger velocity defect near the tip is predicted in the CFD. This structure continues obliquely across the radius and connects to the wake at about 30% of span. The shape of the low speed flow near the tip gap is well matched. Overall, the comparison is fair, apart from the distorted structure generated near the tip and rotating with the relative velocity.

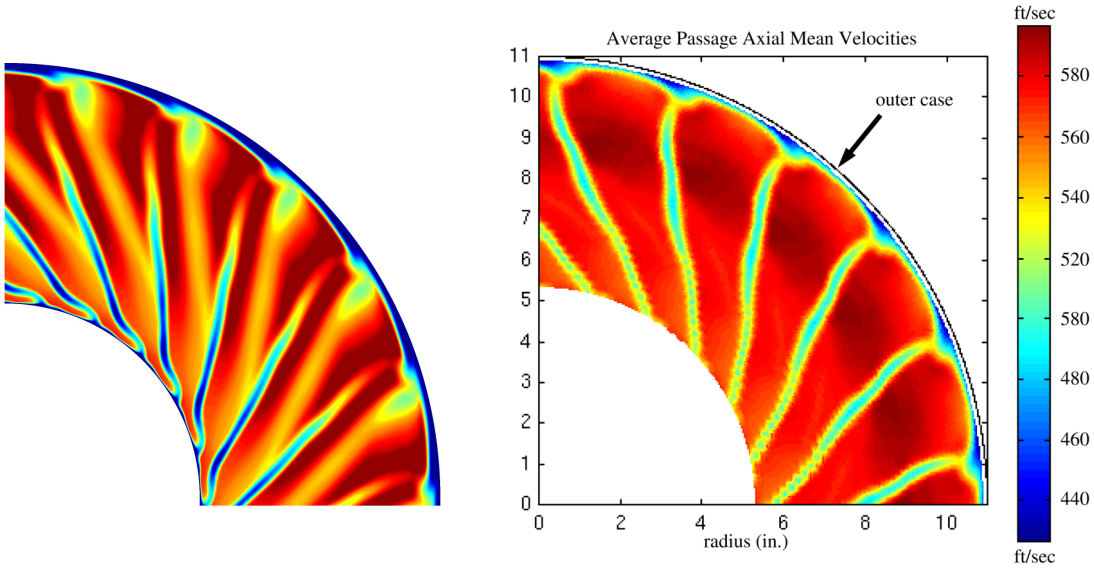

(a) CFD (b) LDV experimental measurement

Figure 4.13: Comparison of experimental and calculated axial velocity distribution downstream of rotor blade at single-point take-off operation

Figure 4.14 reports the same comparison for the absolute tangential velocity. The observations for the axial component are valid also in this case, with the wake trace and the tip vortex clearly visible in both the figures and a spot of lower whirl towards the shroud present only in the numerical contours.

Finally, the shock structure on a constant radius section at 89% of span is illustrated in Figure 4.15. The experimental visualisation shows a detached bow shock that emanates normally along the passage from the suction side at mid chord and is curved in front of the next blade leading edge. The incoming flow, once crossed the bow shock, re-accelerates through an expansion fan, that causes the passage-bow shock curvature in front of the leading edge once it interacts with it. The maximum Mach number of about 1.35 is reached after the expansion, obliquely before entering the channel. The major features of the flow field are captured in the CFD simulation. The detached bow shock stand-off is close to the measured one and even the passage shock impingement location. What is different is a bump in the shock wave near the centre of the passage, causing a velocity defect which was seen in the previous axial cut and not observed in the LDV measurements. This feature was present in all grid levels and its nature could not be attributed with certainty to a numerical issue caused by the mesh topology or to a flow model limitation. Despite these differences, the performance indexes appeared sufficiently accurate and the spanwise passage-averaged profiles in good agreement.

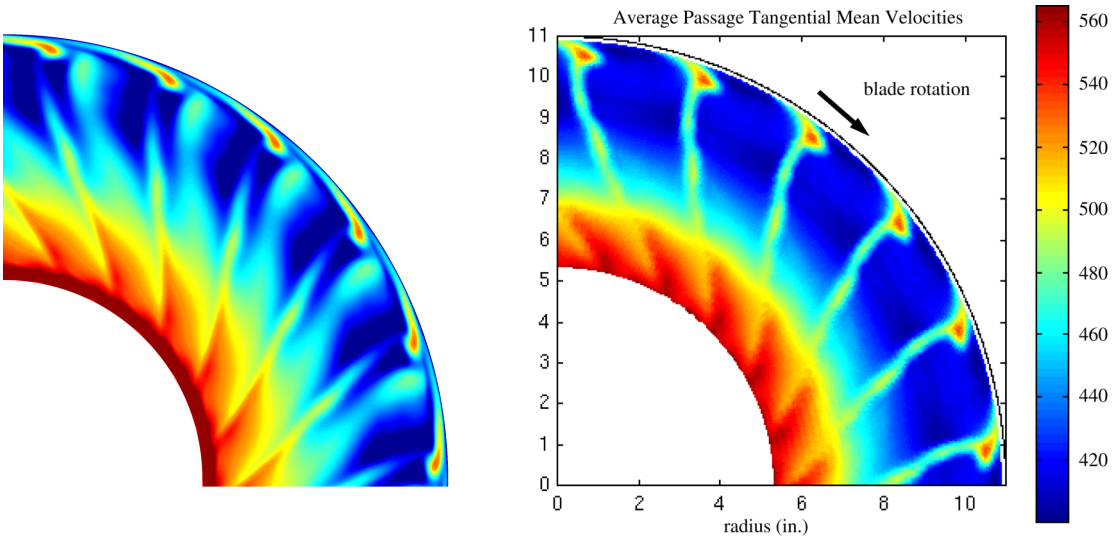

(a) CFD (b) LDV experimental measurement

Figure 4.14: Comparison of experimental and calculated tangential velocity distribution downstream of rotor blade at single-point take-off operation

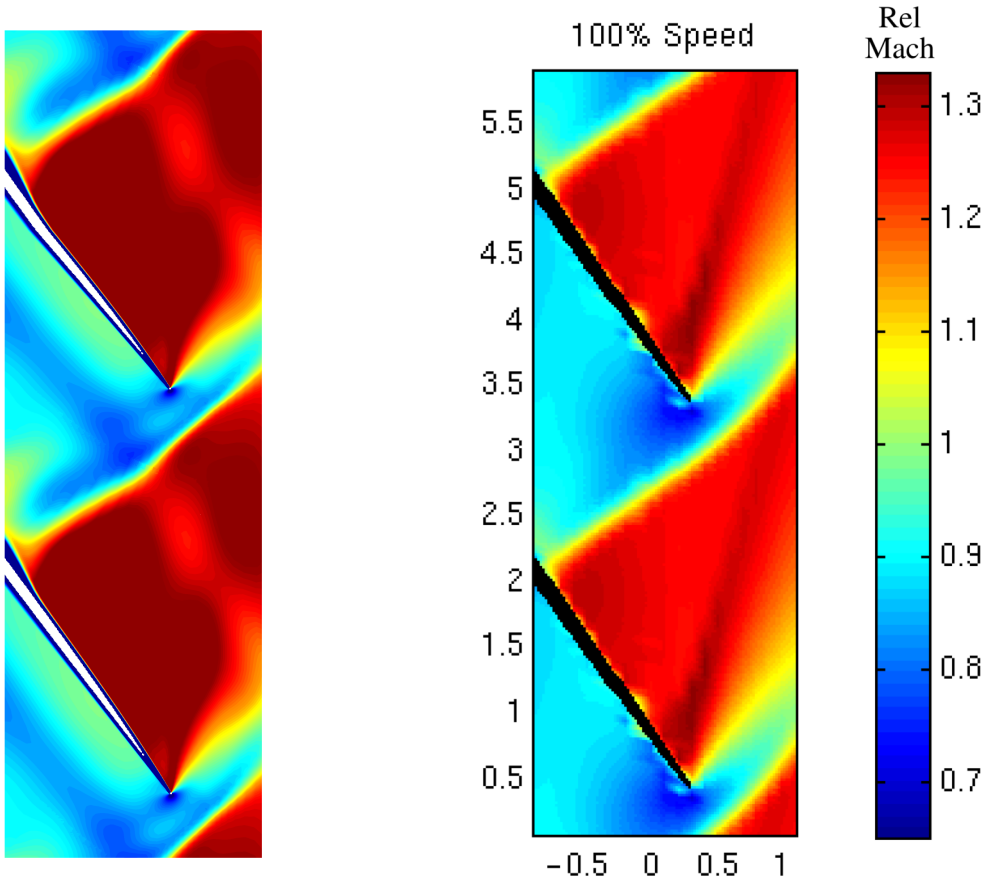

(a) CFD (b) LDV experimental measurement

Figure 4.15: Comparison of experimental and calculated relative Mach number distribution on a constant radius section 263.1 mm from the axis, at single-point take-off operation

4.5 Body Force Model Validation

Once the 3D steady-state single-passage CFD model had been validated against experimental data in different configurations, showing sufficient agreement and correct replication of the main flow features, it was employed to generate the spatial circumferentially-averaged fields needed to extract the forces and invert the selected L/D body force model equations to derive the calibration coefficients. As stated above, the Blade Force Average procedure was used for the normal force extraction, due to its simpler implementation, higher resolution and 3D components output, and the thermodynamic approach was employed to distribute losses based on a linear entropy rise assumption along the streamlines crossing the blade region.

The body force model was first validated for the ducted rotor alone case. As prescribed by its author, the input coefficients were extracted at peak efficiency. ANTARES was then run by prescribing the same boundary conditions set in the reference 3D simulation, that is a constant total pressure and temperature at the domain inlet and an average pressure specification at the outlet, which was varied to obtain the $N_c = 100\%$ speedline. Before evaluating the characteristic maps, the flow fields resulting from the body force solution and the circumferential-averaged 3D reference solution are compared at the calibration point, the peak efficiency. Ideally, the fields should be identical. In practice, they differ because of some error in the force extraction, some possible loss if information during data interpolation from the 3D mesh to the circumferential-average background mesh and to the body force mesh, the metal-blockage only presence, the lack in the model of high-order terms, like circumferential stresses, responsible for turbulent mixing and aerodynamic blockage. It is here believed that in addition to the sole comparison of integral quantities, a careful inspection of the evolution of the flow variables across the blade region is necessary to delineate the features of the body force model and its adherence to the parent simulation used to instruct it. Often in the literature the comparison is limited to characteristic maps or some spanwise profiles. However, the evaluation of the local flow features is important in the first place because the closer the point-to-point match is, the better the integral values will be. In the second place, if the body force is considered for the design of blades subject to non-uniform flow conditions, the local replication of the correct flow parameters is essential. Not only, but even if it is used as a black-box to provide better boundary conditions to powered engine simulations, it is important to closely predict the spanwise profiles, which influence the fan suction and the distortion attenuation, as well as the jet characteristics and thus the thrust figures. For this reason, all over this chapter both integral and local parameters will be presented and thoroughly discussed.

4.5.1 Peak Efficiency baseline Body Force Model

The BFM of equations 4.7is the baseline L/D model first employed at the peak efficiency calibration point. In this condition, if correctly implemented the source terms in the RANS equations should be the very close to the one derived with the force extraction procedure. In this sense, this operating condition does not highlight the reliability

of the selected body force model *per se*, but rather it validates both the force extraction from the 3D CFD and the force inclusion into the axisymmetric solver.

The circumferential-averaged 3D CFD reference solution is simply denoted as CFD in the remainder. Figure 4.16a shows the blade contours of axial velocity. The contours are quite similar and the spatial distributions are in good agreement, with only a slightly higher acceleration before the smeared shock predicted by the BF. This could be due to insufficient blockage, as only the metal one is modelled but the boundary layer growth caused by the impinging shock, that produces aerodynamic blockage, is only partially included as a deviation effect on the β_n^0 factor, but not as a true reduction of the flow capacity. The radial velocity field, depicted in Figure 4.16b, also presents very similar features. Some local differences near the hub and tip can be spotted, but the overall good comparison proves that the 3D force decomposition here adopted was correct and consistent. With the radial force component set as $-f_{n,\theta}\, tan(lean)$ such a good outcome could not be obtained.

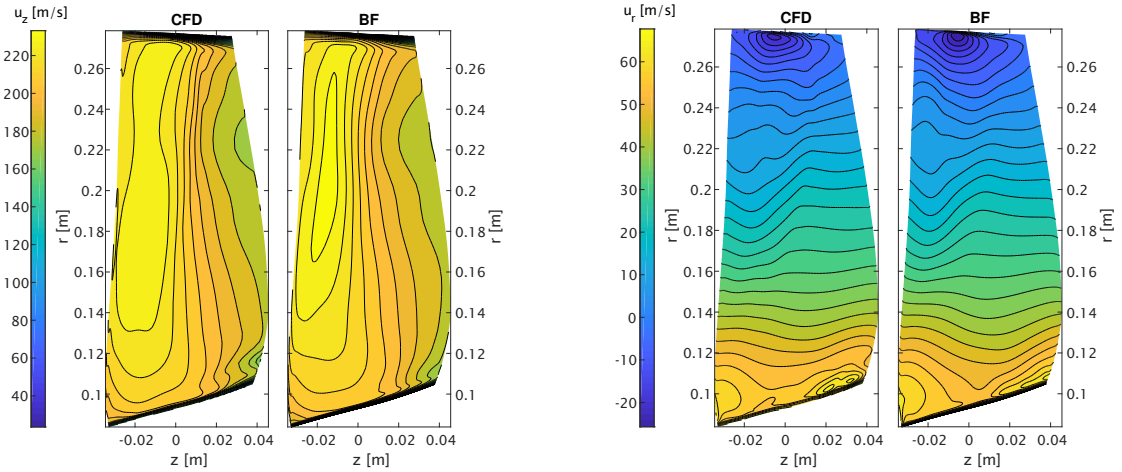

(a) Axial velocity u_z

(b) Radial velocity u_r

Figure 4.16: Velocity contours on the blade for reference CFD solution and baseline body force model at peak efficiency.

The absolute circumferential velocity is illustrated in Figure 4.17a, whilst the relative flow angle is shown in Figure 4.17b. The flow turning is correctly applied in the body force model and both quantities present a close match with the reference solution. The tip and hub trailing edge corner structures are clearly visible in the body force swirl velocity contours. The major difference is a cusp near the trailing edge at a radius of 0.26 [m] in the BF contours, not present in the CFD figure. The close prediction of the relative swirl angle is very important, in order to supply the flow with the correct force magnitude, as the model equations are heavily based on this flow parameter. This makes sure that most aerodynamic and thermodynamic variables can be accurately reproduced across the blade region.

The total pressure ratio distribution on the blade is shown in Figure 4.18a. The

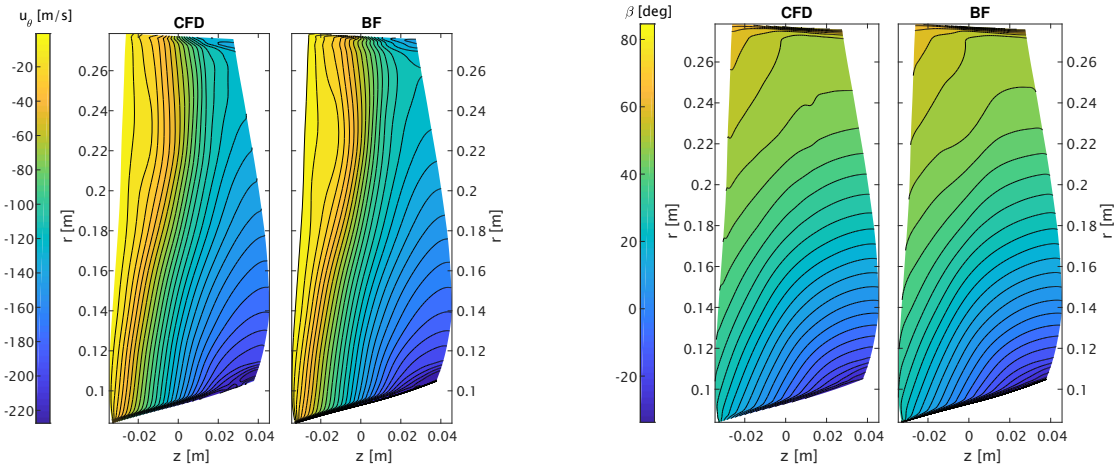

(a) Absolute circumferential velocity u_θ

(b) Relative flow angle β

Figure 4.17: Absolute circumferential velocity and relative swirl angle contours on the blade for reference CFD solution and baseline body force model at peak efficiency.

streamwise variation predicted by the BFM looks similar to the reference solution, but the contours are skewed towards the hub and slightly higher exit values are found in the BFM. The TPR loss at the hub trailing edge corner qualitatively agrees with the CFD, where a more complex pattern is present, though. The outcome suggests that despite the entropy rise was smoothed out by assuming linear streamwise variation and redistributed on the blade region, the loss distribution is consistent and reproduces not only the bulk change, but also some local features. The work exchange, summarised by the Total Temperature Ratio of Figure 4.18b, was also in good agreement and the same consideration for the total pressure rise can be applied to this picture. The most relevant difference, that will be more evident later, is a higher work input at the tip. This region is very hard to be modelled and the absence of force in the tip gap is only the simplest approach, as there the flow pattern is very complicated, resulting from the interaction of the pressure and inertial forces with the shock waves and the boundary layer. An excessive enthalpy rise near the tip was found in many body force simulations and the exact cause could not be discovered. The phenomenon seems to be inherent to the model and a more accurate modelisation might require the introduction of additional stresses to account for higher-order terms, which representation through closed equations appears, however, probably unpracticable.

The flow quantities so far compared prove that the body force model implemented in ANTARES was able to quite accurately reproduce the circumferential-averaged flow field obtained from the single-passage 3D CFD simulation. In order to have a closer insight into the variation of the flow variables across the body force region and ascertain to what extent the source term distributions replicate the reference field, constant span cuts are provided in the next figures. Figure 4.19a reports the flow coefficient at low, mid and high span. As already noticed in the axial velocity distribution in Figure 4.16a, there

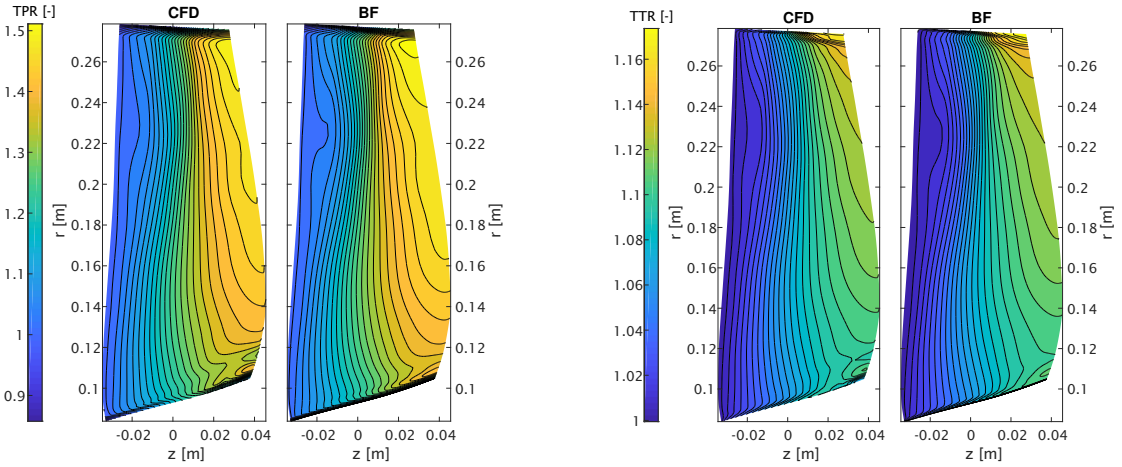

(a) Total Pressure Ratio TPR (b) Total Temperature Ratio TTR

Figure 4.18: Total pressure and total temperature ratio contours on the blade for reference CFD solution and baseline body force model at peak efficiency.

are some differences between the body force and reference solution. The global trend is, however, captured and the exit values are close. It is actually impossible to match either the flow angle and the mass flow rate if both the turning force and the blockage are exactly imposed. In this case, the differences are probably due to a not perfect blockage factor, as either the radial velocity component forming the meridional velocity and the relative flow angle were closely replicated, meaning that the defect is likely to be fall on the axial velocity and the density, both largely affected by the real section area felt by the fluid. Moreover, the work coefficient distribution, linked to the absolute circumferential velocity change through the Euler turbine equation, was remarkably good, as visible in Figure 4.19b.

These constant span cuts demonstrate once more that the flow was fed with the correct force field, in a way that not only the outlet to inlet net evolution was duplicated, but also, only to a slightly lower extent, the point-to-point local correspondence. It is also important, however, to examine the bulk effect and in particular the distributions downstream of the blade, that contain the full history of the external work applied to the fluid by the rotating blades through the body forces. The performance indexes spanwise distribution one axial chord downstream of rotor blade is reported in Figure 4.20. The total pressure and total temperature ratio compare very well with their respective reference curves. The total pressure and total temperature skewness from hub to tip is almost identical far from the endwalls. At the hub, a local total pressure peak is present in the CFD curve, also reproduced by the BFM, although with an overshoot. On the contrary, the same peak is underestimated for the total temperature. As noticed in Figure 4.18b, the tip flow exhibits the largest difference, with a high circumferential velocity jet providing an excessive enthalpy rise. This phenomenon can be observed in the CFD solution, but was exacerbated in the body force simulation and attempts to change the

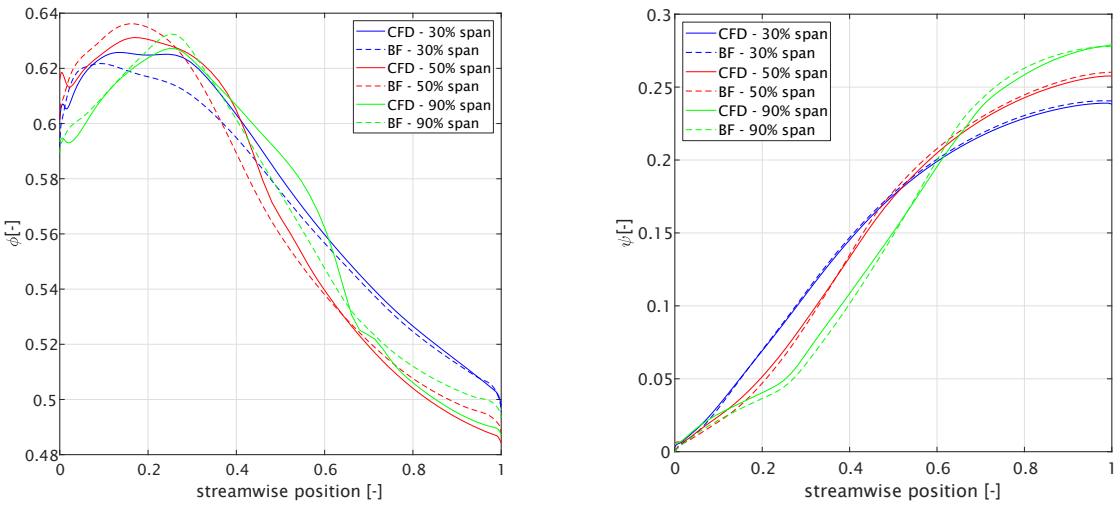

(a) Flow coefficient ϕ (b) Work coefficient ψ

Figure 4.19: Streamwise variation at constant span section of work and flow coefficient for reference CFD solution and baseline body force model at peak efficiency.

normal force distribution near the tip gap did not lead to any modification or improvement of this behaviour, whose understanding results very hard by the inherent nature of the tip leakage flow and the sum of extremely hard and nonlinear phenomena occurring in that region. A direct comparison with the original implementation of Thollet was not possible, as detailed flow data were not provided, but hints of a similar behaviour can be found in his thesis. Moreover, the same author reported in appendix that the initial R4 blade was recambered to ensure a monotone distribution of the κ angle. It is possible that this modification improved the predicted tip flow. Such an arbitrary change of the geometry has been used elsewhere in the body force context to improve the model response, but not in the present implementation, as it hides the real behaviour of the formulation and there is no physics-based closed procedure that dictates its adoption. It rather looks as another calibration procedure that tries to restore the net integral effect on the flow by correcting some model deficiencies.

The isentropic efficiency profile, resulting from the TPR and TTR curves, illustrated in Figure 4.20b, confirms a very good point-to-point correspondence far from the endwalls. The contemporary TPR overshoot and TTR undershoot at the hub resulted into an excessive efficiency, although the local extrema behaviour was captured. Similarly, near the tip the CFD efficiency drop was lower, due to the overpredicted velocity jet in the BFM.

4.5.2 Choking mass flow rate calibration

The baseline L/D body force model described by equations 4.7 was found to overpredict the choking mass flow rate, as a consequence of a too large normal force magnitude

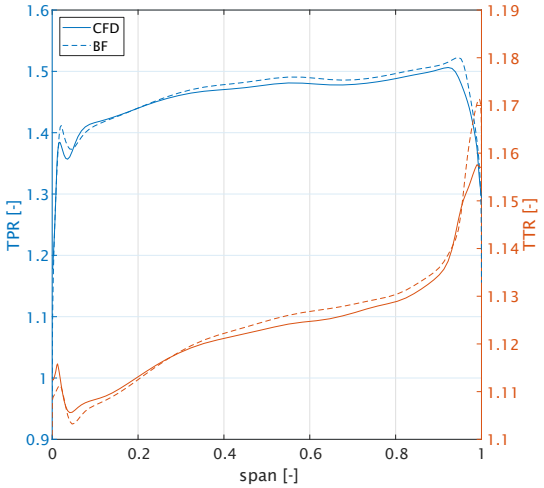

(a) TPR and TPR

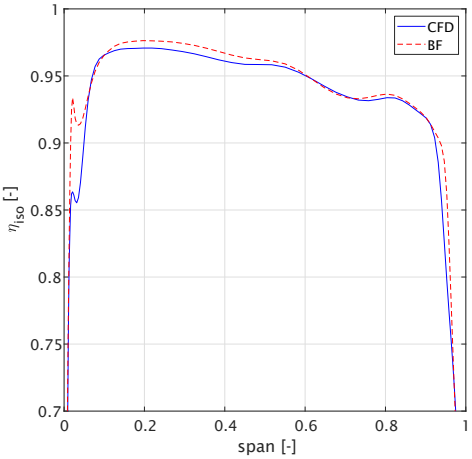

(b) Isentropic efficiency η_{iso}

Figure 4.20: Performance indexes spanwise distribution downstream of rotor blade for reference CFD solution and baseline body force model at peak efficiency.

variation from peak efficiency to choking. As a remediation, Thollet proposed to modify the normal force coefficient, according to the rule [251]:

$$f_n = \frac{2\pi\sigma}{h}\left(\beta - C(z)\,\beta_n^0\right) \tag{4.28}$$

$$C(z) = max\left\{1 + C_0\left(1 - 2\frac{z - z_{LE}}{z_{TE} - z_{LE}}\right), 1\right\} \tag{4.29}$$

The $C(z)$ linear term reduces the difference $\left(\beta - \beta_n^0\right)$ and so the normal force, from leading edge to trailing edge. The offset constant C_0 must be calibrated in order to catch the choking mass flow rate and the model will be referred to as calibrated.

Figure 4.21 illustrates the characteristic maps for the NASA R4 rotor alone case obtained with the baseline and the calibrated body force model. Without the normal force modification, the total temperature and total pressure were slightly overpredicted at the peak efficiency point, whilst the efficiency was quite close. Conversely, the choking mass flow rate was 3% larger then the CFD calculation. The calibration procedure greatly improved the choking flow rate matching and brings the TTR and TPR closer to the reference curves. Conversely, the efficiency results shifted by 1 to 1.5 points. This is known to be a drawback of the calibration approach. Near stall, the TPR and TTR curves slope was higher than the CFD. Such behaviour appears equally present in the Thollet implementation [251], confirming the validity of the ANTARES code.

As visible from the characteristic maps, the integral effect of the blade on the flow must be corrected by introducing the normal force modification, in order to restore a good prediction at choking. Figure 4.22 illustrates the blade-to-blade flow at 30%, 45%,

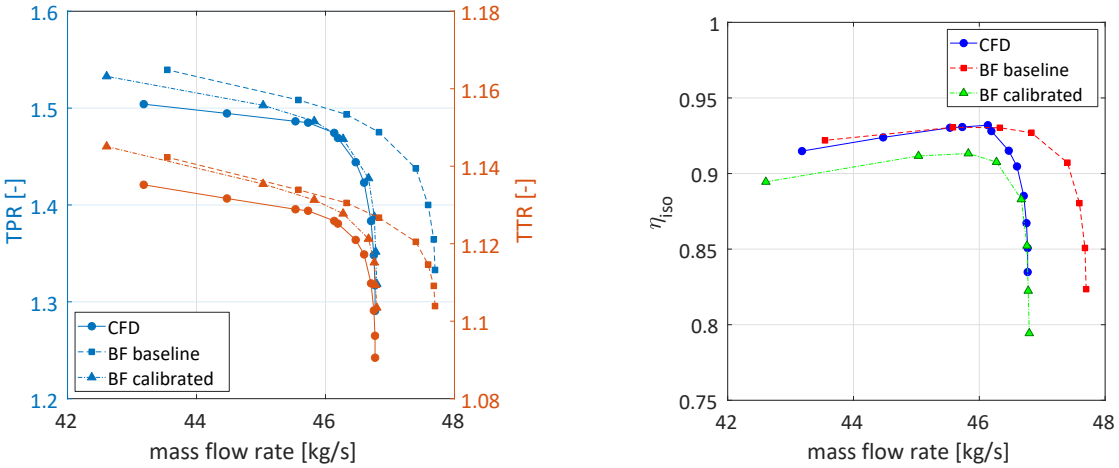

(a) Total Pressure and Total Temperature ratio

(b) Isentropic efficiency

Figure 4.21: Fan characteristic maps using baseline and calibrated BFM vs CFD reference solution

and 60% of span in the single-passage 3D simulation. It can be noticed that near mid-span the shock waves are well within the passage and quite orthogonal. The strong static pressure increase causes the separation of the boundary layer and a large detached area that corresponds to a significative change in the cross-sectional area felt by the flow. The aerodynamic blockage is not automatically modelled in the body force approach, and it is not surprising that such a flow field is not naturally duplicated by the linear elastic normal force rule and the quadratic loss.

The calibration, although improving the prediction of the integral characteristic parameters, alters the original force distribution and causes the loss of correlation of the flow development with the reference CFD solution. Figure 4.23 illustrates the blade contour of the axial velocity near choke for the reference CFD solution, the baseline and the calibrated body force model. It is evident how in the BFM a higher flow acceleration took place, causing a radially oriented shock wave to appear near mid-span. Such an acceleration was not seen in the circumferential-averaged CFD flow field, where the streamwise transition was smoother and above 30% of span the resulting downstream velocity was lowered by the presence of consistent thickening of the boundary layer, giving an exit value lower than the one in the BF analysis. The calibrated model ameliorated this exit velocity value by inducing a higher velocity peak which was terminated by a stronger shock, occurring farther downstream. Despite correcting the spanwise velocity distribution downstream of the trailing edge, the streamwise evolution across the blade region was not improved. Similarly, Figure 4.24a shows that regarding the downstream spanwise distribution of swirl angles in the absolute and relative frame, it was not strictly followed by either of the models, and the calibration had only the effect of increasing the tip jet. Furthermore, the total pressure and total temperature profiles of Figure 4.24b highlights a large difference in the prediction, in particular above 40%

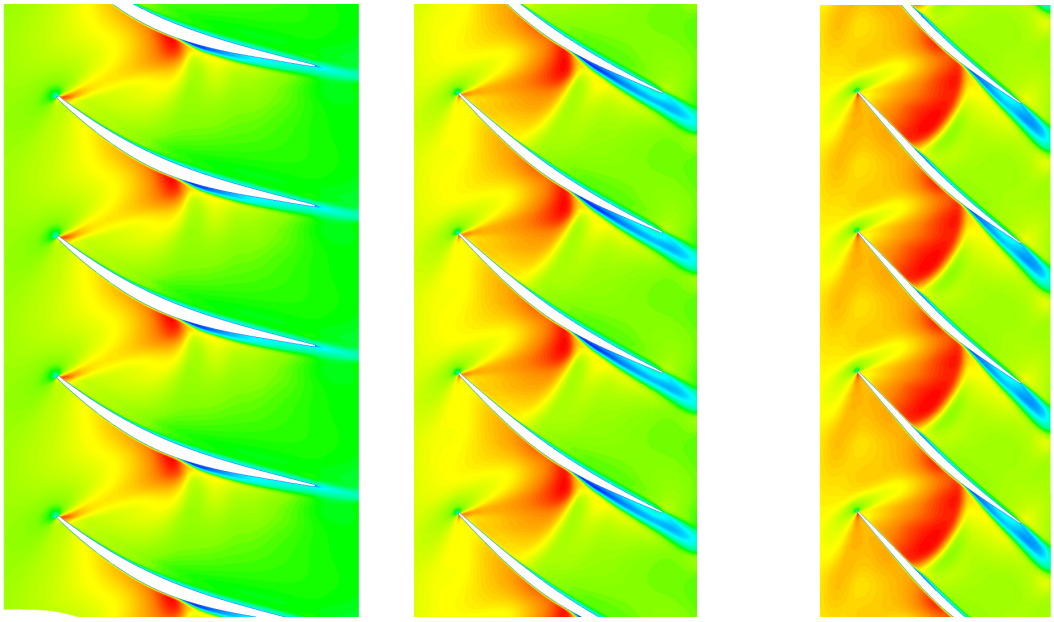

(a) 30% of span (b) 45% of span (c) 60% of span

Figure 4.22: Blade to blade relative Mach number contours near choke for R4 rotor.

of span, where it has already been observed that the BFM did not replicate the CFD behaviour and largely overpredicted the work exchange.

This analysis near choke demonstrates that despite the good match obtained in the calibration point, the model is deficient in capturing the force variation throughout the whole speedline, where it is likely that the substantial change of the flow field cannot be simply modelled by the limited number of parameters and the equation adopted. Although dimensionally correct, the linear dependency of the normal force from the deviation does not fully represent the features of a transonic flow, requiring some arbitrary change to achieve a better match with the reference data. On the other hand, the possibility of devising a closed-form equation where the force magnitude depends on the compressible effects appear remote. Ad-hoc corrections to the incompressible force model have been proposed through a large series of iterations [196] or external models [53]. In the end, there appears to exist a trade-off between the model simplicity and easiness of calibration and its accuracy. Among the existing body force formulation, the one here adopted is judged to possess a good balance of these conflicting features. Possible extensions of the original calibration procedure might account for some non-linear correction to the normal force by considering more than one force extraction point, as in other models [200]. A first investigation of this approach, however, failed to recognize a suitable functional dependency between the force and some flow parameter, and past attempts to systematically derive a compressible force expression did not lead to robust achievements [22]. When the full operating line is concerned, therefore, the limitations of the body force model must be taken into account. On the other hand, if only the peak

efficiency point and its vicinity are regarded, the prediction acquires greater reliability.

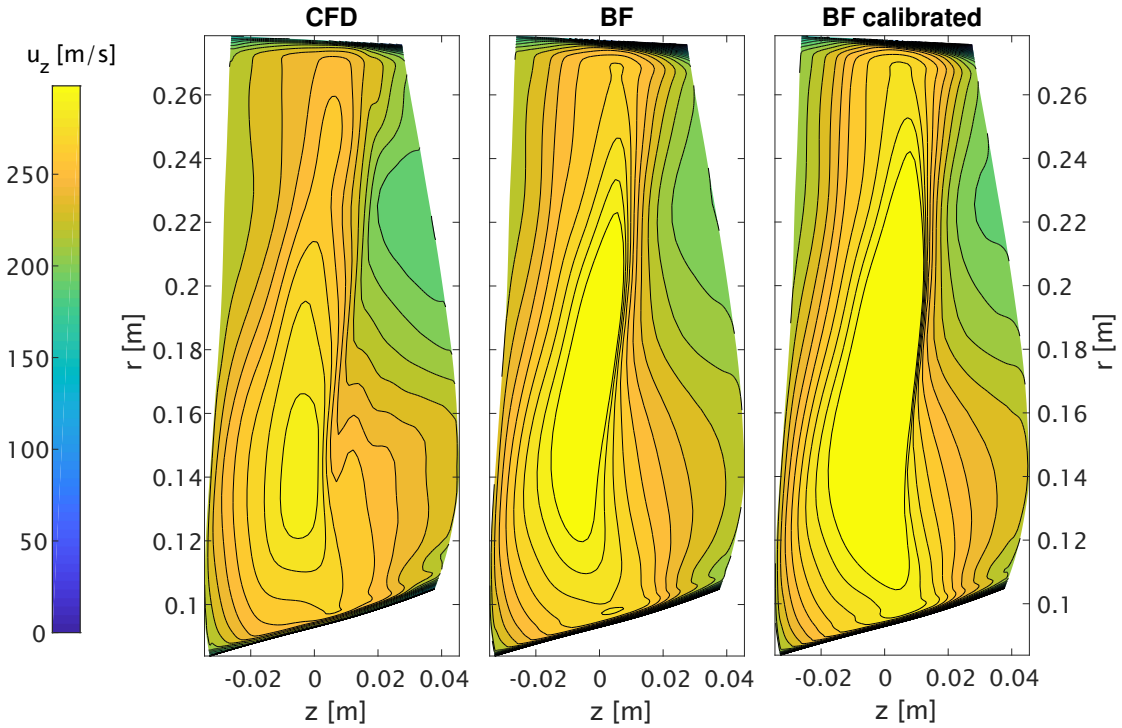

Figure 4.23: Axial velocity contours at near choke for reference CFD solution, baseline and calibrated BFM.

The effect of the choke calibration at peak efficiency is visible in Figure 4.25, depicting the total pressure ratio on the blade. Although slightly reducing the values at the trailing edge and improving the point on the map, an expansion bubble has formed from 50% to 70% of the blade. This side effect, already observed in [252], is better seen in Figure 4.26, where the blanked area in the rightmost figure highlights the fact that the normal force modification caused the compressor blade to expand the flow on a certain portion of the chord from the leading edge. This is an undesirable feature of the calibration approach that in the future should be further inspected and possibly eliminated.

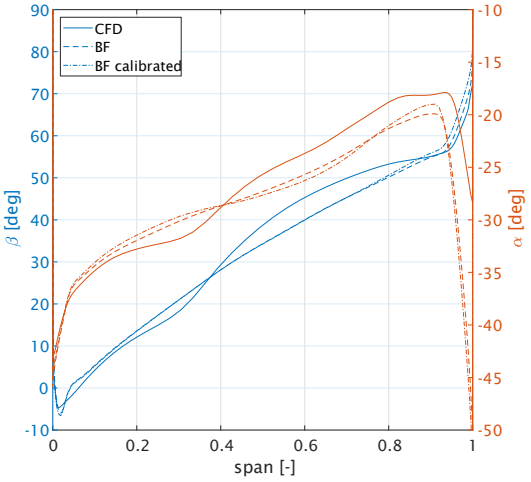

(a) Relative β and absolute α flow angle

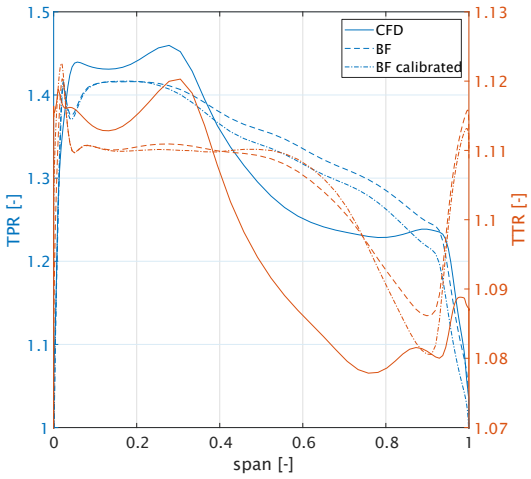

(b) Total Pressure and Total Temperature Ratio

Figure 4.24: Spanwise distributions downstream of rotor blade at near choke for CFD, baseline and calibrated body force model.

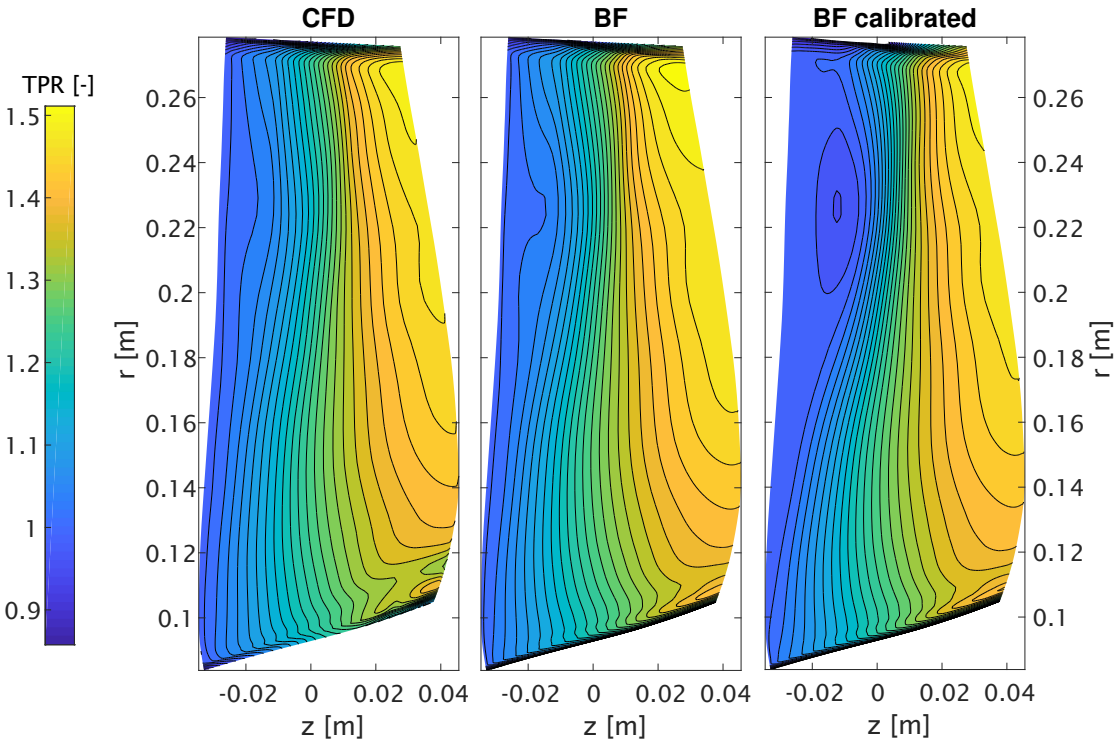

Figure 4.25: Total Pressure Ratio contours at peak efficiency for reference CFD solution, baseline and calibrated BFM.

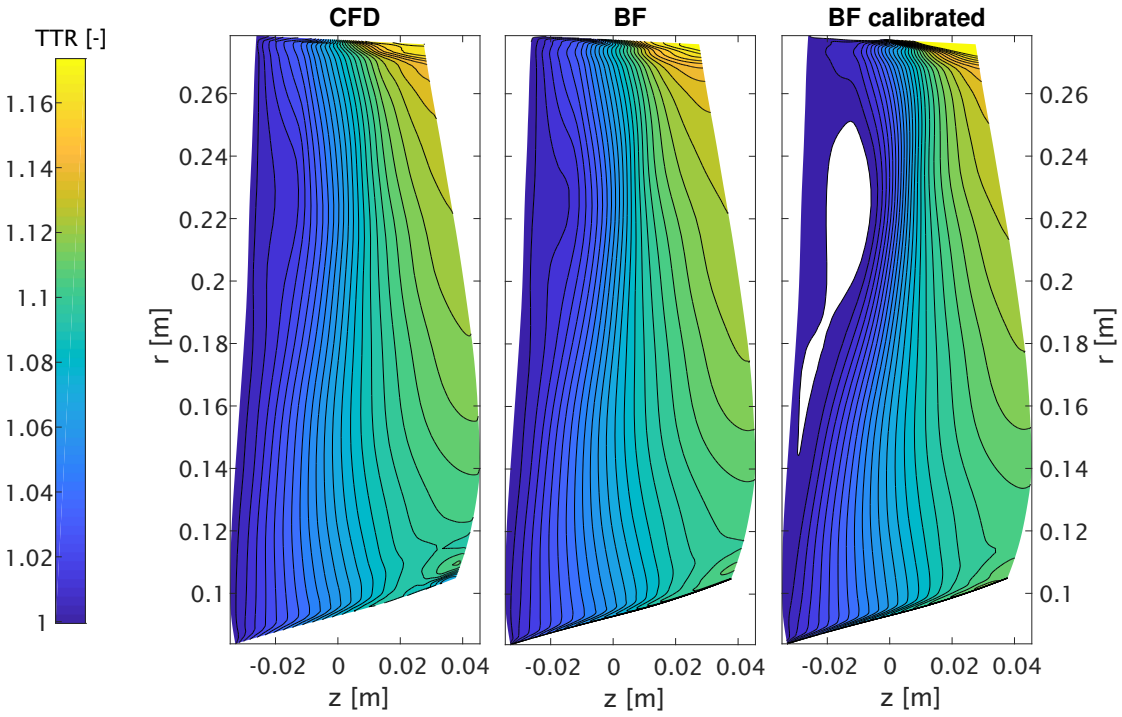

Figure 4.26: Total Temperature Ratio contours at peak efficiency for reference CFD solution, baseline and calibrated BFM. The blank area on the right figure highlights an expansion region caused by the choke calibration procedure.

4.5.3 Near stall condition

In addition to choking, an important working condition that is desirable to be replicated is the near stall operation. The stall is a very complicated and sensitive point that is characterised by a series of unsteady phenomena with different spatial and time scales that can remain stable an bounded or degenerate into a destructive breakdown with the appearance of the surge hysteresis orbit. Several works on body forces were first devoted to detect the stall inception, especially at MIT [87, 131, 135, 195]. The characteristic maps shown in Figure 4.21 show that the body force model overpredicts the TTR and TPR curves slope towards stall, regardless of the choke calibration. It is important, therefore, to compare the CFD and BF simulations near stall, as previously done for the peak efficiency and choke points, in order to detect the differences in the predicted flow fields and performance indexes profiles. Figure 4.27a reports the absolute tangential velocity blade contours for the CFD and the BF model. In the first, a large tip structure trace appeared, with a high tangential velocity region, not present in the latter. The BF values at trailing edge were shifted towards the tip compared to the reference solution, but their profile was quite similar, with the exclusion of the tip difference. The total pressure ratio distribution in Figure 4.27b presents a similar behaviour, with qualitative agreement between the model but a larger compression for BF above 80% of span.

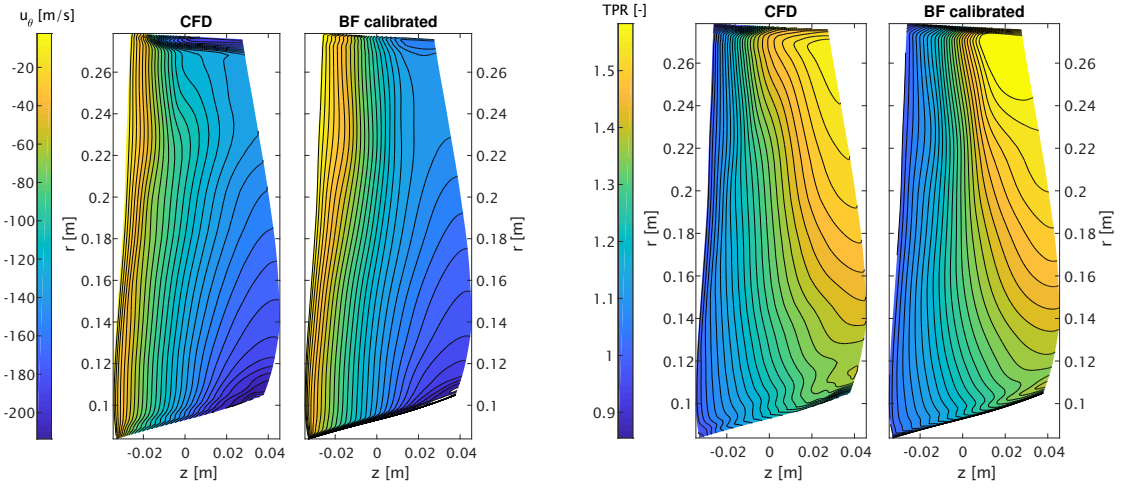

(a) Absolute circumferential velocity (b) Total Pressure Ratio

Figure 4.27: Blade contours at near stall for reference CFD solution and calibrated BFM.

Constant span cuts of work coefficient, shown in Figure 4.28a, further revealed a consistent streamwise variation predicted by the BF model. The lower work coefficient in the first 50% of chord at 90% of span might be the result of the choke calibration, reducing the normal force level in that part. The CFD exhibited a kink that was not found in the BF, where the exit value was larger for all the span sections. The relative tangential velocity distributions at the same locations, Figure 4.28b, confirmed a good match of the flow angles, seen also in the previous working points analysed.

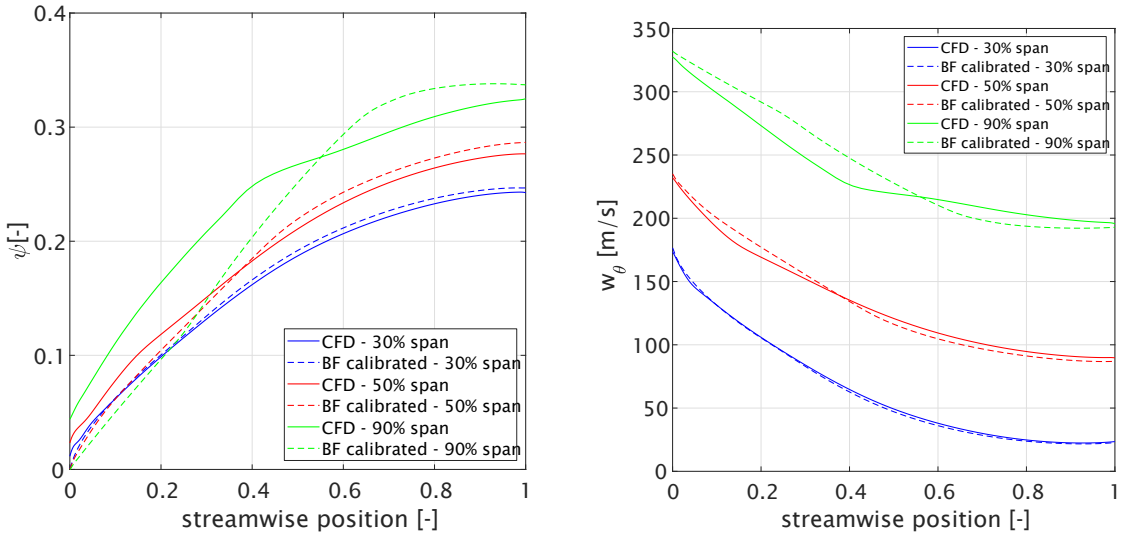

(a) Work coefficient

(b) Relative circumferential velocity

Figure 4.28: Streamwise profiles at near stall for reference CFD solution and calibrated BFM.

Spanwise profiles downstream of rotor blade are depicted in Figure 4.29. The total pressure ratio of Figure 4.29a presented a close match up to mid span, apart from a local minimum near 5% of span coming from the peak efficiency force distribution and lost in the CFD solution. On the upper half of blade, the total pressure shape was almost linearly offset until reaching a peak, that despite having a greater value occurred in the correct position. The total temperature profile, in the same figure, was less close and smoother than the CFD one. Surprisingly, the typical overshoot at tip seen in the other operating points was here very well matched, as this time it was also present in the CFD. The TPR and TTR difference effect is well visible on the isentropic efficiency profile of Figure 4.29b. The shape differed from the CFD and also its integral fell below, as already reported in the maps of Figure 4.21b.

Overall, also at near stall some flow parameters were captured in both shape and magnitude on a region of the blade, like the flow angles and the work coefficient, whilst other were only approximately reproduced. It must be considered that either the choke calibration somehow arbitrarily altered the force distribution affecting the leading to trailing edge evolution of the flow, and it is unlikely that the body force model be able to closely capture the force change from peak efficiency to this troublesome operating point. Moreover, as already stated, the force near tip and in the tip gap (here not present) has an influence on the stall inception and probably a dedicated treatment might be necessary to improve the prediction. What the BF model was able to deliver was the integral representation of the machine performance with a spanwise distribution not completely faithful but certainly more precise than a constant hub-to-tip value.

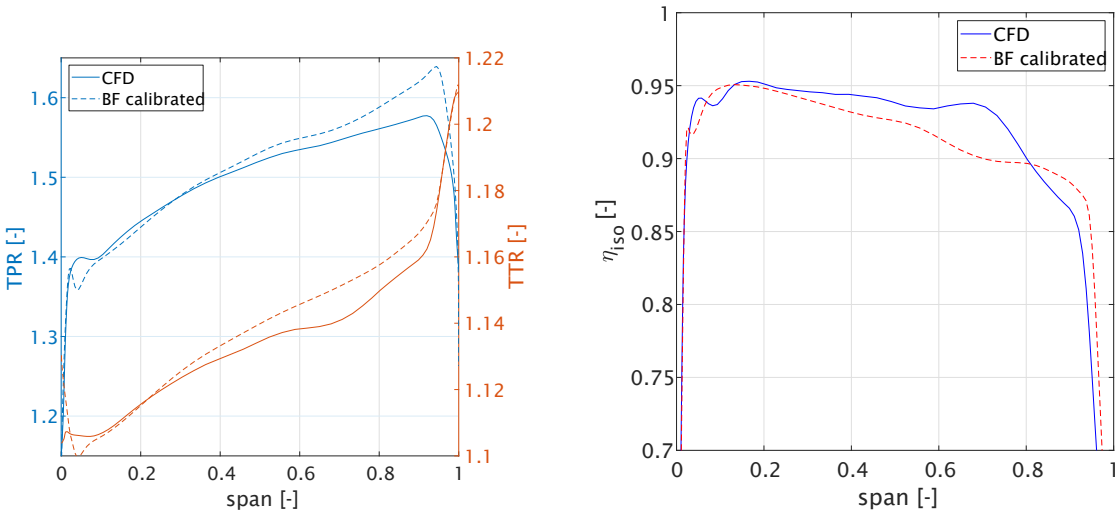

(a) Work coefficient (b) Relative circumferential velocity

Figure 4.29: Spanwise profiles downstream of rotor blade at near stall for reference CFD solution and calibrated BFM.

4.5.4 Force comparison

The flow field of a body force simulation derives from the application of the external force distribution, through the calibration surfaces, and the conditions set at the domain boundaries. The force distribution is actually a function of the local flow parameters and this coupling ensures what Kestner [132] called flow field reconciliation, that is the consistent link between the applied forces and the flow solution, which is in the end determined by the Navier-Stokes balances. For this reason, it is possible that even though the source terms of the body force solutions differ to some extent from those extracted from the CFD calculations and employed to calibrate the BF model, the flow fields show coherent similarities. Although ideally both the flow and the force fields should overlap with their reference counterparts, in practice their coupling allows to fulfil the enforced boundary conditions and recover the attributes of the circumferential-averaged direct simulation even without a perfect agreement of the source terms.

This feature is only kept, however, if the equations expressing the force magnitude replicate the physical behaviour of its variation along the speedline. Therefore, it is interesting to examine the converged body force field and compare it to the one that should have been resulted if perfect match with the circumferential-averaged CFD solution had been obtained. Figure 4.31 illustrates the nondimensional normal force distribution as extracted from the CFD and resulting in converged body force simulations at peak efficiency, before and after the choking calibration procedure. The first two figures compare relatively well. The BF force was larger in magnitude, especially on the hub leading edge corner and in the high-speed region. The values near the trailing edge were instead closer to the CFD one, suggesting a similar exit flow direction, as in fact

proven in 4.5.1.

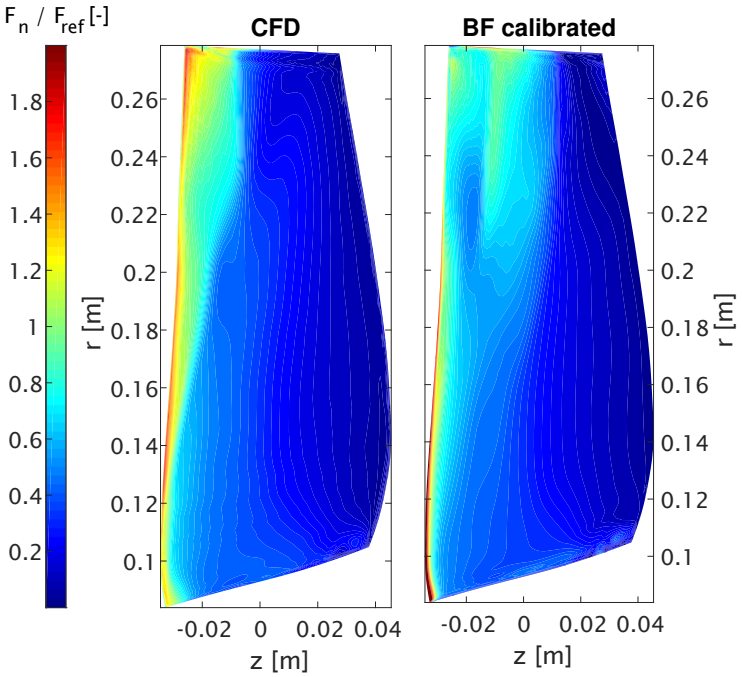

Figure 4.30: Normal force distribution at near stall extracted from CFD and obtained in converged calibrated BF simulation.

The choke calibration alters this distribution with the purpose of reducing the force magnitude in the first 50% of chord and match the choking mass flow rate. This is achieved by increasing the β_n^0 term in order to restrict the difference $\beta - \beta_n^0$ determining the magnitude. Actually, in the first fraction of chord the force looks reduced in the figure. However, it can be noticed that this resulted in a retardation of the high-speed region (which is actually a smeared shock trace, as explained before) and a large overshoot. In practice, the same downstream boundary condition has been fulfilled by adapting the force distribution in that way an amplifying its variation in order to reach a similar exit velocity field.

This analysis recalls the local nature of the body force approach, in which each cell source term responds to the local flow conditions, allowing this methodology to be applied not only in axisymmetric swirl flows, but to fully three-dimensional cases, despite it was formally derived and calibrated from circumferential-averaged only solutions.

As additional remark to the calibration procedure, the normal force modulus is actually reduced only if $\beta - \beta_n^0$ is positive, that is $\beta > \beta_n^0$. Otherwise, an increase of β_n^0 enlarges the magnitude. Confusion might arise due to the fact that the terms force modulus and magnitude have been used. However, as stated in section 4.3, the normal force equation is based on a linear elastic model, in which it acts to reduce the difference $\beta - \beta_n^0$ and bring the relative flow velocity adherent to the streamsurface represented by

the $\beta_n^0(z,r)$ function. A stable behaviour is obtained only if the elastic constant is positive, which is granted by the square and geometric terms in the equation, and the force direction is properly imposed. Exactly as in the one-dimensional case $F = -k(x - x_0)$, where the force points towards the negative x if $x > x_0$ and viceversa, the normal force assumes a positive or negative value in the local $< n, p, b >$ frame given by normal, parallel and binormal versors, according to the difference $\beta - \beta_n^0$. In this respect, equation 4.7 can be interpreted as the real component along the local normal direction, instead of just a modulus that must be correctly signed. If the flow incidence is negative, the choking calibration acts to increase the force magnitude, which might be questionable. A discussion of the stability of the deviation-based normal force is also given in Appendix A of Peters [200], who stressed the change of the force direction, and consequently its sign, across the speedline.

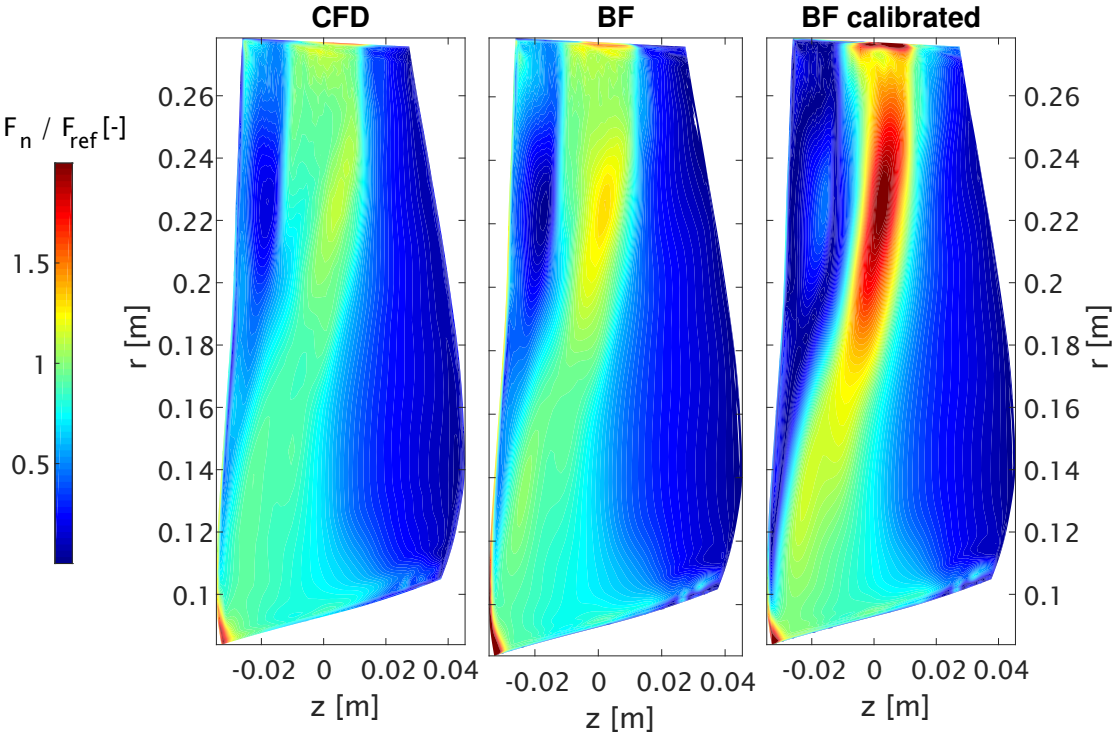

Figure 4.31: Normal force distribution at peak efficiency extracted from CFD and obtained in converged BF simulations before and after choke calibration

The analysis of the force distribution near stall for the CFD and calibrated BF nondimensional normal force is shown in 4.30. By first comparing the reference force with the peak efficiency point, it can be observed how near stall the distribution was almost monotonic, with a peak reached near the leading edge and gently degrading towards the blade exit, and the shock region narrower and almost straight in the last 25% of span. Towards the stall, the normal force, therefore, degraded and the flow was rapidly turned over a short portion near the leading edge due to its incoming incidence with respect to

the metal blade leading edge angle. The body force response was quite similar in the first 50% of span, where it can be exactly recognised the same behaviour. Above it, a larger difference appeared and the BF presented a non-monotonic distribution, as more clearly visible in Figure 4.32.

This non-matching pattern might suggest that the linear elastic force model be not fully valid far from its calibration point, as a first order expansion is strictly accurate in a neighbourhood of the pivot point. The fact that the major variation occurred on the top half of blade is also likely to indicate that compressibility effects come into play, in the form of higher order terms adding further nonlinearity to the force equation. The actual BF model *per se*, as shown in the previous subsection, approximately matched the integral flow parameters and the downstream spanwise profiles, but it did not turn out to be sufficiently accurate to be able to provide a point-to-point local correspondence over the entire speedline. On the other hand, inferring a better law from extracted force fields appears overly complex.

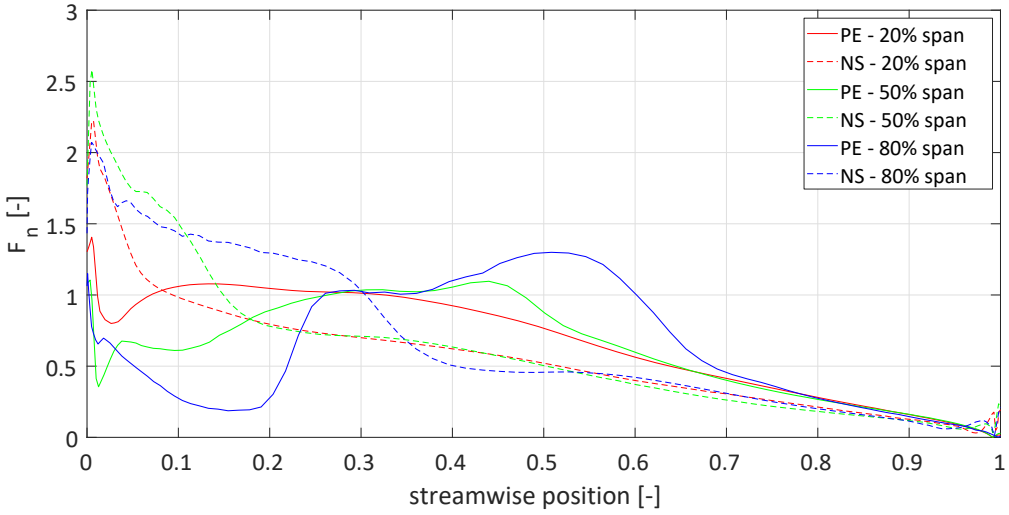

Figure 4.32: Normal force distribution extracted from CFD at peak efficiency and near stall.

The effect of the different force distributions arising across the speedline on the resulting flow field is summarised by the Mach number distributions over the domain in Figure 4.33. The blade distribution differed, as thoroughly described in each section, but outside the force region the agreement was satisfactory, even behind the rotor. The major difference arose near choking, where a sharper compression followed by a re-acceleration took place in the BFM.

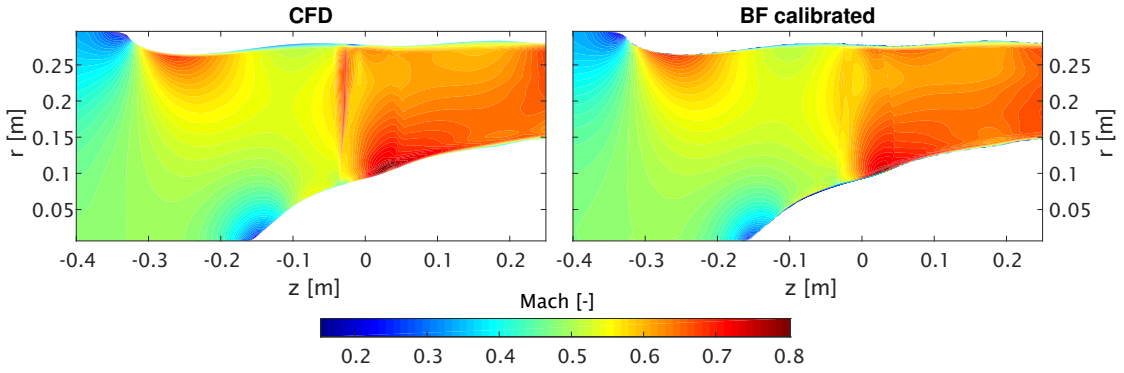

(a) Near stall

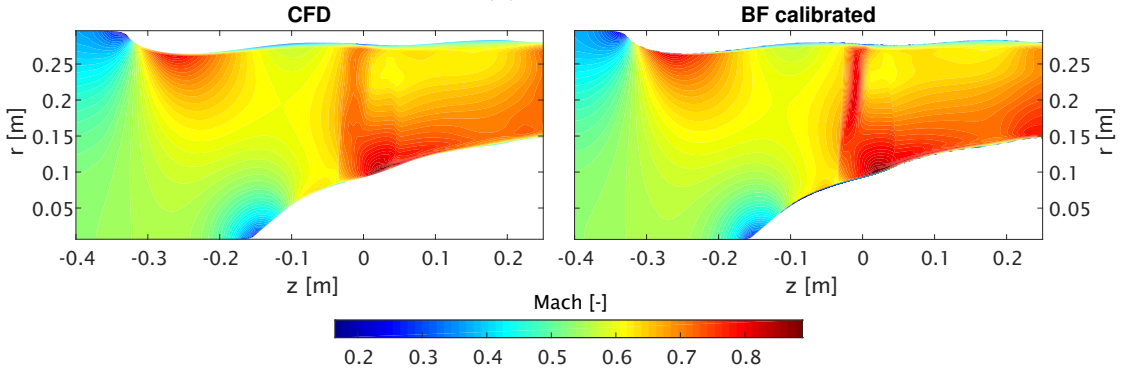

(b) Peak efficiency

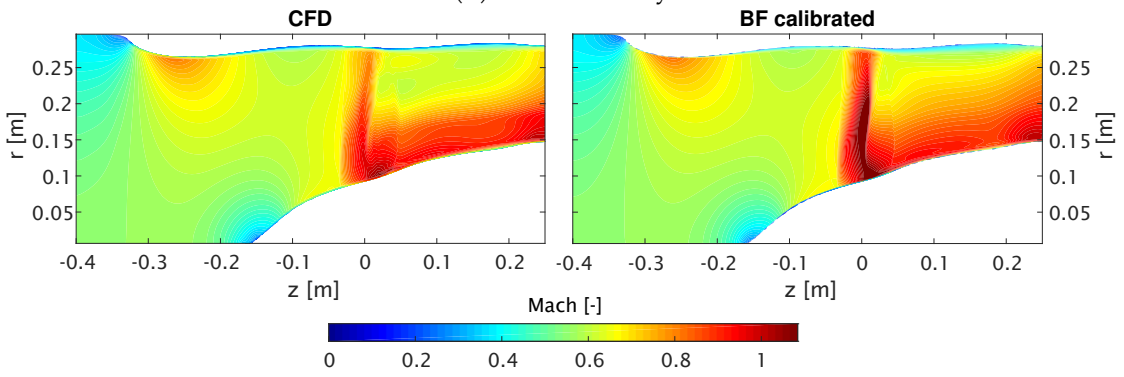

(c) Near choke

Figure 4.33: Mach number contours for ducted rotor alone case at different operating points.

Table 4.5: Swirl flow calculations near peak efficiency.

model	Swirl [deg]	$\dot{m}$ [kg/s]	TPR	TTR	η_{iso}
BF	+5	47.465	1.478	1.133	0.890
CFD	+5	47.276	1.474	1.129	0.906
BF	-5	44.653	1.452	1.123	0.916
CFD	-5	44.476	1.448	1.119	0.934

4.5.5 Swirl flow

The sensitivity of the body force model to properly react to inflow conditions was assessed by imposing a pre-swirl to the incoming flow, of +5°and -5°, near peak efficiency. Table 4.5 summarizes the performance indexes result. The overall agreement was good, meaning that the body force model responded adequately to the variation of incidence. However, some discrepancies could be found by a deeper examination of the calculation outcome. Figure 4.34 compares the spanwise distribution of flow and work coefficient downstream the rotor blade between the CFD and BF solution. The flow coefficient was better captured for a positive swirl, whilst for the negative swirl it has a wavy shape near the tip, not present in the CFD. The work coefficient was well reproduced in both cases below mid-span, but was overpredicted above, with the usual high peak near the tip. The flow swirl angle, shown in Figure 4.35, presented a closer match again for the +5°case and the relative component. For the negative pre-swirl, differences of α up to 7°can be observed from 65% to 90% of span, but the tip values are in better agreement. The efficiency profiles in Figure 4.36 revealed that it was well predicted up to 40% of span, but there is a negative offset from 40% to 90%. The curve shape was closer for the positive swirl. In both cases, an excessive velocity in the first half of chord could be noticed. This is visible in the relative velocity contours on the blade, depicted in Figure 4.37 and it was consistent with the observation that due to the choke calibration a portion of the blade operates an expansion of the fluid, rather than diffusing the relative velocity and increasing the pressure. The exit values are, however, not too distant from the reference solution.

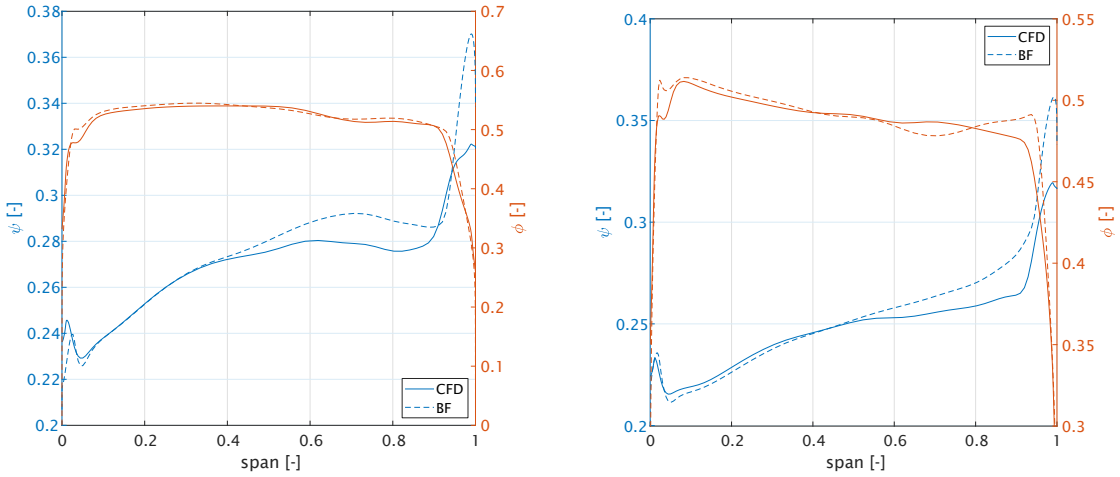

(a) Swirl +5° (b) Swirl -5°

Figure 4.34: Spanwise distributions downstream of rotor blade of work and flow coefficient for pre-swirled flow near peak efficiency.

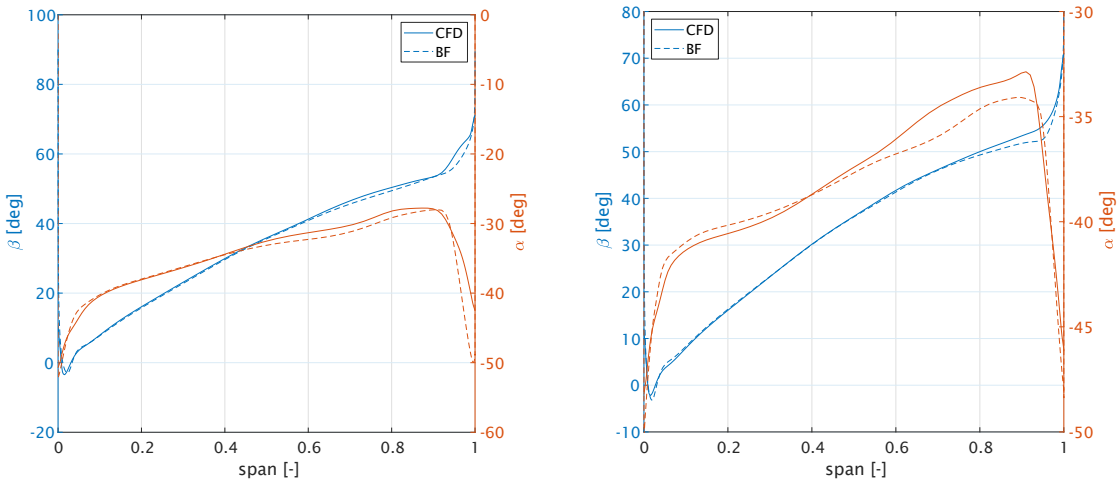

(a) Swirl +5° (b) Swirl -5°

Figure 4.35: Spanwise distributions downstream of rotor blade of swirl angles for pre-swirled flow near peak efficiency.

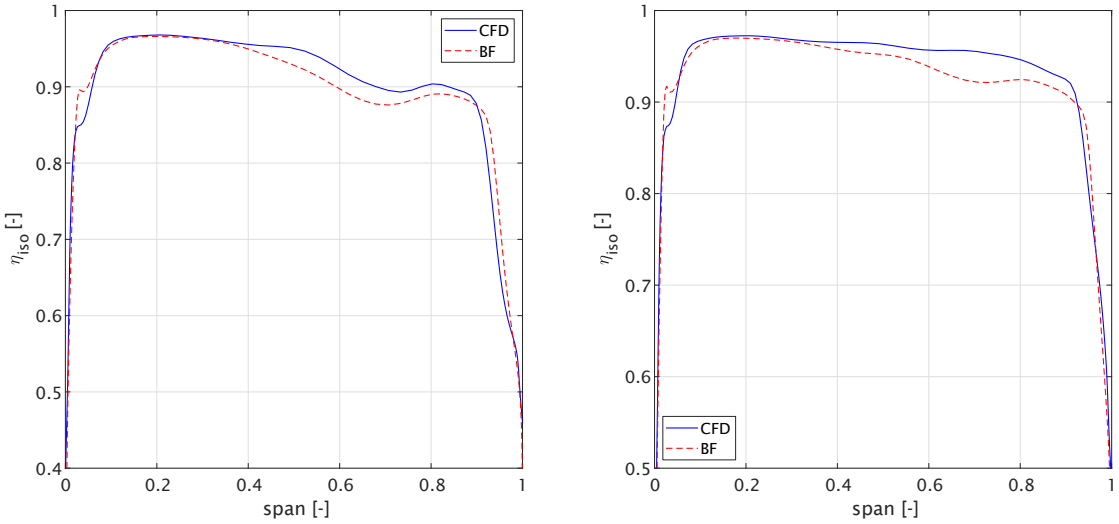

(a) Swirl +5° (b) Swirl -5°

Figure 4.36: Spanwise distributions downstream of rotor blade of isentropic efficiency for pre-swirled flow near peak efficiency.

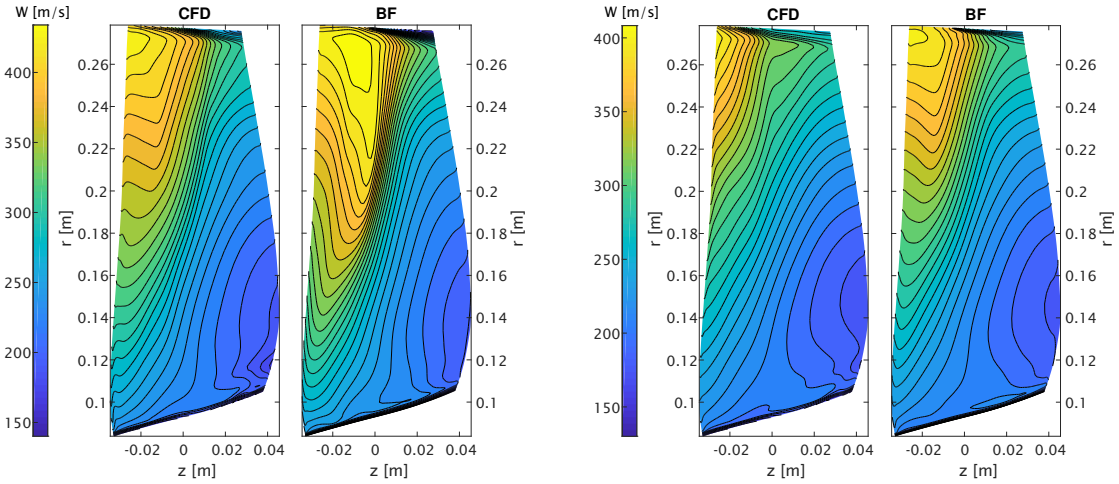

(a) Swirl +5° (b) Swirl -5°

Figure 4.37: Blade contours of relative velocity magnitude for pre-swirled flow near peak efficiency.

4.5.6 Fan+OGV stage

As a final comparison case, the full fan+OGV stage was simulated at single-point with the nacelle immersed into a freestream flow at low and high-speed conditions. To this purpose, the body force model was incorporated into the commercial solver ANSYS Fluent, by means of User Defined Functions (UDF), where the source terms corresponding to the body forces and the necessary pre-processing modules were coded in C programming language. In fact, the simulation of the full engine was, although in an axisymmetric fashion, was not affordable in ANTARES, which is best suited for model development. This section partially anticipates the content of the next chapter, where a dedicated study on intake flows at high incidence is described. The stator blade BF model was calibrated using the developed force extraction procedure. Choking calibration only involved the rotor region. The calibration was done using data derived with a freestream Mach number of 0.10. Given that the force is mainly dependent on the relative flow angles, a calibrated dataset remains valid in the kinematic similitude even when the freestream Mach number is changed, as it will be proved by the good adherence between reference curves extracted from single-passage CFD simulations and axisymmetric BF curves.

A cross sectional view of the computational domain, showing the Mach number distribution over the exterior nacelle and the internal engine duct is given in Figure 4.38, for the case of a freestream Mach of 0.75. This case represent a wind tunnel test at cruise condition of an isolated engine at zero incidence. The comparison of the same case between CFD and experimental data at low speed, presented in 4.4.1, already showed a very good match for the 3D computational model. Considering this higher speed case, a smooth flow over the external nacelle cowl can be observed. The CFD and BF results presents a very similar Mach number distribution, with some local differences due to the different resolution of the solver used, Ansys CFX for the 3D CFD case, and Ansys Fluent for the BFM. For the internal flow, a region of higher Mach number in the first third of rotor chord can be seen, which comes from the choking calibration as previously discussed. In the stator blade region, the CFD circumferentially-averaged solution highlights the presence of hub corner separation at trailing edge. The velocity deficit begins in the second part of the chord at low span and continues downstream, up to the nozzle restriction where the flow reacquires its full velocity distribution. This feature is also present in the BF field, although with a different development. In fact, it originates earlier and presents a higher thickness. Despite the circumferential averaging procedure of the 3D CFD data has a limited resolution near the endwalls, it appears that the hub boundary layer leaving the rotor is thicker, and it is further enlarged across the stator blade. The body force model replicates a physical flow feature present in the higher-fidelity solution, but only with a partial agreement. By examining the angle distribution downstream of the OGVs, showed in Figure 4.39a, it can be noticed that the stator has a large underturning near the endwalls, with a residual swirl of about $2.5°$. Whilst the tip underturning is well matched by the BF model, the hub is not, as a consequence of a lower axial and circumferential velocity, the difference in α being up to $1.5°$. Attempts to improve the prediction in this area by manually altering the force

distribution were unsuccessful. The effect of this behaviour can be also seen in the TPR and TTR profiles downstream of the OGV, reported in Figure 4.39b. Up to 40% of span, the total pressure predicted by the BFM is below the reference solution of about 2.5% in absolute value, whilst it is slightly above at higher span. Overall, the curve shape is well replicated. The situation for the TTR, entirely depending on the rotor, is symmetric, with the tip overshoot already discussed.

In terms of integral quantities, the single-point operation results are summarised in Table 4.6. The mass flow rate predicted by the BF computation is 0.2% higher of the CFD calculation. The TPR is also closely matched. However, due to the rotor tip overprediction, the TTR is too high, which penalises the isentropic efficiency by 1.45% in absolute terms.

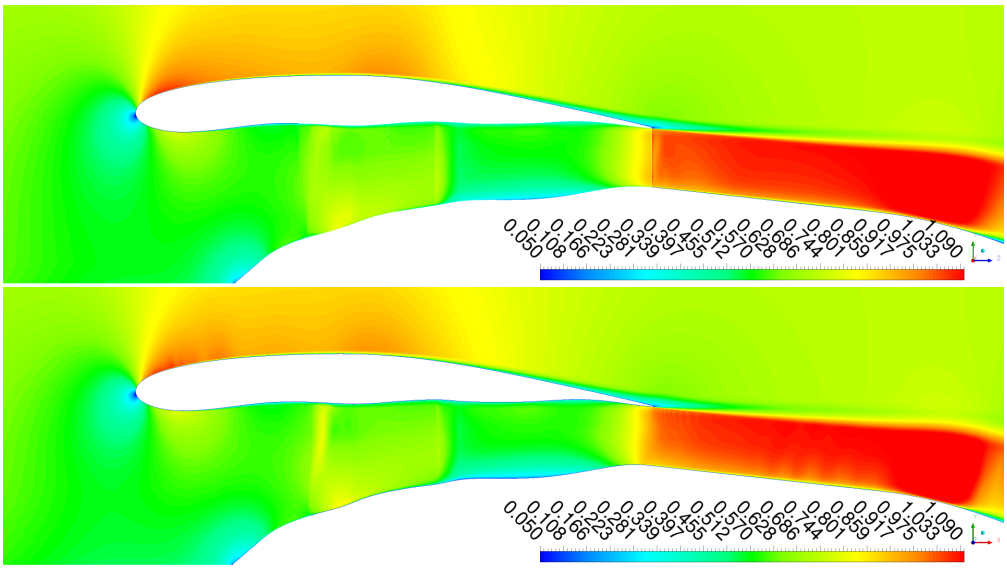

Figure 4.38: Mach number distribution for single-point operation at cruise with CFD (top) and BF model (bottom).

Table 4.6: Integral performance indexes at full stage single-point operation at cruise condition for CFD and BF model.

model	$\dot{m}$ [kg/s]	TPR	TTR	η_{iso}
CFD	45.821	1.461	1.127	0.903
BF	45.912	1.460	1.129	0.889

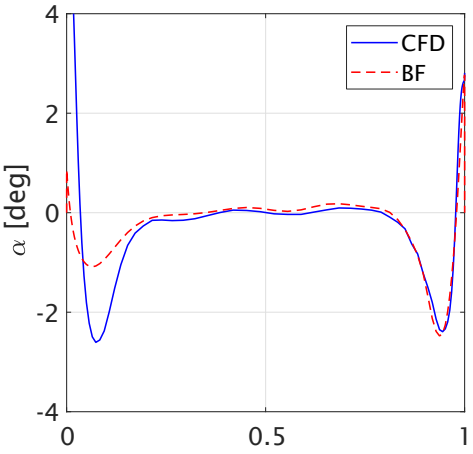

(a) Absolute swirl angle downstream of OGV

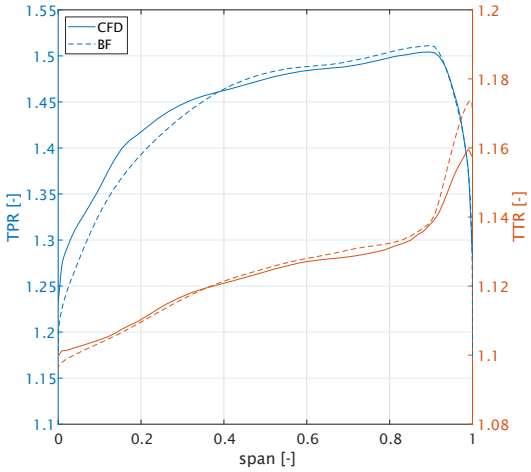

(b) TPR and TTR spanwise profiles downstream of OGV

Figure 4.39: Single-point fan+OGV stage results at $M = 0.75$.

4.6 Conclusion

The Lift/Drag BFM of Thollet has been implemented into the developed computational tool ANTARES and thoroughly investigated using the NASA R4 transonic fan as test case. The study has first assessed the model calibration, for which different theoretical approaches are available to obtain the forcing terms of the circumferential-averaged RANS equations that correspond to the body forces. Previous findings indicating the combination of Blade Force Average (BFA) for normal force extraction and Marble's equation for parallel force redistribution have been confirmed. In addition, in the current formulation a fully three-dimensional normal force accounting has been used, giving good predictions of radial effects in the flow variables.

The method has been validated by comparing the results to higher-fidelity 3D CFD simulations in a series of configurations. The BFM has proven to be able to reproduce the characteristic maps with good accuracy after a tuning of the normal force magnitude had been introduced, as prescribed in the original version of the model. This arbitrary modification causes a change of the streamwise evolution of the flow variables across the blade region, but restores the inlet to outlet variation. Overall, the spanwise distributions downstream of the stage were found close to those extracted from higher-fidelity simulations, which suggests that the lower-order model can be confidently applied to replicate the effect of the full engine in cases were it is required to have a physically responsive modelling, like in propulsion integration. Local discrepancies have been observed yet near the endwall regions. These deviations, which took place in the tip region of the rotor and near the hub of the stator, were responsible for differences in the integral performance metrics. Attempts to locally correct these behaviour were unsuccessful. The application of the BFM approach to different transonic rotors might disclose

more about the limits of tip flow prediction, but a similar feature was observed in the simulation of NASA R67, suggesting that it is an intrinsic defect of the model. The developed set of semi-automatic routines for data extraction from 3D CFD and calculation of the calibration coefficients should allow in the future to apply it to other machines, although a similarity in the force distribution for transonic rotors has emerged from the study.

The BFM formulation appears, therefore, generalisable to study engine/airframe interaction in analysis mode, replacing the overly heavy direct CFD simulations with a much lighter model. The need to instruct it from higher-fidelity simulations restrains its applicability only to the analysis mode and makes it more similar to a surrogate model, that can be used to explore different configurations and operating conditions extrapolating the machine behaviour from a reliable working line. In contrast to this limit, a comparison between the flow field and the characteristic maps is always possible. Given the large number of interpolations and data reduction operations necessary, it is in fact recommended to perform this check on the accuracy prior to simulating outside the calibration point. With the present implementation showing to reliably duplicate the reference data in different conditions, the next chapter reports its use to study intake flows with a coupled fan engine modelling at high-lift conditions.

Chapter 5

Intake flow

The validated body force model described in chapter 4 was employed to study intake flows and compare the fields obtained when the fan is modelled only by prescribing a boundary condition at the fan face. Nacelle intake is a key component of a propulsion unit that has to cope with multiple conflicting requirements. During ground operation, it has to provide the engine with a sufficient flow capacity without an excessive flow acceleration and separation caused by ground interaction or crosswind. At take off rotation and wing maximum lift, the flow must be redirected towards the engine with minimum distortion to avoid non-uniform blade loading inducing local shift of the operating orbits towards stall and aeroelastic stress. At cruise, it must decelerate the flow to an acceptable velocity at the fan face without incurring choking or too high throat Mach number causing shock waves and total pressure losses. Given the inherent multi-objective and multi-point nature of a nacelle intake operation, a careful design is required to satisfy at the same time all the requirements without overly penalising any flight phase. In the UHBPR context, where shorter and slimmer nacelle are sought, a coupled design approach appears to become mandatory.

In this chapter, a sensitivity study on fan modelling for intake flows is presented. The aim of the study was to verify the body force behaviour at different flight regimes which are typically considered for the intake design and assess its suitability to be employed in parametric analysis or optimisations. The test case was again the NASA/GEAE R4 stage with baseline OGV and its nacelle, whose validated CFD and BFM models were discussed in the chapter 4. The work here described was meant to be preparatory for future automatic optimisation of intake cowls and in that respect the observations reported are only preliminary and focused on the identification of suitable criteria to discriminate among better geometries and delineate an initial design space.

5.1 Terminology

Before presenting the numerical approach and the results, some terminology referred to nacelle and intake is given, to avoid any ambiguity during the reading. Figure 5.1 defines some geometric values that will be used hereafter. The highlight point is the

nacelle most upstream point and falls on its leading edge. l_{max} refers to the length from the highlight to the point where the external cowl has its maximum diameter. l_{post} is the length of the remaining part of the external cowl, up to its trailing edge. The sum of l_{max} and l_{post} gives the nacelle length L_{nac}. l_{throat} is the length from the highlight to the intake throat, l_{diff} the remaining length up to the fan face (FF) or the aerodynamic interface plane (AIP). Their proportion with respect to the intake length is indicated by f_{throat} and f_{diff}, respectively.

The ratio between the throat and highlight area, A_{HL}/A_{throat} is the inlet contraction ratio, and determines the throat Mach number. The ratio between the throat and AIP area sets the diffusion rate, $DR = A_{throat}/A_{FF}$. The overall diffuser angle θ_{diff} is $atan((r_{AIP} - r_{throat})/l_{diff})$. The intake aspect ratio $AR_{int} = (r_{HL} - r_{throat})/l_{throat}$. Other design parameters are the leading edge radius and the maximum thickness over the chord of the external cowl, indicating the slimness of the inlet that is important both the cruise drag and the take-off pressure recovery. The leading edge radius will be measured by the parameter f_{nose}, to whom it is proportional.

It is common to define the shape factors in terms of ratios with the nacelle maximum diameter, as this gives immediately and idea of the aspect ratios. Of particular importance to characterise the intake is the L_{intake}/D_{HL} factor, assuming values around 0.5 for traditional designs and down to 0.20 for very aggressive configurations that might be employed in UHBPR engines to reduce the nacelle weight. Equivalently for the nacelle external cowl the ratio L_{nac}/D_{max} is used.

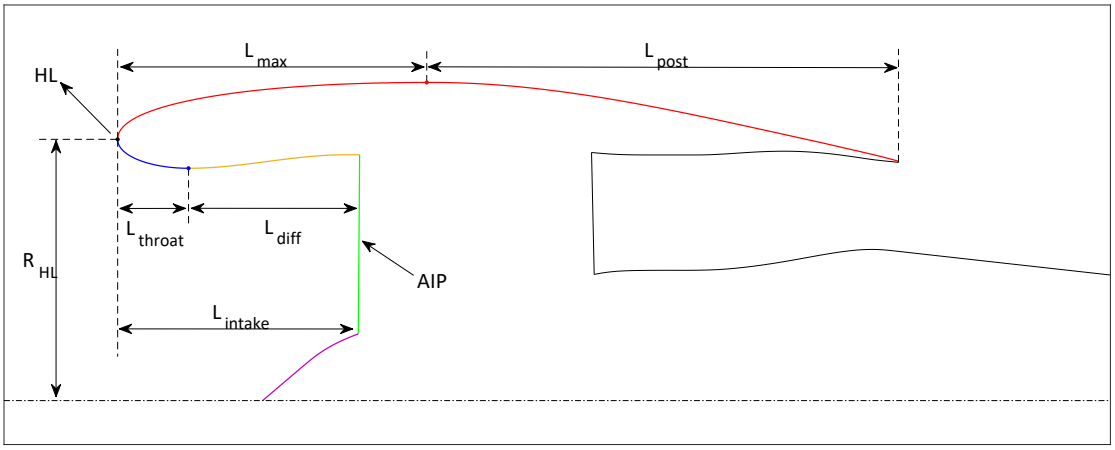

Figure 5.1: Geometric parameters of intake.

A common parameter used to characterise the intake operating condition is the mass flow capture ratio (MFCR), defined as the geometric ratio between the cross-sectional area of the capture streamtube at freestream and degree.the highlight area. As it is purely a geometric factor, the term area capture ratio (ACR) should be preferred, although in the literature it is commonly referred to as MFCR and it will be used as such. It can be expressed as a function of the ingested mass flow rate $\dot{m}$, the freestream con-

Table 5.1: R4 nacelle geometric parameters.

Parameter	Value
L_{nac}/D_{max}	1.229
R_{LE}/L_{nac}	0.02
D_{HL}/D_{max}	0.821
L_{int}/D_{HL}	0.472
A_{HL}/A_{throat}	1.265
L_{throat}/L_{int}	0.288
L_{diff}/L_{int}	0.712
A_{FF}/A_{throat}	1.182
θ_{diff} [deg]	4.508
AR_{int}	0.408

ditions denoted by ∞ subscript and the highlight area A_1:

$$MFCR \text{ or } ACR = \frac{\dot{m}}{\sqrt{\gamma\, R\, T_\infty}\, p_\infty\, M_\infty\, A_1} \tag{5.1}$$

Its value is above one at take off and reduces during climbing, reaching a typical value of 0.7-0.75 at start-of-cruise and around 0.6 at end-of-cruise.

In order to measure the distortion level at teh aerodynamic interface plane, a number of indicators have been developed in industries and academy [86]. In the present work, two commonly used metrics are employed. Considering total pressure readings from a rake placed at a suitable engine inlet location, made up of n radial levels, with m azimuthal probe each, the Index of Circumferential Distortion (IDC) is defined as:

$$IDC = max_{r=1,\dots,n-1}\ 0.5 \left\{ \frac{\overline{P0_r} - P0_r^{min} + \overline{P0_{r+1}} - P0_{r+1}^{min}}{\overline{P0}} \right\} \tag{5.2}$$

r denotes the radial stack and $\overline{P0_r}$ the average total pressure on the r^{th} level. The IDC is useful to detect flow separation on the lip, as it suddenly increases once the detachment has occurred. By comparing the mean to the minimum pressure on the same radial level, it is sensitive to circumferential distortions, but it cannot detect axisymmetric profiles. The Index of Radial Distortion (IDR) is then used, defined as

$$IDR = max_{r=1,\dots,n-1}\ \frac{\overline{P_{face}} - \overline{P0_r}}{\overline{P_{face}}} \tag{5.3}$$

with $\overline{P_{face}}$ the face average total pressure.

These metrics have been used in several works dealing with inlet distortion patterns for civil turbofan engines, e.g [115, 130, 161, 237]. The calculation of the ring average pressure $\overline{P0_r}$ and face average pressure $\overline{P_{face}}$ was compliant with the SAE AIR1419

indications [221]. $\overline{P0_r}$ is the ring integral mean of pressure readings, whilst the face average was computed as an area-averaged value. Regarding the rake arrangement, ARP1420 [220] reports guidelines for its axial location and density. The position of the rake defines the Aerodynamic Interface Plane (AIP), which should be located as close as possible to the engine-face plane, compatibly with the experimental test rig and the interference with the engine. As this study was solely numerical and sampling was totally virtual, the AIP was defined just upstream of the rotor blade leading edge. The recommended typical 5x8 ($n = 5, m = 8$) rake arrangement of [220] was used, with 5 rings enclosing equal area sectors and having 8 theta-equispaced probes each (Figure 5.2)

The total pressure loss in the intake boundary layer or shock waves is measured by the Inlet Pressure Recovery (IPR) factor, $IPR = P0_{AIP}/P0_{\infty}$. In the study, this value was computed over the entire AIP plane directly, thus not from the probes readings.

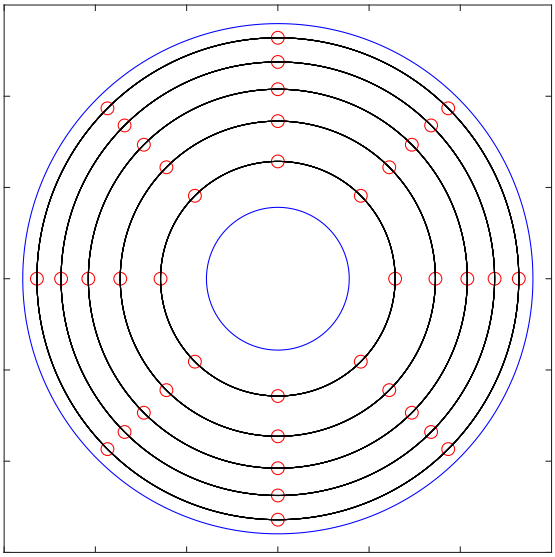

Figure 5.2: 5x8 rake used for distortion indexes calculation.

5.2 Computational model

The analysis involving the isolated nacelle without pylon or bifurcation was carried out using the commercial solver ANSYS Fluent. The incorporation of the body force model was made possible by the use of User Defined Functions (UDF), where the source terms corresponding to the body forces and the necessary pre-processing modules were coded in C programming language. The isolated nacelle was placed in a spherical domain of radius $80\,R_{max}$ on which boundary a Riemann farfield condition with prescribed freestream values was set. For the nacelle powered via boundary conditions, the fan was modelled as a pressure outlet with a floating average pressure spec-

ification, changed during iterations to match the same target mass flow rate obtained in the body force simulation. In practice, this datum is unknown, since it is the result of the interaction between the fan model and the external boundary conditions, and a reference fixed value is set for the mass flow rate, to match a MFCR, for instance. Similarly, the nozzle plane was modelled as a pressure outlet, with the average total pressure and temperature found in the body force computation. Strict mass flow conservation between the fan face and nozzle exit boundary was not enforced. The turbulence model was the Spalart-Allmaras. The computational mesh in the blade region was the same used for the BFM validation. The intake and external cowl were finely meshed to ensure sufficient resolution to capture the shock waves occurring in the lips for high-incidence operation and the drag.

Intake gridding guidelines were derived from a validation case on NACA-1 series intakes. Figure 5.3 reports an example of a grid convergence study for pressure coefficient distribution. A range of Mach numbers and MFCRs was explored. Systematic grid refinement for three grid levels, coarse (20k), medium (40k) and fine (80k), was done. The Grid Convergence Index (CGI) [31] from coarse to medium was largely lower than 0.1% on every case for IPR, suggesting that a medium mesh point distribution on the intakes could be sufficient.

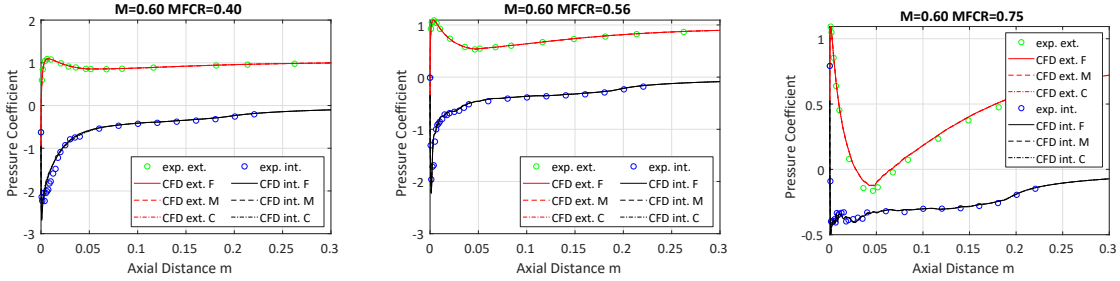

(a) MFCR=0.40 (b) MFCR=0.56 (c) MFCR=0.75

Figure 5.3: Pressure coefficient distribution on NASA 1-85-43.9 lip at $M = 0.60$ and different MFCR for three grid levels.

No core flow was included and the fan nozzle afterbody was prolonged keeping a constant slope. In the exhaust region the mesh was refined in the shear layer zone of the high-speed jet ejected by the nozzle. The axisymmetric mesh was obtained by revolution of a meridional grid with 90 points around the circumference, as suggested in [130], with the exclusion of the axis, where an H-O-H butterfly topology was employed to avoid high skewness. The total grid size for the BF simulations was 10M and 7M for the simulations employing simply boundary conditions.

5.3 Take-off

The first condition considered was at a Mach number of 0.20, corresponding to take-off. In this phase, the intake is exposed to a high-incidence flow either at the rotation

point and at the wing maximum C_l, and it must provide the engine with a clean inflow with minimum distortion and total pressure losses. The reference intake was characterised to evaluate the separation angle of attack, which is usually sought to be sufficiently large to include the wing $C_{l,max}$ incidence. The separation onset was established visually and by means of the IDC index, plotted in Figure 5.4. The geometric parameters of the R4 intake reported in Table 5.1 indicate a quite standard design with a thick lip, that favours the low-speed high-incidence operation. The separation angle of attack, in fact, was found to be 32°.

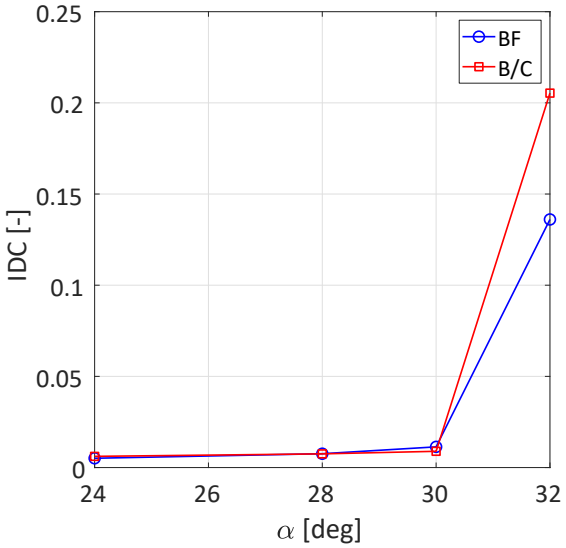

Figure 5.4: IDC index at fan face for $M = 0.20$ with fan modelled through body forces and boundary condition.

The flow field up to separation resulted quite similar for the two models. Figure 5.5 shows the Mach number contours and the streamlines at $\alpha = 28°$. On the intake, the lower lip shock wave had the same location and strength and the stagnation point and the dividing streamlines corresponded well. In the exhaust region, the total pressure and total temperature were uniform on the boundary plane, whilst in the body forces they featured both a radial and circumferential distribution, which is not detected in this meridional cut. As the incidence was increased, the shock location moved upstream and the peak Mach number augmented. Figure 5.6a provides a more detailed view of the intake region at $\alpha = 30°$. No fully separation was noticed, only a thickening of the boundary layer in both cases. Again, the shock location and strength was in substantial agreement. At the AIP, the fan suction in the body forces slightly attenuated the boundary layer thickening. At $\alpha = 32°$ the flow was fully separated and the major differences between the two models were found. Figure 5.6b highlights a large discrepancy for the separation bubble height between the two models. The fan suction helped the flow to follow the lip curvature and accelerate up to the formation of a shock wave located close to the leading edge and preventing the boundary to remain attached. The

separation height had a maximum near 60% of the intake length and then decreased thanks to the presence of the fan, acting to attenuate the distortion and straighten the flow. The distorted region interested the last 20% of the blade span. Conversely, for the pressure-outlet boundary none of these effects were present and the separation increased monotonically without showing any sign of tendency to reattachment. This behaviour was expected and well documented in the literature. Cross-sectional cuts of the flow field at different streamwise locations can better explain the influence of the fan, which propagates upstream due to the induced pre-rotation to the incoming flow. Figure 5.8 shows the relative total pressure p^0/p^0_{ref} contours from fan face to nozzle plane. The low total pressure region caused by the separation on the lower lip rotates in the direction opposite to the fan rotation, indicated in the figure. Downstream of the fan, this pattern rotated on itself mixing a high total pressure area from the tip towards lower span and stretching the radial distribution from the hub towards the shroud. This triangular excursion of total pressure is clearly visible in Figure 5.8c and it was bounded by a higher compression spot which rotated from the bottom line following the absolute whirl. Downstream the OGVs, the flow was on average de-swirled and mostly radial mixing could be observed. This phenomenology was in agreement with the observations of distortion transfer throughout compressor stages. The meridional total pressure distribution depicted in Figure 5.7 highlights the difference between the upper sector operating with minimum distortion and the lower sector operating with a reduced increment of total pressure due to the separation bubble.

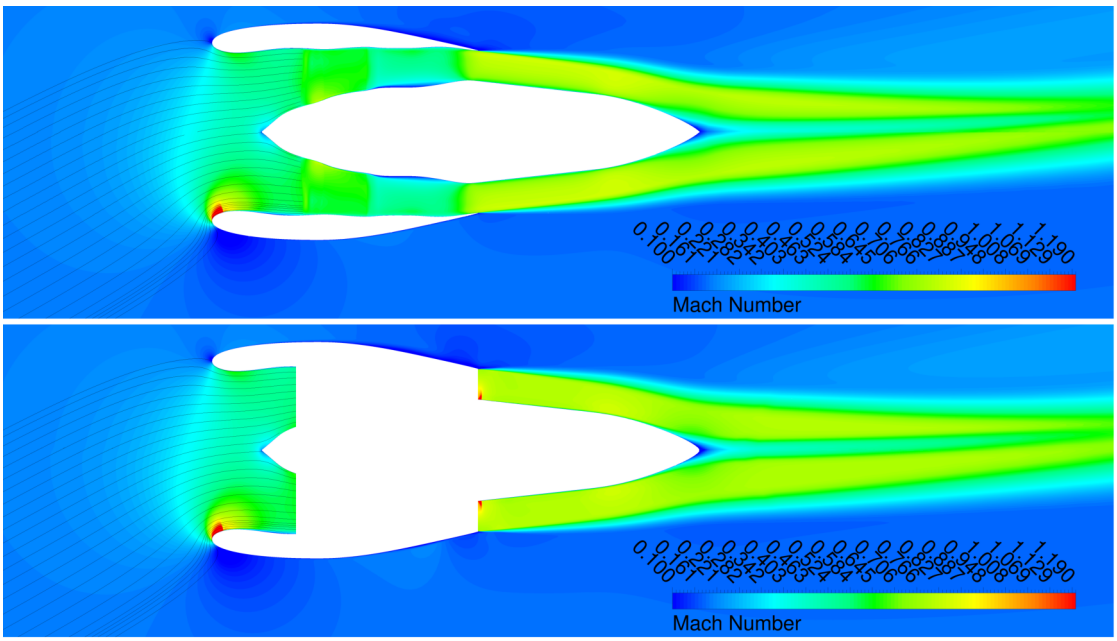

Figure 5.5: Mach number contours and streamlines for $M = 0.20$ and $\alpha = 28°$ with fan modelled through body forces and boundary condition.

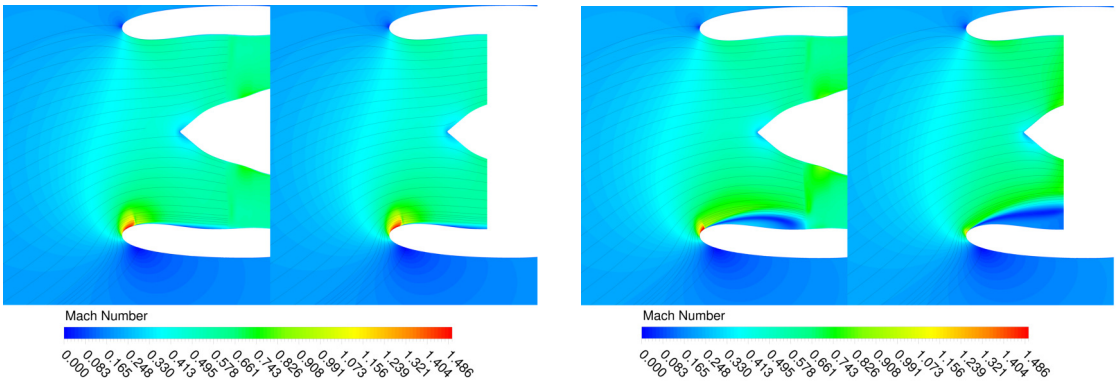

(a) $\alpha = 30°$ (b) $\alpha = 32°$

Figure 5.6: Mach number contours and streamlines near intake lip for $M = 0.20$ with fan modelled through body forces and boundary condition.

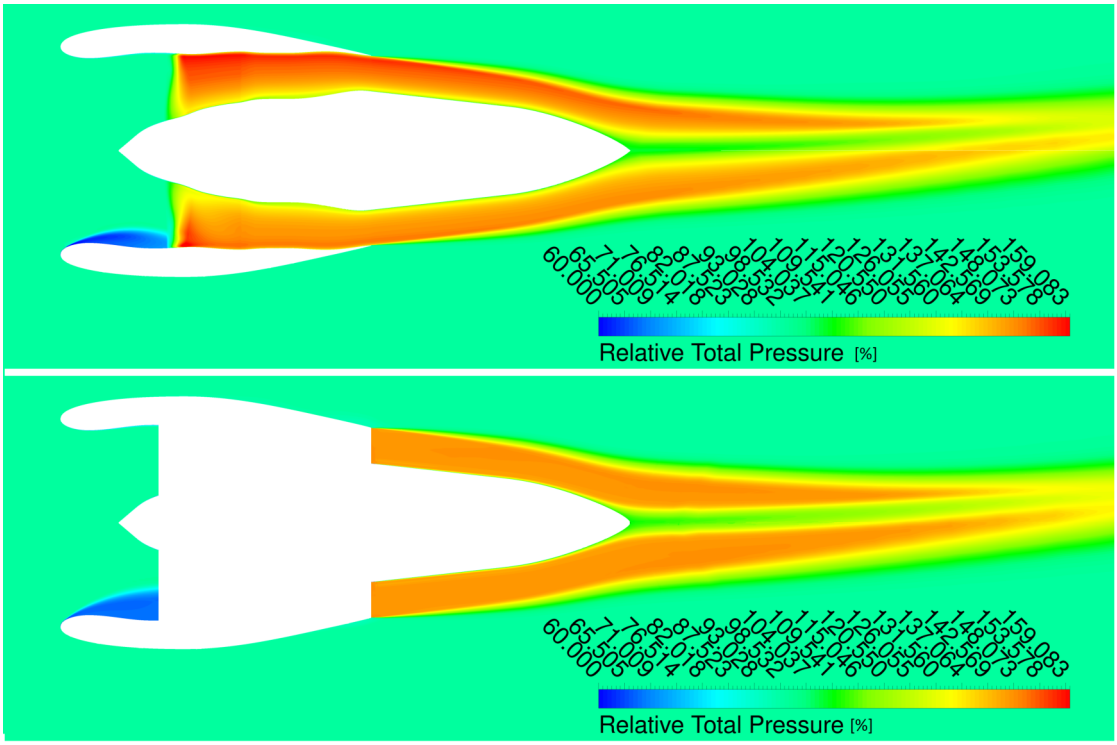

Figure 5.7: Relative Total Pressure distribution at $M = 0.20$ and $\alpha = 32°$ for fan modelled through body forces and boundary condition.

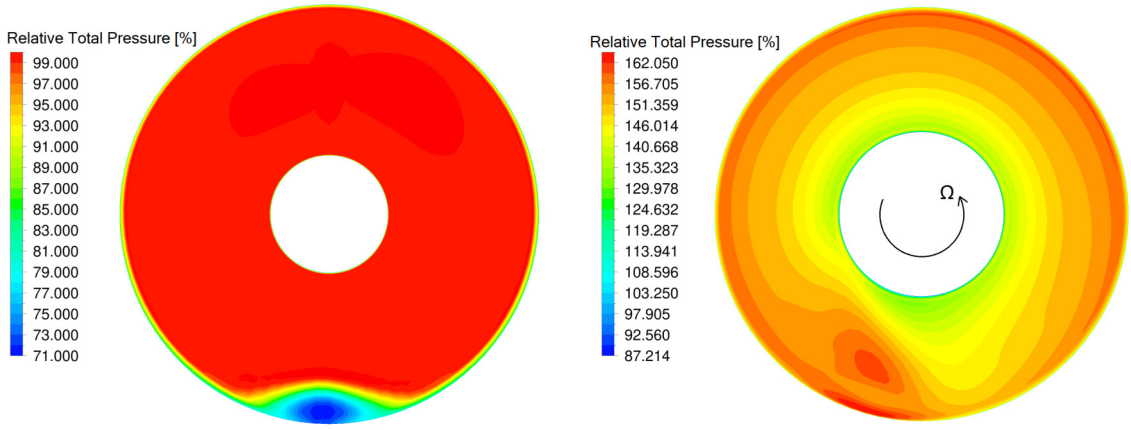

(a) Fan Face

(b) Fan Out

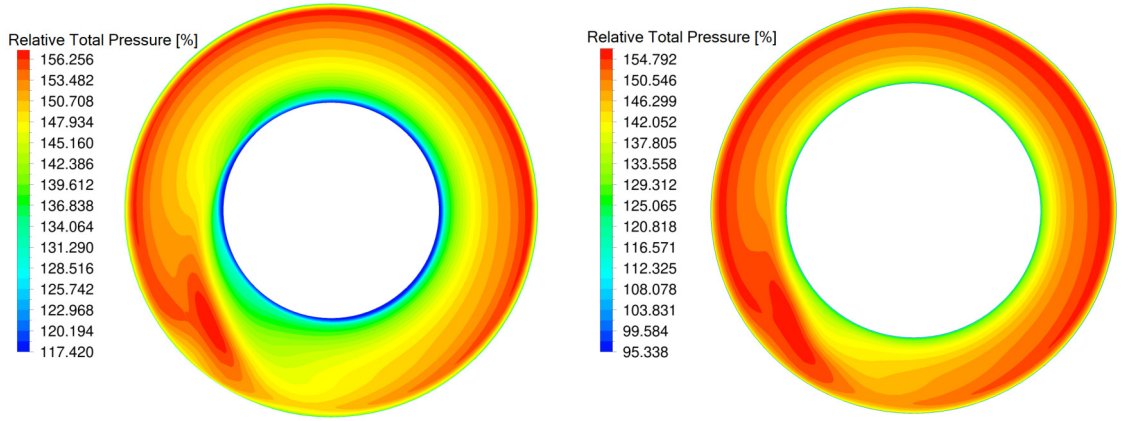

(c) OGV Out

(d) Nozzle

Figure 5.8: Relative total pressure contours at different streamwise locations. $M = 0.20$, $\alpha = 32°$.

5.4 Sensitivity study of intake aerodynamics at high incidence

The computational tools presented above were employed to conduct a sensitivity study of intake aerodynamics at high-incidence conditions. Among the three typical flight regimes that are considered for the intake design, the take-off is of intermediate difficulty, as the cruise shape is dictated by the required flow capacity and the average Mach number at fan face, whereas the crosswind is known to be one of the most difficult certification conditions [43, 155, 218]. At take-off, minimum distortion with sufficient separation-free operation must be ensured. In order to preliminarily evaluate the intake shape effect on these aspects, the take-off rotation point ($\alpha = 16°$) and a target inlet attached operation ($\alpha = 24°$) were chosen for the analysis, based on literature values [201, 305]. The Mach number was 0.25.

The purpose of the study was two fold: to evaluate the impact of intake internal shape on the performance metrics defined above at the two high-incidence points; and to evaluate the sensitivity of these metrics to the fan modelling approach employed (uncoupled approach with boundary conditions (PN) or coupled approach (BF)). The analysis was carried out with a parametric intake model based on B-Splines, with the external nacelle cowl and the highlight point unchanged. For the baseline case the NASA/GEAE R4 engine was kept, the intake being adapted to fit the existing rotor. Whilst these fitting could partially alter the outcome of the investigation, as some parameters result to be constrained, typically the intake is designed to adapt to a given fan and the highlight point position is mostly determined by the nacelle cruise operation, in order to guarantee a MFCR within typical ranges and limit spillage drag. Figure 5.9 shows the parameterised intake. A total of 10 design variables (DV) were employed to change the shape and control the throat length, the contraction ratio, the aspect ratio, the diffusion rate and wall diffusion angle. The intake length was also kept fixed. Whilst it has been found by other authors that for $L_{int}/D_{HL} > 0.40$ the fan effect on the flow development over the intake is limited [30, 200, 251], it was deemed more appropriate to begin the study from a standard intake, as numerous aspects related to the numerical setup and data analysis had to be assessed before reaching a robust, affordable and accurate procedure, that will be devoted in the future to the analysis of more aggressive intakes.

The computational model was similar to that described in the previous section, except for the absence of the nozzle flow. The nacelle was supported by a sting connected to its leading edge and the domain was truncated two chords downstream. Again, in the PN case the engine was modelled as a pressure outlet boundary inside the nacelle duct, with the target mass flow specified as the one obtained with the baseline nacelle for the same freestream conditions. For the BF simulation, the inner duct also comprised the BF fan model, the pressure outlet being placed downstream of the rotor and set at a specified static pressure, matching the same mass flow of the full stage simulations described in the previous section.

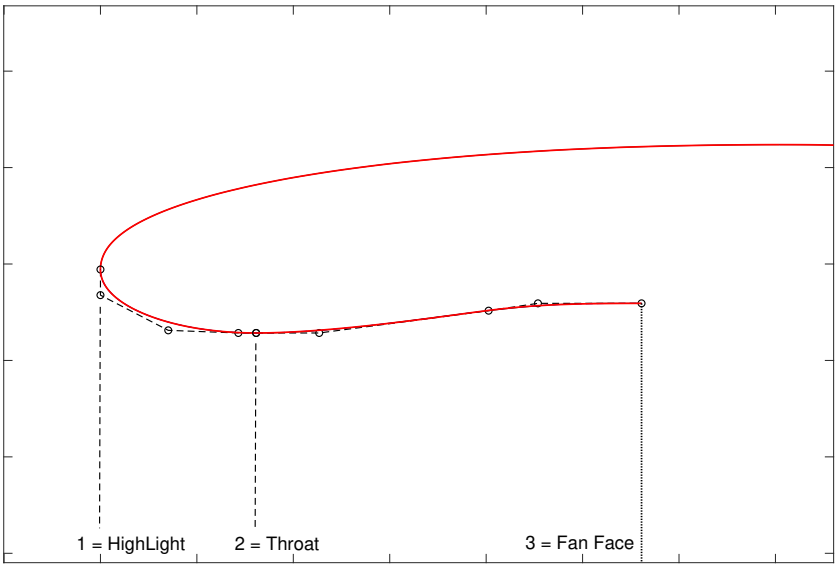

Figure 5.9: Baseline nacelle with B-Splines parameterising the intake shape.

PN results at $\alpha = 16°$ and $\alpha = 24°$

A Design Space Exploration (DSE) was first carried out with a standard boundary conditions approach, denoted as B/C Powered Nacelle (PN). The aim of the DSE was to possibly restrict the ranges of the geometric parameters delimiting the feasible design space. The simulations were conducted at $\alpha = 16°$. The incidence had to be gradually increased up to the maximum value, to avoid numerical divergence, which made the computations time expensive. An initial pool of 100 individuals was generated out of an Halton set. Given the quite large ranges chosen to loosely scan the design space, not all of the generated individuals presented suitable geometric features. Those with misplaced throat position or distorted shapes were discarded and 70 individuals were left for the computation. A total of slightly more than 10000 CPU hours were required to reach $\alpha = 16°$ converged simulations. The outcome of the DSE was analysed for the performance metrics IPR, IDC, IDR versus the geometric parameters.

Figure 5.10 shows the distribution of IDC, IDR, and IPR across the simulated pool. Looking at the IPR first, the figure highlights the presence of two regions, whose bounds are denoted by dashed lines. Between the two lines, only a limited number of individuals can be observed. The IPR is plotted as $(1 - IPR) \times 10$, representing the total pressure losses (0.1 equals to IPR=99%). The upper bound of the lower region fell at around 0.07, corresponding to an IPR of 0.993. The lower bound of the upper region was at around 0.1, corresponding to an IPR of 0.990. The distribution suggested, therefore, that total pressure losses at the AIP in excess of 0.1% were associated to worse individuals. This parameter alone, however, does not fully describe the flow quality, which must be correlated also to the distortion indexes. The IDC should allow to recognize a separated intake, when its value suddenly jumps up. Its distribution actually shows that again

two main regions could be identified, one with values close to zero, and one with values above 0.1. A similar pattern was found also for the IDR. In the present study, however, in order to speed up the already heavy computation, no intermediate converged solution at lower incidence was obtained, thus the gradient of the distortion metrics as a function of α could not be computed. In addition, the distinction in two regions was not completely clear and some points fell between the ideal boundaries.

In summary, it was not possible to discriminate good and bad geometries by looking at a single parameter. In practice, one might simply look at sufficiently high IPR values and distortion criteria below a predefined threshold, without really caring about the presence of a small separation. For the purpose of an automatic procedure, and given the fact that at take-off rotation a flow detachment appears undesirable, a criterium to recognise this event was sought. In the same figure, the right axis indicates the number of reversed faces on the AIP, that is the number of cell faces having a negative axial velocity. This parameter seemed to better correlate to the presence of a flow detachment, as it was more clustered. Therefore, it was used to help categorizing the individuals. Elements featuring a value lower than an empirically found threshold for the number of faces and with the other plotted metrics below 0.1 were marked as attached, and represented with filled symbols in the figure, whilst geometries exceeding the limits are plotted with empty symbols. In this way, only the first set was simulated at a higher incidence. This criterium did not completely exclude the presence of a small separation, but was meant to guarantee that, even if present, the measured flow quality was still acceptable.

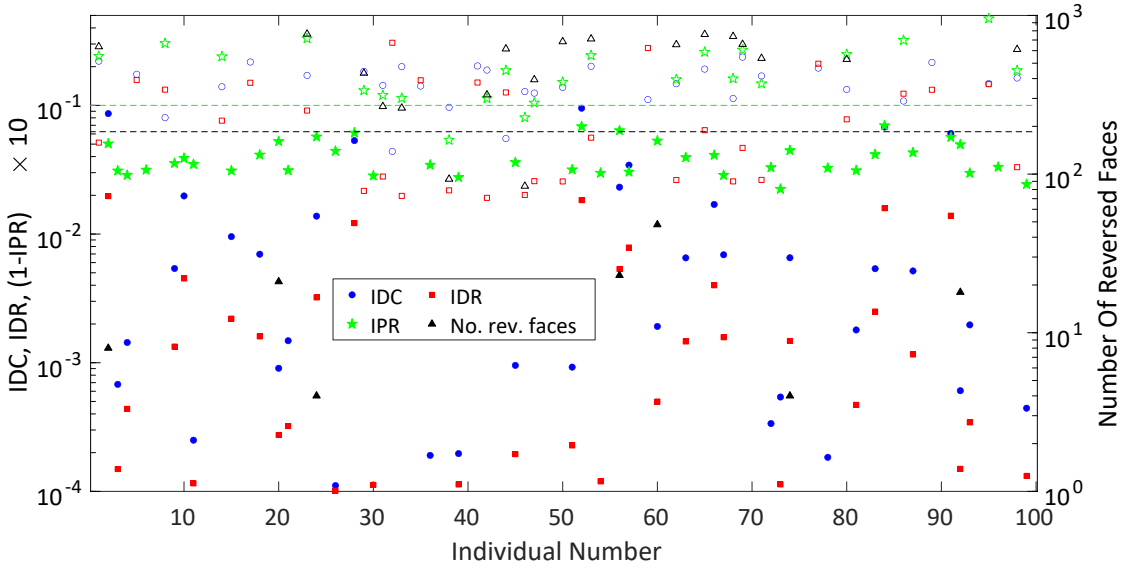

Figure 5.10: Metrics distribution across the simulated pool at $\alpha = 16°$.

With this classification, which is however case and mesh dependent, the association between the three performance metrics could be more easily examined. For instance, the total pressure loss of attached configurations was in most of the cases below 0.6%,

with only three points having a greater value, and anyway below the assumed 1% upper limit. The same held true for the IDC, where only three attached individuals featured a circumferential distortion above 0.07. The situation was less clear for the IDR, as in some cases it did not activate for shapes marked as separated. Individuals falling within this category featured at least one value between $(1 - IPR) \times 10$, IDC and IDR above the 0.1 threshold. For instance, individual number 32 had an IDC of 0.044, but and IDR of 0.3067, as a result of a bad shaping inducing an axisymmetric-like separation involving the full circle. Some other elements had all the values just close to the upper limit. Figure 5.11 compares the relative total pressure at the AIP for individuals number 31, 47, and 46. They did not pass the test because of a slightly higher than limit IDC, total pressure loss and number of reversed faces. The IDC of number 46 was close to that of 47 (0.1281 for the first, versus 0.1247 for the latter), but the IPR was higher in the first. Despite the measured distortion level was comparable, this last sample is visibly better from a qualitative point of view.

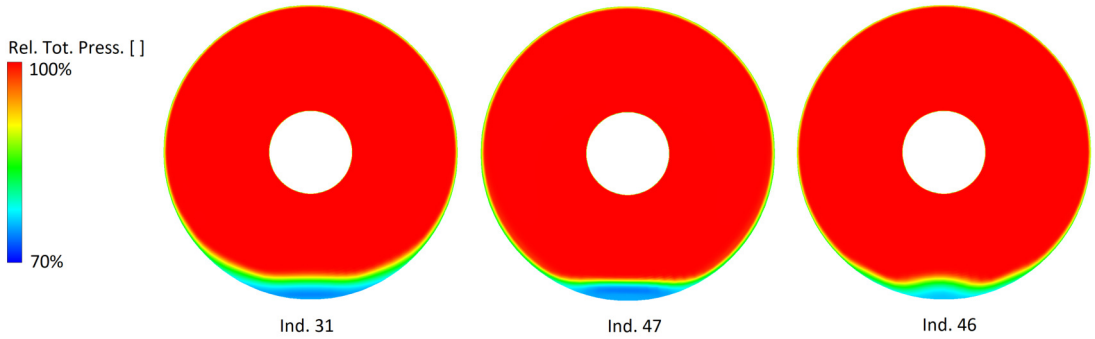

Figure 5.11: Comparison of relative total pressure at AIP for selected samples at $\alpha = 16°$.

Having established a criterium to separate the pool into two categorical groups, the correlation with the intake geometric variables was assessed. Figure 5.12 graphically displays the correlation matrix between the geometric ratios and the performance metrics. The correlation indexes plotted in red were statistically significant. Due to the constraints adopted in terms of intake length, highlight radius, and AIP inner and outer radius, some geometric ratios resulted to be correlated, like the CR and the DR, or the average diffusion angle (*diffa* in the figure) with both of the previous and the $f_{diffuser}$. In terms of performance metrics, the distortion indexes, being virtually binary variable, did not correlate with none of the geometric parameters, except for a weak trend found with the aspect ratio AR. Actually, this last variable appeared the one to be the most correlated with the others. The IDC and the IDR resulted to be highly linearly correlated, whilst a similar negative coefficient was found between them and the IPR, as expected. The IPR was found to correlate positively with the AR, and negatively with the $f_{diffuser}$ (these geometric variables were in turn linked). Despite no clear relationship between the metrics and the design variables could be derived, a tendency of IPR improvement over an extension of the diffuser length, associated to a reduction of lip aspect ratio and

average diffusion angle was observed.

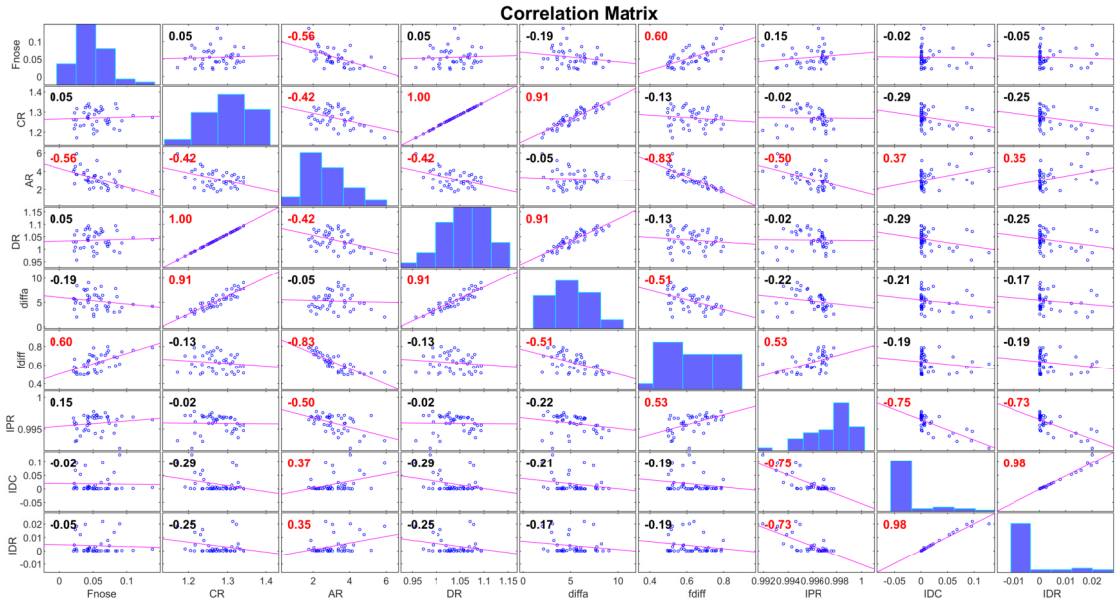

Figure 5.12: Geometric parameters and performance indexes correlation matrix for DSE at $\alpha = 16°$.

The relatively small dataset in the DSE prevented to extract additional information regarding the relation between the intake performance and the DVs. However, the feasible design space could be restricted, given the fact that some portions of the initial ranges were found without any attached solution. Table 5.2 summarizes the new search bounds for optimal shaping at $\alpha = 16°$, that can be used in following studies.

Table 5.2: Intake geometric variables range for attached inlet operation found in the DOE at $\alpha = 16°$.

Parameter	Lower Bound	Upper Bound
f_{nose}	0.02	0.11
CR	1.19	1.34
AR	1.175	5.0
DR	0.97	1.1
f_{throat}	0.2	0.5
avg θ_{diff} [deg]	2.0	9.0

The analysis of the individuals featuring an attached inlet flow was continued at $\alpha = 24°$. Figure 5.13 represents the distribution of the previous metrics, $(1 - IPR) \times 10$, IDC, and IDR. There appear a clearer clustering in two regions, with a threshold at around 0.1. 13 individuals out of 42 simulated fell below this limit for all the parameters, whereas when it was exceeded, large total pressure losses and distortion metrics were computed. Figure 5.14 shows the relationship between the geometric variables and the IPR, highlighting in blue those points entirely below the threshold, and in red those crossing it. By looking at the figure, the research bounds for an inlet operating without an overly separated flow and within an acceptable distortion level at $\alpha = 24°$ could be further restricted.

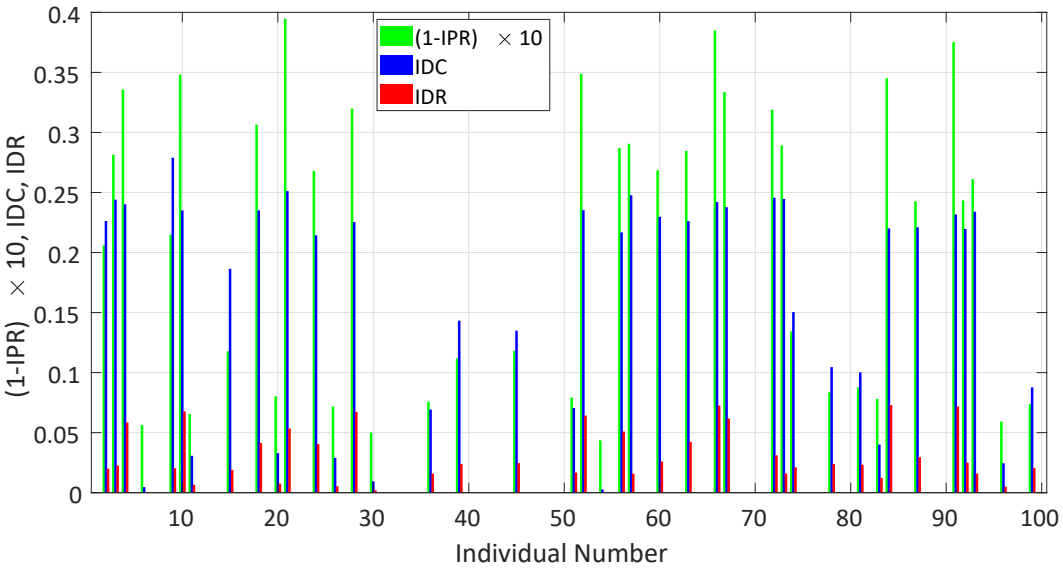

Figure 5.13: Metrics distribution for the individuals simulated at $\alpha = 24°$.

Finally, the best element of the DOE is compared to the baseline. Figure 5.15 shows the isentropic Mach number distribution on the internal cowls for the individual number 54 and the baseline, at both $\alpha = 16°$ and $\alpha = 24°$. At the lower incidence, the shock wave on the keel profile that was present in the baseline has disappeared, with a smoother deceleration up to the AIP. The throat Mach number resulted also lower for the sample, compared to the baseline (0.83 versus 0.90). At $\alpha = 24°$, a shock wave at a similar distance from the highlight was present in both the geometries, although the DOE element featured a lower Mach number peak of 1.4, compared to 1.5 of the baseline. The throat Mach number was quite close, around 0.86. Table 5.3 compares the performance metrics and the geometric parameters. The improvement of the flow deceleration on the bottom profile is associated to an increase of the lip aspect ratio and the contraction ratio, with a slightly thickening of the nose. However, the IPR of the baseline remained slightly better in both cases, possibly due to the lower average diffusion angle, affecting the boundary layer losses on the whole circumference.

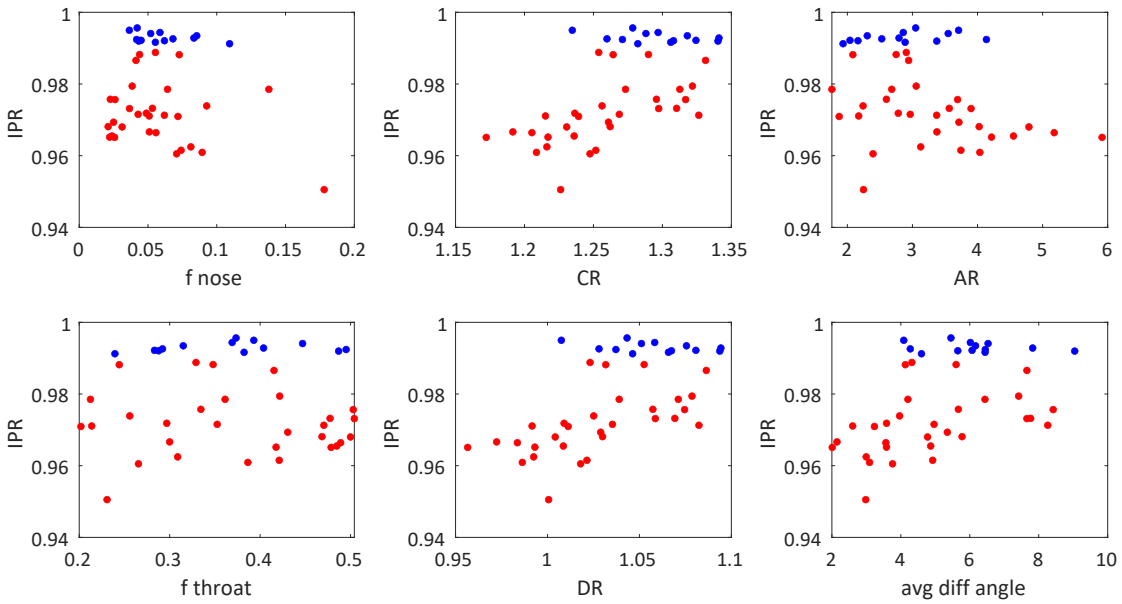

Figure 5.14: IPR vs. geometric parameters at $\alpha = 24°$. Points with all the metrics below 0.1 are depicted in blue, the others in red.

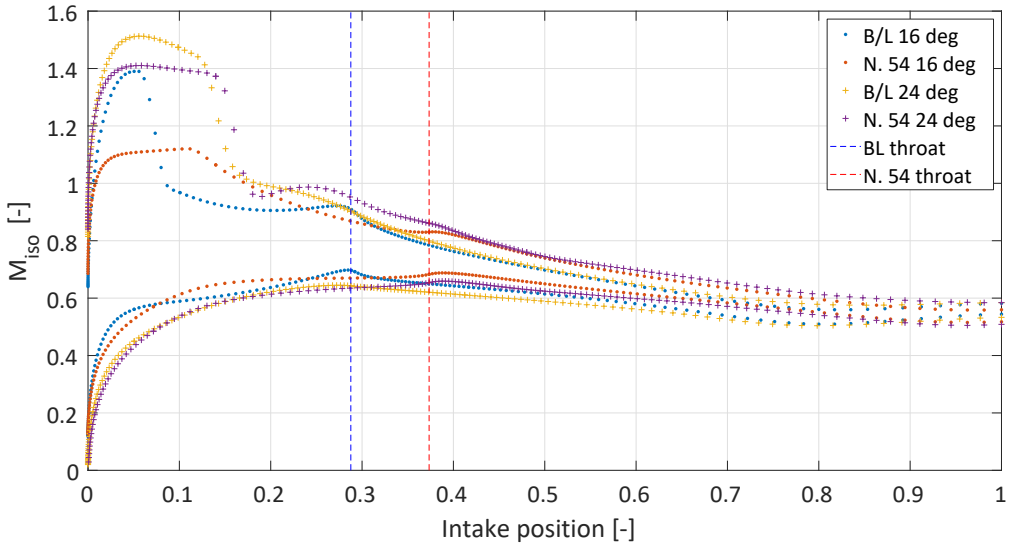

Figure 5.15: Isentropic Mach number distribution for baseline and best DOE sample at $\alpha = 16°$ and $\alpha = 24°$.

Table 5.3: Comparison between baseline and best DOE sample.

Parameter	baseline	best DOE
$IPR\ \alpha = 16°$	0.9976	0.9970
$IDC\ \alpha = 16°$	4.4E-04	3.3E-05
$IDR\ \alpha = 16°$	1.3E-04	1.2E-04
$IPR\ \alpha = 24°$	0.9980	0.9956
$IDC\ \alpha = 24°$	5.9E-03	2.7E-03
$IDR\ \alpha = 24°$	3.0E-03	3.4E-04
f_{nose}	0.0512	0.0421
CR	1.2648	1.2785
AR	2.4517	3.0500
DR	1.0321	1.0433
f_{throat}	0.2877	0.3734
avg θ_{diff} [deg]	4.3965	5.4538

BF results at $\alpha = 16°$

As mentioned above, the DOE pool was simulated at $\alpha = 16°$ also using the coupled approach, where the fan was represented via the body force model. Figure 5.16 summarizes the metrics distribution for the population. Although the outcome appeared similar to that of Figure 5.10 for the PN case, some differences can be highlighted. Starting from the IPR, its distribution was smoother and less distinct than in the previous case, with the total pressure losses at the AIP ranging from 0.3% to 2%. Conversely, the IDC was more clearly clustered, with almost no point falling within 0.01 and 0.03. In addition, it reached much lower values compared to the PN. An analogous distribution can be observed for the IDR, again showing netter bounds. As in Figure 5.10, the elements marked attached in the PN case are here represented with full symbols, the others with empty ones. Interestingly, none of the individuals featuring a separated intake flow in the PN approach were found to operate with a completely attached inlet with the BF, although the extent of the separation was smaller in this second case.

Figure 5.17 shows the absolute variation of the metrics from the BF to the PN. When examining the difference caused by a coupled fan/intake modelling, the boundary conditions must be assessed first. In the body force simulations, the static pressure was set at the fan outlet in order to retrieve the full stage engine mass flow rate, as it would be in a real case where the nozzle exit pressure determines the fan operating point for a given rotational speed. In case of extended separation, the fan might be unable to swallow all the desired mass flow, as this depends on the local features of the incoming flow. Metrics involving the average dynamic pressure, therefore, will be inherently different for this reason, and large deviations can indicate a different predicted flow field. About 20% of the BF simulations showed a significant variation of the average dynamic pressure, associated to a lower-than-target mass flow rate. The cases where this occurred

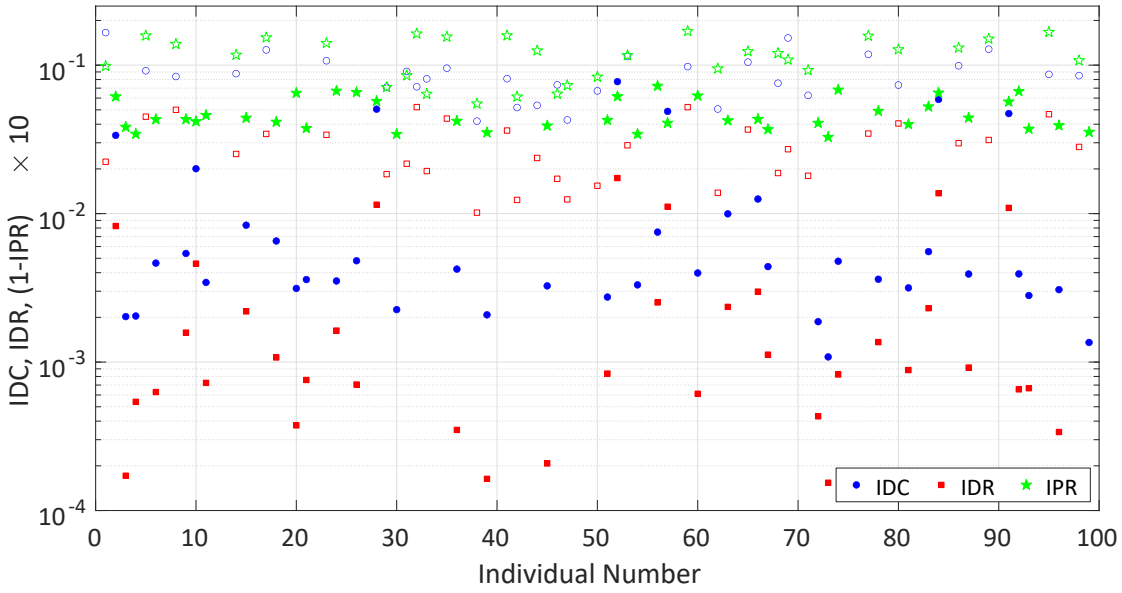

Figure 5.16: Metrics distribution across the simulated pool at $\alpha = 16°$ with the BFM.

were likely to be more sensitive to inlet/fan interaction and must be compared with the PN by restoring the mass flow equivalence. Therefore, when the mass flow of the BF simulation resulted to deviate too much from that of the baseline, this datum was use as input to rerun the PN case and conciliate the boundary conditions.

As visible in the figure, most of the variations were negative, especially in the case of separated intakes, again represented with empty bars. The ΔIDC exceeded -5% for most of individuals in this last group, with the maximum of -0.1363 for intake number 42. The IDR variation was instead more modest and was particularly large for number 8, 44, and 86. Among attached individuals, the IDC difference was also in general small. The intakes having a value close to the upper limit in the PN (e.g. 2, 52, 84, 91), see Figure 5.10, despite featuring a lower index here remained in the upper region.

Figure 5.18 compares the Mach number on a vertical plane for the element number 46, which was close to the upper limit for three out of four criteria in the PN case and was marked as separated due to a higher than 0.1 IDC. The Mach number distribution in the right figure highlights a flow detachment caused by a too small curvature of the front lip. The BF simulation in the left figure shows a smaller separated region and the tendency to flow reattachment close to the fan tip. The relative total pressure contours of Figure 5.19 shows that the bubble remained almost symmetrical in the BF, but with a lower radial penetration.

The total pressure at the AIP for individual number 2, that featured the largest IDC variation among those attached, is shown in Figure 5.20. Although small and confined, a separation bubble was present in the PN, whilst it was much attenuated in the BF. The geometry was marked attached, though, because the IPR was not overly penalised and the IDC was still below 0.1. As visible in Figure 5.21, the separation was induced by an

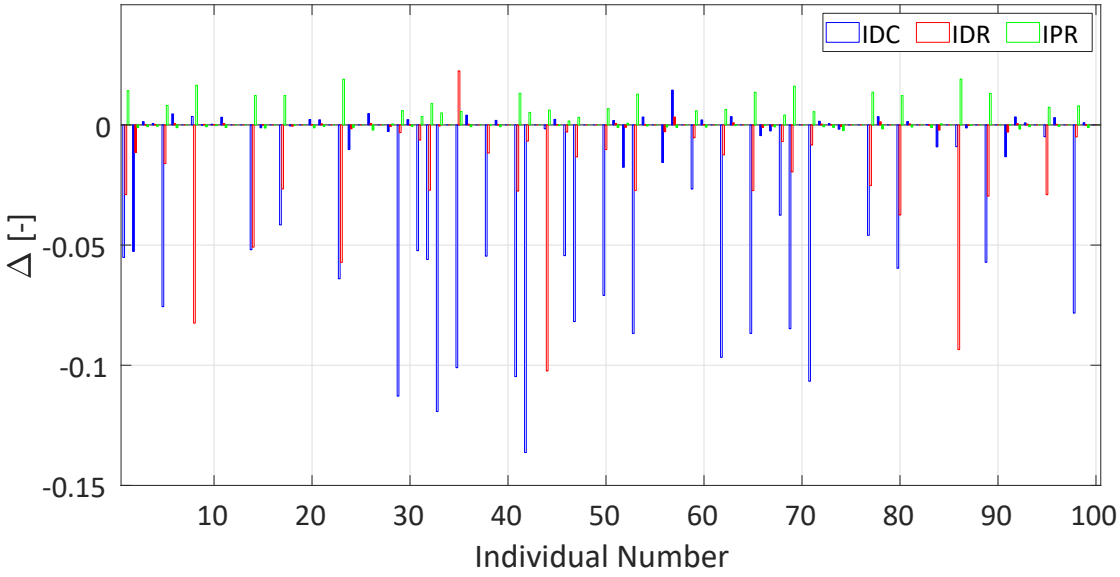

Figure 5.17: Absolute variation between BF and PN at $\alpha = 16°$.

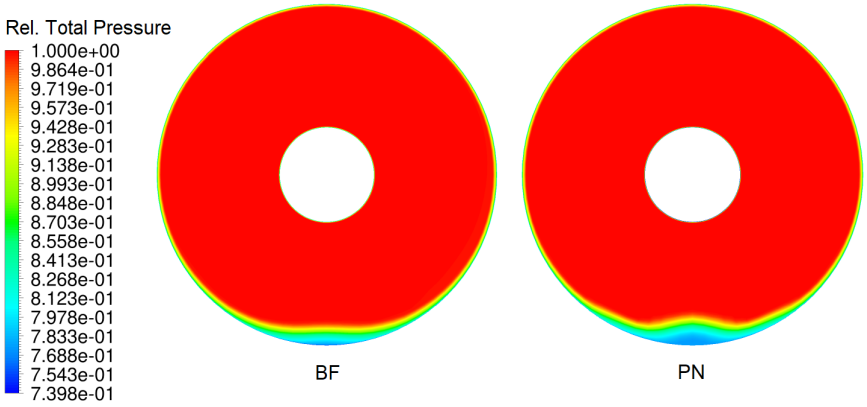

Figure 5.18: Comparison of total pressure distribution at AIP for individual no. 46 with BF and PN at $\alpha = 16°$.

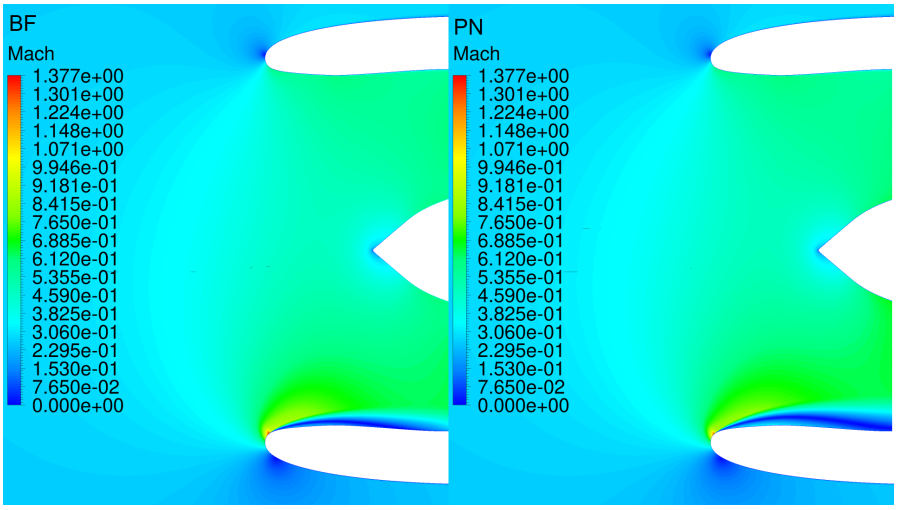

Figure 5.19: Comparison of Mach number distribution for individual no. 46 with BF and PN at $\alpha = 16°$.

excessive maximum diffusion angle, that the flow was not able to bear in the keel profile.

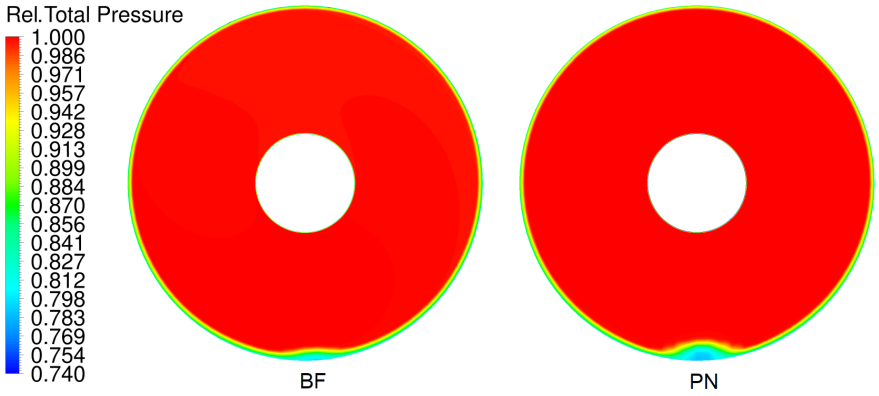

Figure 5.20: Comparison of total pressure distribution at AIP for individual no. 2 with BF and PN at $\alpha = 16°$.

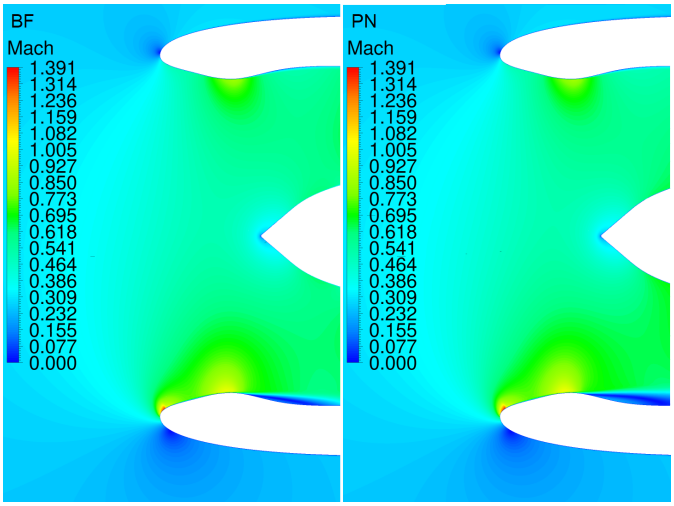

Figure 5.21: Comparison of Mach number distribution for individual no. 2 with BF and PN at $\alpha = 16°$.

5.5 Conclusions

The aerodynamics of intakes operating at high incidence conditions has been examined for a series of shapes in a preliminary DSE. The study was conducted with the standard decoupled approach first, at $\alpha = 16°$ and $\alpha = 24°$. The analysis of the distribution of the performance metrics across the simulated pool highlighted the presence of two major groups, one associated to better individuals featuring limited total pressure losses and distortion levels, and one with activated distortion indexes, indicating an inlet separation. A criterium to distinguish between these two qualitative groups has been devised based on the IPR, the IDC and the IDR indexes, in addition to the number of reversed faces at the AIP. The high level of interdependency of the geometric variables characterising the intake shape prevented to extract a clear figure of their relationship with the performance metrics, also given the relatively small dataset. However, the bounds where optimal geometries are likely to fall, for this specific intake design, have been restricted. Similar considerations have been reported for those individuals simulated at $\alpha = 24°$, where an analogous bivariate distribution for the metrics was found.

The employment of a coupled approach based on BFM has confirmed previous literature evidences related to the attenuating effect of the fan on the distortion level. The outcome of the coupled simulations at $\alpha = 16°$ was in agreement with that of the uncoupled case from a qualitative point of view, although the metrics were systematically shifted towards lower values. This agreement was found only by reconciliation of the boundary conditions, as the mass flow rate is not known a priori in the BFM approach, and it must be equally applied in PN simulations. In terms of flow field, the different separation extent and the non-uniformity at the AIP were evident. As anticipated in the

text, for this specific intake design with $L_{int}/D_{nac} > 0.35$, the presence of the fan was expected to have a primary influence on the flow field, but not much on the separation onset. The study confirmed that the inlets operating with a flow detachment in the PN equally presented a separation bubble in the BF, although much smaller. The effect on the separation incidence shall be assessed with the BFM also at the maximum lift point, and mostly for intakes featuring a shorter cowl, where the fan might allow to enlarge the feasible design space. The preliminary indications from the study are, anyway, useful for the future investigation of more aggressive designs and automatic optimisation of intake shapes.

Chapter 6

Conclusions

Body Force Models have arisen the interest of the scientific community due to the large saving of computational time that they can provide, compared to standard CFD approaches, in a large variety of situations where an active blade row modelling is needed, but not feasible using the direct approach simulating the solid blade walls. As described in chapter 1 and 2, in the framework of the 2050 environmental targets for the civil aviation sector, novel aircraft configurations with embedded propulsion, electric-driven fans and BLI engines are being considered, making the correct fan/airframe interaction an indispensable element for their design and analysis.

Important advances in the body force modelling field have been brought by recent fundamental works at the American MIT and French ISAE schools, where some undesired aspects of previous formulations have been overcome by new model equations and calibration procedures. Despite the new proposed solutions have improved the fidelity and they open to calibration-free force expressions, that are essential for the application in fan blade design, some aspects related to the actual implementation workflow, the impact of the calibration chain and the extent of reproducibility of local flow features remain unreported in the literature, being either not thoroughly studied or not publicly available.

The scope of this PhD programme was to shed light on these partially unknown issues and contribute to studying the applicability of the body force paradigm in fan/airframe coupling. The research stemmed from the need to clarify the best implementation practices, comparing theoretically equivalent approaches having different practical complexities and resolutions, and carry out a systematic comparison between the reference solution and the BFM simulations, in order to assess the reproducibility of relevant flow quantities and the limitations arising from the neglect of high-order terms in the model derivation. To this purpose, it was decided to develop a numerical platform granting the largest freedom in testing different algorithms and providing a basis for future standalone applications or extension to other CFD-based throughflow methods, with a more specific focus to the design. This numerical tool, named ANTARES, was developed from scratch and solves the compressible RANS equations in axisymmetric form. The workflow for its generation has been described in chapter 3, where the series

of successive advancements in complexity are reported and the correctness of the code is proven through several validation and verification cases.

With the availability of a flow solver, a common test case in the literature already used for BF assessment was first validated using standard CFD and then employed to study the BFM capabilities. It was the NASA/GEAE R4 stage, made up of a modern high BPR transonic rotor and OGVs, installed in a flight model nacelle. Chapter 4 reports the activities carried out to validate and examine the selected body force model, the L/D model of Thollet [251]. The first aspect considered regarded the calibration, that is the calculation of the coefficient distribution over the meridional blade surface that form the local force equation. By comparing the force extraction methods from the 3D CFD reference solution in terms of accuracy, resolution and implementation complexity, Kiwada's Blade Force Average resulted a good compromise for the normal force derivation, as it does not require local interpolation on the 3D blade surface and provides directly the 3D normal force vector components. A fully 3D normal force decomposition has been derived, in order to preserve the extracted force modulus and direction and include lean. The validity of the proposed decomposition was verified by the good replication of the radial components in BFM simulations. For the parallel force, instead, as suggested by Thollet, Marble's thermodynamic approach was found convenient from a numerical standpoint, although the entropy rise evolution is assumed a priori as linear, and this can lead to negative parallel force values near the endwalls, where streamline curvature can convect entropy outside the boundary layer and give a decrease from leading to trailing edge. In general, no arbitrary geometry modification or force alteration has been introduced. Conversely, the literature reports in some cases blade recambering or force redistribution as ways to improve the local accuracy. Whilst probably effective, this alteration is not known a priori and must be found empirically for each problem studied, which can make the calibration procedure more complicated.

The results obtained with the present BFM implementation appeared comparable to the others found in the literature in terms of overall performance metrics. The point-to-point correspondence of the circumferential-averaged CFD solution and the axisymmetric BFM simulation was analysed at the peak efficiency calibration point and also at off-design, i.e near choke and near stall. Whilst at the calibration point the local adherence of the two flow fields was remarkably good, at off-design the correspondence was found to be only integral for some flow variables. A discussion of the choking mass flow rate calibration procedure devised by the L/D model author has been given. This point represents a weakness of the model, as it is necessary to restore a good match at choking in integral terms, but it alters the flow development over the whole speedline and causes the loss of the local correspondence on the blade region. As a matter of fact, the assumed linear dependence of the normal force expressions on the relative flow angle might be valid only in the neighbourhood of the calibration point. The compressibility effects taking place at choking, with a large increase of the aerodynamic blockage and the complexity of the near stall operation appear to be of difficult inclusion into a semi-analytical expression. In other terms, the need for a lean model with a simple calibration procedure and a little dependency on external parameters has to

cope with some inevitable limitations. Overall, if the interest is primarily on the effect that the fan has on the flow development over the intake system, some deviations might be acceptable, as the model represents a sort of active boundary condition fully coupled to the incoming flow. Instead, for the purpose of blade design, differences in the local flow features are less tolerable. In addition to the effects of choke calibration, endwall flows have been found to be different from the reference solution. For the rotor, the discrepancy occurred at the blade tip, where no force was put inside the tip gap. The complexity of the phenomena associated with tip leakage, the presence of additional terms not modelled, like circumferential and mixing stresses, and the reported sensitivity of the normal force treatment on the machine stability make the task of faithfully replicating the tip flow extremely challenging. For the stator, the deviation was found as an excessive hub separation. Attempts to improve the modelling in both these zones by altering the force distributions were unsuccessful, leaving room for future research.

Apart from these regions, the comparisons made between circumferential-averaged CFD and BFM solutions in the variety of the NASA R4 configurations studied, from ducted rotor alone to full stage into an isolated nacelle, were satisfactory. The good duplication of both the external and the internal flow field makes the BFM a possible candidate to study installed engine. In fact, as described in the chapter 1, also in typical aircraft configurations the adoption of UHBPR turbofans rises the question whether a classic engine-decoupled approach is sufficient to evaluate the mutual effects of installation on the airframe and the propulsor operation. On the airframe side, the use of BFM for short intake design has been already reported in the literature. In chapter 5 a dedicated analysis on intake flows is reported, with the purpose of putting the basis for future automatic optimisation of intake shape using the coupled approach, which gives different results from a decoupled model as the intake length is reduced, according to the literature.

In conclusion, the research has contributed to highlight some aspects of the chosen body force model that were not completely clear and pave the way to future elaborations. From an implementation point of view, the pre-processing phase is quite involved and requires a certain time investment before being able to build the coefficient distributions on the blade surface. If properly calibrated, the model has proven to be able to capture the overall inlet/outlet evolution of the flow variables and replicate circumferential-averaged spanwise profiles with good accuracy, especially close to the force extraction point. This opens to the possibility of employing it in coupled airframe/engine simulations, where a standard pressure boundary leads to unphysical results, such as in the case of short or S-shaped intakes. Moreover, the replication of radial profiles makes the model interesting even for studying the jet/airframe interaction in standard wing-mounted turbofan, where the tighter installation foreseen for UHBPR units makes the jet cross-distribution likely to be more important, in particular when interfering with the high-lift surfaces. The double nature of the method, that allows to derive information both on the external flow and the turbomachinery behaviour, makes the list of potential applications countless. From the point of view of the engine operation, it has been applied to study the response to inlet distortions, proving to being able to replicate many

features that are found in unsteady RANS simulations. Although not directly considered in this study, the design of distortion-tolerant fans represents another field where the low computational cost of the model could help in the design space exploration and identification of suitable geometries for future BLI engines.

Appendices

Appendix A

Finite Volume Method

A.1 Finite Volume Method

The application of FVM is straightforward, as it involves the integration of a differential equation over a portion of the computational domain. Let us consider a system of conservation laws, as it is the compressible Navier-Stokes equations of fluid dynamics, written in integral conservation form:

$$\frac{\partial \vec{\mathbf{U}}}{\partial t} + \vec{\nabla} \cdot \overline{\overline{\mathbf{F}}}_c = \vec{\nabla} \cdot \overline{\overline{\mathbf{F}}}_d \tag{A.1}$$

where:

$$\vec{\mathbf{U}} = \begin{Bmatrix} \rho \\ \rho u \\ \rho v \\ \rho w \\ E \end{Bmatrix} \qquad \overline{\overline{\mathbf{F}}}_{c_{ij}} = \rho u_i u_j + \delta_{ij} p \qquad \overline{\overline{\mathbf{F}}}_d = 2\mu \frac{1}{2}(\vec{\nabla}\vec{\mathbf{V}} + \vec{\nabla}\vec{\mathbf{V}}^T) - \frac{2}{3}\mu \vec{\nabla} \cdot \vec{\mathbf{V}}\, \overline{\overline{I}} \tag{A.2}$$

Integration over the finite volume Ω leads to:

$$\int_\Omega \frac{\partial \vec{\mathbf{U}}}{\partial t} d\Omega + \int_\Omega \vec{\nabla} \cdot \overline{\overline{\mathbf{F}}}_c d\Omega = \int_\Omega \vec{\nabla} \cdot \overline{\overline{\mathbf{F}}}_d d\Omega \tag{A.3}$$

For a stationary volume and applying divergence theorem:

$$\frac{\partial}{\partial t} \int_\Omega \vec{\mathbf{U}} d\Omega + \oint_{\partial\Omega} \overline{\overline{\mathbf{F}}}_c \cdot \hat{n} dA = \oint_{\partial\Omega} \overline{\overline{\mathbf{F}}}_d \cdot \hat{n} dA \tag{A.4}$$

The surface integral can be replaced by a summation over the faces f enclosing the finite volume Ω:

$$\frac{\partial}{\partial t} \int_\Omega \vec{\mathbf{U}}\, d\Omega + \sum_{f \in \Omega} \oint_f \overline{\overline{\mathbf{F}}}_c \cdot \hat{n}\, dA_f = \sum_{f \in \Omega} \oint_f \overline{\overline{\mathbf{F}}}_d \cdot \hat{n}\, dA_f \tag{A.5}$$

So far the equations have remained exact. The fundamental of the method is the replacement of exact fluxes $\overline{\overline{\mathbf{F}}} \cdot \hat{n}$ integrated over the faces with an approximate value, obtained through a numerical integration formula at quadrature points q_i with weights ω_i:

$$\oint_f \overline{\overline{\mathbf{F}}} \cdot \hat{n} \, dA_f = \sum_{q_i \in f} \left[\omega_i \overline{\overline{\mathbf{F}}} \cdot \hat{n} A \right]_{q_i} \tag{A.6}$$

The choice of the quadrature formula determines, among others, the accuracy of the method. For a simple mean value integration with q_i located in the centre of the face and $\omega_i = 1$, one has a second order accurate method. Higher order discretisation can be obtained using more integration points and Gauss-Lobatto rule, for instance. However, since flux computation has the largest computational cost in FVM, high-order discretisations are extremely heavy and can be obtained more cheaply with FDM or FEM approach, thus in practice most FVM are limited to second order accuracy. With the flux approximation, which must be further disclosed, one gets the so-called semi-discretised equation, where the time derivative term still holds:

$$\frac{\partial}{\partial t} \int_\Omega \vec{\mathbf{U}} d\Omega + \sum_{f \in \Omega} \left[\overline{\overline{\mathbf{F}}}_c \cdot \hat{n} A \right]_f = \sum_{f \in \Omega} \left[\overline{\overline{\mathbf{F}}}_d \cdot \hat{n} A \right]_f \tag{A.7}$$

By defining the mean cell value of the conserved quantity ϕ in cell Ω as:

$$\overline{\phi} = \frac{1}{\Omega} \int_\Omega \phi \, \partial\Omega \tag{A.8}$$

one gets:

$$\frac{\partial}{\partial t} \vec{\overline{\mathbf{U}}} \, \Omega + \sum_{f \in \Omega} \left[\overline{\overline{\mathbf{F}}}_c \cdot \hat{n} A \right]_f = \sum_{f \in \Omega} \left[\overline{\overline{\mathbf{F}}}_d \cdot \hat{n} A \right]_f \tag{A.9}$$

This expression is meaningful and reflects the whole physics of the conservation law, which is directly embedded into the method: the variation of the conserved mean quantity $\overline{\mathbf{U}}$ in the volume Ω is determined by the balance of the flux through its boundary $\partial\Omega$, made up of a closed patch of faces. If the flux balance is null, the time derivative vanishes and the quantity remains constant. If $\dfrac{\partial \mathbf{U}}{\partial t} = 0, \ \forall t$ the solution is stationary and steady-state is reached. Hereafter, the mean cell quantity will be indicated without the bar, to keep a lean notation.

A.2 Domain geometric discretisation

The discretisation procedure, as it has been highlighted, corresponds to a geometric discretisation: the computational domain is divided into a set of sub-domains, in each of which the integral conservation law is enforced. Considering a stationary solution, this equates to computing the value of a flow quantity $\phi = \phi(x, y, z)$ at a discrete number of points $\mathbf{x} = \{\mathbf{x}_i = (x, y, z)_i\}$ on its spatial domain. The division of the computational

domain into patches originates a geometric and functional hierarchy. The deriving tree is important in establishing the relationship between the entities involved in the discretisation and calculation and must be codified somehow into each numerical solver dealing with generic domains.

The locations at which evolved quantities are stored and known determines the type of the FVM: cell-centred or node-centred. In the first class, the variables are known at the cell centroid and represent the cell average. In the second class, they are stored on the vertex of the grid and an auxiliary control volume formed by the centroid of the cells sharing that vertex, referred to as median-dual volume, is used. None of the approaches exhibits a net advantage over the other. The first one is somehow more natural, as it reflects the discretisation procedure, but it is more sensitive to grid distortion than cell-vertex median dual schemes, which suffers in contrast at sharp corners or points shared by multiple grids. The flow solver here developed employs the cell-centred approach. In equation A.8, the cell average $\overline{\phi}$ in general agrees with the value of $\phi\left(x,t\right)$ at the centre of the interval to $\mathcal{O}\left(\Delta x^2\right)$ [151], which must be considered when constructing higher-order schemes [156].

A.3 Flux calculation procedure

Before further examining the advancement of the solution in time, it is worth disclosing the main task of a FVM, which is flux calculation. Back to Navier-Stokes equations, $\overline{\overline{\mathbf{F}}}_c$ and $\overline{\overline{\mathbf{F}}}_d$ refer to the convective and diffusive flux tensors, respectively. The flux per unit area at point q is thus computed as $\mathbf{F}(\vec{\mathbf{U}}_q) = \overline{\overline{\mathbf{F}}}(\vec{\mathbf{U}}_q)\cdot\hat{n}_q$. In addition to a quadrature rule for the calculation of the flux integral over the faces of control volume, another approximation is introduced, which is the concept of numerical flux function. In fact, the functional $\tilde{\mathbf{F}}$ used to calculate flux at quadrature points q_i can differ from the physical flux $\mathbf{F}$ and represents some sort of approximation:

$$\mathbf{F}_{q_i} = \mathbf{F}(\vec{\mathbf{U}}_{q_i}) = \tilde{\mathbf{F}}_{q_i} \tag{A.10}$$

For any particular choice of $\tilde{F}$ a discretisation scheme results. The nature of the numerical flux function, therefore, can determine the order of convergence and the accuracy of the method. In general, the numerical flux function depends on a series of states evaluated at specified points:

$$\tilde{F}_i = \tilde{F}(U_{i-m},\ldots,U_i,\ldots,U_{i+n}) \tag{A.11}$$

The consistency of the method requires it replicates the physical flux at state U when computed at states U_i all equal to U:

$$\tilde{F}(U_i,U_i,\ldots,U_i) = F(U_i) \tag{A.12}$$

The numerical flux function differs according to the type of flux considered, in our case the convective and diffusive flux, and should mimic its physical counterpart. Without entering into the multitude of discretisation schemes available for hyperbolic and

elliptic equations, here the methods employed for the convective and diffusive fluxes will be only reported. The set of states U_i upon which the numerical flux $\tilde{F}_i$ depends is called the stencil of the scheme. Intuitively, the larger the stencil, the more accurately the flux will approximate the real one. Moreover, depending on the distribution of the stencil, one can have central schemes, with an equal number of points on all sides of the quadrature point, or one-sided schemes, which in the case of convective fluxes become upwind or downwind, according to the flow direction. The choice of the type of scheme is related to the nature of the phenomenon and to accuracy, stability and consistency.

In the following, the flux schemes used in the developed solver for the convective and the diffusive part will be treated separately, given their different nature and complexity.

A.3.1 Convective flux

The convective flux $\mathbf{F}_c = \overline{\overline{\mathbf{F}}}_c \cdot \hat{n}$ is expressed in the one-dimensional case as:

$$\mathbf{F}_c = \left\{ \begin{array}{c} \rho u \\ \rho u u + p \\ (E+p)u \end{array} \right\} \tag{A.13}$$

The inviscid Navier-Stokes equations are best known as the Euler equations, that form a system of hyperbolic conservation laws. The hyperbolicity in time of the Euler equations relates to the fact that the eigenvalues of the convective flux Jacobian $[\mathbf{A}](\vec{\mathbf{U}}) = \dfrac{\partial \vec{\mathbf{F}}}{\partial \vec{\mathbf{U}}}$ are all real and distinct in one dimension, as long as the speed of sound remains positive. The hyperbolicity of the equations expresses the propagation of information along waves travelling at finite speed. Useful reads for numerical solution of hyperbolic systems of conservation laws are Toro [262], Leveque [151], Pirozzoli [206]. This fundamental property has important consequences on the numerical schemes used to approximate the flux function and it justifies the employment of time marching methods also for steady-state solution. The directional propagation leads naturally to one-sided schemes, and in particular to upwind ones, for numerical stability. In the finite volume context, the calculation of the flux at grid face $i+1/2$, shared between cells i and $i+1$, can be carried out in the Flux Difference Splitting (FDS) approach considering the Riemann problem arising at the face [18], where one wants to compute the solution of the initial value problem given by two initial discontinuous states separated at the local space axis, coincident with the face location $x_{i+1/2}$. In this context, the numerical flux function assumes the role of a Riemann solver, which in practice will give an approximate result, since the analytical solution for 1D Euler equations is known, but too expensive to be computed, and is more conveniently solved in an approximate way. The Riemann solver operates by taking the two discontinuous values at both sides of the face, often referred to as the left and right states, and giving the convective flux:

$$\mathbf{F}_{i+1/2} = \tilde{\mathbf{F}}(\mathbf{U_L}, \mathbf{U_R}) \tag{A.14}$$

The left and right states must be extrapolated from the respective cell centre to the face, and are denoted boundary extrapolated values. This operation is called solution recon-

struction and sets the theoretical order of the scheme. For constant extrapolation one has a first order scheme, for linear reconstruction a second order one and so on. In the present implementation, the first-order Godunov scheme, Roe's solver [216] and Toro's HLLC [262] are available. The approximate solvers employ linear reconstruction, which makes them second order accurate on smooth solutions.

The Riemann solver of Roe is a flux-difference scheme, which is based on the linearisation of the flux Jacobian around a reference state, computed using a specific averaging technique. The methods can be shown to amount to a central scheme with a numerical dissipation based on the Roe average Jacobian $|\tilde{\mathbf{A}}|$:

$$\mathbf{F}_{i+1/2} = \tilde{\mathbf{F}}(\mathbf{U_L}, \mathbf{U_R}) = \frac{1}{2}\left(\mathbf{F}(\mathbf{U_L}) + \mathbf{F}(\mathbf{U_L})\right) - \frac{1}{2}|\tilde{\mathbf{A}}|\left(\mathbf{U_L} - \mathbf{U_R}\right) \tag{A.15}$$

The HLLC solver of Toro is based on elementary wave decomposition of the Riemann problem employing all the three kinds of shock, expansion and contact discontinuities. The Godunov intercell flux is computed once estimates of wave speeds have been provided, using alternatives formulations. See [262] for a complete description.

Note that these numerical flux functions have been derived in the one-dimensional case, but are commonly used in general dimensions, as the flux across an intercell boundary is regarded as a locally 1D problem. For non Cartesian grids, the rotational invariance of the Euler equations is exploited. In fact, it can be shown that the three-dimensional flux

$$\overline{\mathbf{F}}\left(\mathbf{U}\right) \cdot \hat{n} = \left[\mathbf{T}\right]^{-1} \overline{\mathbf{F}}\left(\left[\mathbf{T}\right]\mathbf{U}\right) = \left[\mathbf{T}\right]^{-1} \overline{\mathbf{F}}\left(\mathbf{U_n}\right) \tag{A.16}$$

where $[\mathbf{T}] = [\mathbf{T}](\hat{n})$ is the rotation matrix from the reference frame to a frame with the abscissa lying on the normal direction and the ordinate in the tangential direction (i.e. along the face).

A.3.2 Diffusive flux

The viscous part of the Navier-Stokes equations corresponds to a diffusive flux, which must be again computed at the intercell boundary. The elliptic nature of diffusion, represented by the steady Poisson equation $\nabla^2\phi = 0$, makes central schemes suitable to approximate the state at cell face. The computation of the viscous flux reduces to approximating the gradient of velocity and temperature at the face. Whilst simple arithmetic average of cell-centre gradients can be sufficient in smooth and equispaced grids, for typical problems adding more terms helps increasing the resolution and stability [124, 181]. In the current implementation, the formula given in equation 3.4 is used for gradient approximation on the face.

A.4 Gradient reconstruction

As become evident above, when briefly presenting the flux calculation procedure, the solution must either be extrapolated from the point where it is evolved to the quadrature points where flux is to be computed, or the gradient of the solution must be known

for diffusive flux. Gradient reconstruction constitutes a key and heavy task in a finite volume solver. Considering a two-dimensional case, the solution around a point (x_i, y_i) can be expressed in Taylor series up to a desired accuracy:

$$\begin{aligned}\phi(x_i, y_i) \approx \tilde{\phi}(x_i, y_i) = \phi|_i + \left.\frac{\partial \phi}{\partial x}\right|_i (x - x_i) + \left.\frac{\partial \phi}{\partial y}\right|_i (y - y_i) \\ + \frac{1}{2}\left.\frac{\partial^2 \phi}{\partial x^2}\right|_i (x - x_i)^2 + \frac{1}{2}\left.\frac{\partial^2 \phi}{\partial y^2}\right|_i (y - y_i)^2 + \\ \frac{1}{2}\left.\frac{\partial^2 \phi}{\partial x \partial y}\right|_i (x - x_i)(y - y_i) + \mathcal{O}(x^3, y^3)\end{aligned} \quad \text{(A.17)}$$

For a second order scheme, squared terms can be neglected and a reconstructed value is simply:

$$\phi_j = \phi(x_j, y_j) = \phi(x_i, y_i) + \nabla\phi|_i \cdot (x_j - x_i, y_j - y_i) \quad \text{(A.18)}$$

A.4.1 Green-Gauss gradient reconstruction

The Ostrogradskij or Green-Gauss theorem can be directly applied to estimate the gradient of a cell value:

$$\nabla\overline{\phi} = \frac{1}{V}\int_\Omega \nabla\phi \, dV = \frac{1}{V}\int_\Omega \nabla \cdot \phi \mathbf{I} \, dV = \frac{1}{V}\oint_{\partial\Omega} \phi \, \hat{n} \, dA \quad \text{(A.19)}$$

The formula uses the same calculation method of the other fluxes and can reuse most the structure of the core solver. The function value at the face centre can be obtained by linear interpolation of cell values:

$$\phi_{ij} = g_c \, \phi_i + (1 - g_c) \, \phi_j, \qquad g_c = \frac{|r_{iF}|}{|r_{iF} + r_{jF}|} \quad \text{(A.20)}$$

A.4.2 Least Square Gradient reconstruction

The least square gradient reconstruction [186] is a conservative reconstruction technique applicable to generic grids. It is based on a Taylor expansion of the mean cell gradient and requires the solution of a constrained overdetermined system of equations. Considering the Taylor series of the two-dimensional field ϕ of equation A.17, conservation of the mean requires:

$$\overline{\phi_i} = \frac{1}{\Delta A_i}\int_{\Omega_i} \tilde{\phi}_i dA \quad \text{(A.21)}$$

Substituting the reconstructed value $\tilde{\phi}_i$ in the integral, one obtains:

$$\overline{\phi}_i = \phi|_i + \left.\frac{\partial \phi}{\partial x}\right|_i \overline{x}_i + \left.\frac{\partial \phi}{\partial y}\right|_i \overline{y}_i + \frac{1}{2}\left.\frac{\partial^2 \phi}{\partial x^2}\right|_i \overline{x^2}_i + \frac{1}{2}\left.\frac{\partial^2 \phi}{\partial x^2}\right|_i \overline{y^2}_i + \frac{1}{2}\left.\frac{\partial^2 \phi}{\partial x \partial y}\right|_i \overline{xy}_i + \ldots \quad \text{(A.22)}$$

The geometric moments are computed as:

$$\overline{x^m y^n} = \frac{1}{A_i} \int_{\Omega_i} (x - x_i)\,(y - y_i)\,dA \tag{A.23}$$

In addition to conservation of the mean value of cell i, also the reconstruction error in the neighbouring cells must be minimised. Imposing this condition quickly results into an overdetermined set of equations, as the unknown gradient terms, up to k_{th} order, are less than the number of equations, coming from the fact that adding more neighbours in the reconstruction stencil makes it more robust and accurate, in presence of non smooth grids and fields. Applying conservation of the mean for a neighbour cell j, one gets to the following expression:

$$\begin{aligned}\overline{\phi}_j = \phi_i + \left.\frac{\partial \phi}{\partial x}\right|_i (\overline{x}_j + (x_j - x_i)) + \left.\frac{\partial \phi}{\partial y}\right|_i \left(\overline{y}_j + (y_j - y_i)\right) + \\ \frac{1}{2}\left.\frac{\partial^2 \phi}{\partial x^2}\right|_i (\overline{x}_j + (x_j - x_i))^2 + \frac{1}{2}\left.\frac{\partial^2 \phi}{\partial x^2}\right|_i \left(\overline{y}_j + (y_j - y_i)\right)^2 + \\ \frac{1}{2}\left.\frac{\partial^2 \phi}{\partial x \partial y}\right|_i \left(\overline{y}_j + (y_j - y_i)\right)\left(\overline{y}_j + (y_j - y_i)\right) + \dots\end{aligned} \tag{A.24}$$

The final system of equations is obtained by collecting together all these error minimisation relations. By defining:

$$\widehat{x^n y^m}_{ij} = \frac{1}{A_j} \int_{\Omega_j} ((x - x_j) + (x_j - x_i))^n + ((y - y_j) + (y_j - y_i))^m dA \tag{A.25}$$

the system reads, for a second order reconstruction, neglecting higher than first order derivatives:

$$\begin{bmatrix} 1 & \overline{x}_i & \overline{y}_i \\ w_{i1} & \hat{x}_{i1} & \hat{x}_{i1} \\ w_{i2} & \hat{x}_{i2} & \hat{x}_{i2} \\ \vdots & \vdots & \vdots \\ w_{in} & \hat{x}_{in} & \hat{x}_{in} \end{bmatrix} \left\{ \begin{array}{c} \phi \\ \overline{\frac{\partial \phi}{\partial x}} \\ \overline{\frac{\partial \phi}{\partial x}} \end{array} \right\} = \left\{ \begin{array}{c} \overline{\phi}_i \\ w_{i1}\overline{\phi}_1 \\ w_{i2}\overline{\phi}_2 \\ \vdots \\ w_{in}\overline{\phi}_n \end{array} \right\} \tag{A.26}$$

and has two unknowns and n equations, as many as the size of the stencil. The first row can be removed by Gauss elimination, the remaining system solved either directly using Moore-Penrose pseudo inverse, with Singular Value Decomposition (SVD) to avoid problems for ill-conditioned matrices [124], or also QR factorisation via Hoseholder transformation [182]. The terms w_{ik} are weights that highly improve the reconstruction in non-regular and unstructured grids. They can be computed in a variety of ways, with inverse distant weighting the most popular:

$$w_{ik} = \frac{1}{|\mathbf{r}_i - \mathbf{r}_j|^q},\ q \geq 1 \tag{A.27}$$

Whilst this is standard practice, to distinguish the method from its first variants, the literature sometimes refers to it as weighted least square. In the current implementation, to avoid storing the pseudo-inverse matrix, that is mesh-dependent and not varying for fixed domains, but requires at least 8 double precision real per elements, only the geometric moments are computed at the code entry and are reused every time to form the system, which reduces to a square one in two dimensions for second-order reconstruction.

A.5 Time discretisation

The choice of a flux discretisation for equation 3.1 gives an ordinary differential equation (ODE) in time:

$$\Omega \frac{\partial}{\partial t}\mathbf{U} = -\sum_{f\in\Omega}\left[\mathbf{F}_c \cdot \hat{n}A\right]_f + \sum_{f\in\Omega}\left[\mathbf{F}_d \cdot \hat{n}A\right]_f = \mathbf{R}\left(\mathbf{U}\right) \tag{A.28}$$

where the fluxes can be summarised by the right hand side of the equation and $\mathbf{R}\left(\mathbf{U}\right)$ is called the residual. The nonlinear ODE can be solved using any of the standard methods, provided that they possess the required numerical stability. In fact, some combinations of flux discretisation schemes and time marching techniques are unconditionally unstable and cannot be used. A classical example is the forward-in-time, centred-in-space (FTCS) discretisation of the 1D linear advection equation

$$\frac{u_{n+1} - u_n}{\Delta t} + a\frac{u_{i+1} - u_{i-1}}{2\Delta x}$$

The stability of a scheme can be studied using the von Neumann analysis, which is based on the assumption of a periodic solution in space. For a thorough discussion of numerical stability, see Hirsch [107]. Qualitatively, it can be stated that *the domain of dependence of the differential equation should be entirely contained in the numerical domain of dependence of the discretised equations*. This poses a limitation in the choice of the time step of the time marching technique, which is expressed by a maximum allowed Courant-Friedrichs-Lewy (CFL) number:

$$CFL = a\frac{\Delta t}{\Delta x} \tag{A.29}$$

where a is the advection velocity.

A.5.1 Explicit Runge-Kutta method

Runge-Kutta methods are a class of numerical algorithms for ODE. They are based on the idea of evaluating the residual at several intermediate steps between t^n and t^{n+1} and combine them to advance the solution. Each intermediate step is called stage, and

a k-stage method can be written in general as:

$$U^{(1)} = U^n \tag{A.30}$$

$$U^{(k)} = U^{(1)} + \Delta t \sum_{j=1}^{k-1} \alpha_{jk} R^{(j)} \tag{A.31}$$

$$U^{(n+1)} = U^{(n)} + \Delta t \sum_{j=1}^{k} \beta_j R^{(j)} \tag{A.32}$$

The algorithm depends upon the coefficients α_{jk} and β_j. In the above formulation, however, all the intermediate residuals contribute to the solution at next time level, with a high memory overhead. Low storage forms have then been devised, written as:

$$U^{(1)} = U^n \tag{A.33}$$

$$U^{(k)} = U^{(1)} + \Delta t \alpha_k R^{(k-1)} \tag{A.34}$$

$$U^{(n+1)} = U^{(n)} + \Delta t \sum_{j=1}^{k} \beta_j R^{(j)} \tag{A.35}$$

$$\tag{A.36}$$

with $\sum_{j=1}^{k} \beta_j = 1$ and often $\beta_k = 1, \beta_j = 0, j < k$.

A popular method is the three-stage, third order TVD scheme of Shu and Osher [89], 3.10, with a maximum CFL of $1/n_d$, where n_d is the dimension of the problem.

A.5.2 Implicit time stepping

In the implicit time stepping method, the newly searched solution at next time level is written as an implicit equation that cannot be readily inverted, if not solving a linear system. Consider for instance the first-order backward Euler method:

$$\frac{u^{n+1} - u^n}{\Delta t} = R(u^{n+1}) \tag{A.37}$$

The residual being expressed at unknown time level, it is not possible to directly explicit the solution u^{n+1} and the equation must be solved using an appropriate method. Before elaborating more on how to solve it, the notation must be made clearer.

Referring to a system of conservation laws, such is the Navier-Stokes equations, the above expression holds for each cell in the discretised domain. The solution u actually is a vector of five components in three dimensions and correpsonds to the conserved variable $\mathbf{U}_i$ in the cell i. The residual R^{n+1} is actually again a five component vector in 3D, with the right hand side of each solved scalar equation in cell i: $\mathbf{R}_i$. Now, the residual includes the convective and diffusive fluxes, plus any source term. It is a function, through the numerical scheme, of the solution values in the cells forming the stencil. If the scheme is linear, then $\mathbf{R}$ is a linear combination of the cell values involved in the

computational molecule for cell i into consideration. Thus, for each cell a linear equation can be written and advancing the solution at $n+1$ requires solving a linear system. The system matrix is sparse and banded and a variety of iterative methods can be applied to invert it. If either the schemes used to form the residual are non-linear or the source terms are, then $\mathbf{R}_i$ is a nonlinear combination of all the variables involved in the computational stencil. It can be written as:

$$\mathbf{R}_i^n = \mathbf{R}\left(\mathbf{U}_{i-k}^n, \dots, \mathbf{U}_i^n, \dots, \mathbf{U}_{i+m}^n\right) \tag{A.38}$$

For higher order schemes, it is also function of the limited gradients of the conservative variables:

$$\mathbf{R}_i^n = \mathbf{R}\left(\mathbf{U}_j^n, \nabla\mathbf{U}_j^n, \psi_j, \dots\right) \tag{A.39}$$

In order to solve the nonlinear equation for the cell mean value $\mathbf{U}_i^{n+1}$

$$\Omega\frac{\left(\mathbf{U}_i^{n+1} - \mathbf{U}_i^n\right)}{t^{n+1} - t^n} = \mathbf{R}_i^{n+1} \tag{A.40}$$

it is possible to linearise the residual around $\mathbf{U}^n$:

$$\mathbf{R}_i^{n+1} \approx \mathbf{R}_i^n + \sum_{j\in C(i)} \left.\frac{\partial\mathbf{R}_i}{\partial\mathbf{U}_j}\right|_n \left(\mathbf{U}_j^{n+1} - \mathbf{U}_j^n\right) \tag{A.41}$$

where $C(i)$ is the set of cells upon which the residual $\mathbf{R}_i$ depends. In this way, the equation A.40 becomes:

$$\Omega\frac{\left(\mathbf{U}_i^{n+1} - \mathbf{U}_i^n\right)}{t^{n+1} - t^n} = \mathbf{R}_i^n + \sum_{j\in C(i)} \left.\frac{\partial\mathbf{R}_i}{\partial\mathbf{U}_j}\right|_n \left(\mathbf{U}_j^{n+1} - \mathbf{U}_j^n\right) \tag{A.42}$$

By setting $\Delta\mathbf{U}_i^n = \left(\mathbf{U}_i^{n+1} - \mathbf{U}_i^n\right)$ we have:

$$\left(\frac{\Omega}{\Delta t}\right)\Delta\mathbf{U}_i^n - \frac{\partial\mathbf{R}_i^n}{\partial\mathbf{U}_j^n}\Delta\mathbf{U}_j^n = \mathbf{R}_i^n \tag{A.43}$$

By writing this equation for each cell $i = 1, \dots, n$ a block linear system is assembled, whose components are $m \times m$ matrices, with m equal to the number of evolved quantities, five for 3D Navier-Stokes. It can be noted that the residual linearisation has only affected the left hand side of equation A.40, meaning that the order of accuracy and the solution at $n+1$ are unchanged by this first order expansion, the solution being determined solely by the flux balance. Instead, the quantities on the left hand side determine the way the solution is evolved from t^n to t^{n+1}.

For steady-state calculations, the time derivative must drop at convergence. The $\Omega/\Delta t$ term in the equations represents a relaxation factor and, conversely from explicit time stepping, can assume much larger values, according to the time advancement method and the approximation used for forming and solving the linear system. As $\Delta t \to 0$, the

equation reduces to a Newton step, which is a method converging at second order towards the root. There are, in fact, a variety of algorithms that can be applied to solve the arising linear system. Their behaviour and efficiency depends not only on their intrinsic approach, but also on the approximations used in deriving the residual Jacobians. Indeed, their exact expression can be extremely complicated to be derived analytically, due to the fact that it depends on many variables and their gradients, as in equation A.39. Numerical derivatives could be computed using finite differences [134]. The fact that the Jacobians do not influence the final solution allows for some approximation in their computations. A typical approach consists in deriving them using first-order schemes, for instance the Rusanov one for convective fluxes, and the thin shear layer approximation with centred derivatives for the diffusive fluxes [18]. These have expressions much more easily handled and computationally affordable. Unfolding the full Jacobian expression using chain rule is also possible, either analytically or using automated differentiation [187]. This is typically used in conjunction with Newton-Krylov linear system algorithms, in order to restore second order convergence to steady state, but at the cost of a much larger storage requirement, as Jacobians must be kept in memory and for each cell it is at least a 6x6 matrix for a one equation turbulence model, like Spalart-Allmaras.

Solution of linear system

After forming the linear system arising from the expansion of Jacobians around time level n, a suitable technique must be adopted to solve it for the unknown time increments $\Delta\mathbf{U}_i^n$. When first order approximation of Jacobians is employed, a popular solution strategy is based on Lower-Upper Symmetric Gauss-Sidel (LU-SGS) iterative method [18]. In equation A.43, the global system can be written as:

$$\left(\frac{\Omega}{\Delta t}\mathbf{I} - \mathbf{M}\right)\Delta\mathbf{Q}^n = \mathbf{R} \tag{A.44}$$

where $\mathbf{Q}$ is now the symbol for the conservative variable vector. The implicit block matrix, whose element are 5×5 matrices as well, for 3D Navier-Stokes, can be decomposed as [282]:

$$\frac{\Omega}{\Delta t}\mathbf{I} - \mathbf{M} = \mathbf{L} + \mathbf{D} + \mathbf{U} = (\mathbf{L} + \mathbf{D})\,\mathbf{D}^{-1}\,(\mathbf{U} + \mathbf{D}) - \mathbf{L}\mathbf{D}^{-1}\mathbf{U} \tag{A.45}$$

where $\mathbf{L}$ is a block lower triangular matrix, $\mathbf{U}$ is a block upper triangular matrix, and $\mathbf{U}$ is a block diagonal matrix. If $\mathbf{L}\mathbf{D}^{-1}\mathbf{U}$ is small and can be neglected, equation A.44 can be rewritten as

$$(\mathbf{L} + \mathbf{D})\,\mathbf{D}^{-1}\,(\mathbf{U} + \mathbf{D})\,\Delta\mathbf{U}^n = \mathbf{R} \tag{A.46}$$

With this decomposition, the above equation can be inverted with the following two sweeps approach:

$$\begin{cases} \mathbf{D}\Delta\mathbf{Q}^\star = -\mathbf{R}^n - \mathbf{L}\Delta\mathbf{Q}^\star \\ \mathbf{D}\Delta\mathbf{Q}^n = \mathbf{D}\Delta\mathbf{Q}^\star - \mathbf{U}\Delta\mathbf{Q}^n \end{cases} \tag{A.47}$$

The first equation represents the forward sweep, and the second the backward. The name comes from the way the computational domain is looped. In order to highlight the $\mathbf{L}, \mathbf{D}$ and $\mathbf{U}$ matrices, equation A.43 can be expanded as:

$$\underbrace{\left(\frac{\Omega}{\Delta t}\mathbf{I} - \frac{\partial \mathbf{R}_i^n}{\partial \mathbf{Q}_i^n}\right)}_{\mathbf{D}} \Delta \mathbf{Q}_i^n - \underbrace{\sum_{j \in L(i)} \frac{\partial \mathbf{R}_i^n}{\partial \mathbf{Q}_j^n}}_{\mathbf{L}} \Delta \mathbf{Q}_j^n - \underbrace{\sum_{j \in U(i)} \frac{\partial \mathbf{R}_i^n}{\partial \mathbf{Q}_j^n}}_{\mathbf{U}} \Delta \mathbf{Q}_j^n = \mathbf{R}_i^n \tag{A.48}$$

$L(i)$ and $U(i)$ are the set of lower and upper cells, with respect to cell i, respectively. They depend on domain numbering and with suitable choice of cell numeration these sets can be such that they can be accessed independently during the forward and backward sweep [229, 295]. The residual Jacobians are, in fact, the Jacobian of the convective and viscous fluxes. As stated above, some levels of approximation are possible in their derivation. The simplest one is to express them using Rusanov flux computed with first order expansion, i.e. with cell centre values [6]:

$$\mathbf{R}_i^n = \sum_{j \in C(i)} \left(\mathbf{F}_{ij} \cdot \hat{n}_{ij} S_{ij}\right) \tag{A.49}$$

$$\mathbf{F}_{ij}^n = \left[\frac{1}{2}\left(\mathbf{F}_i + \mathbf{F}_j - [\mathbf{A}]_{ij}\left(\mathbf{Q}_j - \mathbf{Q}_i\right)\right)\right] \cdot \hat{n}_{ij} S_{ij} \tag{A.50}$$

If the dissipation matrix of the Rusanov flux is approximated by its spectral radius, $[\mathbf{A}]_{ij} = \lambda_{ij}\mathbf{I}$, with

$$\lambda_{ij} = |\mathbf{V} \cdot \hat{n}_{ij}| + a + \frac{2\left(\mu + \mu_t\right)}{\rho |\hat{n}_{ij} \cdot (\mathbf{r_j} - \mathbf{r_i})|} \tag{A.51}$$

Then, for a closed control volume, the flux integral

$$\sum_{j \in C(i)} \left(\mathbf{F}_i \cdot \hat{n}_{ij} S_{ij}\right) = 0 \tag{A.52}$$

with F_i constant for first order approximation is zero in equation A.49, and the contribution to the $\mathbf{D}$ matrix is only due to $\left(\lambda_{ij}\mathbf{I}\right)\mathbf{Q}_i$. The other terms depending on $\mathbf{Q}_j$ go either in $\mathbf{L}$ or $\mathbf{U}$, according to the position of the cell considered. By introducing the additional approximation for which:

$$\frac{\partial \mathbf{R}_i^n}{\partial \mathbf{Q}_j^n} \Delta \mathbf{Q}_j^n = \frac{\partial \mathbf{F}_{ij}^n}{\partial \mathbf{Q}_j^n} \Delta \mathbf{Q}_j^n \approx \mathbf{F}\left(\mathbf{Q}_j + \Delta \mathbf{Q}_j\right) - \mathbf{F}\left(\mathbf{Q}_j\right) \tag{A.53}$$

equation A.48 can be written as:

$$\left(\frac{\Omega}{\Delta t}\mathbf{I}+\frac{1}{2}\sum_{j\in C(i)}\lambda_{ij}S_{ij}\mathbf{I}\right)\Delta\mathbf{Q}_i^n+ \\ +\frac{1}{2}\sum_{j\in L(i)}\left[\mathbf{F}\left(\mathbf{Q}_j+\Delta\mathbf{Q}_j\right)-\mathbf{F}\left(\mathbf{Q}_j\right)\right]+ \\ +\frac{1}{2}\sum_{j\in U(i)}\left[\mathbf{F}\left(\mathbf{Q}_j+\Delta\mathbf{Q}_j\right)-\mathbf{F}\left(\mathbf{Q}_j\right)\right]=\mathbf{R}_i^n \quad \text{(A.54)}$$

and can be solved with the forward and backward sweeps of A.47.

An improvement of the above method is to retain the full matrix of the flux Jacobian of first order Rusanov flux. The dissipation matrix can be taken as the Roe matrix, coherently with the flux used to compute the right hand side residual, and the viscous flux Jacobian can be approximated by a matrix $\mathbf{J}_v$ derived, for instance, using the thin shear layer approximation of the Navier-Stokes equations or some better estimation [204]. In this way, we resort to the block feature of the system and the so-called block LU-SGS (BLU-SGS). Although computationally more expensive than the LU-SGS variant, it can offer substantial reduction of iterations required and effective time saving [34]. Furthermore, also the number of sweeps can be increased to reduce the error in solution update at each time step. Again, for a large number of sweeps the benefit brought by improved accuracy is offset by the computational time [34, 193, 291]. In parallel computation, finally, the communication strategy is cumbersome and requires care and optimal tuning, as the computational domain is split among various processes that must sweep each portion individually [188].

An example of the influence of the degree of residual approximation on the convergence behaviour is shown in Figure A.2. The problem solved was an inviscid 2D circular bump channel at transonic regime. The circular bump acts as a convergent-divergent nozzle and causes the formation of an oblique shock wave multiply reflected, starting from the kink where the arc joins the straight wall, as visible in Figure A.1. The LU-SGS and BLU-SGS algorithm have been implemented for the Euler solution and applied with different sweeps. A substantial reduction of the number of iteration for a six order of magnitude drop of the total energy residual was achieved with the BLU-SGS, Figure A.2a. However, the computational cost of the full matrix approximation is much higher than the LU-SGS, where only vector operations on the diagonal are involved. Despite the slow convergence speed, the time cost of LU-SGS is still better than BLU-SGS. Although the code was not optimised, this highlights the fact that the development of an implicit flow solver requires particular care, since the theoretically better performance of more advanced methods can be offset by a heavy computational cost, such that there must be an optimal trade-off between the number of iterations and the time-cost per iteration.

The programming cost of a turbulent implicit solver is very high. Despite it offers great advantage in stability convergence, the mathematical and numerical methods are

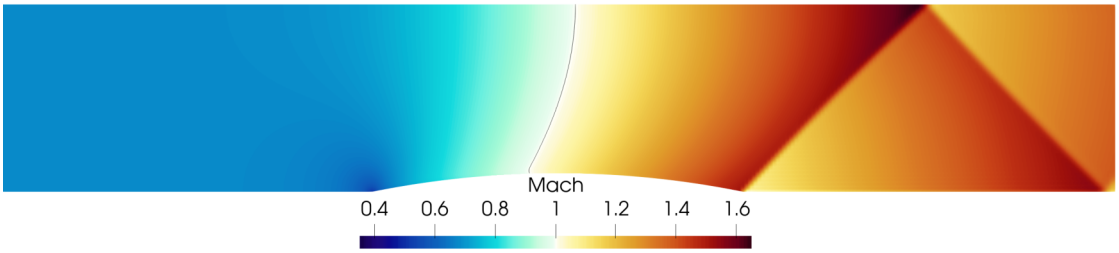

Figure A.1: Mach number contours for the 2D circular bump problem at transonic regime. The $M = 1$ isoline is shown in black.

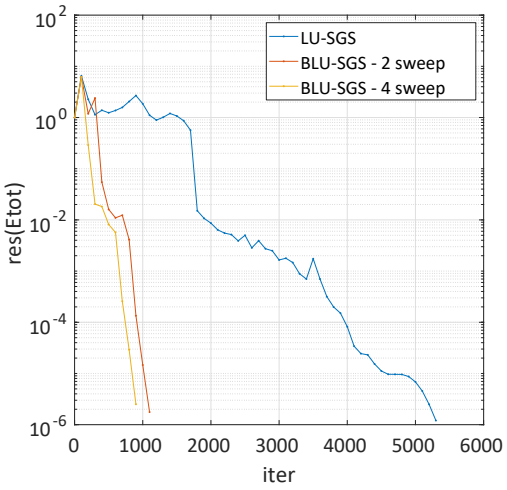

(a) Convergence history for Total Energy residuals as a function of the sweeping algorithm

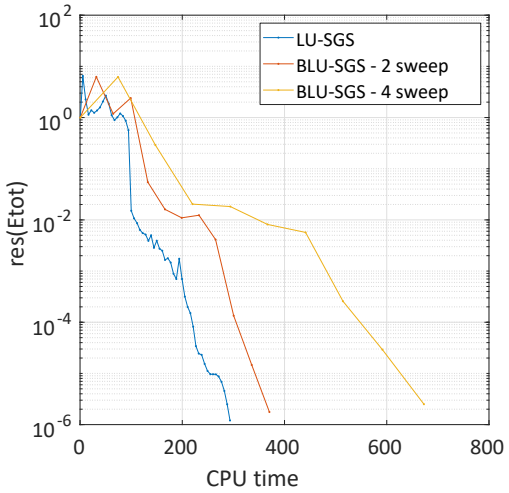

(b) Convergence time for Total Energy residuals as a function of the sweeping algorithm

Figure A.2: 2D circular bump channel at transonic regime. Comparison of ITS algorithms on convergence history.

very complicated and the implementation on a formally unstructured code is cumbersome. Moreover, it adds complexity to the already critical task of parallelisation. As shown in the example reported in Figure A.2, the employment of more accurate methods must cope with the heavier computational cost, and without a careful programming strategy and optimisation the net improvement on the convergence time can become negative. In addition, a fully implicit treatment of boundary conditions must be adopted. A possible way is expressing the contribution to the Jacobian from the ghost cell l as a function of the boundary cell i [11]:

$$\frac{\partial \mathbf{F}}{\partial \mathbf{U}_l} \Delta \mathbf{U}_l = \frac{\partial \mathbf{F}}{\partial \mathbf{U}_l} [\mathbf{C}] \, \Delta \mathbf{U}_i \tag{A.55}$$

The relation $[\mathbf{C}] \, \Delta \mathbf{U}_i$ links the variation of the ghost cell value $\Delta \mathbf{U}_l$ with that of the interior boundary cell $\Delta \mathbf{U}_i$. By further disclosing this expression, it appears that:

$$\begin{aligned} \Delta \mathbf{U}_l &= \frac{\partial \mathbf{U}_l}{\partial \mathbf{U}_i} \Delta \mathbf{U}_i = \\ &= \frac{\partial \mathbf{U}_l}{\partial \mathbf{V}_l} \frac{\partial \mathbf{V}_l}{\partial \mathbf{V}_i} \frac{\partial \mathbf{V}_i}{\partial \mathbf{U}_i} \Delta \mathbf{U}_i \end{aligned} \tag{A.56}$$

where $\mathbf{U}$ is the conservative variable and $\mathbf{V}$ the primitive variable. In fact, boundary conditions are often expressed in terms of the primitive variables. The matrix $[\mathbf{C}] = \dfrac{\partial \mathbf{V}_l}{\partial \mathbf{V}_i}$ must be derived for each kind of boundary condition and added to the residual of the interior boundary cell i at each iteration. The two changes from primitive to conservative variables and vice versa require two more matrix-matrix multiplication. The cost of the operation itself is high, and the analytical differentiation of the link between the imposed ghost value and the boundary interior value can be very complicated, by the fact that the simplest isentropic equations are highly nonlinear.

A number of other issues could be added regarding implementation and efficiency of implicit methods, although they are believed to fall outside the scope of the present work. The possibility of using very high Courant numbers without encountering instability represents the major motivation to employ implicit algorithms. For LU-SGS approach, the time step appears in the diagonal matrix and it helps improving the diagonal dominance of the system, which is of great importance for the approximate LDU decomposition to hold. A suitable choice of CFL is often combined with a relaxation parameter multiplying the diagonal terms of the dissipation matrix, again to control diagonal dominance. In practice, CFL can be ramped from start of iterations and values as high as 10^5 can be reached. For infinite time-step, the solution update becomes a Newton method. This is used in Newton-Krylov solvers, usually employing Generalised Minimal Residual (GMRES) in combination with preconditioning techniques and line search relaxation, again with different levels of approximation and storage strategies [121, 172, 180]. These algorithms, however, are much more complicated in the implementation and parallelisation than LU-SGS, despite offering convergence in a very limited number of iterations.

Appendix B

Additional test cases for flow solver development

The appendix provides additional test cases used for the validation and verification of the numerical solver during its development.

B.1 Linear advection equation

Figure B.1 compares different time-marching algorithms for SOU+SUPERBEE for the advection of a square wave with linear velocity, see Section 3.3. After one second of physical time interval with a CFL = 0.5. The RK46NL low dissipation and low dispersion explicit Runge-Kutta algorithm [14] behaves as good as the semi-implicit Crank-Nicholson scheme, the latter combining one step of backward and one step of forward Euler. The Adams-Moulton scheme is similar to RK4, while the explicit first-order backward Euler is very diffusive, as expected. Even for smoother solutions, a small discontinuity in the derivative can cause the appearance of the dispersion error. This is shown in Figure B.2, where the same grid as before was used for propagation of a sine wave. The snapshot is at $t = 4s$, in order to emphasize the behaviour of each scheme. Again, the FOU has almost completely dissipated the initial compactness of the solution, while limited SOU remarks the compressive nature of SUPERBEE and the more diffusive attribute of MINMOD. The QUICK algorithm has kept a smooth solution with minimum oscillations for this specific case.

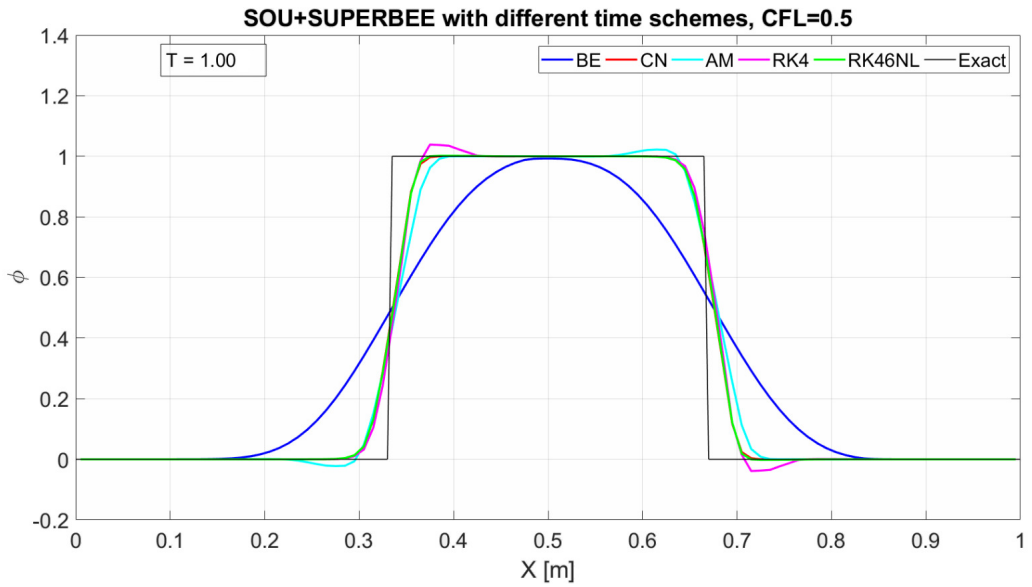

Figure B.1: Comparison of time scheme for linear advection of a square wave using SOU in space. Grid size is 100 cells. CFL = 0.5

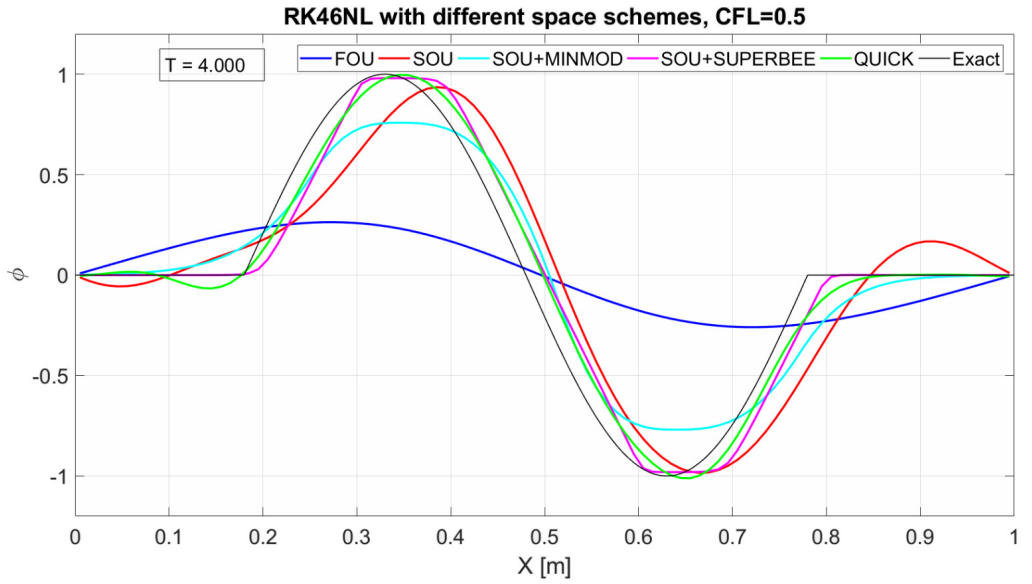

Figure B.2: Comparison of spatial scheme for linear advection of a sine wave using RK46NL in time. Grid size is 100 cells. CFL = 0.5

B.2 2D Euler equations

B.2.1 2D Riemann Problem of Schulz

An interesting test case for the Euler equations is the 2D Riemann problem of Schulz [226]. It is solved in a square domain with transmissive boundary conditions on each side. The domain is divided into four regions where primitive variables are constant, but different in each sector. The resulting solution is a very complex flow field with a series of waves interacting and bringing Kelvin-Helmholtz instability and vortex roll-up. The structures evolve at unlimited subscales and they can be captured by a very fine discretisation employing high order methods, such as WENO reconstruction. Therefore, it is a good way of assessing the effectiveness of the adopted limiter and the resolution of the methods. In the numerical simulation, the computational grid had 400x400 equally spaced elements and a MUSCL-TVD scheme with the HLLC Riemann solver was employed, together with RK3-TVD [262] for time integration. Figure B.4 shows the density gradient magnitude in logarithmic scale, allowing to appreciate the main discontinuity waves and some instabilities that are captured by the code. The discretisation was, however, relatively coarse for a 2^{nd} order method. A comparison with a 4^{th} order discretisation on a mesh much finer, with a characteristic dimension of 1/1818 [265] in the lower left quadrant, compared to 1/400 for the current code, shows in Figure B.3 that there was a good overall match between the solutions, with an apparent blur for the lower order discretisation.

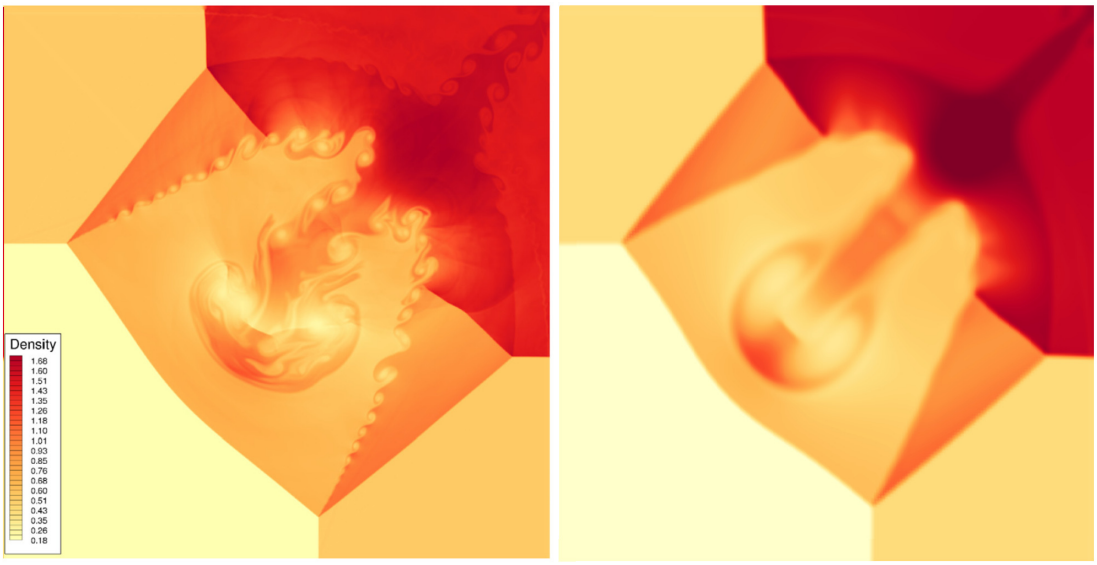

Figure B.3: 2D Riemann problem of Schulz. Density field after 1 s. (a) 4^{th} order MUSCL of [265], h = 1/1818. (b) 2^{nd} order MUSCL, current code, h = 1/400

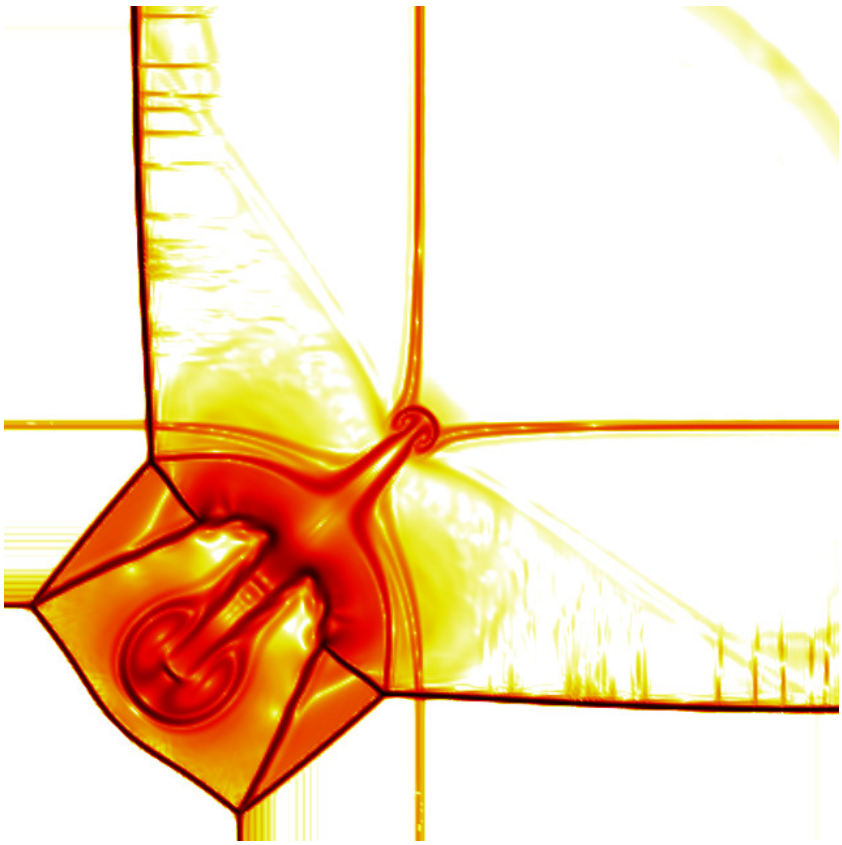

Figure B.4: 2D Riemann problem of Schulz. Density gradient magnitude after 1 s.

B.2.2 Double Mach reflection

Another popular verification case for inviscid flows is the double Mach reflection problem of Woodward and Colella [289]. It was derived from several wind tunnel tests of planar waves impinging on edges, and it consists in a normal shock wave travelling down a tube and hitting a wedge, from which it is reflected through a complex pattern of structures and instabilities of unbounded subscale. Numerically, it can be simulated by proper imposition of boundary conditions in a rotated domain, where the wedge wall is horizontal and the Mach 10 shock wave looks inclined, at 60°. Ahead of the wave, $\rho = 1.4$ and $p = 1.0$. Figure B.5a shows the density result at $t = 0.2s$ for the present 2^{nd} order solver on a square grid with $h = 1/300$. The solution is compared to that of Tsoutsanis, obtained with a 4^{th} order MUSCL solver using the same limiter, Figure B.5b. The flow field is in good agreement, exhibiting similarity for the shock and discontinuity waves, the position of the triple point and the contours shape. The Kelvin-Helmholtz instabilities arising in the inner Mach stem are obviously better resolved by the high-order solver, but the validity of the current implementation appears confirmed.

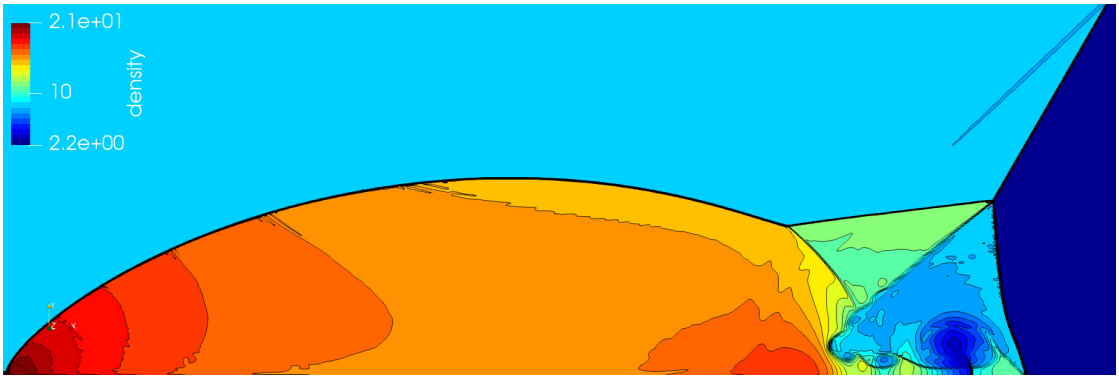

(a) Present 2^{nd} order solver

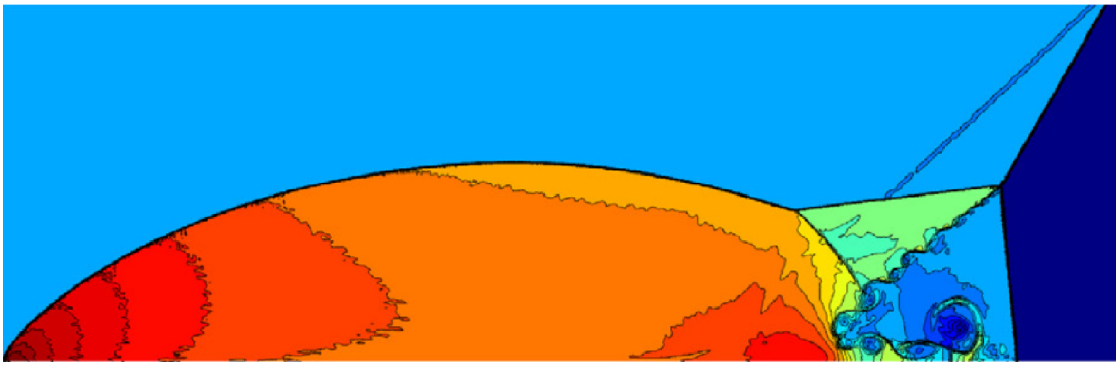

(b) 4^{th} order solver of Tsoutsanis [265]

Figure B.5: Double Mach reflection problem.

B.3 2D Navier-Stokes equations

B.3.1 Stokes First Problem

Stokes first problem deals with the flow near an impulsively started plate at speed V. An exact similarity solution is given by

$$v = V\, erf\left(\frac{y}{2\sqrt{(\nu\, t)}}\right) \tag{B.1}$$

The case can be conveniently simulated with a shear layer on the y velocity component v. A rectangular domain, with periodic boundary conditions on the upper and lower side, and constant imposed freestream values at the left and right side, was initialised with $v = -V$ for $x < 0$ and $v = V$ for $x > 0$, and zero u. The result at $t = 0.5s$ for $\nu = 0.01$, $\gamma = 1.4$, $p = 1/\gamma$, $V = 0.1$ is shown in Figure B.6a. The error scaling for v in L_∞, L_1 and L_2 norm is reported in Figure B.6b, which proves that the parabolic equation is solved with second order accuracy in space.

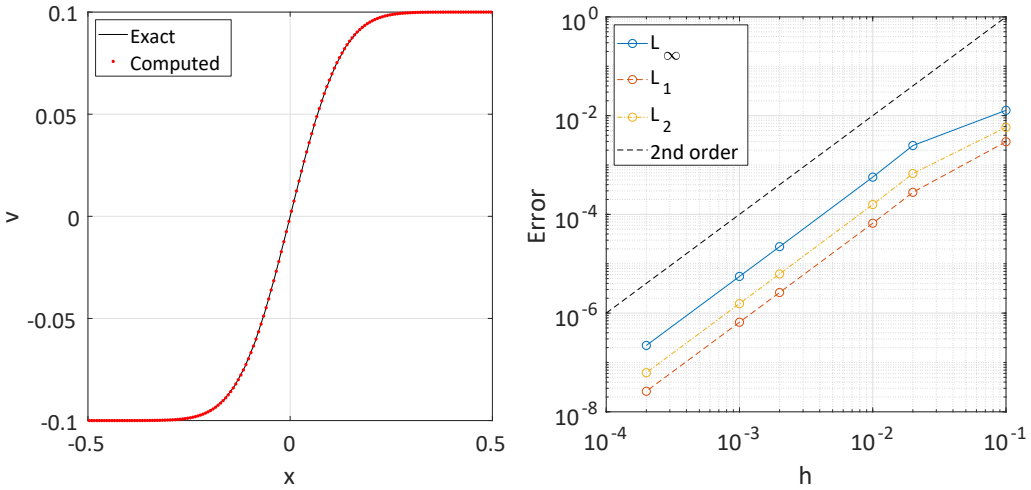

(a) Velocity profile (b) Velocity error scaling

Figure B.6: Stokes first problem

B.3.2 Laminar flow past a circular cylinder

The laminar flow past a circular cylinder is a largely studied problem that is commonly used for code verification, as it is characterised by a variety of regimes and quite complex phenomena that must be correctly captured by a direct Navier-Stokes solver. In the incompressible case, the leading parameter determining the flow type is the Reynolds number based on diameter D, $Re = U_\infty\, D/\nu$. At low Reynolds, a laminar steady separation bubble forms behind the cylinder. When the Reynolds number exceeds approximately 70, the flow becomes unsteady and the vortex shedding begins, in which there

appears an oscillation of the wake with a periodic detachment of a von Karman vortex. The solution becomes steady again in the fully turbulent regime. If the fluid is compressible, the Mach number becomes a second non-dimensional parameter and relevant cases for the purpose of numerical methods are for instance those of the cylinder confined in a channel, with the shock structure being reflected by the lower and upper walls, the interaction of more than one body and solution methods for moving objects or geometries with sharp interfaces, in particular in the framework of FD codes using the Immersed Boundary Method (IBM) [276].

For the present code, the main interest was in the verification of the laminar flow structures, the periodic vortex shedding, the computation of forces for a body immersed into a fluid and the correct replication of shock structures. By changing the Reynolds and the Mach number, these flow regimes were examined and compared with reference solutions found in the literature. The computational grid consisted of an O-type topology with smoothed wall-clustered cells and a circular domain of diameter $100D$, an example of which is shown in Figure B.7. The typical grid size for computations ranged from 50k to 120k elements, with refined grids used for compressible cases. At the boundary, a Riemann far-field condition, based on 1D inviscid Riemann invariant, was imposed. The truncated domain would require some specific treatment at the boundaries, like characteristic non-reflecting boundary conditions (NRBC), but they were not implemented in the current code, as they are more difficult to impose in unstructured finite volume solvers and typically escaped in the RANS approach, which was the final target of the development line.

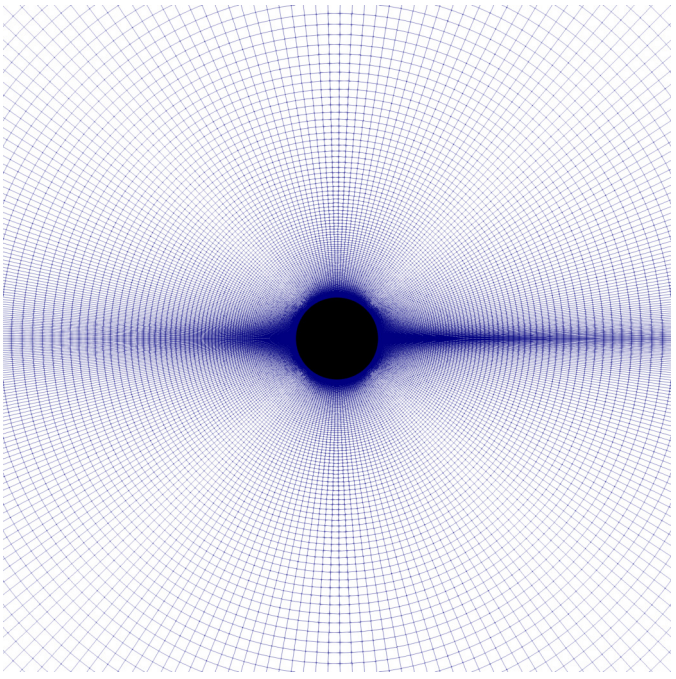

Figure B.7: Example of grid used for laminar flow past a circular cylinder

Steady flow

The first set of solutions were obtained in the nearly incompressible regime, $M = 0.1$ at $Re < 80$. Figure B.8a shows the velocity magnitude contours and streamlines at $Re = 40$, while Figure B.8b illustrates the normal vorticity ω_z contours and streamlines at $Re = 30$, highlighting the physical dimensions characterising the separation bubble, that are compared to those found by other authors in Table B.1. The results appear within the ranges found in the literature and verify the implemented numerical method. The pressure coefficient distribution over the circumference at $Re = 40$ is compared in Figure B.9a with that of incompressible SUPG-FEM code of Sen [227], deemed accurate for this class of problems, showing good agreement. Also the variation of the drag coefficient with Reynolds, reported in Figure B.9b, matches the one found by the same author.

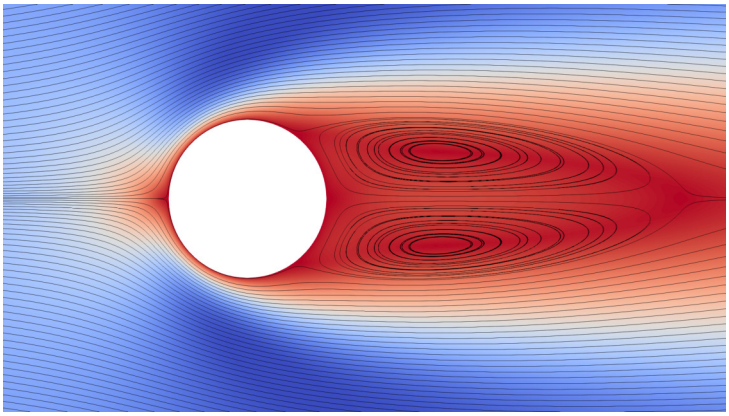

(a) Velocity magnitude and streamlines at $Re = 40$

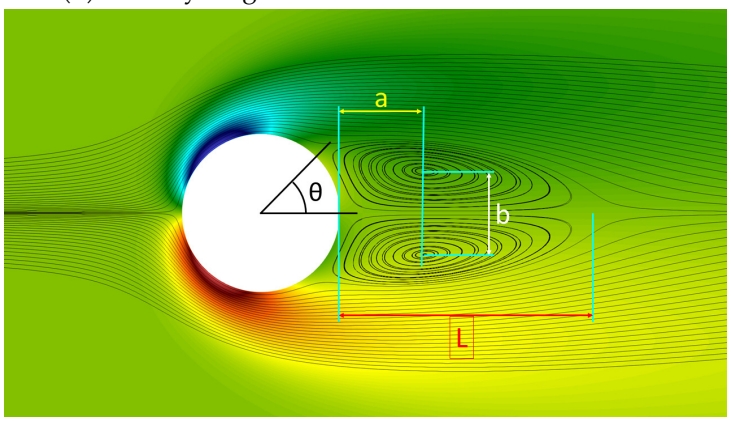

(b) Vorticity magnitude and streamlines, $Re = 30$. Characteristic physical dimension of the separation region are indicated

Figure B.8: Steady laminar flow around a cylinder.

Table B.1: Comparison of separation bubble lengths for steady laminar flow around circular cylinder at $Re = 30$.

Author	Re_D	M	a/D	b/D	L/D	θ	C_d
Coutanceau and Bouard [exp] [46]	30	-	0.54	0.54	1.55	50.00	-
Tritton [exp.] [264]	30	-	-	-	-	-	1.74
Pinelli [205]	30	-	0.56	0.52	1.80	48.05	1.80
Present	30	0.1	0.54	0.53	1.60	48.70	1.71

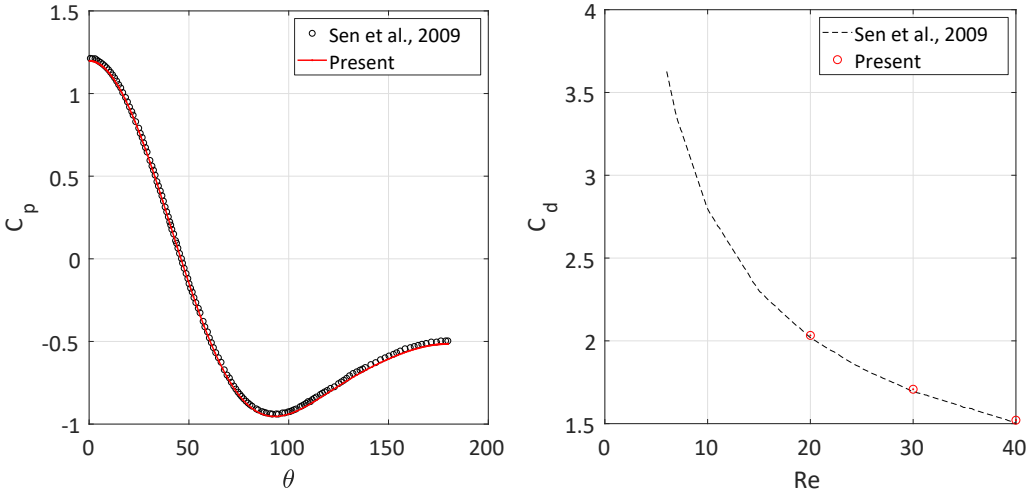

(a) Pressure coefficient distribution at $Re = 30$. Present code and Sen [227]

(b) Variation of drag coefficient vs Reynolds number. Present code and Sen [227]

Figure B.9: Steady laminar flow around a cylinder

Vortex shedding

When Re_D exceeds a critical value around 70, the flow turns into a periodic unsteady motion, with a fluctuating pressure field and an oscillating separation bubble, from which vortices are detached and convected downstream, in the so-called vortex shedding. Figure B.10 illustrates the instantaneous z-vorticity contours for a case at $Re = 185$ and $M = 0.1$ showing the phenomenon. The comparison of the characteristic frequency of the oscillation, represented by the nondimensional Strouhal number $St = D\omega/U_\infty$, where ω is the shedding frequency, is given in Table B.2. The parameters are comparable with those of other authors, whose code were truly incompressible and based on different discretisation approaches.

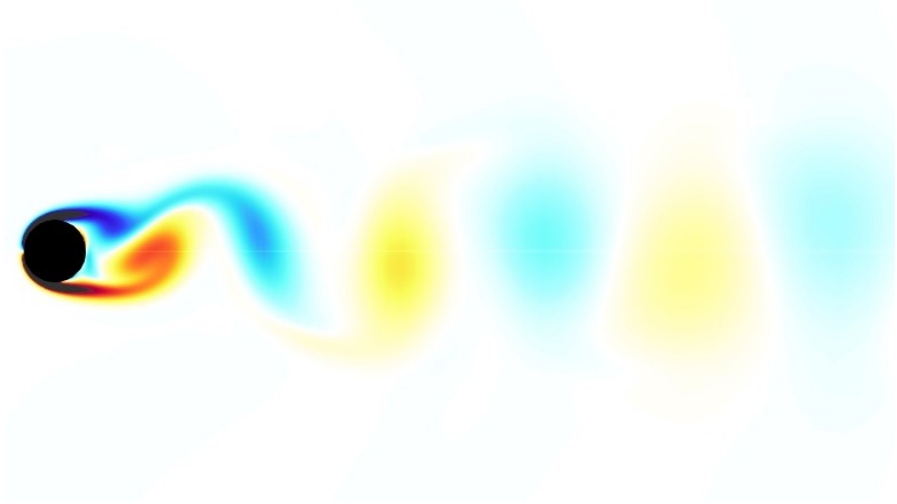

Figure B.10: Instantaneous z-vorticity contour for laminar flow past a cylinder at $Re_D = 185$.

Table B.2: Characteristic coefficients for laminar flow around a cylinder at $Re = 185$.

Author	C_D	C_L^{rms}	St
Pinelli [205]	1.430	0.423	0.196
Vanella [275]	1.377	0.461	-
Guilmineau [94]	1.280	0.443	0.195
Lu [159]	1.310	0.422	0.195
Present	1.330	0.450	0.191

High-speed flow

The last studied problem was the high-speed compressible regime, where a detached shock wave is formed in front of the cylinder. Density and Mach number contours at

$M = 2.0$ and $Re = 300$ are shown in Figure B.11a and B.11b. The computed flow field was symmetrical, with a strong bow shock and a wake region. The shock front did not follow the circular mesh arrangement, resulting in a sharp capturing only near the central axis, with blurred contours far away. This is inevitable with the circular farfield domain employed. However, the shock standoff was 0.7, which is in agreement with literature data, for instance referred to Riahi [210], who employed and IBM in the open source FV solver OpenFOAM.

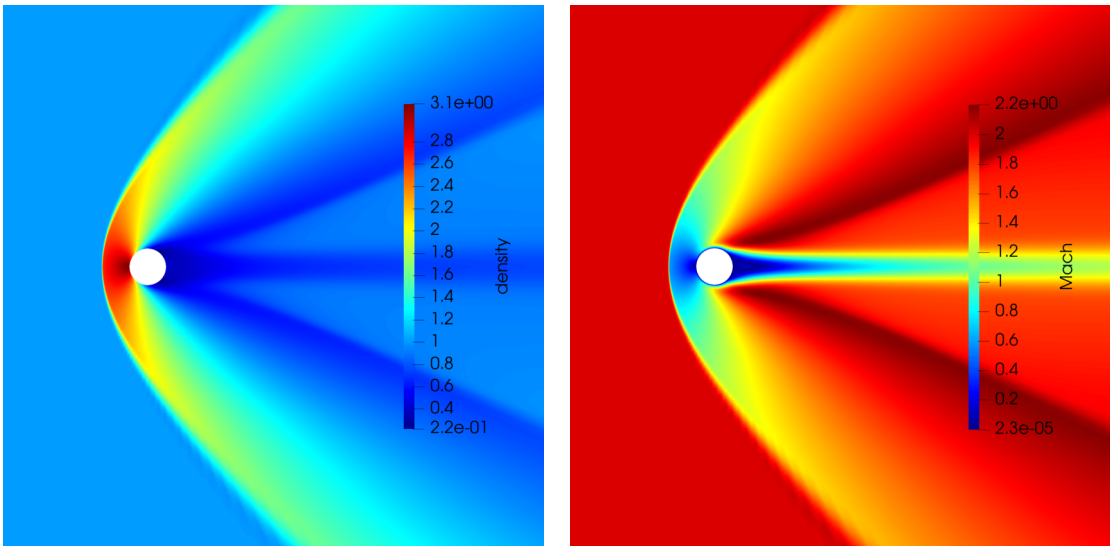

(a) Density contours (b) Mach number contours

Figure B.11: Supersonic laminar flow around a cylinder, $M = 2.0$, $Re = 300$

B.3.3 Other verification cases

Apart from analytical solutions, which are very limited indeed for Navier-Stokes equations, a wide number of verification cases is available in the literature for a code-to-code or numerical versus experimental data comparison. Among them some omitted cases are the Stokes second problem, the Poiseuille flow, the 2D Taylor-Green vortex, all possessing an analytical solution, the double shear layer, heat conduction in a pipe, the lid-driven cavity. This last problem is shown in Figure B.12. In all these simulations consistent solutions were obtained, confirming the validity of the implementation.

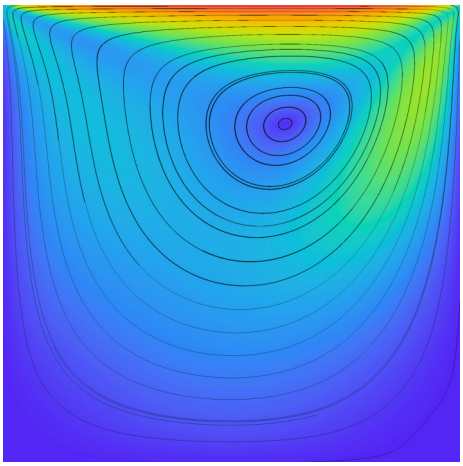

(a) Velocity magnitude contours and streamlines

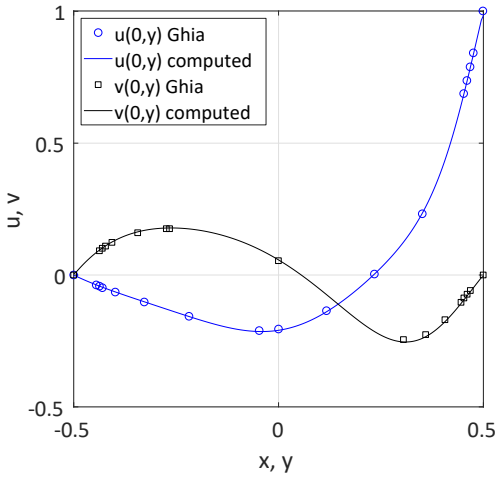

(b) Velocity profiles, present code and Ghia [80]

Figure B.12: Lid-driven cavity problem at $Re = 100$, $t = 10s$. Upper wall slides horizontally without leakage.

B.4 2D RANS

B.4.1 2D turbulent flat plate

The 2D zero pressure gradient turbulent flat plate was used as verification case, relying on the data present in the NASA TMR repository. The first problem was at low speed, with $M = 0.2$ and $Re = 5 \times 10^6$. The plate was modelled with an isothermal no-slip wall, while freestream conditions were imposed elsewhere. The outcome of the simulation was compared with the reference NASA code CFL3D, as shown in Figure B.13. Figure B.13b illustrates the law of the wall $y^+ = \frac{y u_\tau}{\nu}$ vs $u^+ = \frac{u}{u_\tau}$, $u_\tau = \sqrt{\frac{\tau_w}{\rho}}$, for the present implementation and CFL3D. The curves are closely overlapped and no difference can be spotted. Figure B.13a depicts the turbulent viscosity ratio. The reference solution was computed on a finer grid, which can explain the slight difference, that does not spoil a very good agreement tough.

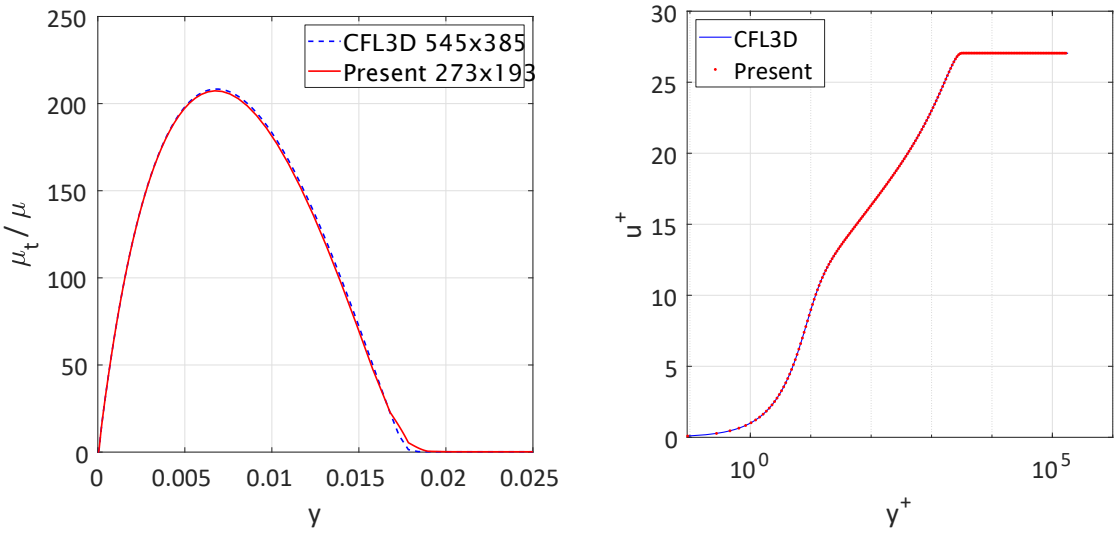

(a) Turbulent viscosity ratio at x = 0.97

(b) Law of the wall at x = 0.97

Figure B.13: 2D zero pressure gradient turbulent flat plate, $M = 0.2$, $Re = 5 \times 10^6$

The same problem also appears as an extended case at $M = 2.0$, $Re = 15 \times 10^6$ on NASA TMR. The result of the present code is again compared to CFL3D in Figure B.14. The skin friction coefficient vs Re_θ, in Figure B.14a exhibits a trend very similar to the reference solution, found on a finer grid, with only an almost constant offset. The wall law in Figure B.14b was extracted at $Re_\theta = 10000$ and it appears very well matched, implicitly remarking the validity of the previous image.

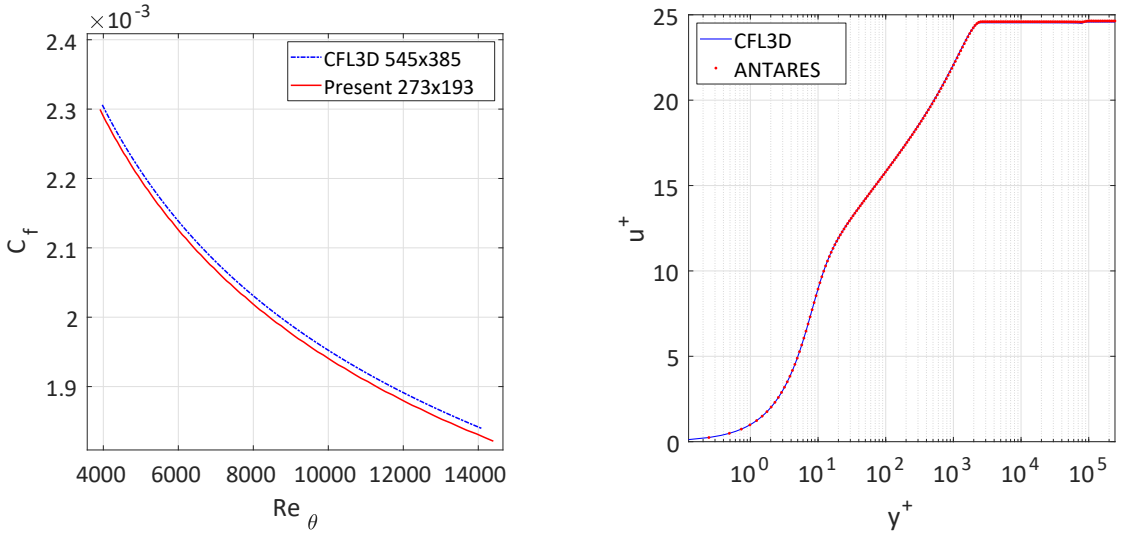

(a) Skin friction coefficient vs Re_θ

(b) Law of the wall at $Re_\theta = 10000$

Figure B.14: 2D zero pressure gradient turbulent flat plate at high speed, $M = 2.0$, $Re = 15 \times 10^6$

B.4.2 2D bump channel

The very good correspondence between the implemented SA model and the reference solutions for the previous case indicates a correct inclusion of the turbulence terms in the present code and the capability of correctly resolving the boundary layer profile. It is also important to verify that wakes are consistently and robustly handled by the solution method. To this purpose, another NASA TMR case, the 2D bump channel was considered. The problem is very similar to the previous one, but at a certain streamwise location the wall has a bump causing a downstream separation with the thickening of the boundary layer and the activation of the production and destruction source terms, fed by the generated vorticity in the wake. Figure B.15 illustrates the turbulent viscosity ratio μ_t/μ in the boundary layer, highlighting the wake growth behind the bump (the horizontal scale has been stretched to magnify the curvature). Figure B.16a reports the wall skin friction coefficient for reference NASA codes FUN3D and CFL3D and the current solver. The shape of the reconstructed coefficient is close to the reference one, but an overshoot can be noticed at $x = 0.7$, with some slighter undershoots at $x = 0.5$ and $x = 1$. This discrepancy can be attributed to the factor 5 difference between the mesh size of the NASA outputs and the one here used, as a larger number of elements was too time expensive for a serial calculation, and possible interpolation differences. On the other hand, the pressure coefficient distribution depicted in Figure B.16b has a very good agreement, so that the result could be regarded confidently.

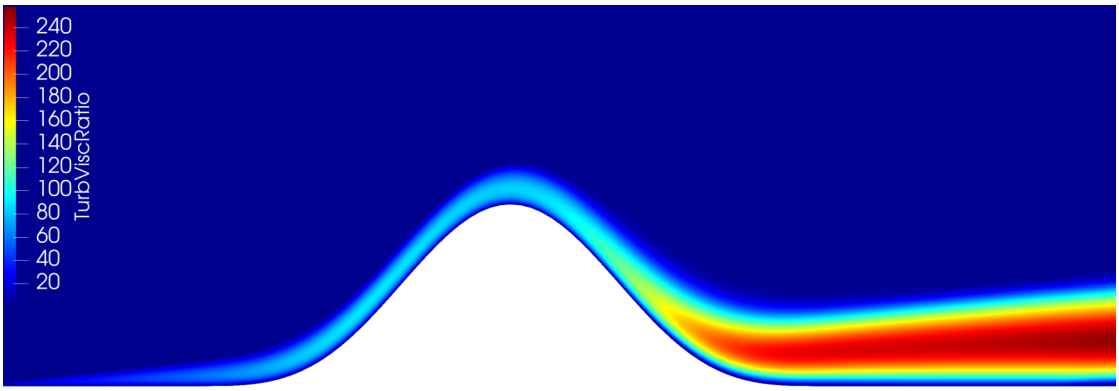

Figure B.15: Turbulent viscosity ratio for 2D bump channel problem

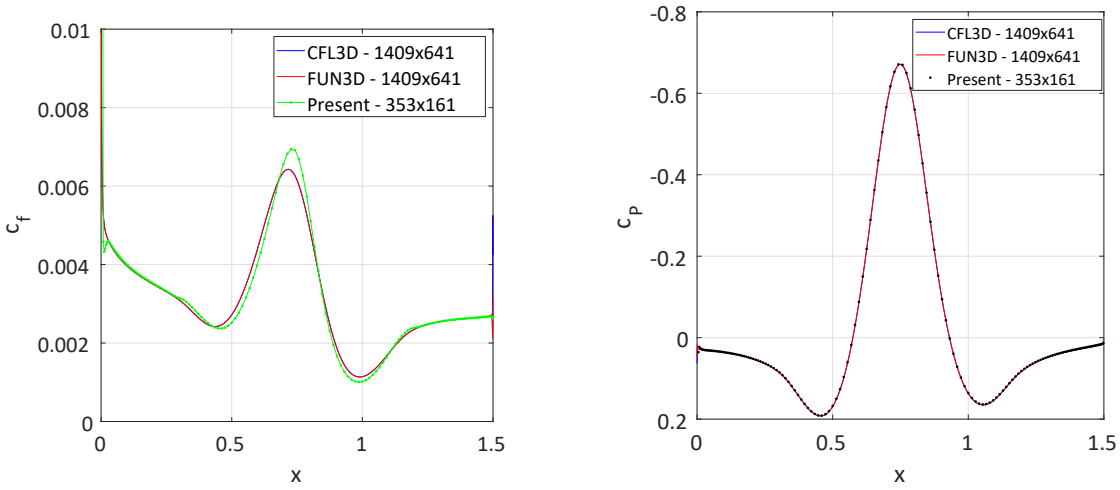

(a) Wall skin friction coefficient

(b) Wall pressure coefficient

Figure B.16: 2D bump channel $M = 0.2$, $Re = 3 \times 10^6$

Bibliography

[1] J. Adamczyk. *Model equation for simulating flows in multistage turbomachinery*. Tech. rep. NASA, 1984. URL: https://ntrs.nasa.gov/search.jsp?R=19850003728.

[2] H. Dogus Akaydin and Shishir A. Pandya. "Implementation of a body force model in OVERFLOW for propulsor simulations". In: *35th AIAA Applied Aerodynamics Conference, 2017*. Reston, Virginia: American Institute of Aeronautics and Astronautics, 2017. ISBN: 9781624105012. DOI: 10.2514/6.2017-3572. URL: https://arc.aiaa.org/doi/10.2514/6.2017-3572.

[3] Moritz Albert and Dieter Bestie. "Aerodynamic design optimization of nacelle and intake". In: *Proceedings of the ASME Turbo Expo*. Vol. 2. American Society of Mechanical Engineers Digital Collection, 2013. ISBN: 9780791855133. DOI: 10.1115/GT2013-94857.

[4] Steven R Allmaras, Forrester T Johnson, and Philippe R Spalart. *Modifications and Claricatations for the Implementation of the Spalart-Allmaras Turbulence Model*. Tech. rep. 2012, pp. 9–13.

[5] Kayla Aloyo, Christopher A. Perullo, and Dimitri N. Mavris. "An assessment of ultra high bypass engine architecture and installation considerations". In: *50th AIAA/ASME/SAE/ASEE Joint Propulsion Conference 2014*. American Institute of Aeronautics and Astronautics Inc., 2014. ISBN: 9781624103032. DOI: 10.2514/6.2014-3685.

[6] Antonis F. Antoniadis, Panagiotis Tsoutsanis, and Dimitris Drikakis. "Assessment of high-order finite volume methods on unstructured meshes for RANS solutions of aeronautical configurations". In: *Computers and Fluids* 146 (2017), pp. 86–104. ISSN: 00457930. DOI: 10.1016/j.compfluid.2017.01.002.

[7] Stephane Baralon, Lars-Erik Eriksson, and Ulf Hall. "Evaluation of Higher-Order Terms in the Throughflow Approximation Using 3D Navier-Stokes Computations of a Transonic Compressor Rotor". In: *Volume 1: Aircraft Engine; Marine; Turbomachinery; Microturbines and Small Turbomachinery*. American Society of Mechanical Engineers, 1999. ISBN: 978-0-7918-7858-3. DOI: 10.1115/99-GT-074. URL: https://asmedigitalcollection.asme.org/GT/proceedings/GT1999/78583/Indianapolis,Indiana,USA/248135.

[8] Stephane Baralon, Lars-Erik Eriksson, and Ulf Håll. "Validation of a Through-flow Time-Marching Finite-Volume Solver for Transonic Compressors". In: *Volume 1: Turbomachinery*. American Society of Mechanical Engineers, 1998. ISBN: 978-0-7918-7862-0. DOI: 10.1115/98-GT-047. URL: https://asmedigitalcollection.asme.org/GT/proceedings/GT1998/78620/Stockholm,Sweden/248452.

[9] Timoth Barth and Dennis Jespersen. "The design and application of upwind schemes on unstructured meshes". In: *27th Aerospace Sciences Meeting*. Reston, Virigina: American Institute of Aeronautics and Astronautics, 1989. DOI: 10.2514/6.1989-366. URL: http://arc.aiaa.org/doi/10.2514/6.1989-366.

[10] Sebastian Barthmes et al. "Unsteady CFD simulation of transonic axial Compressor stages with distorted inflow". In: *Notes on Numerical Fluid Mechanics and Multidisciplinary Design*. Ed. by Rolf Radespiel et al. Vol. 131. Springer, Cham, 2016, pp. 321–331. DOI: 10.1007/978-3-319-21127-5_18. URL: http://link.springer.com/10.1007/978-3-319-21127-5{_}18.

[11] P. Batten, M. A. Leschziner, and U. C. Goldberg. "Average-State Jacobians and Implicit Methods for Compressible Viscous and Turbulent Flows". In: *Journal of Computational Physics* 137.1 (1997), pp. 38–78. ISSN: 00219991. DOI: 10.1006/jcph.1997.5793.

[12] Emmanuel Benichou et al. "Body Force Modeling of the Aerodynamics of a Low-Speed Fan under Distorted Inflow". In: *International Journal of Turbomachinery, Propulsion and Power* 4.3 (2019), p. 29. ISSN: 2504-186X. DOI: 10.3390/ijtpp4030029. URL: https://www.mdpi.com/2504-186X/4/3/29.

[13] Scott Berger, Marsha; Aftosmis, Michael; Murman. *Analysis of Slope Limiters on Irregular Grids*. Tech. rep. NAS Tech. Rep NAS-05-007, 2005.

[14] Julien Berland, Christophe Bogey, and Christophe Bailly. "Low-dissipation and low-dispersion fourth-order Runge-Kutta algorithm". In: *Computers and Fluids* 35.10 (2006), pp. 1459–1463. ISSN: 00457930. DOI: 10.1016/j.compfluid.2005.04.003.

[15] Jeffrey J Berton and M.D. Guynn. "Multi-Objective Optimization of Turbofan Design Parameters for an Advanced, Single-Aisle Transport". In: *AIAA* September (2010), pp. 1–17. DOI: 10.2514/6.2010-9168. URL: http://arc.aiaa.org/doi/10.2514/6.2010-9168http://www-psao.grc.nasa.gov/publications/AIAA-2010-9168.pdf.

[16] J. Bijewitz et al. "Architectural Comparison of Advanced Ultra-High Bypass Ratio Turbofans for Mesium to Long Range Application". In: *Deutscher Luft- und Raumfhahrtkongress 2014*. DLR, 2014, p. 12. URL: http://www.dglr.de/publikationen/2015/340105.pdf.

[17] N. T. Birch. "2020 vision: the prospects for large civil aircraft propulsion". In: *Aeronautical Journal* 104.1038 (2000), pp. 347–352. ISSN: 00019240. DOI: 10.1017/s0001924000063971. URL: https://www.cambridge.org/core/journals/aeronautical-journal/article/2020-vision-the-prospects-for-large-civil-aircraft-propulsion/8D62D10E909787E2B9F047C7A11CE4FF.

[18] Jiri Blazek. *Computational Fluid Dynamics: Principles and Applications: Third Edition*. Elsevier Ltd, 2015, pp. 1–447. ISBN: 9780128011720. DOI: 10.1016/C2013-0-19038-1.

[19] J. Borradaile. "Towards the optimum ducted UHBR engine". In: *24th Joint Propulsion Conference*. Boston, MA: American Institute of Aeronautics and Astronautics (AIAA), 1988. DOI: 10.2514/6.1988-2954. URL: https://doi.org/10.2514/6.1988-2954.

[20] Anthony Bouchard. "Wall Distance Evaluation Via Eikonal Solver for RANS Applications". PhD thesis. Montreal: École Polytechnique de Montréal), 2017.

[21] Keith Michael Boyer. "An Improved Streamline Curvature Approach for Off-Design Analysis of Transonic Compression Systems". PhD Thesis. Virginia Polytechnic Institute and State University, 2001. URL: https://vtechworks.lib.vt.edu/handle/10919/27507.

[22] Maximilian Lewis; Brand. "An Improved Blade Passage Model for Estimating Off-Design Axial Compressor Performance". Master Thesis. Massachusetts Institute of Technology, 2013.

[23] Olaf Brodersen. "Computation of Engine-Airframe Installation Drag". In: *MEGAFLOW - Numerical Flow Simulation for Aircraft Design*. Ed. by Fassbender J.K Kroll N. Berlin: Springer Berlin Heidelberg, 2005, pp. 151–161. DOI: 10.1007/3-540-32382-1_11. URL: http://link.springer.com/10.1007/3-540-32382-1{_}11.

[24] Thierry Buffard and Stéphane Clain. "Monoslope and multislope MUSCL methods for unstructured meshes". In: *Journal of Computational Physics* 229.10 (2010), pp. 3745–3776. ISSN: 0021-9991. DOI: 10.1016/J.JCP.2010.01.026. URL: https://www.sciencedirect.com/science/article/pii/S0021999110000495?via{\%}3Dihub.

[25] Nicholas K. Burgess and Dimitri J. Mavriplis. "Robust computation of turbulent flows using a discontinuous Galerkin method". In: *50th AIAA Aerospace Sciences Meeting Including the New Horizons Forum and Aerospace Exposition*. 2012. DOI: 10.2514/6.2012-457.

[26] W Burgsmuller et al. "Preparation and Use of TPS-Technique for Low Speed Investigations on Transport Aircraft". In: *International Forum on Turbine Powered Simulation* (1995).

[27] Wolfgang Burgsmüller and Heinz Hoheisel. "ENIFAIR — EU research into engine integration on future transport aircraft". In: *Air & Space Europe* 2.2 (2000), pp. 81–85. ISSN: 1290-0958. DOI: 10.1016/S1290-0958(00)80047-7. URL: https://www.sciencedirect.com/science/article/pii/S1290095800800477.

[28] Alan Burlot et al. "Method comparison for fan performance in short intake nacelle". In: *2018 Applied Aerodynamics Conference*. Reston, Virginia: American Institute of Aeronautics and Astronautics, 2018. ISBN: 9781624105593. DOI: 10.2514/6.2018-4204. URL: https://arc.aiaa.org/doi/10.2514/6.2018-4204.

[29] Teng Cao, Paul Hield, and Paul G. Tucker. "Hierarchical immersed boundary method with smeared geometry". In: *Journal of Propulsion and Power*. Vol. 33. 5. Reston, Virginia: American Institute of Aeronautics and Astronautics, 2017, pp. 1151–1163. ISBN: 9781624103933. DOI: 10.2514/1.B36190. URL: http://arc.aiaa.org/doi/10.2514/6.2016-2130.

[30] Teng Cao et al. "Fan-Intake interaction under high incidence". In: *Journal of Engineering for Gas Turbines and Power* 139.4 (2017). ISSN: 15288919. DOI: 10.1115/1.4034701. URL: https://asmedigitalcollection.asme.org/gasturbinespower/article/doi/10.1115/1.4034701/444279/FanIntake-Interaction-Under-High-Incidence.

[31] Ismail B. Celik et al. "Procedure for estimation and reporting of uncertainty due to discretization in CFD applications". In: *Journal of Fluids Engineering, Transactions of the ASME* 130.7 (2008), pp. 0780011–0780014. ISSN: 00982202. DOI: 10.1115/1.2960953.

[32] Marco Ceze and Krzysztof J. Fidkowski. "Pseudo-transient continuation, solution update methods, and CFL strategies for DG discretizations of the RANS-SA equations". In: *21st AIAA Computational Fluid Dynamics Conference*. 2013. DOI: 10.2514/6.2013-2686.

[33] A. W. Chen and E. N. Tinoco. "PAN AIR applications to aero-propulsion integration". In: *Journal of Aircraft* 21.3 (1984), pp. 161–167. ISSN: 00218669. DOI: 10.2514/3.48241. URL: https://arc.aiaa.org/doi/10.2514/3.48241.

[34] R. F. Chen and Z. J. Wang. "Fast, block lower-upper symmetric Gauss-Seidel scheme for arbitrary grids". In: *AIAA journal* 38.12 (2000), pp. 2238–2245. ISSN: 00011452. DOI: 10.2514/2.914.

[35] R. V. Chima. "A three-dimensional unsteady CFD model of compressor stability". In: *Proceedings of the ASME Turbo Expo*. Vol. 6 PART B. ASMEDC, 2006, pp. 1157–1168. ISBN: 079184241X. DOI: 10.1115/GT2006-90040. URL: https://asmedigitalcollection.asme.org/GT/proceedings/GT2006/4241X/1157/316830.

[36] R. V. Chima et al. "CFD models of a serpentine inlet, fan, and nozzle". In: *48th AIAA Aerospace Sciences Meeting Including the New Horizons Forum and Aerospace Exposition*. Reston, Virigina: American Institute of Aeronautics and Astronautics, 2010. ISBN: 9781600867392. DOI: 10.2514/6.2010-33. URL: http://arc.aiaa.org/doi/10.2514/6.2010-33.

[37] Taek Jin; Choi. "Development of an effective computational methodology for multi-stage compressor map generation". Master Thesis. Massachusetts Institute of Technology, 2001.

[38] Monica D. Christiansen and Russel L. Thornock. "Propulsion aerodynamic workshop III, performance analyses of a dual separate flow reference nozzle, dual confluent flow reference nozzle, and two single flow convergent nozzles". In: *53rd AIAA/SAE/ASEE Joint Propulsion Conference, 2017*. American Institute of Aeronautics and Astronautics Inc, AIAA, 2017. ISBN: 9781624105111. DOI: 10.2514/6.2017-4659.

[39] Robert Christie. "Propulsion System Integration and Modelling Synthesis". PhD Thesis. University of Cranfield, 2016, p. 227.

[40] Robert Christie, Alexander Heidebrecht, and David MacManus. "An automated approach to nacelle parameterization using intuitive class shape transformation curves". In: *Journal of Engineering for Gas Turbines and Power* 139.6 (2017). ISSN: 15288919. DOI: 10.1115/1.4035283.

[41] P. Cinnella and C. Content. "High-order implicit residual smoothing time scheme for direct and large eddy simulations of compressible flows". In: *Journal of Computational Physics* 326 (2016), pp. 1–29. ISSN: 10902716. DOI: 10.1016/j.jcp.2016.08.023.

[42] S. Clain, D. Rochette, and R. Touzani. "A multislope MUSCL method on unstructured meshes applied to compressible Euler equations for axisymmetric swirling flows". In: *Journal of Computational Physics* 229.13 (2010), pp. 4884–4906. ISSN: 10902716. DOI: 10.1016/j.jcp.2010.03.004. URL: https://linkinghub.elsevier.com/retrieve/pii/S0021999110001142.

[43] Yann Colin. " Simulation numérique de la distorsion générée par une entrée d'air de moteur civil par vent de travers". PhD thesis. Université de Tolouse - ISAE, 2007.

[44] European Commission. *A Vision for 2020*. Tech. rep. Luxembourg: European Commission, 2001. URL: https://www.acare4europe.org/sites/acare4europe.org/files/document/Vision2020{_}0.pdf.

[45] ENOVAL Consortium. *ENOVAL Technology Brochure*. Tech. rep. EIMG, 2018, p. 46. URL: www.enoval.eu.

[46] Madeleine Coutanceau and Roger Bouard. "Experimental determination of the main features of the viscous flow in the wake of a circular cylinder in uniform translation. Part 1. Steady flow". In: *Journal of Fluid Mechanics* 79.2 (1977), pp. 231–256. ISSN: 14697645. DOI: 10.1017/S0022112077000135.

[47] Eugene E. Covert. *Thrust and Drag of Aircraft: Prediction and Verification*. Progress in astronautics and aeronautics. American Institute of Aeronautics and Astronautics, 1984, pp. 213–223. ISBN: 9780930403003. DOI: 10.2514/6.1984-611.

[48] Jiahuan Cui et al. "Low order modeling for fan and outlet guide vanes in aeroengines". In: *Journal of Turbomachinery* 141.3 (2019). ISSN: 15288900. DOI: 10.1115/1.4042202. URL: https://asmedigitalcollection.asme.org/GT/proceedings/GT2018/51012/Oslo,Norway/272377.

[49] David L. Daggett, Stephen T. Brown, and Ron T. Kawai. *Ultra-efficient Engine Diameter Study*. Tech. rep. NASA, 2003. URL: https://ntrs.nasa.gov/search.jsp?R=20030061085.

[50] S. V. Damle, T. Q. Dang, and D. R. Reddy. "Throughflow method for turbomachines applicable for all flow regimes". In: *Journal of Turbomachinery* 119.2 (1997), pp. 256–262. ISSN: 15288900. DOI: 10.1115/1.2841108. URL: https://asmedigitalcollection.asme.org/turbomachinery/article/119/2/256/420364/Throughflow-Method-for-Turbomachines-Applicable.

[51] R Davy et al. "Installation Effects Characterization of VHBPR engine PART II: Experimental study using Particle Image Velocimetry". In: *AIAA paper, AIAA* 3253 (2009), p. 2009.

[52] R. Decher and D. Tegler. "High accuracy force accounting procedures for turbopowered simulatortesting". In: *11th Propulsion Conference*. 1975. DOI: 10.2514/6.1975-1324. URL: https://arc.aiaa.org/doi/abs/10.2514/6.1975-1324.

[53] J. J. Defoe, M. Etemadi, and D. K. Hall. "Fan Performance Scaling With Inlet Distortions". In: *Journal of Turbomachinery* 140.7 (2018). ISSN: 0889-504X. DOI: 10.1115/1.4039433. URL: https://asmedigitalcollection.asme.org/turbomachinery/article/doi/10.1115/1.4039433/369489/Fan-Performance-Scaling-With-Inlet-Distortions.

[54] Jeffrey Defoe, Alex Narkaj, and Zoltan Spakovszky. "A Body-Force Based Methodology For Predicting Multiple-Pure-Tone Noise: Validation". In: *16th AIAA/CEAS Aeroacoustics Conference*. Reston, Virigina: American Institute of Aeronautics and Astronautics, 2010. ISBN: 978-1-60086-955-6. DOI: 10.2514/6.2010-3747. URL: http://arc.aiaa.org/doi/10.2514/6.2010-3747.

[55] Jeffrey Defoe, Alexander Narkaj, and Z. S. Spakovszky. "A novel MPT noise prediction methodology for highly-integrated propulsion systems with inlet flow distortion". In: *15th AIAA/CEAS Aeroacoustics Conference (30th AIAA Aeroacoustics Conference)*. Reston, Virigina: American Institute of Aeronautics and Astronautics, 2009. ISBN: 9781563479748. DOI: 10.2514/6.2009-3366. URL: http://arc.aiaa.org/doi/10.2514/6.2009-3366.

[56] Christopher T. DeGroot and Anthony G. Straatman. "A finite-volume model for fluid flow and nonequilibrium heat transfer in conjugate fluid-porous domains using general unstructured grids". In: *Numerical Heat Transfer, Part B: Fundamentals* 60.4 (2011), pp. 252–277. ISSN: 10407790. DOI: 10.1080/10407790.2011.601180. URL: http://www.tandfonline.com/doi/abs/10.1080/10407790.2011.601180.

[57] Mandeep Deka et al. "A new Green–Gauss reconstruction on unstructured meshes. Part I: Gradient reconstruction". In: *Journal of Computational Physics* (2018). ISSN: 0021-9991. DOI: 10.1016/J.JCP.2018.10.023. URL: https://www.sciencedirect.com/science/article/pii/S0021999118306909?via{\%}3Dihub.

[58] Yeming Deng, Yufei Zhang, and Haixin Chen. "Drag prediction and decomposition of a real aircraft based on middle-field and far-field methods". In: *7th European Conference for Aeronautics and Space Ciences* C (2017). DOI: 10.13009/EUCASS2017-380. URL: https://www.eucass.eu/doi/EUCASS2017-380.pdf.

[59] J. D. Denton. "Throughflow Calculations for Transonic Axial Flow Turbines". In: *Journal of Engineering for Power* 100.2 (1978), pp. 212–218. ISSN: 0022-0825. DOI: 10.1115/1.3446336. URL: https://asmedigitalcollection.asme.org/gasturbinespower/article/100/2/212/403866/Throughflow-Calculations-for-Transonic-Axial-Flow.

[60] J. D. Denton and W. N. Dawes. "Computational fluid dynamics for turbomachinery design". In: *Proceedings of the Institution of Mechanical Engineers, Part C: Journal of Mechanical Engineering* 213.2 (1999), pp. 107–124. ISSN: 09544062. DOI: 10.1243/0954406991522211. URL: http://journals.sagepub.com/doi/10.1243/0954406991522211.

[61] D. Destarac and J. Van Der Vooren. "Drag/thrust analysis of jet-propelled transonic transport aircraft; Definition of physical drag components". In: *Aerospace Science and Technology* 8.6 (2004), pp. 545–556. ISSN: 12709638. DOI: 10.1016/j.ast.2004.03.004.

[62] R. Devine et al. "Comparison of conventional and compression pylon designs for an under wing nacelle". In: *Journal of Aircraft* 46.1 (2009), pp. 325–328. ISSN: 00218669. DOI: 10.2514/1.34967. URL: https://arc.aiaa.org/doi/10.2514/1.34967.

[63] F Dezitter et al. "Installation effects characterization of VHBR engines part III: CFD assessment for jet mixing". In: *AIAA paper, AIAA* 3370 (2009), p. 2009.

[64] Boris Diskin and James Thomas. *Accuracy of Gradient Reconstruction on Grids with High Aspect Ratio*. Tech. rep. NIA, 2008. URL: https://ntrs.nasa.gov/archive/nasa/casi.ntrs.nasa.gov/20090007493.pdf.

[65] Boris Diskin and James L. Thomas. "Comparison of Node-Centered and Cell-Centered Unstructured Finite-Volume Discretizations: Inviscid Fluxes". In: *AIAA Journal* 49.4 (2011), pp. 836–854. ISSN: 0001-1452. DOI: 10.2514/1.J050897. URL: https://arc.aiaa.org/doi/10.2514/1.J050897.

[66] G. Doornbos and W. B. De Wolf. *Engine/Airframe Interference Drag At Cruise Conditions, Using Propulsion Simulation.* Tech. rep. NLR TR 82012 U. Marknesse: NLR, 1982.

[67] D. Dusa, D. Lahti, and D. Berry. "Investigation of subsonic nacelle performance improvement concept". In: American Institute of Aeronautics and Astronautics (AIAA), 1982. DOI: 10.2514/6.1982-1042.

[68] Richard P. Dwight, Peter Lucas, and Hester Bijl. "Solution Methods and Acceleration Techniques in Computational Fluid Dynamics (CFD)". In: *Encyclopedia of Aerospace Engineering*. Chichester, UK: John Wiley & Sons, Ltd, 2010. DOI: 10.1002/9780470686652.eae062. URL: http://doi.wiley.com/10.1002/9780470686652.eae062.

[69] D. Eckert et al. "Low speed twin engine simulation on a large scale transport aircraft model in the DNW". In: *International Counsil of the Aeronautical Sciences*. International Counsil of the Aeronautical Sciences. 1982.

[70] Boris Epstein and Sergey Peigin. "Automatic Optimization of Wing–Body–Under-the-Wing-Mounted-Nacelle Configurations". In: *Journal of Aircraft* 53.3 (2016), pp. 691–700. ISSN: 0021-8669. DOI: 10.2514/1.C033641. URL: http://arc.aiaa.org/doi/10.2514/1.C033641.

[71] S. D. Erbslõh, W. J. Crowthert, and J. R. Frutos. "Control of compressor face total pressure distortion on a high bypass turbofan intake using air-jet vortex generators". In: *2nd AIAA Flow Control Conference*. Reston, Viriginia: American Institute of Aeronautics and Astronautics, 2004. ISBN: 9781624100307. DOI: 10.2514/6.2004-2206. URL: http://arc.aiaa.org/doi/10.2514/6.2004-2206.

[72] European Commission. *FlightPath 2050*. Tech. rep. Luxembourg: ACARE, 2011. DOI: 10.2777/50266. URL: https://ec.europa.eu/transport/sites/transport/files/modes/air/doc/flightpath2050.pdf.

[73] Yitong Fan and Weipeng Li. "Review of far-field drag decomposition methods for aircraft design". In: *Journal of Aircraft* 56.1 (2019), pp. 11–21. ISSN: 00218669. DOI: 10.2514/1.C034781. URL: https://arc.aiaa.org/doi/10.2514/1.C034781.

[74] Xiaoming Fang, Yufei Zhang, and Haixin Chen. "Transonic nacelle aerodynamic optimization based on hybrid genetic algorithm". In: *17th AIAA/ISSMO Multidisciplinary Analysis and Optimization Conference*. American Institute of Aeronautics and Astronautics Inc, AIAA, 2016. ISBN: 9781624104398. DOI: 10.2514/6.2016-3833.

[75] James Felder, Hyun Kim, and Gerald Brown. "Turboelectric Distributed Propulsion Engine Cycle Analysis for Hybrid-Wing-Body Aircraft". In: *47th AIAA Aerospace Sciences Meeting including The New Horizons Forum and Aerospace Exposition*. 2009. DOI: 10.2514/6.2009-1132. eprint: https://arc.aiaa.org/doi/pdf/10.2514/6.2009-1132. URL: https://arc.aiaa.org/doi/abs/10.2514/6.2009-1132.

[76] S. J. Gallimore. "Viscous throughflow modeling of axial compressor bladerows using a tangential blade force hypothesisr". In: *Journal of Turbomachinery* 120.4 (1998), pp. 662–670. ISSN: 15288900. DOI: 10.1115/1.2841775. URL: https://asmedigitalcollection.asme.org/turbomachinery/article/120/4/662/438822/Viscous-Throughflow-Modeling-of-Axial-Compressor.

[77] H. E. Gallus, C. A. Poensgen, and J. Zeschky. "Three-Dimensional Unsteady Flow in a Single Stage Axial-Flow Turbine and Compressor". In: *Unsteady Aerodynamics, Aeroacoustics, and Aeroelasticity of Turbomachines and Propellers*. New York, NY: Springer New York, 1993, pp. 487–505. DOI: 10.1007/978-1-4613-9341-2_24. URL: http://link.springer.com/10.1007/978-1-4613-9341-2{_}24.

[78] M. G. Gasparo and S. Pieraccini. "Implicit residual smoothing in a parallel 2D explicit Euler solver". In: *International Journal of Computer Mathematics* 72.3 (1999), pp. 313–324. ISSN: 00207160. DOI: 10.1080/00207169908804855.

[79] Heiko Geyr and Cord Rossow. "A Correct Thrust Determination Method for Turbine Powered Simulators in Wind Tunnel Testing". In: *41st AIAA/ASME/SAE/ASEE Joint Propulsion Conference & Exhibit*. Reston, Viriginia: American Institute of Aeronautics and Astronautics, 2005. ISBN: 978-1-62410-063-5. DOI: 10.2514/6.2005-3707. URL: http://arc.aiaa.org/doi/abs/10.2514/6.2005-3707.

[80] U. Ghia, K. N. Ghia, and C. T. Shin. "High-Re solutions for incompressible flow using the Navier-Stokes equations and a multigrid method". In: *Journal of Computational Physics* 48.3 (1982), pp. 387–411. ISSN: 10902716. DOI: 10.1016/0021-9991(82)90058-4.

[81] Daniel Giesecke et al. "Evaluation of ultra-high bypass ratio engines for an overwing aircraft configuration". In: *Journal of the Global Power and Propulsion Society* 2 (2018), pp. 493–515. DOI: 10.22261/JGPPS.8SHP7K. URL: http://dx.doi.org/10.22261/JGPPS.8SHP7K.

[82] H. Glauert. *The Elements of Aerofoil and Airscrew Theory*. Cambridge: Cambridge University Press, 1983. ISBN: 9780511574481. DOI: 10.1017/CBO9780511574481. URL: http://ebooks.cambridge.org/ref/id/CBO9780511574481.

[83] Benjamin Godard, Edouard de Jaeghere, and Nicolas Gourdain. "Efficient design investigation of a turbofan in distorted inlet conditions". In: *Proceedings of the ASME Turbo Expo*. Vol. 2A-2019. American Society of Mechanical Engineers (ASME), 2019. ISBN: 9780791858554. DOI: 10.1115/GT2019-90471.

[84] Benjamin Godard et al. "Methodologies for turbofan inlet aerodynamics prediction". In: *35th AIAA Applied Aerodynamics Conference, 2017*. American Institute of Aeronautics and Astronautics Inc, AIAA, 2017. ISBN: 9781624105012. DOI: 10.2514/6.2017-3413.

[85] Benjamin Godard et al. "Methodologies for Turbofan Inlet Aerodynamics Prediction". In: *35th AIAA Applied Aerodynamics Conference*. Reston, Virginia: American Institute of Aeronautics and Astronautics, 2017. ISBN: 978-1-62410-501-2. DOI: 10.2514/6.2017-3413. URL: https://arc.aiaa.org/doi/10.2514/6.2017-3413.

[86] E.L. Goldsmith and J. Seddon. *Practical intake aerodynamic design*. AIAA education series. American Institute of Aeronautics and Astronautics, 1993. ISBN: 9781563470646. URL: https://books.google.it/books?id=8-tGAQAAIAAJ.

[87] Yifang Gong. "A computational model for rotating stall and inlet distortions in multistage compressors". PhD Thesis. Massachussets Institute of Technology, 1999.

[88] A. D. Gosman. *Heat and mass transfer in recirculating flows*. Academic Press, 1969, p. 338. ISBN: 0122919505.

[89] Sigal Gottlieb and Chi-Wang Shu. "Total variation diminishing Runge-Kutta schemes". In: *Mathematics of Computation of the American Mathematical Society* 67.221 (1998), pp. 73–85. ISSN: 0025-5718. DOI: 10.1090/s0025-5718-98-00913-2.

[90] Ioannis Goulos et al. "Aerodynamic Design of Separate-Jet Exhausts for Future Civil Aero-engines - Part I: Parametric Geometry Definition and Computational Fluid Dynamics Approach". In: *Journal of Engineering for Gas Turbines and Power* 138.8 (2016). ISSN: 15288919. DOI: 10.1115/1.4032649.

[91] Ioannis Goulos et al. "Aerodynamic Design of Separate-Jet Exhausts for Future Civil Aero-engines - Part II: Design Space Exploration, Surrogate Modeling, and Optimization". In: *Journal of Engineering for Gas Turbines and Power* 138.8 (2016). ISSN: 15288919. DOI: 10.1115/1.4032652.

[92] W. R. Graham, C. A. Hall, and M. Vera Morales. "The potential of future aircraft technology for noise and pollutant emissions reduction". In: *Transport Policy* 34 (2014), pp. 36–51. ISSN: 0967070X. DOI: 10.1016/j.tranpol.2014.02.017. URL: https://www.sciencedirect.com/science/article/abs/pii/S0967070X14000481?via{\%}3Dihub.

[93] A. Guha. "Optimum fan pressure ratio for bypass engines with separate or mixed exhaust streams". In: *Journal of Propulsion and Power* 17.5 (2001), pp. 1117–1122. ISSN: 07484658. DOI: 10.2514/2.5852. URL: http://arc.aiaa.org/doi/abs/10.2514/2.5852.

[94] E. Guilmineau and P. Queutey. "A numerical simulation of vortex shedding from an oscillating circular cylinder". In: *Journal of Fluids and Structures* 16.6 (2002), pp. 773–794. ISSN: 08899746. DOI: 10.1006/jfls.2002.0449.

[95] Jin Guo and Jun Hu. "A three-dimensional computational model for inlet distortion in fan and compressor". In: *Proceedings of the Institution of Mechanical Engineers, Part A: Journal of Power and Energy* 232.2 (2018), pp. 144–156. ISSN: 20412967. DOI: 10.1177/0957650917719811. URL: http://journals.sagepub.com/doi/10.1177/0957650917719811.

[96] Mark D. Guynn et al. *Refined Exploration of Turbofan Design Options for an Advanced Single-Aisle Transport*. Tech. rep. NASA, 2011. URL: https://ntrs.nasa.gov/search.jsp?R=20110004165.

[97] R. Haelterman, J. Vierendeels, and D. Van Heule. "Optimization of the Runge-Kutta iteration with residual smoothing". In: *Journal of Computational and Applied Mathematics* 234.1 (2010), pp. 253–271. ISSN: 03770427. DOI: 10.1016/j.cam.2009.12.023.

[98] F. Haider, J.-P. Croisille, and B. Courbet. "Stability analysis of the cell centered finite-volume Muscl method on unstructured grids". In: *Numerische Mathematik* 113.4 (2009), pp. 555–600. ISSN: 0029-599X. DOI: 10.1007/s00211-009-0242-6. URL: http://link.springer.com/10.1007/s00211-009-0242-6.

[99] Cesare A. Hall and Daniel Crichton. "Engine Design Studies for a Silent Aircraft". In: *Journal of Turbomachinery* 129.3 (July 2006). Ed. by ASME, pp. 479–487. ISSN: 0889-504X. DOI: 10.1115/1.2472398. eprint: https://asmedigitalcollection.asme.org/turbomachinery/article-pdf/129/3/479/5728241/479_1.pdf. URL: https://doi.org/10.1115/1.2472398.

[100] D. K. Hall, E. M. Greitzer, and C. S. Tan. "Analysis of fan stage conceptual design attributes for boundary layer ingestion". In: *Journal of Turbomachinery* 139.7 (2017). ISSN: 15288900. DOI: 10.1115/1.4035631. URL: https://asmedigitalcollection.asme.org/turbomachinery/article/doi/10.1115/1.4035631/378863/Analysis-of-Fan-Stage-Conceptual-Design-Attributes.

[101] David Kenneth Hall. "Analysis of Civil Aircraft Propulsors with Boundary Layer Ingestion". PhD Thesis. Massachusetts Institute of Technology, 2015.

[102] G. W. Hall. "Application of Boundary Layer Theory to Explain Some Nozzle and Venturi Flow Peculiarities". In: *Proceedings of the Institution of Mechanical Engineers* 173.1 (1959), pp. 837–870. ISSN: 0020-3483. DOI: 10.1243/pime_proc_1959_173_066_02.

[103] A. E. Harris, J. T. Kutney, and F. B. Ogilvie. "25 years of turbine powered simulation succes". In: *International Forum on Turbine Powered Simulation*. International Forum on Turbine Powered Simulation. 1995.

[104] Ami Harten. "High resolution schemes for hyperbolic conservation laws". In: *Journal of Computational Physics* 49.3 (1983), pp. 357–393. ISSN: 10902716. DOI: 10.1016/0021-9991(83)90136-5. URL: https://www.sciencedirect.com/science/article/pii/0021999183901365.

[105] Jakob P. Haug and Reinhard Niehuis. "Full annulus simulations of a transonic axial compressor stage with distorted inflow at transonic and subsonic blade tip speed". In: *12th European Conference on Turbomachinery Fluid Dynamics and Thermodynamics, ETC 2017*. Vol. 3. 1. Multidisciplinary Digital Publishing Institute, 2017, p. 7. DOI: 10.3390/ijtpp3010007. URL: http://www.mdpi.com/2504-186X/3/1/7.

[106] David Jarrod Hill. "Compressor Performance Scaling in the Presence of Non-Uniform Flow". PhD Thesis. University of Windsor, 2017.

[107] Charles Hirsch. *Numerical Computation of Internal and External Flows: The Fundamentals of Computational Fluid Dynamics*. Elsevier Ltd, 2007. ISBN: 9780750665940. DOI: 10.1016/B978-0-7506-6594-0.X5037-1.

[108] BK Hodder. *An investigation of engine influence on inlet performance (conducted in the Ames 40- by 80-foot wind tunnel)*. Tech. rep. Seattle, WA: NASA, 1981. URL: https://ntrs.nasa.gov/search.jsp?R=19810021546http://scholar.google.com/scholar?hl=en{\&}btnG=Search{\&}q=intitle:An+investigation+of+engine+influence+on+inlet+performance(conducted+in+the+Ames+40-+by+80-foot+wind+tunnel){\#}0.

[109] H. Hoheisel. "Aerodynamic aspects of engine-aircraft integration of transport aircraft". In: *Aerospace Science and Technology* 1.7 (1997), pp. 475–487. ISSN: 1270-9638. DOI: 10.1016/S1270-9638(97)90009-2. URL: https://www.sciencedirect.com/science/article/abs/pii/S1270963897900092.

[110] H. Hoheisel, H. Frhr, and V. Geyr. "The influence of engine thrust behaviour on the aerodynamics of engine airframe integration". In: *CEAS Aeronautical Journal* 3.1 (2012), pp. 79–92. ISSN: 18695590. DOI: 10.1007/s13272-012-0044-x.

[111] John R. Hooker et al. "Over wing nacelle installations for improved energy efficiency". In: *31st AIAA Applied Aerodynamics Conference*. Reston, Virginia: American Institute of Aeronautics and Astronautics, 2013. DOI: 10.2514/6.2013-2920. URL: http://arc.aiaa.org/doi/10.2514/6.2013-2920.

[112] M. A. Howard and S. J. Gallimore. "Viscous Throughflow Modeling for Multistage Compressor Design". In: *Journal of Turbomachinery* 115.2 (1993), pp. 296–304. ISSN: 0889-504X. DOI: 10.1115/1.2929235. URL: https://asmedigitalcollection.asme.org/turbomachinery/article/115/2/296/419942/Viscous-Throughflow-Modeling-for-Multistage.

[113] Entsung Hsiao et al. "Actuator duct model of turbomachinery components for powered-nacelle Navier-Stokes calculations". In: *Journal of Propulsion and Power* 17.4 (2001), pp. 919–927. ISSN: 07484658. DOI: 10.2514/2.5825. URL: https://arc.aiaa.org/doi/10.2514/2.5825.

[114] M. E. Hubbard. "Multidimensional Slope Limiters for MUSCL-Type Finite Volume Schemes on Unstructured Grids". In: *Journal of Computational Physics* 155.1 (1999), pp. 54–74. ISSN: 00219991. DOI: 10.1006/jcph.1999.6329. URL: https://www.sciencedirect.com/science/article/pii/S0021999199963295.

[115] J. D. Hubble and R. E. Smith. *Evaluation of an Airjet Distortion Generator Used to Produce Steady- State, Total-Pressure Distortion at the Inlet of a General Electric F101-GE-100 Turbofan Engine*. Tech. rep. US Dept of the Air Force, 1979. DOI: 10.21236/ADA072743. URL: http://www.dtic.mil/docs/citations/ADA072743.

[116] Jerome Huber et al. "Characterization of Installation Effects for HBPR Engine, Part 4: Assessment of Jet Acoustics". In: *15th AIAA/CEAS Aeroacoustics Conference (30th AIAA Aeroacoustics Conference)*. 2009. DOI: 10.2514/6.2009-3371. eprint: https://arc.aiaa.org/doi/pdf/10.2514/6.2009-3371. URL: https://arc.aiaa.org/doi/abs/10.2514/6.2009-3371.

[117] David Hue, Quentin Chanzy, and Sâm Landier. "DPW-6: Drag analyses and increments using different geometries of the common research model airliner". In: *Journal of Aircraft* 55.4 (2018), pp. 1509–1521. ISSN: 00218669. DOI: 10.2514/1.C034139. URL: https://arc.aiaa.org/doi/10.2514/1.C034139.

[118] Christopher E. Hughes. *Aerodynamic Performance of Scale-Model Turbofan Outlet Guide Vanes Designed for Low Noise*. Tech. rep. Cleveland, Ohio: NASA Glenn Research Center, 2001, p. 38.

[119] Christopher E. Hughes. "Aircraft engine technology for green aviation to reduce fuel burn". In: *3rd AIAA Atmospheric Space Environments Conference*. Reston, Viriginia: American Institute of Aeronautics and Astronautics, 2011. ISBN: 9781624101434. DOI: 10.2514/6.2011-3531. URL: http://arc.aiaa.org/doi/10.2514/6.2011-3531.

[120] Christopher E. Hughes et al. *Fan Noise Source Diagnostic Test - Rotor Alone Aerodynamic Performance Results*. Tech. rep. Cleveland, Ohio: NASA Glenn Research Center, 2005, p. 28.

[121] Francesca Iacono and Georg May. "Convergence acceleration for simulation of steady-state compressible flows using high-order schemes". In: *19th AIAA Computational Fluid Dynamics Conference*. 2009. ISBN: 9781563479755. DOI: 10.2514/6.2009-4132.

[122] IATA. *IATA Vision 2050*. Tech. rep. Singapore: IATA, 2011. URL: https://www.iata.org/pressroom/facts{_}figures/documents/vision-2050.pdf.

[123] R. Jackson, N.B. Wood, and A. Boston. "The efficient modeling of blade lean effects within the turbomachinery throughflow method". In: *International Journal of Heat and Fluid Flow* 10.1 (1989), pp. 32–39. ISSN: 0142-727X. DOI: 10.1016/0142-727X(89)90052-0. URL: https://www.sciencedirect.com/science/article/pii/0142727X89900520.

[124] Alireza Jalali and Carl F. Ollivier Gooch. "Higher-Order Finite Volume Solution Reconstruction on Highly Anisotropic Meshes". In: *21st AIAA Computational Fluid Dynamics Conference*. Reston, Virginia: American Institute of Aeronautics and Astronautics, 2013. DOI: 10.2514/6.2013-2565. URL: http://arc.aiaa.org/doi/10.2514/6.2013-2565.

[125] I. K. Jennions and P. Stow. "A Quasi-Three-Dimensional Turbomachinery Blade Design System: Part I—Throughflow Analysis". In: *Journal of Engineering for Gas Turbines and Power* 107.2 (1985), pp. 301–307. ISSN: 0742-4795. DOI: 10.1115/1.3239715. URL: https://asmedigitalcollection.asme.org/gasturbinespower/

article/107/2/301/407963/A-QuasiThreeDimensional-Turbomachinery-Blade.

[126] Hai-liang Jin et al. "A time-marching throughflow model and its application in transonic axial compressor". In: *Journal of Thermal Science* 19.6 (2010), pp. 519–525. ISSN: 1003-2169. DOI: 10.1007/s11630-010-0418-5. URL: http://link.springer.com/10.1007/s11630-010-0418-5.

[127] W. G. Joo and T. P. Hynes. "The application of actuator disks to calculations of the flow in turbofan installations". In: *Journal of Turbomachinery* 119.4 (1997), pp. 733–741. ISSN: 15288900. DOI: 10.1115/1.2841183. URL: https://asmedigitalcollection.asme.org/turbomachinery/article/119/4/733/436674/The-Application-of-Actuator-Disks-to-Calculations.

[128] George Karypis and Vipin Kumar. "Multilevelk-way Partitioning Scheme for Irregular Graphs". In: *Journal of Parallel and Distributed Computing* 48.1 (1998), pp. 96–129. ISSN: 07437315. DOI: 10.1006/jpdc.1997.1404.

[129] Aaron Katz and Venkateswaran Sankaran. "High aspect ratio grid effects on the accuracy of Navier–Stokes solutions on unstructured meshes". In: *Computers & Fluids* 65 (2012), pp. 66–79. ISSN: 0045-7930. DOI: 10.1016/J.COMPFLUID.2012.02.012. URL: https://www.sciencedirect.com/science/article/abs/pii/S0045793012000667?via{\%}3Dihub.

[130] Stefan Kennedy et al. "Computational investigation of inlet distortion at high angles of attack". In: *Journal of Aircraft* 51.2 (2014), pp. 361–376. ISSN: 00218669. DOI: 10.2514/1.C031789. URL: http://arc.aiaa.org/doi/10.2514/1.C031789.

[131] Jonathan; Kerner. "An Assessment of Body Force Representations for Compressor Stall Simulation". Master Thesis. Massachusetts Institute of Technology, 2010.

[132] Brian K. Kestner et al. "Ultra high bypass ratio engine sizing and cycle selection study for a subsonic commercial aircraft in the N+2 timeframe". In: *Proceedings of the ASME Turbo Expo*. Vol. 1. American Society of Mechanical Engineers (ASME), 2011, pp. 127–137. DOI: 10.1115/GT2011-45370.

[133] Hyoungjin Kim and Meng Sing Liou. "Flow simulation and optimal shape design of N3-X hybrid wing body configuration using a body force method". In: *Aerospace Science and Technology* 71 (2017), pp. 661–674. ISSN: 12709638. DOI: 10.1016/j.ast.2017.09.046.

[134] Joo Sung Kim and Oh Joon Kwon. "Improvement on Block LU-SGS scheme for unstructured mesh Navier-Stokes computations". In: *40th AIAA Aerospace Sciences Meeting and Exhibit*. 2002. DOI: 10.2514/6.2002-1061.

[135] George; Kiwada. "Development of a Body Force Description for Compressor Stability Assessment". Master Thesis. Massachusetts Institute of Technology, 2008.

[136] Salim Koc, Hyoung Jin Kim, and Kazuhiro Nakahashi. "Aerodynamic design of wing-body-nacelle-pylon configuration". In: *17th AIAA Computational Fluid Dynamics Conference*. Reston, Viriginia: American Institute of Aeronautics and Astronautics, 2005. ISBN: 9781624100536. DOI: 10.2514/6.2005-4856. URL: http://arc.aiaa.org/doi/10.2514/6.2005-4856.

[137] J. W. Kooi, L. de Haij, and G. H. Hegen. "Engine simulation with turbofan powered simulators in the german-dutch wind tunnels". In: *22nd AIAA Aerodynamic Measurement Technology and Ground Testing Conference*. 2002. DOI: 10.2514/6.2002-2919. URL: https://arc.aiaa.org/doi/abs/10.2514/6.2002-2919.

[138] Joost Kooi et al. "TPS Calibration Procedures". In: *International Forum on Turbine Powered Simulation* (1995).

[139] Anjaney Pramod; Kottapalli. "Development of a Body Force Model for Centrifugal Compressors". Master Thesis. Massachusetts Institute of Technology, 2013.

[140] Ganesh Krishnan, Christopher A. Perullo, and Dimitri N. Mavris. "An assessment of relative technology benefits of a variable pitch fan and variable area nozzle". In: *49th AIAA/ASME/SAE/ASEE Joint Propulsion Conference*. Reston, Virginia: American Institute of Aeronautics and Astronautics, 2013. ISBN: 9781624102226. DOI: 10.2514/6.2013-3604. URL: http://arc.aiaa.org/doi/10.2514/6.2013-3604.

[141] Brenda M. Kulfan. "Universal parametric geometry representation method". In: *Journal of Aircraft*. Vol. 45. 1. 2008, pp. 142–158. DOI: 10.2514/1.29958.

[142] Brenda M. Kulfan and John E. Bussoletti. ""Fundamental" parametric geometry representations for aircraft component shapes". In: *Collection of Technical Papers - 11th AIAA/ISSMO Multidisciplinary Analysis and Optimization Conference*. Vol. 1. 2006, pp. 547–591. ISBN: 1563478234. DOI: 10.2514/6.2006-6948.

[143] R.; L. Wiart; O. Atinault; J.-C. Boniface; Barrier. "Aeropropulsive Performance of the NOVA Configurations". In: *30th Congress of the International Council of the Aeronautical Sciences*. Daejeon, Korea: ICAS, 2016. URL: http://www.icas.org/ICAS{_}ARCHIVE/ICAS2016/data/papers/2016{_}0092{_}paper.pdf.

[144] Martin Laban, B. Soemarwoto, and Joost Kooi. "Reshaping Engine Nacelles for Testing in Wind Tunnels with Turbofan Propulsion Simulators". In: American Institute of Aeronautics and Astronautics (AIAA), 2005. DOI: 10.2514/6.2005-3703.

[145] Michael J. Larkin and Paul S. Schweige. *Ultra High Bypass Nacelle Aerodynamics*. Tech. rep. NASA, 1992, p. 73.

[146] ASME, ed. *Conceptual Design and Mission Analysis for a Geared Turbofan and an Open Rotor Configuration*. Vol. Volume 1: Aircraft Engine; Ceramics; Coal, Biomass and Alternative Fuels; Wind Turbine Technology. Turbo Expo: Power for Land, Sea, and Air. June 2011, pp. 359–370. DOI: 10.1115/GT2011-46451. eprint: https://asmedigitalcollection.asme.org/GT/proceedings-pdf/GT2011/54617/359/2756082/359_1.pdf. URL: https://doi.org/10.1115/GT2011-46451.

[147] B. E. Launder and D. B. Spalding. *Mathematical Models of Turbulence*. London/New York: Academic Press, 1972. DOI: 10.1002/zamm.19730530619. URL: http://doi.wiley.com/10.1002/zamm.19730530619.

[148] B. J. Lee, May Fun Liou, and Meng Sing Liou. "Conceptual aerodynamic design of a tail-cone thruster system under axi-symmetric inlet distortion". In: *Proceedings of the ASME Turbo Expo*. Vol. 2A-2018. American Society of Mechanical Engineers (ASME), 2018. ISBN: 9780791850992. DOI: 10.1115/GT2018-75861.

[149] Bram van Leer. "Towards the ultimate conservative difference scheme. V. A second-order sequel to Godunov's method". In: *Journal of Computational Physics* 32.1 (1979), pp. 101–136. ISSN: 10902716. DOI: 10.1016/0021-9991(79)90145-1. URL: https://www.sciencedirect.com/science/article/pii/0021999179901451.

[150] Ruiwu Lei, Junqiang Bai, and Danyang Xu. "Aerodynamic optimization of civil aircraft with wing-mounted engine jet based on adjoint method". In: *Aerospace Science and Technology* 93 (2019), p. 105285. ISSN: 12709638. DOI: 10.1016/j.ast.2019.07.018. URL: https://www.sciencedirect.com/science/article/pii/S1270963819310491?via{\%}3Dihub.

[151] Randall J. LeVeque. *Finite Volume Methods for Hyperbolic Problems*. Cambridge University Press, 2002. ISBN: 9780521810876. DOI: 10.1017/CBO9780511791253. URL: https://www.cambridge.org/core/product/identifier/9780511791253/type/book.

[152] Bo Li et al. "Development and application of a throughflow method for high-loaded axial flow compressors". In: *Science China Technological Sciences* 59.1 (2016), pp. 93–108. ISSN: 1862281X. DOI: 10.1007/s11431-015-5947-4. URL: http://link.springer.com/10.1007/s11431-015-5947-4.

[153] Jing Li et al. "Aerodynamic design optimization of nacelle/pylon position on an aircraft". In: *Chinese Journal of Aeronautics* 26.4 (2013), pp. 850–857. ISSN: 10009361. DOI: 10.1016/j.cja.2013.04.052. URL: https://www.sciencedirect.com/science/article/pii/S1000936113001039?via{\%}3Dihub.

[154] Qiushi Li et al. "Development of a coupled supersonic inlet-fan Navier–Stokes simulation method". In: *Chinese Journal of Aeronautics* 31.2 (2018), pp. 237–246. ISSN: 10009361. DOI: 10.1016/j.cja.2017.11.011. URL: https://www.sciencedirect.com/science/article/pii/S1000936117302583?via{\%}3Dihub.

[155] Kaili Liu et al. "NUMERICAL INVESTIGATION ON ENGINE INLET DISTORTION UNDER CROSSWIND FOR A COMMERCIAL TRANSPORT AIRCRAFT". In: *ICAS 2014*. ICAS, 2014, ICAS–98–5.6.1. URL: https://www.icas.org/ICAS_ARCHIVE/ICAS2014/data/papers/2014_0560_paper.pdf.

[156] Yilang Liu and Weiwei Zhang. "Accuracy preserving limiter for the high-order finite volume method on unstructured grids". In: *Computers and Fluids* 149 (2017), pp. 88 –99. ISSN: 0045-7930. DOI: https://doi.org/10.1016/j.compfluid.2017.03.008. URL: http://www.sciencedirect.com/science/article/pii/S0045793017300889.

[157] Emmanuel Lorin, Amine Ben Haj Ali, and Azzeddine Soulaimani. "An accurate positivity preserving scheme for the Spalart-Allmaras turbulence model. Application to aerodynamics". In: *Collection of Technical Papers - 36th AIAA Fluid Dynamics Conference*. Vol. 4. 2006, pp. 2270–2301. ISBN: 1563478102. DOI: 10.2514/6.2006-3743.

[158] Weiyu Lu et al. "Thermodynamic and aerodynamic analysis of an air-driven fan system in low-cost high-bypass-ratio turbofan engine". In: *Energies* 12.10 (2019), p. 1917. ISSN: 19961073. DOI: 10.3390/en12101917. URL: https://www.mdpi.com/1996-1073/12/10/1917.

[159] X. Y. Lu and C. Dalton. "Calculation of the timing of vortex formation from an oscillating cylinder". In: *Journal of Fluids and Structures* 10.5 (1996), pp. 527–541. ISSN: 08899746. DOI: 10.1006/jfls.1996.0035.

[160] Yunfei Ma et al. "Comparative studies of RANS versus large eddy simulation for fan-intake interaction". In: *Journal of Fluids Engineering, Transactions of the ASME* 141.3 (2019). ISSN: 1528901X. DOI: 10.1115/1.4041393. URL: https://asmedigitalcollection.asme.org/fluidsengineering/article/doi/10.1115/1.4041393/457725/Comparative-Studies-of-RANS-Versus-Large-Eddy.

[161] David G. MacManus et al. "Complex aeroengine intake ducts and dynamic distortion". In: *AIAA Journal*. Vol. 55. 7. American Institute of Aeronautics and Astronautics Inc., 2017, pp. 2395–2409. DOI: 10.2514/1.J054905. URL: https://arc.aiaa.org/doi/abs/10.2514/1.J054905.

[162] Benoit Malouin, Jean Yves Trépanier, and Éric Laurendeau. "Installation and interference drag decomposition via RANS far-field methods". In: *Aerospace Science and Technology* 54 (2016), pp. 132–142. ISSN: 12709638. DOI: 10.1016/j.ast.2016.04.020.

[163] Benoit Malouin et al. "Engine pre-entry thrust and standard net thrust evaluation based on the far-field method". In: *Aerospace Science and Technology* 45 (2015), pp. 50–59. ISSN: 12709638. DOI: 10.1016/j.ast.2015.04.014.

[164] Benoit Malouin et al. "Internal drag evaluation for a through-flow nacelle using a far-field approach". In: *Journal of Aircraft* 52.6 (2015), pp. 1847–1857. ISSN: 00218669. DOI: 10.2514/1.C033093.

[165] F. Marble. "Three Dimensional Flow in Turbomachines". In: *volume X of High Speed Aerodynamics and Jet Propulsion*. Ed. by William R. Hawthorne. Princeton Universit Press, 1964. ISBN: 9781400885985.

[166] Carlos Márquez Gutiérrez et al. "Validation of Actuator Disk Simulations of CROR Propulsion Systems at Low-Speed Flight Conditions". In: *30th AIAA Applied Aerodynamics Conference*. Reston, Virigina: American Institute of Aeronautics and Astronautics, 2012. ISBN: 978-1-62410-185-4. DOI: 10.2514/6.2012-2787. URL: http://arc.aiaa.org/doi/10.2514/6.2012-2787.

[167] D. J. Mavriplis and A. Jameson. "Multigrid solution of the Navier-Stokes equations on triangular meshes". In: *AIAA Journal* 28.8 (1990), pp. 1415–1425. ISSN: 00011452. DOI: 10.2514/3.25233.

[168] J. E. McCall, P. Tracksdorf, and K. Heining. "Advanced ducted engine nacelle aerodynamics and integration testing". In: *Journal of Engineering for Gas Turbines and Power* 114.4 (1992), pp. 802–808. ISSN: 15288919. DOI: 10.1115/1.2906660. URL: https://doi.org/10.1115/1.2906660.

[169] Bruce G. McKay. "Next generation propulsion & air vehicle considerations". In: *45th AIAA/ASME/SAE/ASEE Joint Propulsion Conference and Exhibit*. Reston, Virginia: American Institute of Aeronautics and Astronautics, 2009. ISBN: 9781563479762. DOI: 10.2514/6.2009-4803. URL: http://arc.aiaa.org/doi/abs/10.2514/6.2009-4803.

[170] M. Méheut et al. "Assessment of fan/airframe aerodynamic performance using 360° uRANS computations: Code-to-code comparison between ONERA, DLR, NLR and airbus". In: *AIAA Scitech 2019 Forum*. American Institute of Aeronautics and Astronautics Inc, AIAA, 2019. DOI: 10.2514/6.2019-0582.

[171] Christopher Michalak and Carl Ollivier-Gooch. "Accuracy preserving limiter for the high-order accurate solution of the Euler equations". In: *Journal of Computational Physics* 228.23 (2009), pp. 8693–8711. ISSN: 0021-9991. DOI: 10.1016/J.JCP.2009.08.021. URL: https://www.sciencedirect.com/science/article/pii/S0021999109004641.

[172] Christopher Michalak and Carl Ollivier-Gooch. "Globalized matrix-explicit Newton-GMRES for the high-order accurate solution of the Euler equations". In: *Computers and Fluids* 39.7 (2010), pp. 1156–1167. ISSN: 00457930. DOI: 10.1016/j.compfluid.2010.02.008.

[173] MIDAP Study group. *Guide to in-Flight Thrust Measurement of Turbo- jets and Fan Engines. Agardograph No. 237, Technical Report No. AG-237*. Tech. rep. London: AGARD, 1979.

[174] Kevin Mikkelsen and Richard Brasket. "An Equation Set for ASME Nozzle Discharge and Thrust Coefficients". In: *49th AIAA Aerospace Sciences Meeting*. 2011. DOI: 10.2514/6.2011-1265. URL: https://arc.aiaa.org/doi/abs/10.2514/6.2011-1265.

[175] Kevin L. Mikkelsen et al. "Initial subscale performance measurements of the AIAA dual separate flow reference (DSFR) nozzle". In: *51st AIAA/SAE/ASEE Joint Propulsion Conference*. 2015. ISBN: 9781624103216. DOI: 10.2514/6.2015-3883. URL: https://arc.aiaa.org/doi/abs/10.2514/6.2015-3883.

[176] D. L. Motycka. "Reynolds number and fan/inlet coupling effects on subsonic transportinlet distortion". In: *Journal of Propulsion and Power* 1.3 (1985), pp. 229–234. ISSN: 07484658. DOI: 10.2514/3.22785. URL: http://arc.aiaa.org/doi/10.2514/3.22785.

[177] F. Moukalled, L. Mangani, and M. Darwish. *The Finite Volume Method in Computational Fluid Dynamics*. Vol. 113. Fluid Mechanics and Its Applications. Cham: Springer International Publishing, 2016. ISBN: 978-3-319-16873-9. DOI: 10.1007/978-3-319-16874-6. URL: http://link.springer.com/10.1007/978-3-319-16874-6.

[178] NASA. *NASA DPW*. URL: https://aiaa-dpw.larc.nasa.gov/ (visited on 02/20/2020).

[179] NASA. *Turbulence Modeling Resource*. 2020. URL: https://turbmodels.larc.nasa.gov/ (visited on 02/25/2020).

[180] Amir Nejat and Carl Ollivier-Gooch. "A high-order accurate unstructured finite volume Newton-Krylov algorithm for inviscid compressible flows". In: *Journal of Computational Physics* 227.4 (2008), pp. 2582–2609. ISSN: 10902716. DOI: 10.1016/j.jcp.2007.11.011. URL: http://arc.aiaa.org/doi/10.2514/6.2005-5341.

[181] Hiroaki Nishikawa. "Beyond interface gradient: A general principle for constructing diffusion schemes". In: *40th AIAA Fluid Dynamics Conference*. Reston, Virigina: American Institute of Aeronautics and Astronautics, 2010. ISBN: 9781617389221. DOI: 10.2514/6.2010-5093. URL: http://arc.aiaa.org/doi/10.2514/6.2010-5093.

[182] Hiroaki Nishikawa. "Efficient gradient stencils for robust implicit finite-volume solver convergence on distorted grids". In: *Journal of Computational Physics* 386 (2019), pp. 486–501. ISSN: 0021-9991. DOI: 10.1016/J.JCP.2019.02.026. URL: https://www.sciencedirect.com/science/article/pii/S0021999119301433?via{\%}3Dihub.

[183] Hiroaki Nishikawa. "From hyperbolic diffusion scheme to gradient method: Implicit Green–Gauss gradients for unstructured grids". In: *Journal of Computational Physics* 372 (2018), pp. 126–160. ISSN: 0021-9991. DOI: 10.1016/J.JCP.2018.06.019. URL: https://www.sciencedirect.com/science/article/pii/S0021999118303978?via{\%}3Dihub.

[184] F. Noera and A. Satta. "Through Flow Calculation in Axial Flow Turbines Using a Quasi-Orthogonal Solver". In: *Volume 1: Turbomachinery*. American Society of Mechanical Engineers, 1998. ISBN: 978-0-7918-7862-0. DOI: 10.1115/98-GT-503. URL: https://asmedigitalcollection.asme.org/GT/proceedings/GT1998/78620/Stockholm,Sweden/248632.

[185] Guilherme Oliveira, Luis Gustavo Trapp, and Antonini Puppin-Macedo. "Engine-Airframe Integration Methodology for Regional Jet Aircrafts with Underwing Engines". In: *41st Aerospace Sciences Meeting and Exhibit*. Reston, Viriginia: American Institute of Aeronautics and Astronautics, 2003. ISBN: 978-1-62410-099-4. DOI: 10.2514/6.2003-934. URL: http://arc.aiaa.org/doi/10.2514/6.2003-934.

[186] Carl Ollivier-Gooch and Michael Van Altena. "A High-Order-Accurate Unstructured Mesh Finite-Volume Scheme for the Advection–Diffusion Equation". In: *Journal of Computational Physics* 181.2 (2002), pp. 729–752. ISSN: 0021-9991. DOI: 10.1006/JCPH.2002.7159. URL: https://www.sciencedirect.com/science/article/pii/S0021999102971597.

[187] Paul Orkwis and Kirk Vanden. "On the accuracy of numerical versus analytical Jacobians". In: American Institute of Aeronautics and Astronautics (AIAA), 1994. DOI: 10.2514/6.1994-176.

[188] Evelyn Otero and Peter Eliasson. "Acceleration on stretched meshes with line-implicit LU-SGS in parallel implementation". In: *International Journal of Computational Fluid Dynamics* 29.2 (2015), pp. 133–149. ISSN: 10290257. DOI: 10.1080/10618562.2015.1021692.

[189] John J. Otter et al. "Installation aerodynamics of civil aero-engine exhaust systems". In: *Aerospace Science and Technology* 89 (2019), pp. 345–355. ISSN: 12709638. DOI: 10.1016/j.ast.2019.03.046. URL: https://www.sciencedirect.com/science/article/pii/S1270963818315815?via{\%}3Dihub.

[190] Roberto Pacciani, Michele Marconcini, and Andrea Arnone. "A CFD Based Throughflow Method With Three-Dimensional Flow Features Modelling". In: *12th European Conference on Turbomachinery Fluid Dynamics and Thermodynamics, ETC 2017*. Vol. 2. 3. Multidisciplinary Digital Publishing Institute, 2017, p. 11. DOI: 10.3390/ijtpp2030011. URL: http://www.mdpi.com/2504-186X/2/3/11.

[191] Roberto Pacciani et al. "A CFD-based throughflow method with an explicit body force model and an adaptive formulation for the S2 streamsurface". In: *Proceedings of the Institution of Mechanical Engineers, Part A: Journal of Power and Energy* 230.1 (2016), pp. 16–28. ISSN: 20412967. DOI: 10.1177/0957650915607091. URL: http://journals.sagepub.com/doi/10.1177/0957650915607091.

[192] Jin Seok Park, Sung Hwan Yoon, and Chongam Kim. "Multi-dimensional limiting process for hyperbolic conservation laws on unstructured grids". In: *Journal of Computational Physics* 229.3 (2010), pp. 788–812. ISSN: 10902716. DOI: 10.1016/j.jcp.2009.10.011. URL: https://www.sciencedirect.com/science/article/pii/S0021999109005567?via{\%}3Dihub.

[193] M. Parsani et al. "Implicit LU-SGS algorithm for high-order methods on unstructured grid with p-multigrid strategy for solving the steady Navier-Stokes equations". In: *Journal of Computational Physics* 229.3 (2010), pp. 828–850. ISSN: 10902716. DOI: 10.1016/j.jcp.2009.10.014.

[194] Suhas Vasant Patankar. "Heat and mass transfer in turbulent boundary layers". PhD Thesis. Imperial College London, 1967. URL: https://spiral.imperial.ac.uk/handle/10044/1/17489.

[195] A. Patel. "Assessment of a Body Force Representation for Compressor Stability Estimation". Master Thesis. Massachusetts Institute of Technology, 2009.

[196] Krishna Patel. "A Novel Numerical Approach for Generation and Propagation of Rotor-Stator Interaction Noise". Master Thesis. University of Windsor, 2016.

[197] N. J. Peacock and J. H.R. Sadler. "Advanced propulsion systems for large subsonic transports". In: *Journal of Propulsion and Power* 8.3 (1992), pp. 703–708. ISSN: 07484658. DOI: 10.2514/3.23535.

[198] Oren Peles and Eli Turkel. "Acceleration methods for multi-physics compressible flow". In: *Journal of Computational Physics* 358 (2018), pp. 201–234. ISSN: 10902716. DOI: 10.1016/j.jcp.2017.10.011.

[199] G. Persico and S. Rebay. "A penalty formulation for the throughflow modeling of turbomachinery". In: *Computers and Fluids* 60 (2012), pp. 86–98. ISSN: 00457930. DOI: 10.1016/j.compfluid.2012.03.001. URL: https://www.sciencedirect.com/science/article/abs/pii/S0045793012000886.

[200] Andreas Peters. "Ultra-Short Nacelles for Low Fan Pressure Ratio Propulsors". PhD Thesis. Massachusetts Institute of Technology, 2014.

[201] Andreas Peters et al. "Ultra-short nacelles for low fan pressure ratio propulsors". In: *Proceedings of the ASME Turbo Expo*. Vol. 1A. 2. American Society of Mechanical Engineers Digital Collection, 2014. ISBN: 9780791845578. DOI: 10.1115/GT2014-26208. URL: https://asmedigitalcollection.asme.org/turbomachinery/article/doi/10.1115/1.4028235/378472/Ultrashort-Nacelles-for-Low-Fan-Pressure-Ratio.

[202] Milan V. Petrovic and Alexander Wiedermann. "Through-flow analysis of air-cooled gas turbines". In: *Proceedings of the ASME Turbo Expo*. Vol. 8. PARTS A, B, AND C. American Society of Mechanical Engineers Digital Collection, 2012, pp. 2363–2372. ISBN: 9780791844748. DOI: 10.1115/GT2012-69854. URL: https://asmedigitalcollection.asme.org/turbomachinery/article/doi/10.1115/1.4023463/378079/ThroughFlow-Analysis-of-AirCooled-Gas-Turbines.

[203] N. B. Petrovskaya. "Data dependent weights in discontinuous weighted least-squares approximation with anisotropic support". In: *Calcolo* 48.1 (2011), pp. 127–143. ISSN: 0008-0624. DOI: 10.1007/s10092-010-0032-7. URL: http://link.springer.com/10.1007/s10092-010-0032-7.

[204] Chi-Tuân Pham. *Viscous flux and turbulence models linearization for aerodynamic shape optimization for turbomachineries*. Tech. rep. 2006. URL: https://pastel.archives-ouvertes.fr/pastel-00002058.

[205] A. Pinelli et al. "Immersed-boundary methods for general finite-difference and finite-volume Navier-Stokes solvers". In: *Journal of Computational Physics* 229.24 (2010), pp. 9073–9091. ISSN: 10902716. DOI: 10.1016/j.jcp.2010.08.021.

[206] Sergio Pirozzoli. *Numerical Methods for High-Speed Flows*. Tech. rep. Rome: Università di Roma - La Sapienza, 2010, p. 37.

[207] A. P. Plas et al. "Performance of a Boundary Layer Ingesting (BLI) propulsion system". In: *Collection of Technical Papers - 45th AIAA Aerospace Sciences Meeting*. Vol. 8. Reston, Virigina: American Institute of Aeronautics and Astronautics, 2007, pp. 5368–5388. ISBN: 1563478900. DOI: 10.2514/6.2007-450. URL: http://arc.aiaa.org/doi/10.2514/6.2007-450.

[208] Gary G. Podboy et al. *Fan Noise Source Diagnostic Test - LDV Measured Flow Field Results*. Tech. rep. Cleveland, Ohio: NASA Glenn Research Center, 2003, p. 33.

[209] Gary G. Podboy et al. *Steady and Unsteady Flow Field Measurements Within a NASA 22-Inch Fan Model*. Tech. rep. Cleveland, Ohio: NASA Glenn Research Center, 2003, p. 35.

[210] H. Riahi et al. "A pressure-corrected Immersed Boundary Method for the numerical simulation of compressible flows". In: *Journal of Computational Physics* 374 (2018), pp. 361–383. ISSN: 10902716. DOI: 10.1016/j.jcp.2018.07.033.

[211] Martina Ricci et al. "CFD-Based Throughflow Analysis of Transonic Flows in Steam Turbines". In: *Journal of Turbomachinery* (2019), pp. 1–20. DOI: 10.1115/1.4044871. URL: https://asmedigitalcollection.asme.org/GT/proceedings/GT2019/58578/Phoenix,Arizona,USA/1066564https://doi.org/10.1115/1.4044871.

[212] Sebastian Ritter. "Impact of different UHBR-engine positions on the aerodynamics of a high-liftwing". In: *Notes on Numerical Fluid Mechanics and Multidisciplinary Design* 131 (2016), pp. 367–380. ISSN: 16122909. DOI: 10.1007/978-3-319-21127-5_22. URL: http://link.springer.com/10.1007/978-3-319-21127-5{_}22.

[213] Melissa B. Rivers and Ashley Dittberner. "Experimental Investigations of the NASA Common Research Model". In: *Journal of Aircraft* 51.4 (2014), pp. 1183–1193. ISSN: 0021-8669. DOI: 10.2514/1.C032626. URL: http://arc.aiaa.org/doi/10.2514/1.C032626.

[214] Matthew Robinson, David G MacManus, and Christopher Sheaf. "Aspects of aero-engine nacelle drag". In: *Proceedings of the Institution of Mechanical Engineers, Part G: Journal of Aerospace Engineering* 233.5 (2019), pp. 1667–1682. ISSN: 20413025. DOI: 10.1177/0954410018765574. URL: http://journals.sagepub.com/doi/10.1177/0954410018765574.

[215] Matthew Robinson et al. "Short and slim nacelle design for ultra-high BPR engines". In: *AIAA SciTech Forum - 55th AIAA Aerospace Sciences Meeting*. American Institute of Aeronautics and Astronautics Inc., 2017. ISBN: 9781624104473. DOI: 10.2514/6.2017-0707.

[216] P L Roe and J Pike. "Efficient Construction and Utilisation of Approximate Riemann Solutions". In: *Proc. Of the Sixth Int'L. Symposium on Computing Methods in Applied Sciences and Engineering, VI*. Amsterdam, The Netherlands, The Netherlands: North-Holland Publishing Co., 1985, pp. 499–518. ISBN: 0-444-87597-2. URL: http://dl.acm.org/citation.cfm?id=4673.4820.

[217] Ralf Rudnik, Cord Christian Rossow, and Heiko Frhr V. Geyr. "Numerical simulation of engine/airframe integration for high-bypass engines". In: *Aerospace Science and Technology* 6.1 (2002), pp. 31–42. ISSN: 12709638. DOI: 10.1016/S1270-9638(01)01139-7. URL: https://www.sciencedirect.com/science/article/pii/S1270963801011397.

[218] Yannis Sadoudi. "Simulation numérique de l'interaction soufflante/nacelle en présence de vent de travers". PhD thesis. Université de Tolouse - ISAE, 2016.

[219] SAE. *Advanced Ducted Propulsor In-Flight Thrust Determination AIR540*. Tech. rep. Troy, Michigan USA: SAE International, 2014, p. 392.

[220] SAE. *Gas Turbine Engine Inlet Flow Distortion Guidelines*. Aerospace Recommended Practice. Society of Automotive Engineering, 1978.

[221] SAE. *Inlet Total-Pressure-Distortion Considerations for Gas-Turbine Engines*. Aerospace Information Report. Society of Automotive Engineering, 1994.

[222] Andreas Schmitz, Marcel Aulich, and Eberhard Nicke. "Novel approach for loss and flow-turning prediction using optimized surrogate models in two-dimensional compressor design". In: *Proceedings of the ASME Turbo Expo*. Vol. 7. PARTS A, B, AND C. ASMEDC, 2011, pp. 1103–1114. ISBN: 9780791854679. DOI: 10.1115/GT2011-45086. URL: https://asmedigitalcollection.asme.org/GT/proceedings/GT2011/54679/1103/358092.

[223] Andreas Schmitz et al. "Novel performance prediction of a transonic 4.5 stage compressor". In: *Proceedings of the ASME Turbo Expo*. Vol. 8. PARTS A, B, AND C. American Society of Mechanical Engineers, 2012, pp. 2123–2134. ISBN: 9780791844748. DOI: 10.1115/GT2012-69003. URL: https://asmedigitalcollection.asme.org/GT/proceedings/GT2012/44748/2123/365346.

[224] Rainer Schnell et al. "Integration- and intake-induced flow distortions and their impact on aerodynamic fan performance". In: *Notes on Numerical Fluid Mechanics and Multidisciplinary Design*. Ed. by Rolf Radespiel et al. Vol. 131. Springer, Cham, 2016, pp. 251–269. DOI: 10.1007/978-3-319-21127-5_15. URL: http://link.springer.com/10.1007/978-3-319-21127-5{_}15.

[225] Dirk Schoenweitz, Marius Theune, and Rainer Schnell. "Inlet Distortion Sensitivity of Fans with Different Pressure Ratios". In: *ISABE-2015*. 2015.

[226] Carsten W. Schulz-Rinne, James P. Collins, and Harland M. Glaz. "Numerical Solution of the Riemann Problem for Two-Dimensional Gas Dynamics". In: *SIAM Journal on Scientific Computing* 14.6 (1993), pp. 1394–1414. ISSN: 1064-8275. DOI: 10.1137/0914082.

[227] Subhankar Sen, Sanjay Mittal, and Gautam Biswas. "Steady separated flow past a circular cylinder at low Reynolds numbers". In: *Journal of Fluid Mechanics* 620 (2009), pp. 89–119. ISSN: 00221120. DOI: 10.1017/S0022112008004904.

[228] Patrick R. Shea et al. "Turbine powered simulator calibration and testing for hybrid wing body powered airframe integration". In: *54th AIAA Aerospace Sciences Meeting*. 2016. ISBN: 9781624103933. DOI: 10.2514/6.2016-0011. URL: https://arc.aiaa.org/doi/abs/10.2514/6.2016-0011.

[229] Chun Shen et al. "Implementation of density-based implicit LU-SGS solver in the framework of OpenFOAM". In: *Advances in Engineering Software* 91 (2016), pp. 80–88. ISSN: 18735339. DOI: 10.1016/j.advengsoft.2015.10.007.

[230] Nikhil Vijay Shende and Yair Mor–Yossef. "Robust implementation of the Spalart-Allmaras turbulence model for unstructured grid". In: *ECCOMAS CFD 2010*. Lisboa, Portugal, 2005. URL: http://congress2.cimne.com/eccomas/proceedings/cfd2010/papers/01387.pdf.

[231] Chi-Wang Shu. *Numerical Methods for Hyperbolic Conservation Laws*. Tech. rep. DAM - Brown University, 2006.

[232] Thierry Sibilli and Mark Savill. "Computational fluid dynamics drag prediction and decomposition for propulsive system integration". In: *Proceedings of the ASME Turbo Expo*. Vol. 1. American Society of Mechanical Engineers Digital Collection, 2011, pp. 257–264. ISBN: 9780791854617. DOI: 10.1115/GT2011-46214.

[233] Thierry Sibilli et al. "Numerical Simulation of Propulsion System Integration for Very High Bypass Ratio Engines". In: *Volume 1: Aircraft Engine; Ceramics; Coal, Biomass and Alternative Fuels; Controls, Diagnostics and Instrumentation*. American Society of Mechanical Engineers, 2012, pp. 185–193. ISBN: 978-0-7918-4467-0. DOI: 10.1115/GT2012-68908. URL: https://asmedigitalcollection.asme.org/GT/proceedings/GT2012/44670/185/289193.

[234] Jean-Francois Simon. "Contribution to Throughflow Modelling for Axial Flow Turbomachine". PhD Thesis. Université de Liège, 2007.

[235] Jean-François Simon and Olivier Léonard. "Modeling of 3-D losses and deviations in a throughflow analysis tool". In: *Journal of Thermal Science* 16.3 (2007), pp. 208–214. ISSN: 1003-2169. DOI: 10.1007/s11630-007-0208-x. URL: http://link.springer.com/10.1007/s11630-007-0208-x.

[236] J.F. Simon, J. P. Thomas, and O. Léonard. "On the Role of the Deterministic and Circumferential Stresses in Throughflow Calculations". In: *Journal of Turbomachinery* 131.3 (2009). ISSN: 0889-504X. DOI: 10.1115/1.2992514. URL: https://asmedigitalcollection.asme.org/turbomachinery/article/doi/10.1115/1.2992514/462408/On-the-Role-of-the-Deterministic-and.

[237] M. Sivapragasam et al. "An air jet distortion generation system". In: *International Journal of Rotating Machinery* 2014 (2014). ISSN: 15423034. DOI: 10.1155/2014/961452.

[238] Stephen C. Smith, Marian Nemec, and Steven E. Krist. "Integrated nacelle-wing shape optimization for an Ultra- High Bypass fanjet installation on a single-aisle transport configuration". In: *51st AIAA Aerospace Sciences Meeting including the New Horizons Forum and Aerospace Exposition 2013*. Reston, Viriginia: American Institute of Aeronautics and Astronautics, 2013. ISBN: 9781624101816. DOI: 10.2514/6.2013-543. URL: http://arc.aiaa.org/doi/10.2514/6.2013-543.

[239] Emre Sozer, Christoph Brehm, and Cetin C. Kiris. *Gradient Calculation Methods on Arbitrary Polyhedral Unstructured Meshes for Cell-Centered CFD Solvers*. Tech. rep. NASA, 2014. URL: https://ntrs.nasa.gov/search.jsp?R=20140011550.

[240] P. R. Spalart and S. R. Allmaras. "One-equation turbulence model for aerodynamic flows". In: *Recherche aerospatiale* 1 (1994), pp. 5–21. ISSN: 00341223. DOI: 10.2514/6.1992-439.

[241] Raymond J. Spiteri and Steven J. Ruuth. "A new class of optimal high-order strong-stability-preserving time discretization methods". In: *SIAM Journal on Numerical Analysis* 40.2 (2002), pp. 469–491. ISSN: 00361429. DOI: 10.1137/S0036142901389025.

[242] A. Spurr. "The prediction of 3D transonic flow in turbomachinery using a combined throughflow and blade-to-blade time marching method". In: *Topics in Catalysis* 2.4 (1980), pp. 189–199. ISSN: 0142727X. DOI: 10.1016/0142-727X(80)90013-2. URL: https://www.sciencedirect.com/science/article/pii/0142727X80900132.

[243] Tomasz P Stańkowski et al. "Aerodynamics of aero-engine installation". In: *Proceedings of the Institution of Mechanical Engineers, Part G: Journal of Aerospace Engineering* 230.14 (2016), pp. 2673–2692. ISSN: 0954-4100. DOI: 10.1177/0954410016630332. URL: http://journals.sagepub.com/doi/10.1177/0954410016630332.

[244] Arne Stuermer. "DLR TAU-Code uRANS Turbofan Modeling for Aircraft Aerodynamics Investigations". In: *Aerospace* 6.11 (2019), p. 121. ISSN: 2226-4310. DOI: 10.3390/aerospace6110121. URL: https://www.mdpi.com/2226-4310/6/11/121.

[245] A. Sturmayr and C. Hirsch. "Shock Representation by Euler Throughflow Models and Comparison with Pitch-Averaged Navier-Stokes Solutions. . ISABE". In: *ISABE-99* (1999), pp. 99–7281. URL: https://apps.dtic.mil/docs/citations/ADA373363.

[246] P. K. Sweby. "HIGH RESOLUTION SCHEMES USING FLUX LIMITERS FOR HYPERBOLIC CONSERVATION LAWS." In: *SIAM Journal on Numerical Analysis* 21.5 (1984), pp. 995–1011. ISSN: 00361429. DOI: 10.1137/0721062. URL: https://www.jstor.org/stable/2156939.

[247] Alexandros Syrakos et al. "A critical analysis of some popular methods for the discretisation of the gradient operator in finite volume methods". In: *Physics of Fluids* 29.12 (2017), p. 127103. ISSN: 1070-6631. DOI: 10.1063/1.4997682. URL: http://aip.scitation.org/doi/10.1063/1.4997682.

[248] Alexandros Syrakos et al. "A critical analysis of some popular methods for the discretisation of the gradient operator in finite volume methods". In: *Physics of Fluids* 29.12 (2017), p. 127103. ISSN: 1070-6631. DOI: 10.1063/1.4997682. URL: http://aip.scitation.org/doi/10.1063/1.4997682.

[249] Fernando Tejero et al. "Effects of Aircraft Integration on Compact Nacelle Aerodynamics". In: American Institute of Aeronautics and Astronautics (AIAA), 2020. DOI: 10.2514/6.2020-2225.

[250] Fernando Tejero et al. "Multi-objective optimisation of short nacelles for high bypass ratio engines". In: *Aerospace Science and Technology* 91 (2019), pp. 410–421. ISSN: 12709638. DOI: 10.1016/j.ast.2019.02.014.

[251] William Thollet. "Body force modeling of fan-airframe interactions". PhD thesis. Université de Tolouse - ISAE, 2017.

[252] William Thollet et al. "Assessment of body force methodologies for the analysis of intake-fan aerodynamic interactions". In: *Proceedings of the ASME Turbo Expo*. Vol. 2C-2016. American Society of Mechanical Engineers, 2016. ISBN: 9780791849712. DOI: 10.1115/GT2016-57014. URL: https://asmedigitalcollection.asme.org/GT/proceedings/GT2016/49712/Seoul,SouthKorea/236620.

[253] William Thollet et al. "Body-force modeling for aerodynamic analysis of air intake – fan interactions". In: *International Journal of Numerical Methods for Heat & Fluid Flow* 26.7 (2016), pp. 2048–2065. ISSN: 0961-5539. DOI: 10.1108/HFF-07-2015-0274. URL: https://www.emerald.com/insight/content/doi/10.1108/HFF-07-2015-0274/full/html.

[254] J. P. Thomas and O. Léonard. "Toward a High Order Throughflow—Investigation of the Nonlinear Harmonic Method Coupled With an Immersed Boundary Method for the Modeling of the Circumferential Stresses". In: *Journal of Turbomachinery* 134.1 (2012). ISSN: 0889-504X. DOI: 10.1115/1.4003256. URL: https://asmedigitalcollection.asme.org/turbomachinery/article/doi/10.1115/1.4003256/468915/Toward-a-High-Order-ThroughflowInvestigation-of.

[255] R. L. Thornock and E. F. Brown. "An experimental study of compressible flow through convergent-conical nozzles, including a comparison with theoretical results". In: *Journal of Fluids Engineering, Transactions of the ASME* 94.4 (1972), pp. 926–930. ISSN: 1528901X. DOI: 10.1115/1.3425591. URL: https://doi.org/10.1115/1.3425591.

[256] Russel L. Thornock. "Comparison of Participant Analyses with Experimental Results for Conical Nozzle Flowfields and Performance". In: American Institute of Aeronautics and Astronautics (AIAA), 2013. DOI: 10.2514/6.2013-3735.

[257] Russel L. Thornock. "Propulsion AerodynamicWorkshop II, Summary of Participant Results for a Dual Separate Flow Reference Nozzle, Including Some Experimental Results". In: American Institute of Aeronautics and Astronautics (AIAA), 2016. DOI: 10.2514/6.2016-4503.

[258] Tinoco and Edward N. *An Evaluation and Recommendations for Further CFD Research Based on the NASA Common Research Model (CRM) Analysis from the AIAA Drag Prediction Workshop (DPW) Series*. Tech. rep. Seattle, WA: Boeing Company and NASA, 2019. URL: https://ntrs.nasa.gov/search.jsp?R=20190027400.

[259] Edward N. Tinoco et al. "Summary Data from the Sixth AIAA CFD Drag Prediction Workshop: CRM Cases". In: *Journal of Aircraft* 55.4 (2018), pp. 1352–1379. ISSN: 0021-8669. DOI: 10.2514/1.C034409. URL: https://arc.aiaa.org/doi/10.2514/1.C034409.

[260] Renato Tognaccini. "Drag computation and breakdown in power-on conditions". In: *Journal of Aircraft* 42.1 (2005), pp. 245–252. ISSN: 00218669. DOI: 10.2514/1.8510.

[261] Daniel M. Tompkins et al. "Experimental validation of modifications to a TDI model 2700 turbine powered simulator to simulate a high-bypass ratio engine". In: *50th AIAA/ASME/SAE/ASEE Joint Propulsion Conference 2014*. 2014. ISBN: 9781624103032. DOI: 10.2514/6.2014-3888. URL: https://arc.aiaa.org/doi/abs/10.2514/6.2014-3888.

[262] Eleuterio F. Toro. *Riemann solvers and numerical methods for fluid dynamics: A practical introduction*. Berlin, Heidelberg: Springer Berlin Heidelberg, 2009, pp. 1–724. ISBN: 9783540252023. DOI: 10.1007/b79761. URL: http://link.springer.com/10.1007/b79761.

[263] M. Trautmann et al. "Modifications to the gradient schemes on unstructured cell centered grids for the accurate determination of gradients near conductivity changes". In: *Physics of Fluids* 31.4 (2019), p. 047104. ISSN: 1070-6631. DOI: 10.1063/1.5089734. URL: http://aip.scitation.org/doi/10.1063/1.5089734.

[264] D. J. Tritton. "Experiments on the flow past a circular cylinder at low Reynolds numbers". In: *Journal of Fluid Mechanics* 6.4 (1959), pp. 547–567. ISSN: 14697645. DOI: 10.1017/S0022112059000829.

[265] Panagiotis Tsoutsanis. "Extended bounds limiter for high-order finite-volume schemes on unstructured meshes". In: *Journal of Computational Physics* 362 (2018), pp. 69–94. ISSN: 0021-9991. DOI: 10.1016/J.JCP.2018.02.009. URL: https://www.sciencedirect.com/science/article/pii/S0021999118300858?via{\%}3Dihub.

[266] P. G. Tucker. "Differential equation-based wall distance computation for DES and RANS". In: *Journal of Computational Physics* 190.1 (2003), pp. 229–248. ISSN: 00219991. DOI: 10.1016/S0021-9991(03)00272-9.

[267] Paul G. Tucker et al. "Computations of wall distances based on differential equations". In: *AIAA Journal* 43.3 (2005), pp. 539–549. ISSN: 00011452. DOI: 10.2514/1.8626.

[268] Daniel L. Tweedt. *Computational Aerodynamic Simulations of a 1215 ft/sec Tip Speed Transonic Fan System Model for Acoustic Methods Assessment and Development*. Tech. rep. Cleveland, Ohio: AP Solutions, Inc., 2014, p. 54.

[269] James C. Tyacke, Zhong-Nan Wang, and Paul G. Tucker. "LES-RANS of installed ultra-high-bypass-ratio coaxial jet aeroacoustics with flight stream". In: *AIAA Journal* 57.3 (2019), pp. 1215–1236. ISSN: 00011452. DOI: 10.2514/1.J057057.

[270] Simon Übelacker, Rainer Hain, and Christian J. Kähler. "Flow investigations in a stalling nacelle inlet under disturbed inflow". In: *Notes on Numerical Fluid Mechanics and Multidisciplinary Design* 131 (2016). Ed. by Rolf Radespiel et al., pp. 271–283. ISSN: 16122909. DOI: 10.1007/978-3-319-21127-5_16. URL: http://link.springer.com/10.1007/978-3-319-21127-5{_}16.

[271] Makoto Ueno et al. "Far-field drag analysis of NASA common research model simulations by JAXA". In: *20th AIAA Computational Fluid Dynamics Conference 2011*. 2011. ISBN: 9781624101489. DOI: 10.2514/6.2011-3699.

[272] Bram Van Leer. "Towards the ultimate conservative difference scheme III. Upstream-centered finite-difference schemes for ideal compressible flow". In: *Journal of Computational Physics* 23.3 (1977), pp. 263–275. ISSN: 10902716. DOI: 10.1016/0021-9991(77)90094-8. URL: https://www.sciencedirect.com/science/article/pii/0021999177900948.

[273] Bram Van Leer. "Towards the ultimate conservative difference scheme. IV. A new approach to numerical convection". In: *Journal of Computational Physics* 23.3 (1977), pp. 276–299. ISSN: 10902716. DOI: 10.1016/0021-9991(77)90095-X. URL: https://www.sciencedirect.com/science/article/pii/002199917790095X.

[274] Dale E. Van Zante et al. *Testing and Performance Verifi cation of a High Bypass Ratio Turbofan Rotor in an Internal Flow Component Test Facility*. Tech. rep. Cleveland, Ohio: NASA Glenn Research Center, 2009, p. 26.

[275] Marcos Vanella and Elias Balaras. "A moving-least-squares reconstruction for embedded-boundary formulations". In: *Journal of Computational Physics* 228.18 (2009), pp. 6617–6628. ISSN: 10902716. DOI: 10.1016/j.jcp.2009.06.003.

[276] Francesco De Vanna, Francesco Picano, and Ernesto Benini. "A sharp-interface immersed boundary method for moving objects in compressible viscous flows". In: *Computers and Fluids* 201 (2020), p. 104415. ISSN: 0045-7930. DOI: https://doi.org/10.1016/j.compfluid.2019.104415. URL: http://www.sciencedirect.com/science/article/pii/S0045793019303731.

[277] John Vassberg et al. "Development of a Common Research Model for Applied CFD Validation Studies". In: *26th AIAA Applied Aerodynamics Conference*. 2008. DOI: 10.2514/6.2008-6919. eprint: https://arc.aiaa.org/doi/pdf/10.2514/6.2008-6919. URL: https://arc.aiaa.org/doi/abs/10.2514/6.2008-6919.

[278] V. Venkatakrishnan. "Convergence to Steady State Solutions of the Euler Equations on Unstructured Grids with Limiters". In: *Journal of Computational Physics* 118.1 (1995), pp. 120–130. ISSN: 00219991. DOI: 10.1006/jcph.1995.1084. URL: https://www.sciencedirect.com/science/article/pii/S0021999185710844.

[279] Jan B. Vos, Stephane Sanchi, and Alain Gehri. "DPW4 results using different grids including near-field/far-field drag analysis". In: *28th AIAA Applied Aerodynamics Conference*. Vol. 1. American Institute of Aeronautics and Astronautics Inc., 2010. ISBN: 9781617389269. DOI: 10.2514/6.2010-4552.

[280] A Vuillemin, O Piccin, and R Davy. "Installation Effects Characterization of VHBR Engines–Part I: Experimental Setup and Wind Tunnel Improvement". In: *AIAA/CEAS Aeroacoustics Conference*. AIAA, 2007.

[281] Thomas K. III Walker. "The Development and Requirements of a Body Force Database from Two-Dimensional and Streamline Curvature Calculations". Master Thesis. Massachusetts Institute of Technology, 2009.

[282] Gang Wang, Yuewen Jiang, and Zhengyin Ye. "An improved LU-SGS implicit scheme for high Reynolds number flow computations on hybrid unstructured mesh". In: *Chinese Journal of Aeronautics* 25.1 (2012), pp. 33–41. ISSN: 10009361. DOI: 10.1016/S1000-9361(11)60359-2.

[283] Zhong Nan Wang, James Tyacke, and Paul Tucker. *Large eddy simulation of serration effects on an ultra-high-bypass-ratio engine exhaust jet*. 2018. DOI: 10.1016/j.crme.2018.07.003.

[284] Fabian Wartzek et al. "Realistic inlet distortion patterns interacting with a transonic compressor stage". In: *Notes on Numerical Fluid Mechanics and Multidisciplinary Design*. Ed. by Rolf Radespiel et al. Vol. 131. Springer, Cham, 2016, pp. 285–302. DOI: 10.1007/978-3-319-21127-5_17. URL: http://link.springer.com/10.1007/978-3-319-21127-5{_}17.

[285] Rob Watson et al. "Improved hierarchical modelling for aerodynamically coupled systems". In: *Proceedings of the ASME Turbo Expo*. Vol. 2B-2017. American Society of Mechanical Engineers, 2017. ISBN: 9780791850794. DOI: 10.1115/GT2017-65223. URL: https://asmedigitalcollection.asme.org/GT/proceedings/GT2017/50794/Charlotte,NorthCarolina,USA/241523.

[286] H. R. Welge and J. R. Ongarato. "Powered engine simulator procedures and experience for the DC-10 wing engine". In: *Journal of Aircraft* 8.7 (1971), pp. 523–529. ISSN: 00218669. DOI: 10.2514/3.59132. URL: https://doi.org/10.2514/3.59132.

[287] D.H. Wilkinson. *Calculation of Blade-to-Blade Flow in a Turbomachine by Streamline Curvature*. Tech. rep. Central Electricity Generating Board, 1970. URL: http://naca.central.cranfield.ac.uk/reports/arc/rm/3704.pdf.

[288] W.B. de Wolf. *Possibilities and Limitations of VHBR and UHBPR Turbofan Simulations in Engine/Airframe Integration Wind Tunnel Experiments*. Tech. rep. Braunschweig: NLR, 1996, p. 25.

[289] Paul Woodward and Phillip Colella. *The numerical simulation of two-dimensional fluid flow with strong shocks*. 1984. DOI: 10.1016/0021-9991(84)90142-6.

[290] Frank L. Wright. "Comparison of least squares curve fit and individual sample statistical analysis results of calibration data for the velocity coefficient of a flow nacelle". In: *AIAA 25th Plasmadynamics and Lasers Conference, 1994*. 1994. DOI: 10.2514/6.1994-2587. URL: https://arc.aiaa.org/doi/abs/10.2514/6.1994-2587.

[291] Michael J. Wright, Graham V. Candler, and Marco Prampolini. "Data-parallel lower-upper relaxation method for the navier-stokes equations". In: *AIAA Journal* 34.7 (1996), pp. 1371–1377. ISSN: 00011452. DOI: 10.2514/3.13242.

[292] Hao Xia and Paul G. Tucker. "Finite volume distance field and its application to medial axis transforms". In: *International Journal for Numerical Methods in Engineering* 82.1 (2009), n/a–n/a. ISSN: 00295981. DOI: 10.1002/nme.2762. URL: http://doi.wiley.com/10.1002/nme.2762.

[293] Jing Lei Xu, Chao Yan, and Jing Jing Fan. "Computations of wall distances by solving a transport equation". In: *Applied Mathematics and Mechanics (English Edition)* 32.2 (2011), pp. 141–150. ISSN: 02534827. DOI: 10.1007/s10483-011-1401-8.

[294] Xinyu Yang, Hailong Tang, and Min Chen. "Performance modeling and optimization assessment of variable pitch fan for ultrafan engine". In: *2018 Joint Propulsion Conference*. American Institute of Aeronautics and Astronautics Inc, AIAA, 2018. DOI: 10.2514/6.2018-4400.

[295] Shuai Ye et al. "The implementation of an implicit LU-SGS scheme steady solver based on OpenFOAM". In: *2017 3rd IEEE International Conference on Computer and Communications, ICCC 2017*. Vol. 2018-Janua. Institute of Electrical and Electronics Engineers Inc., 2018, pp. 2484–2489. ISBN: 9781509063505. DOI: 10.1109/CompComm.2017.8322982.

[296] Dennis Yoder, Vance Dippold, and Nicholas Georfiadis. *Wind-US Results for the AIAA 1st Propulsion Aerodynamics Workshop*. AIAA 1st Propulsion Aerodynamics Workshop. 2012.

[297] Dennis Yoder, Vance Dippold, and Nicholas Georfiadis. *Wind-US Results for the AIAA 1st Propulsion Aerodynamics Workshop*. AIAA 2nd Propulsion Aerodynamics Workshop. 2012.

[298] H. Yoshihara. *AGARD Rep. No 712 Special course on subsonic/transonic aerodynamic interference for aircraft*. Tech. rep. Neuilly-sur-Seine: AGARD, 1983, p. 291.

[299] Sheng Tao Yu. *Convenient method to convert two-dimensional CFD codes into axisymmetric ones*. 1993. DOI: 10.2514/3.23649.

[300] Fan Zhang. *A vertex-weighted-Least-Squares gradient reconstruction*. Tech. rep. Dalian University of Technology, 2017. arXiv: 1702.04518. URL: http://arxiv.org/abs/1702.04518.

[301] Fan Zhang, Jun Liu, and Biaosong Chen. "Modified multi-dimensional limiting process with enhanced shock stability on unstructured grids". In: *Computers & Fluids* 161 (2018), pp. 171–188. ISSN: 0045-7930. DOI: 10.1016/J.COMPFLUID.2017.11.019. URL: https://www.sciencedirect.com/science/article/abs/pii/S0045793017304279?via{\%}3Dihub.

[302] J.B. Zhang. "Effects of treatment of the source terms in turbulent models on the convergence rate". In: *22nd ICAS CONGRESS 2000*. Harrogate, UK: ICAS, 2000. URL: https://www.icas.org/ICAS{_}ARCHIVE/ICAS2000/ABSTRACTS/ICA0732.HTM.

[303] Yufei Zhang et al. "Drag prediction method of powered-on civil aircraft based on thrust drag bookkeeping". In: *Chinese Journal of Aeronautics* 28.4 (2015), pp. 1023–1033. ISSN: 10009361. DOI: 10.1016/j.cja.2015.06.015.

[304] Yufei Zhang et al. "Performance prediction of conical nozzle using navier-stokes computation". In: *Journal of Propulsion and Power*. Vol. 31. 1. American Institute of Aeronautics and Astronautics Inc., 2015, pp. 192–203. DOI: 10.2514/1.B35164.

[305] R. A. Zimbrick and J. L. Colehour. "Investigation of very high bypass ratio engines for subsonic transports". In: *Journal of Propulsion and Power* 6.4 (1990), pp. 490–496. ISSN: 07484658. DOI: 10.2514/3.25461.